

Guoqiang Zhang
Gaolin Wang
Nannan Zhao
Dianguo Xu

Permanent Magnet Synchronous Motor Drives for Gearless Traction Elevators


 Springer


Permanent Magnet Synchronous Motor Drives for Gearless Traction Elevators


Guoqiang Zhang · Gaolin Wang · Nannan Zhao ·
Dianguo Xu

Permanent Magnet Synchronous Motor Drives for Gearless Traction Elevators

 Springer

Guoqiang Zhang 
School of Electrical Engineering
and Automation
Harbin Institute of Technology
Harbin, Heilongjiang, China

Gaolin Wang 
School of Electrical Engineering
and Automation
Harbin Institute of Technology
Harbin, Heilongjiang, China

Nannan Zhao 
School of Electrical Engineering
and Automation
Harbin Institute of Technology
Harbin, Heilongjiang, China

Dianguo Xu
School of Electrical Engineering
and Automation
Harbin Institute of Technology
Harbin, Heilongjiang, China

ISBN 978-981-16-9317-5 ISBN 978-981-16-9318-2 (eBook)
<https://doi.org/10.1007/978-981-16-9318-2>

© The Editor(s) (if applicable) and The Author(s), under exclusive license to Springer Nature Singapore Pte Ltd. 2022

This work is subject to copyright. All rights are solely and exclusively licensed by the Publisher, whether the whole or part of the material is concerned, specifically the rights of translation, reprinting, reuse of illustrations, recitation, broadcasting, reproduction on microfilms or in any other physical way, and transmission or information storage and retrieval, electronic adaptation, computer software, or by similar or dissimilar methodology now known or hereafter developed.

The use of general descriptive names, registered names, trademarks, service marks, etc. in this publication does not imply, even in the absence of a specific statement, that such names are exempt from the relevant protective laws and regulations and therefore free for general use.

The publisher, the authors and the editors are safe to assume that the advice and information in this book are believed to be true and accurate at the date of publication. Neither the publisher nor the authors or the editors give a warranty, expressed or implied, with respect to the material contained herein or for any errors or omissions that may have been made. The publisher remains neutral with regard to jurisdictional claims in published maps and institutional affiliations.

This Springer imprint is published by the registered company Springer Nature Singapore Pte Ltd.
The registered company address is: 152 Beach Road, #21-01/04 Gateway East, Singapore 189721, Singapore

Preface

This book focuses on the permanent magnet synchronous motor (PMSM) drives for gearless traction elevators. Both basic principles and experimental evaluation have been addressed. This is achieved by providing in-depth study on a number of major topics such as speed detection at low-speed operation, starting torque strategy based on dichotomy and staircase methods, fuzzy self-tuning method, MPC and ADRC. The comprehensive and systematic treatment of control strategies for cost-effective gearless PMSM traction elevators and practical issues are the major features of the book, which is particularly suited for readers who are interested to learn the control strategies for cost-effective gearless PMSM traction elevators. The book could benefit researchers, engineers and graduate students in fields of AC motor drives and control strategies for cost-effective gearless PMSM traction elevators, etc.

This book begins with an overview of PMSM traction system. The difference between geared and gearless traction elevators and the brief introduction of cost-effective gearless PMSM traction elevators are discussed in Chap. 1.

Chapter 2 presents the mathematical model of gearless PMSM traction elevators, including the vector control and the dynamic model of PMSM drives for gearless traction elevators.

Chapter 3 discusses the initial position detection for PMSM traction drives with low-cost incremental encoder. The high-frequency signal injection-based initial position detection is comprehensively illustrated.

Chapter 4 presents the speed detection method at low-speed operation. The speed detection based on NTD theory and the signal processing for the sin/cos encoder are discussed.

Weight-transducerless control is popular and necessary for cost-effective gearless PMSM traction elevators. From Chaps. 5–9, different weight-transducerless starting torque compensations of gearless PMSM drive are comprehensively discussed. Chapter 5 introduces the starting torque control based on dichotomy and staircase methods. The fuzzy self-tuning torque control strategy is illustrated in Chap. 6.

Chapter 7 presents the starting torque control strategy based on the offset-free model predictive control theory. The enhanced MPC for rollback mitigation is discussed in Chap. 8. And finally, Chap. 9 presents the ADRC strategy.

Harbin, China

Guoqiang Zhang
Gaolin Wang
Nannan Zhao
Dianguo Xu

Contents

1 Permanent Magnet Synchronous Motor Traction System—An Overview	1
1.1 Background	1
1.2 Geared Versus Gearless Traction Elevators	2
1.2.1 Energy Consumption	2
1.2.2 Volume	3
1.2.3 Use and Maintenance	3
1.3 Basic of PMSM Traction Machines	4
1.4 Applications of Low-Resolution Encoder in Elevators	5
1.5 Applications of Weight-Transducerless Elevators	7
1.6 Summary	9
References	9
2 Mathematical Model of Gearless PMSM Traction Elevators	11
2.1 Introduction	11
2.1.1 PMSM Applications	11
2.1.2 PMSM Classification	12
2.2 Mathematical Model of PMSM	15
2.2.1 Coordinate Transformation	15
2.2.2 Mathematical Model of SPMSM	23
2.2.3 Mathematical Model of IPMSM	26
2.3 Vector Control of PMSM	29
2.3.1 $i_d = 0$ Vector Control Mode	29
2.3.2 Maximum Torque Per Ampere Control	30
2.3.3 Flux-Weakening Control	32
2.4 Dynamic Model of Gearless PMSM Traction Elevators	34
2.5 Summary	36
References	37

3	Initial Position Detection for PMSM Traction Drives	39
3.1	Introduction	39
3.2	Basic Principle of Saliency-Tracking-Based Methods	41
3.2.1	HF Mathematical Model of PMSM	42
3.3	HF Sinusoidal Signal Injection-Based Method	43
3.3.1	HF Rotating Sinusoidal Signal Injection-Based Method	43
3.3.2	HF Pulsating Sinusoidal Signal Injection-Based Method	45
3.4	HF Square-Wave Signal Injection-Based Method	48
3.4.1	Basic Principle	48
3.4.2	Experimental Comparison	52
3.5	Initial Magnet Polarity Detection	55
3.5.1	Conventional Initial Magnet Polarity Detection Method	55
3.5.2	Proposed Continuous Initial Magnet Polarity Detection Method	59
3.6	Experimental Evaluation	60
3.7	Summary	66
	References	66
4	Speed Detection Method at Low-Speed Operation	67
4.1	Introduction	67
4.2	Limitation of the Conventional Speed Calculation	68
4.3	Speed Detection Based on the NTD Theory	69
4.4	Frequency–Response Analysis and Parameter Selection	74
4.5	Signal Processing of the SIN/COS Encoder	77
4.6	Simulation and Experimental Results	79
4.6.1	Simulation Results	79
4.6.2	Experimental Results	81
4.7	Summary	84
	References	86
5	Starting Torque Control Based on Dichotomy and Staircase Methods	89
5.1	Introduction	89
5.2	Torque Compensation Based on Dichotomy Method	90
5.3	Torque Compensation Based on Staircase Method	93
5.4	Experimental Evaluation	95
5.5	Summary	101
	References	102
6	Fuzzy Self-tuning Torque Control Strategy	105
6.1	Introduction	105
6.2	Analysis of the Brake Releasing Process	106
6.3	Starting Torque Control Strategy	109

- 6.4 Design of the Fuzzy Self-tuning Torque Compensator 112
- 6.5 Experimental Evaluation 116
- 6.6 Summary 116
- References 120
- 7 Starting Torque Control Strategy Based on Offset-Free Model**
- Predictive Control Theory** 123
- 7.1 Introduction 123
- 7.2 Dynamic Model of Elevator Traction System 124
- 7.3 Offset-Free MPC for Anti-rollback During the Elevator Startup 126
 - 7.3.1 Establishment of the Offset-Free MPC for Elevator Startup 126
 - 7.3.2 Cost Function Design 129
 - 7.3.3 Stability Analysis of the Proposed Speed Controller 130
- 7.4 Simulation and Experimental Evaluation 132
 - 7.4.1 Simulation Results 132
 - 7.4.2 Experimental Results 133
- 7.5 Summary 138
- References 140
- 8 Enhanced MPC for Rollback Mitigation During Elevator Startup** 141
- 8.1 Introduction 141
- 8.2 Analysis of the Conventional MPC 142
- 8.3 Establishment of the Enhanced MPC Speed Controller 144
- 8.4 Stability Analysis and Parameter Selection of the ESO 147
- 8.5 Application of the NTD in Speed Sampling 149
- 8.6 Analysis of Parameter Selection 151
- 8.7 Experimental Evaluation 152
 - 8.7.1 Experimental Setup 152
 - 8.7.2 Performance of NTD 153
 - 8.7.3 Performance of the Internal Current Loop Adopting PI Regulator 153
 - 8.7.4 Experimental Comparison Between Conventional and Proposed Enhanced MPC 154
 - 8.7.5 Control Performance Comparison of PI, Conventional MPC and Proposed Enhanced MPC 155
- 8.8 Summary 156
- References 160
- 9 ADRC Strategy for Gearless PMSM Traction Elevators** 163
- 9.1 Introduction 163
- 9.2 Establishment of ESO for Direct-Drive Elevator Traction System 164
- 9.3 Stability Analysis and Parameter Selection 167

- 9.4 NLEF Controller 171
- 9.5 Experimental Evaluation 174
 - 9.5.1 Experimental Setup 174
 - 9.5.2 Performance of the Inner Current Loop 175
 - 9.5.3 Experimental Results of ESO with Different Gain B 176
 - 9.5.4 Experimental Results of ESO Combining with NLEF 177
- 9.6 Summary 180
- References 180

Chapter 1

Permanent Magnet Synchronous Motor Traction System—An Overview



1.1 Background

As a vertical lifting vehicle, the elevator has become an important building equipment in high-rise buildings and public places [1]. With the development of computer technology and power electronics technology, the modern elevator has become a typical mechatronics product. The traction elevator is the most widely used modern elevator, and its core component is the traction machine and the corresponding control system. The traction machine used in elevators is mainly the permanent magnet synchronous traction machine and the traditional asynchronous traction machine. With the people's growing demand for the reliability and comfort of the elevator system, the permanent magnet synchronous elevator traction machine is more and more widely used in the elevator system, gradually replacing the asynchronous traction machine as the mainstream. At present, there are more than 400 registered elevator enterprises in China, but large foreign enterprises such as Otis, Schindler, KONE, Thyssen, Mitsubishi, Hitachi, Fujida and Toshiba account for nearly 80% of China's elevator market. Foreign investors gathered in China's elevator industry, almost all the world's large elevator companies entered China, and the most advanced elevator products competed to be produced in China. The introduction of advanced technology and advanced management has played a strong role in promoting domestic elevator enterprises.

The proposal and development of gearless traction, i.e., direct-drive traction technology, have brought the advantages of high efficiency and energy saving, space saving (no machine room or small machine room), good dynamic performance and convenient maintenance to the elevator system. Direct-drive traction technology has become the mainstream of the new traction technology. Modern elevators with direct-drive traction mode put forward higher requirements for traction machine control system, which are mainly reflected in starting comfort, low-speed stability, anti-disturbance robustness and high-efficiency operation. Traction machine is the heart of the elevator. However, the practical application of the gearless permanent magnet traction machine system in recent years also reflects the weakness of some key

technologies. Aiming at enriching the theoretical system of control methods for the modern gearless elevator permanent magnet traction system, this book provides some solutions to the corresponding key scientific problems and lays a theoretical basis for the application of the related key technologies.

1.2 Geared Versus Gearless Traction Elevators

In recent years, with the elevator industry steadily developing, the proportion of gearless traction machines in the elevator traction machine industry increases continuously. Compared with the traditional geared traction machine, the gearless traction machine has unique advantages. This chapter mainly compares two kinds of traction machines as shown in Fig. 1.1 from the perspective of application.

1.2.1 Energy Consumption

The permanent magnet synchronous gearless traction machine uses permanent magnets rather than an excitation current to generate a magnetic field. The mechanical transmission efficiency can reach 98% because the gear box is eliminated and the traction wheel is directly driven by the electric motor. And, the power factor of gearless traction machine can be close to 1 due to the synchronous motor. It can also be used as a generator to regenerate power when the elevator goes up with no load or when it goes down with rated load.

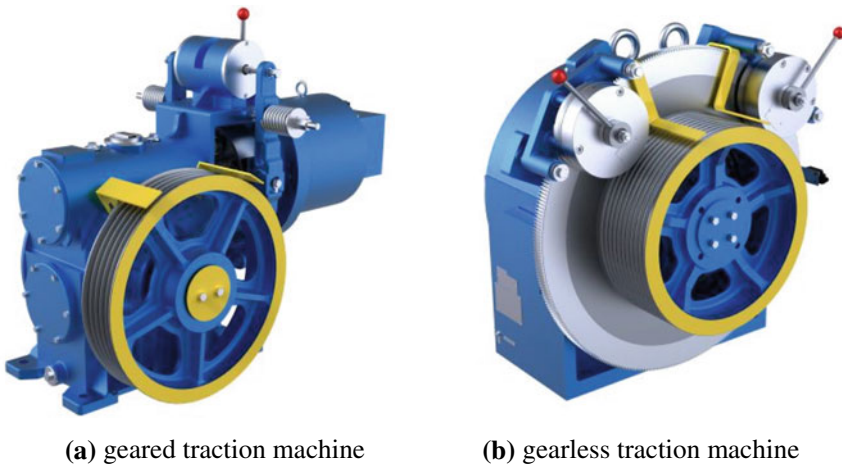


Fig. 1.1 Two kinds of elevator traction machines

The asynchronous geared traction machine uses an ordinary three-phase asynchronous motor. In order to generate a rotating magnetic field and electromagnetic force, the coil of stator and rotor needs to pass current. Due to the mechanical transmission structure in the transmission process, the transmission efficiency of asynchronous geared traction machine is only about 70%. The power factor of asynchronous traction machine is also low, which can only reach about 0.8 under rated load. This value will further reduce when the elevator switches between the state of starting and braking frequently.

1.2.2 Volume

The structure of permanent magnet synchronous gearless traction machine is compact and small in volume. Therefore, it can be used in a small space. However, the asynchronous geared traction machine is mainly suitable for elevators with cabin, which increases the building area and wastes public resources.

Due to the existence of a series of transmission mechanisms such as the worm and the worm gear, the traditional asynchronous geared traction machine usually occupies huge room. Therefore, in the construction process, buildings with asynchronous gear host are usually covered with elevator machine room above the hoistway to place asynchronous traction machine, gearbox and other transmission mechanisms. This not only wastes the available area for houses with tight construction area, but also amplifies the noise during operation due to the echo in the machine room, which has become a main factor affecting the quality of life for users. Without a transmission mechanism, PMSM gearless traction machine can effectively reduce the installation area compared with the geared traction machine. At the same time, it can also reduce the mechanical noise during operation.

1.2.3 Use and Maintenance

The mechanical structure of the gearless traction machine is simple because the traction machine is the directly driven motor and does not need a mechanical transmission mechanism. Simultaneously, there is no need for a complicated lubrication system because of the absence of mechanical mechanism, which reduces the environmental pollution.

The traditional geared traction machine needs a complex lubrication system to reduce the heat and mechanical wear caused by slippage. Therefore, the geared traction machine needs to replace the lubricating oil regularly, which not only increases the cost of maintenance, but also pollutes the environment unavoidably. What is more, since the hardness of the turbine material is lower than the worm, the surface of the gear may corrode progressively due to high friction and the root of the gear may fracture due to large bending stress.

1.3 Basic of PMSM Traction Machines

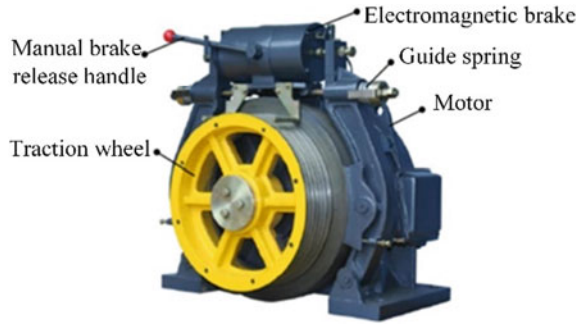
The introduction of permanent magnet synchronous motors into the elevator traction transmission field has enabled the rapid development of the gearless traction technology. In order to meet the low-speed operating conditions of the elevator, the number of pole pairs of the gearless induction motor must be large, which would increase the component of excitation current and reduce the efficiency. Since rotor magnetic field of the permanent magnet synchronous motor is established by permanent magnets, the stator current does not need to excite the magnetic field. Therefore, the operating efficiency of permanent magnet synchronous motor is high. Due to the complex structure, large space occupation, high manufacturing and maintenance costs, the DC gearless motor has been replaced by the AC motor. The permanent magnet synchronous motor also has the advantages of strong output torque capacity, great following and anti-disturbance performance due to the use of high magnetic energy material. Especially when running at low speed, the motor has accurate positioning, high-speed regulation accuracy and strong rapid response capability. By optimization design, the permanent magnet synchronous motor can run at low speed under large load torque, which gives full play to the advantages of gearless traction technology.

After more than a century of development, the structure of the traction machine has undergone an evolution from geared to gearless and the traction drive mode has been developed from traditional reel drive to friction traction, which not only greatly reduces the volume of the entire transmission system, but also increases the applicability of the system. However, the development of science and technology has made people have higher performance requirements for elevator products. The emergence of small machine room and machine room-less elevator products has promoted the development of elevator technology toward high efficiency, high transmission ratio, compact structure and low noise.

The elevator is mainly composed of a motor, a brake and a traction wheel. The brake is an essential component to ensure the safe work of elevator. When the elevator is running abnormally, the brake will apply a large braking friction force to the traction sheave through the guide springs on both sides, which will lock the traction sheave tightly. By holding the manual brake release handle and pressing it down, the brake can be manually opened. When the elevator is running normally, a large alternating current or direct current is needed to release the brake. When the elevator is running stably, only a small current is needed to maintain the released state of the brake. It is necessary to check whether the brake is already in the open state before the traction machine runs. If the traction machine runs without opening the brake, the system will carry a large load and generate a large current, which may cause the damage of the system. Furtherly, it may even damage the brakes and other safety components if no over-current protection measure is taken.

The traction wheel is also an important part of the gearless traction machine as shown in Fig. 1.2, whose quality is directly related to the operation of the elevator traction machine. The wire rope suspends the elevator car and the counterweight

Fig. 1.2 Diagram of permanent magnet traction elevator



through the traction wheel, and drives the car to move up and down. The groove pitch difference and diameter are the main parameters of the traction wheel, which have a relationship with the suspension ratio and speed of the traction machine. The appropriate wire rope must be selected according to the specific requirements, and the groove pitch diameter difference is an important factor to judge the quality of the traction sheave. If the groove pitch diameter difference is too large, the steel wire rope embedded in the traction sheave rope groove will be unevenly stressed and then the speed between the steel ropes will be slipping. These will further aggravate the groove pitch diameter difference and seriously affect the safety and longevity.

1.4 Applications of Low-Resolution Encoder in Elevators

In a high-performance vector control system for permanent magnet traction elevators, the closed-loop feedback of the motor speed and position is required. The control performance greatly depends on the accuracy of the rotor position. A high-precision encoder will be installed on the shaft section of traditional permanent magnet synchronous motor to accurately detect the position information. However, high-resolution sensors are expensive, which will increase the cost of the system. And, the cable and interface of high-precision encoder will increase the complexity of hardware and reduce the reliability. What is more, the installation of sensors increases the size and volume of the system. When working in harsh conditions, the high-precision encoder cannot work reliably due to the effect of environmental humidity and temperature. Therefore, low-resolution photoelectric encoders are still used to detect position and calculate rotation speed in some occasions.

The photoelectric encoder is a sensor that converts mechanical quantities into pulses or digital quantities through photoelectric conversion. The photoelectric encoder is composed of a circular code disk and a photoelectric detection device. The code disk is engraved with circular light-transmissive and opaque slits at equal intervals, which are called code channels. The rotating shaft rotates coaxially with the code disk at the same speed. The detection device is composed of electronic components such as light-emitting diodes. The pulse signal passing through the slit is output

by the detection device. The angle information of the current rotating shaft can be reflected by calculating the number of output pulses of the photoelectric encoder per second.

There are two types of photoelectric encoders; one is incremental photoelectric encoder, and the other is absolute photoelectric encoder. Incremental photoelectric encoder processes a series of pulses through an additional circuit to obtain a digital quantity. The code disk of the photoelectric encoder is generally made of glass material, whose surface is coated with a layer of opaque metal film. And, the code track is engraved on the film, the number of which ranges from several hundred to several thousand. In this way, the entire circumference of the code wheel is equally divided into n light-transmitting grooves. Incremental photoelectric encoders output three groups of square wave pulses of A-phase, B-phase and Z-phase, which follow the principle of photoelectric conversion. The A-phase and B-phase are used to determine the rotation direction of the code disk, of which the number is the same and the phase difference is 90° . And, the Z-phase is used for the reference point positioning. Every pulse of Z-phase represents one revolution of the code disk.

Absolute photoelectric encoders directly output digital quantities. There are several concentric code tracks which consist of light-transmissive and opaque sectors along the radial direction of the code disk. The number of code channels is equal to the number of binary digits on the code disk. The number of sectors between two adjacent code channels is doubled. The light source and the photosensitive element are on both sides of the code disk. The photosensitive elements convert corresponding level signals according to whether they receive light to form a binary number. The characteristic of absolute encoder is that the digital code can be read out at any position of the shaft. The number of code channels is proportional to the resolution. For example, an n -bit encoder must have n code channels. The accuracy of the absolute encoder depends on the number of bits of the code channel.

The absolute encoder can be directly connected to the computer without other digital conversion equipment since the output is binary digital code. The light-transmissive and opaque line patterns are the difference between an absolute encoder and an incremental encoder. Under the same accuracy, the code disk size of the incremental encoder is smaller than the absolute encoder. Since the incremental encoder cannot display the absolute position of the angle coordinate, it must be reset to zero every time after starting. The absolute encoder can directly read the value of the angle coordinate, and the information will not be lost after the power is cut off.

At present, a lot of researches have been carried out to investigate this issue. The literatures are mainly divided into model-based and non-model-based methods. The model-based method needs to detect the rotor position through the motor model and the parameters, such as Luenberger observer and sliding mode observer. The mechanical equation of PMSM is always used to ensure the estimated position converges to the actual one. Careful selection of the observer bandwidth is needed to ensure accurate estimation of the position and speed. A sliding mode control method combined with extended state observer (ESO) was presented to estimate the position and speed [2]. In this method, ESO was used to observe the lumped disturbance, which could obtain less observation error of position. A cascaded observer was proposed to reduce

the speed detection error in [3]. This observer used a second-order sliding mode controller to get the rotor position accurately. It needed to consider the system convergence carefully when using combination of two kinds of observers, which would increase the order of the system.

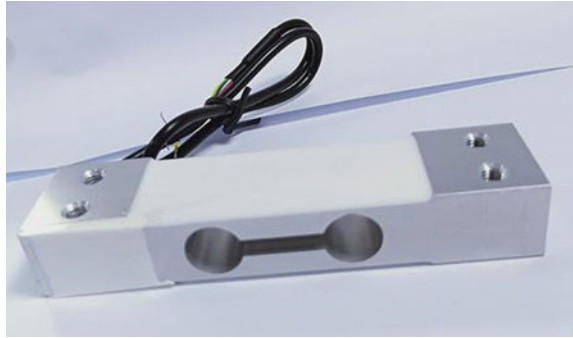
In order to improve the bandwidth of the position and speed observers, the adaptive law can be applied in the model-based method. The observers can adjust the response by adaptive law, which will help to improve the dynamic performance of the system. A sliding mode observer using the adaptive law based on the least square method was proposed to suppress the harmonics generated by the nonlinear characteristics of the inverter. Meanwhile, the adaptive law based on the frequency tracking controller was used to track the back-EMF of the motor according to the variation of operating frequency [4]. If the motor parameters are inaccurate, the high-precision rotor position would be difficult to obtain.

The non-model-based method is mainly divided into the interpolation method and the filtering method. For the interpolation method, the detection of position signal mainly depends on the selection of appropriate interpolation basis functions to predict the position of the next sampling period. The precision of the position signal after fitting is determined by the carrier frequency of the control system. In general, the precision is higher than that of the position signal obtained by the encoder. Therefore, the speed acquired by differential fitting position signal has fewer fluctuations. The fitting precision of the position is related to the selection of the interpolation basis function. The interpolation method tends to produce noise in rotor position, and it will cause the phase delay of the estimated position.

Another non-model-based method is the filtering method, which can obtain continuous position by dealing with the original discrete position signals. With the development of digital control system, filtering schemes are convenient to be used in the rotor position estimation. It can effectively extract the harmonics in the back-EMF signal. A least square adaptive filter was used to obtain the harmonics of the back-EMF, which can realize the frequency adaption [5]. The existing filtering method can estimate the rotor position and the speed using the lower-bits encoder such as Hall sensors. Once the resolution of the encoder increases, the harmonic frequencies in the rotor position would become higher. These methods have the common way of constructing harmonics, which could get distorted if the frequency of the harmonics is close to the PWM frequency of the system. Hence, it still needs further study in the filtering methods to improve the precision of position using the ordinary-resolution encoder in low-speed operation.

1.5 Applications of Weight-Transducerless Elevators

The weight transducer converts the quality signal into a measurable electrical signal as shown in Fig. 1.3. Classified by conversion method, it can be divided into eight types: photoelectric, hydraulic, electromagnetic force, capacitive, magnetic pole change form, vibrating gyroscope and resistance strain types. Among them, the resistance

Fig. 1.3 Weight transducer

strain-type weight transducer is most widely used. It is mainly composed of an elastic element, a resistance strain gauge, a measuring circuit and a transmission cable. When the elastic material occurs elastic deformation under the action of external force, the resistance strain gauge pasted on the material surface is also deformed. Then, the resistance value of strain gauge will change. Through measuring circuit, the change will be converted into voltage or current signal. This is the complete process of transforming external force into electrical signals by resistance strain-type weight transducer.

There is a trend toward using low-speed and large-torque permanent magnet traction machines to achieve gearless transmission in elevators. This kind of direct-drive elevator traction system has many advantages, such as great riding comfort, high efficiency, low mechanical noise and small space occupation. When the elevator starts, the mode of control will switch from leveling parking to running. If the electromagnetic brake is suddenly released during the conversion, the unknown load torque will be applied to the traction machine.

When the elevator starts, it switches from the leveling parking mode to the running mode. Considering that the electromagnetic brake is suddenly released during the conversion, the unknown load torque will be applied to the traction machine. During switching, considering that the electromagnetic brake is suddenly released, an unknown load torque will be applied. At this time, balancing the torque is particularly important to achieve the comfort experience of passengers. In order to achieve a balance between the electromagnetic torque and the load torque rapidly, the traditional control scheme is to install a weight transducer at the bottom of the elevator car. According to the feedback of torque from the weight transducer, the traction machine is controlled to generate electromagnetic torque.

However, the feedforward compensation has some disadvantages. The colinearity of the car load and the distortion of anti-vibration rubber will degrade when the usage time of weight transducer becomes longer. In addition, weight transducers will not only reduce the system robustness, but also increase the cost. Therefore, the weight-transducerless control is an emerging technique for the gearless elevator traction machine drives. During the brake releasing, when the elevator operates from the standby mode to the running mode, both the sliding distance and mechanical

vibration should be considered in order to ensure the riding comfort of the elevator. The generated torque of the traction machine must track the unknown load torque accurately and quickly. In this book, different kinds of weight-transducerless control strategies for PMSM traction drives are presented in the following.

1.6 Summary

This chapter provides a background on the development of the permanent magnet synchronous motor traction system. First, a detailed comparison is made between conventional geared traction machines and gearless traction machines in terms of energy consumption, volume together with use and maintenance. Through comparison, the superiority of the gearless traction machines is shown. Next, the basic of PMSM traction machines is presented, as well as the main technical problems encountered in the current application of PMSM traction machines. These include the application of low-resolution encoders in PMSM traction machines and the problems in the application of weight-transducerless elevators.

References

1. Feng L, Anwen S, Yinnan Z et al (2014) A rapid and high-accuracy control scheme of starting torque for elevators without a weight transducer. In: 2014 IEEE 23rd international symposium on industrial electronics (ISIE), pp 733–738
2. Wang Y, Feng Y, Zhang X et al (2020) A new reaching law for ant disturbance sliding-mode control of PMSM speed regulation system. *IEEE Trans Power Electron* 35(4):4117–4126
3. Liang D, Li J, Qu R et al (2018) Adaptive second-order sliding-mode observer for PMSM sensorless control considering VSI nonlinearity. *IEEE Trans Power Electron* 33(10):8994–9004
4. Bao D, Pan X, Wang Y et al (2018) Adaptive synchronous-frequency tracking-mode observer for the sensorless control of a surface PMSM. *IEEE Trans Ind Appl* 54(6):6460–6471
5. Wu X, Huang S, Liu K et al (2020) Enhanced position sensorless control using bilinear recursive least squares adaptive filter for interior permanent magnet synchronous motor. *IEEE Trans Power Electron* 35(1):681–698

Chapter 2

Mathematical Model of Gearless PMSM Traction Elevators



2.1 Introduction

2.1.1 PMSM Applications

Generally, the electrical motor is divided into three types, the DC motor, the induction motor (IM) and the synchronous motor. Among these types of motors, the PMSM has been widely developed in the industry and household applications for its high power density, high efficiency, high power factor and excellent control performance. The PMSM has been applied in these areas:

1. **The aeronautic and astronautic applications.** The requirements of the power density and the control performance are very strict in the aeronautic and astronautic applications. Hence, PMSM is a suitable choice for the aeronautic applications to reduce the launching cost of the whole system. Meanwhile, the high power density of PMSM drive system could improve the performance of the astronautic applications.
2. **The electric vehicle (EV) applications.** The EV is the future traffic solution, which is supported by worldwide governments and companies. Due to the rapid development of the EV, PMSM is widely applied as the power supply element for the high power density and high efficiency.
3. **The industry applications.** For high-performance equipment, such as the computer numerical control (CNC), the robot drives and the servo systems, the excellent control performance of PMSM could satisfy the requirements.
4. **The domestic appliance.** The high power density of PMSM could reduce the power cost of the drive system effectively, which is an important concern in the household applications, such as the vacuum cleaner, the washing machine, the air-conditioner and the refrigerator. Meanwhile, the direct-drive traction system could reduce the volume and enhance the reliability, compared with the conventional traction drive system using the IM drive system and the gear box.

5. **The fan and pump applications.** The power consumption of the fan and pump applications could be effectively reduced by applying the high-efficiency PMSM, which could reduce the whole power consumption and benefit the environment.
6. **Traction elevator system.** In high-rise buildings, the direct-drive traction machine system using PMSM can reduce volume, reduce cost and improve operation efficiency.

Hence, the PMSM has a promising future in the energy conversion applications, which deserves to be studied further. However, there are also some disadvantages of the PMSM influencing its application:

1. **The cost of the drive system.** The cost of PMSM drive system is relatively higher than the IM drive system, which is suitable for the applications concerning the high performance and the high efficiency, such as the aeronautics, astronautics, EV, CNC and servo drive system applications. As for the general industry applications, the drive system cost is an important issue; hence, it is necessary to optimize the design of PMSM to reduce the cost.
2. **Irreversible demagnetization.** Irreversible demagnetization could occur when the PMSM operates in excessively high temperature and low temperature. If the PMSM suffers inrush current or severe mechanical vibration, the irreversible demagnetization could also happen, which could reduce the performance of the motor or even disable the normal operation.

2.1.2 PMSM Classification

Despite these disadvantages, PMSM is so far the optimal solution of the future power energy conversion between the electric power and the mechanical power. The development of PMSM focuses on the high performance, high power density, high speed and high-level integration. There are many classification methods for PMSM. According to the position of the armature winding, it can be divided into the inner rotor type and the outer rotor type. According to the direction of the working magnetic field, it can be divided into the radial magnetic field type and the axial magnetic field type. According to the current waveform flowing through the armature winding, it can be divided into the permanent magnet brushless DC motor (PMBLDCM) powered by square wave or trapezoidal wave and PMSM powered by sine wave. According to the presence or absence of the starting winding on the rotor, it can be divided into PMSM without the starting winding and PMSM with the starting winding. The motor without the starting winding is powered by the inverter which starts and adjusts the speed along with the increase of the frequency. The motor with starting winding can not only operate at variable speeds, but also start at a certain frequency and voltage using the asynchronous torque generated by the starting winding [1, 2].

The most important difference between PMSM and other motors is the rotor magnetic circuit structure, which will be analyzed and discussed in detail. When the magnetic circuit is different, the performance, the control system, the manufacturing process and the applicable occasions of the motor are also different. According to the installation position of the permanent magnet on the rotor, PMSM can be divided into two types: surface permanent magnet synchronous motor (SPMSM) and interior permanent magnet synchronous motor (IPMSM). The permanent magnet of SPMSM is located on the surface of the rotor core, whereas the permanent magnet of IPMSM is located inside the rotor. For each rotor structure, a sinusoidal distribution of air gap magnetic field should be produced as much as possible.

The rotor magnetic circuit structure of SPMSM can also be divided into the raised type and the plug-in type. For the application of the rare earth in PMSM, the relative permeability of permanent magnet materials is close to 1. Therefore, the surface raised rotor belongs to non-salient pole rotor structure in terms of the electromagnetic performance, which leads to the symmetric orthogonal magnetic path, and the impedances of the d- and q-axes are the same ($X_d = X_q$). However, there is the ferromagnetic material between the two adjacent permanent magnetic poles of the surface plug-in rotor, so it belongs to the salient pole rotor structure in terms of electromagnetic performance. Hence, the orthogonal magnetic path magnetic circuit is asymmetrical, and $X_d > X_q$.

Figure 2.1a shows the surface raised rotor magnetic circuit structure. As for the simple structure, the lower manufacturing cost and the smaller moment of inertia, this kind of structure is widely used in PMBDCM and PMSM, which operate in a narrow constant power range. In addition, the permanent magnet poles in the surface raised rotor structure are easy to achieve the optimal design, which could make the air gap magnetic field close to the sinusoidal distribution. Hence, the surface-raised rotor magnetic circuit structure can significantly improve the performance of the motor and the entire drive system.

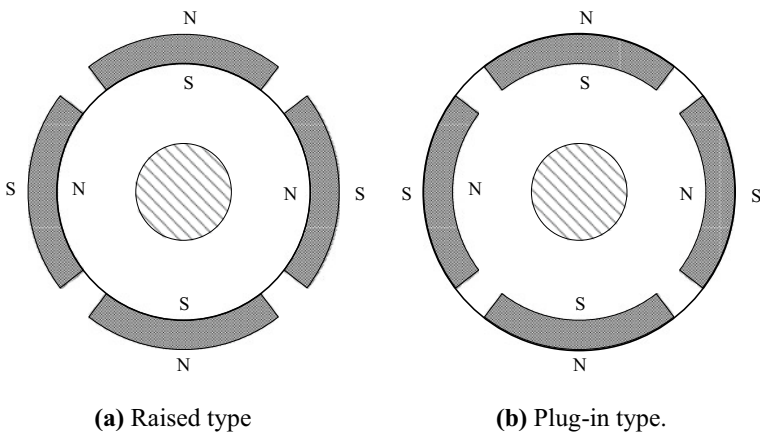


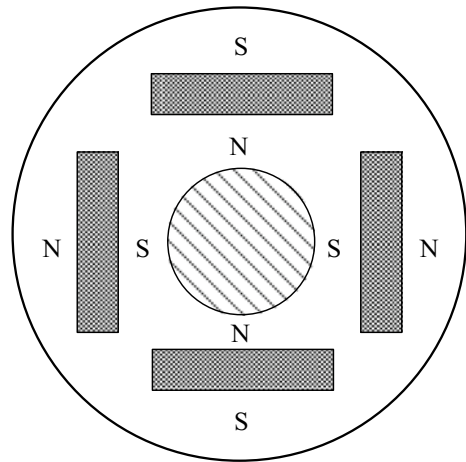
Fig. 2.1 Surface rotor magnetic circuit structure

Figure 2.1b shows the surface plug-in rotor magnetic circuit structure. This kind of structure can make full use of the reluctance torque generated by the asymmetry of the rotor magnetic circuit. Therefore, the power density and the dynamic performance of the motor can be improved compared with the motor with surface plug-in rotor structure. In addition, its manufacturing process is relatively simple. Hence, it is often used in some variable speed PMSMs. However, there are larger magnetic flux leakage and higher manufacturing costs of the motors with this kind of structure compared with the surface raised rotor structure.

As for the simpler manufacturing process and the lower cost of the rotor magnetic circuit structure, it is especially suitable to be applied in PMBDCM. However, as the starting winding cannot be installed on the rotor surface, there is no asynchronous starting capability and it is only suitable for occasions where the starting requirements are not strict.

Figure 2.2 shows the interior rotor magnetic circuit structure. Permanent magnets in the interior rotor are protected by pole pieces. The reluctance torque generated by the asymmetry of the rotor magnetic circuit structure can improve the overload capacity and the power density of the motor. Meanwhile, the d-axis inductance of IPMSM is usually larger than that of SPMSM, so it is easy to weaken the magnetic field and expand the operation speed. It should be noted that the X_d , X_q and X_d/X_q (saliency ratio) of IPMSM are different when the rotor magnetic circuit structure is different. Larger saliency ratio could improve the pull-in synchronization ability, the reluctance torque and the overload capability of the motor.

Fig. 2.2 Interior rotor magnetic circuit structure



2.2 Mathematical Model of PMSM

2.2.1 Coordinate Transformation

A. Coordinate Representation of the Vector Space

Let $\alpha_1, \alpha_2, \dots, \alpha_n$ be the linear independent vectors of the vector space F [3, 4], where

$$\alpha_1 = \begin{bmatrix} \alpha_{11} \\ \alpha_{12} \\ \vdots \\ \alpha_{1n} \end{bmatrix}, \alpha_2 = \begin{bmatrix} \alpha_{21} \\ \alpha_{22} \\ \vdots \\ \alpha_{2n} \end{bmatrix}, \dots, \alpha_n = \begin{bmatrix} \alpha_{n1} \\ \alpha_{n2} \\ \vdots \\ \alpha_{nn} \end{bmatrix}. \quad (2.1)$$

Then, any vector \mathbf{x} can be represented as

$$\mathbf{x} = x_1\alpha_1 + x_2\alpha_2 + \dots + x_n\alpha_n. \quad (2.2)$$

The vectors $\alpha_1, \alpha_2, \dots, \alpha_n$ are a basis of F , and $(x_1, x_2, x_n)^T$ is the coordinate of \mathbf{x} , where F is called as the n -dimensional vector space. It can be seen that there are many different bases of F , whereas the coordinate representation of \mathbf{x} is unique in a particular basis. Equation (2.2) could be presented as

$$\mathbf{x} = (\alpha_1, \alpha_2, \dots, \alpha_n) \begin{bmatrix} x_1 \\ x_2 \\ \vdots \\ x_n \end{bmatrix}. \quad (2.3)$$

Equation (2.3) is the general expression in the three-phase PMSM drive system, which could be generalized as

$$\begin{bmatrix} u_a \\ u_b \\ u_c \end{bmatrix} = \mathbf{R} \begin{bmatrix} i_a \\ i_b \\ i_c \end{bmatrix} + \mathbf{L} \frac{d}{dt} \begin{bmatrix} i_a \\ i_b \\ i_c \end{bmatrix} + \psi_f \mathbf{f}(\theta_e) \quad (2.4)$$

where $u_a, u_b, u_c, i_a, i_b, i_c, \mathbf{R}, \mathbf{L}, \psi_f$ and θ_e are the three-phase voltage vectors, the three-phase current vectors, the resistor matrix, the inductance matrix, the permanent magnet flux and the rotor position, respectively. As for the three-phase SPMSM, the inductance matrix mainly contains the self-inductance and the mutual inductance of the three-phase windings. Since the air gap of the SPMSM is uniform, the self-inductance and the mutual inductance of the three-phase windings are constant values and independent of the rotor position. As for the IPMSM, the air gap of the IPMSM is asymmetric; hence, the self-inductance and the mutual inductance of the three

-phase windings are closely related to the rotor position. The inductance matrices of both the SPMSM and the IPMSM are coupling and dependent of the rotor position.

B. Basis Transformation and Coordinate Transformation

Let vectors $\alpha_1, \alpha_2, \dots, \alpha_n$ and $\beta_1, \beta_2, \dots, \beta_n$ be two bases of the vector space. Any vector \mathbf{x} could be represented as

$$\mathbf{x} = (\alpha_1, \alpha_2, \dots, \alpha_n) \begin{bmatrix} x_{\alpha 1} \\ x_{\alpha 2} \\ \vdots \\ x_{\alpha n} \end{bmatrix} = (\beta_1, \beta_2, \dots, \beta_n) \begin{bmatrix} x_{\beta 1} \\ x_{\beta 2} \\ \vdots \\ x_{\beta n} \end{bmatrix} \quad (2.5)$$

where $\mathbf{x}_\alpha = (x_{\alpha 1}, x_{\alpha 2}, \dots, x_{\alpha n})^T$ and $\mathbf{x}_\beta = (x_{\beta 1}, x_{\beta 2}, \dots, x_{\beta n})^T$ are the coordinate representation at the two different bases. The relationship between the two bases could be presented as

$$(\beta_1, \beta_2, \dots, \beta_n) = (\alpha_1, \alpha_2, \dots, \alpha_n) \begin{bmatrix} p_{11} & p_{12} & \cdots & p_{1n} \\ p_{21} & p_{22} & \cdots & p_{2n} \\ \vdots & \vdots & & \vdots \\ p_{n1} & p_{n2} & \cdots & p_{nn} \end{bmatrix}. \quad (2.6)$$

Hence, the $n \times n$ nonsingular matrix transition matrix \mathbf{P} could be presented as

$$\mathbf{P} = \begin{bmatrix} p_{11} & p_{12} & \cdots & p_{1n} \\ p_{21} & p_{22} & \cdots & p_{2n} \\ \vdots & \vdots & & \vdots \\ p_{n1} & p_{n2} & \cdots & p_{nn} \end{bmatrix}. \quad (2.7)$$

\mathbf{P} could be applied to realize the transition between two bases $\alpha_1, \alpha_2, \dots, \alpha_n$ and $\beta_1, \beta_2, \dots, \beta_n$.

$$\begin{bmatrix} x_{\alpha 1} \\ x_{\alpha 2} \\ \vdots \\ x_{\alpha n} \end{bmatrix} = \begin{bmatrix} a_{11} & a_{12} & \cdots & a_{1n} \\ a_{21} & a_{22} & \cdots & a_{2n} \\ \vdots & \vdots & & \vdots \\ a_{n1} & a_{n2} & \cdots & a_{nn} \end{bmatrix} \begin{bmatrix} x_{\beta 1} \\ x_{\beta 2} \\ \vdots \\ x_{\beta n} \end{bmatrix} = \mathbf{P} \begin{bmatrix} x_{\beta 1} \\ x_{\beta 2} \\ \vdots \\ x_{\beta n} \end{bmatrix}. \quad (2.8)$$

C. Jordan Canonical Form Theorem and Diagonalization

The coupling effect in the motor drive system mainly exists in the inductance matrix, which needs to be specially considered in the motor control strategy. Hence, the decoupling control method is applied to eliminate the effect of the mutual inductance on the control performance. As for the existence of the

mutual inductance, the inductance matrix is similar to the circulant matrix, which could be presented as

$$A = \begin{bmatrix} a_1 & a_2 & a_3 & \cdots & a_n \\ a_n & a_1 & a_2 & \cdots & a_{n-1} \\ a_{n-1} & a_n & a_1 & \cdots & a_{n-2} \\ \vdots & \vdots & \vdots & \ddots & \vdots \\ a_2 & a_3 & a_n & \cdots & a_1 \end{bmatrix}. \quad (2.9)$$

The matrix A is defined as the circulant matrix, and the previous row forward one step is the next row. Hence, the decoupling method for A is essential to be concerned for the motor control strategy.

The diagonalization is an important tool to realize the decoupling control, which is closely related to the Jordan canonical form. The Jordan canonical form is formed of the Jordan block, and it is an upper triangular matrix that could be presented as

$$J_k(\lambda) = \begin{bmatrix} \lambda & 1 & & & \\ & \lambda & 1 & & \\ & & \lambda & \ddots & \\ & & & \ddots & 1 \\ & & & & \lambda \end{bmatrix}. \quad (2.10)$$

where λ is the unique Jordan block of a complex matrix. It could be transformed by the special matrix, which consists of the corresponding eigenvectors. There are k times of λ in the main diagonal, and all other elements are zero. The Jordan matrix consisting of the Jordan blocks could be presented as

$$J(\lambda) = \begin{bmatrix} J_{n1}(\lambda) & & & \\ & J_{n2}(\lambda) & & \\ & & \ddots & \\ & & & J_{nq}(\lambda) \end{bmatrix}. \quad (2.11)$$

The Jordan matrix $J(\lambda)$ plays an important role in the decoupling control strategy. The dynamic system could be totally decoupled by the transformation when the dimensional k of all the Jordan blocks of the coupled matrix is one. For the motor drive system, it is essential to study the diagonalization of the inductance matrix to realize the decoupling control.

The diagonalization transformation of a matrix is closely related to its eigenvalues and eigenvectors. The eigenvalue λ of the matrix A could be presented as

$$A\mathbf{x} = \lambda\mathbf{x}, \mathbf{x} \in C^n, \mathbf{x} \neq 0, \lambda \in C \quad (2.12)$$

where \mathbf{x} is the eigenvector corresponding to eigenvalue λ . If the matrix \mathbf{A} is regarded as a linear transformation, the effect of this transformation on the eigenvector \mathbf{x} is to expand (or shorten) λ times compared with the original vector.

The transformation matrix \mathbf{P} consists of all the eigenvectors, which could be presented as

$$\mathbf{P} = [\mathbf{P}_1 \mathbf{P}_2 \cdots \mathbf{P}_s]. \quad (2.13)$$

Hence, the relationship between the matrix \mathbf{A} and the transformation matrix \mathbf{P} could be presented as

$$\mathbf{AP} = \mathbf{P}\mathbf{J}(\lambda) = \mathbf{P} \begin{bmatrix} \mathbf{J}_1 & & & \\ & \mathbf{J}_2 & & \\ & & \ddots & \\ & & & \mathbf{J}_s \end{bmatrix} \quad (2.14)$$

where $\mathbf{J}(\lambda)$ is the Jordan matrix of matrix \mathbf{A} . According to the division of the Jordan blocks, the transformation between the matrix \mathbf{A} and the Jordan matrix $\mathbf{J}(\lambda)$ could be presented as

$$\begin{aligned} \mathbf{A}[\mathbf{P}_1 \mathbf{P}_2 \cdots \mathbf{P}_s] &= [\mathbf{P}_1 \mathbf{P}_2 \cdots \mathbf{P}_s]\mathbf{J}(\lambda) \\ &= [\mathbf{P}_1 \mathbf{P}_2 \cdots \mathbf{P}_s] \begin{bmatrix} \mathbf{J}_1 & & & \\ & \mathbf{J}_2 & & \\ & & \ddots & \\ & & & \mathbf{J}_s \end{bmatrix} \end{aligned} \quad (2.15)$$

where

$$[\mathbf{AP}_1 \mathbf{AP}_2 \cdots \mathbf{AP}_s] = [\mathbf{P}_1\mathbf{J}_1 \mathbf{P}_2\mathbf{J}_2 \cdots \mathbf{P}_s\mathbf{J}_s] \quad (2.16)$$

The relationship between every Jordan block and the matrix \mathbf{A} could be presented as

$$\mathbf{AP}_i = \mathbf{P}_i\mathbf{J}_i (i = 1, 2, \dots, s). \quad (2.17)$$

\mathbf{P}_i could be presented as

$$\mathbf{P}_i = (\mathbf{X}_{i1}, \mathbf{X}_{i2}, \dots, \mathbf{X}_{in_i}) \quad (2.18)$$

where $\mathbf{X}_{i1}, \mathbf{X}_{i2}, \dots, \mathbf{X}_{in_i}$ are the independent eigenvectors of the matrix \mathbf{A} . Substituting (2.18) into (2.17),

$$\begin{cases} \mathbf{A}\mathbf{X}_{i1} = \lambda_i \mathbf{X}_{i1} \\ \mathbf{A}\mathbf{X}_{i2} = \mathbf{X}_{i1} + \lambda_i \mathbf{X}_{i2} \\ \vdots \\ \mathbf{A}\mathbf{X}_{in_i} = \mathbf{X}_{in_i-1} + \lambda_i \mathbf{X}_{in_i} \end{cases} \quad (2.19)$$

It can be seen that \mathbf{X}_{i1} is the eigenvector of the matrix \mathbf{A} corresponding to eigenvalue λ_i . All other eigenvectors $\mathbf{X}_{i1}, \mathbf{X}_{i1}, \dots, \mathbf{X}_{in_i}$ could be obtained by (2.12). Hence, all the column vectors of \mathbf{P} could be calculated. Every Jordan block \mathbf{J}_i is corresponding to the eigenvalue λ_i . As for the eigenvalue λ_i , the number of the Jordan block \mathbf{J}_i is equal to its geometric multiplicity. The order of all the corresponding Jordan block \mathbf{J}_i for the eigenvalue λ_i is equal to its algebraic multiplicity.

D. Coordinate Frame in Motor Drives

The three-phase currents i_a, i_b and i_c of the three-phase PMSM could be presented as

$$\begin{cases} i_a = I_m \cos \omega_0 t \\ i_b = I_m \cos(\omega_0 t - \frac{2}{3}\pi) \\ i_c = I_m \cos(\omega_0 t + \frac{2}{3}\pi) \end{cases} \quad (2.20)$$

where I_m and ω_0 are the magnitude and the angular speed of the motor current, respectively. The symmetric three-phase currents could be presented in the space three-dimensional coordinate frame:

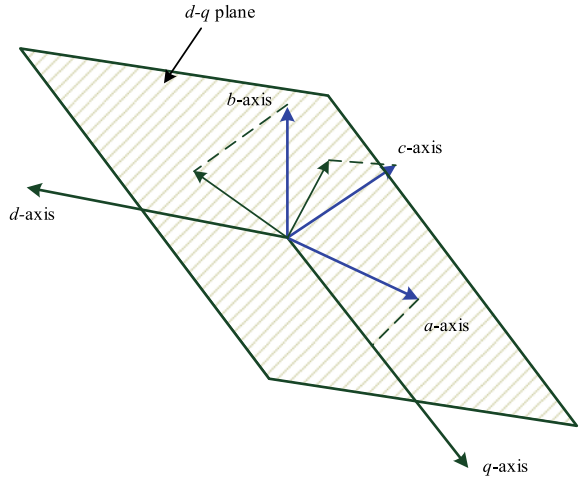
$$\begin{aligned} \mathbf{I} &= i_a \mathbf{i}_A + i_b \mathbf{i}_B + i_c \mathbf{i}_C \\ &= I_m \cos \omega_0 t \mathbf{i}_A + I_m \cos\left(\omega_0 t - \frac{2}{3}\pi\right) \mathbf{i}_B + I_m \cos\left(\omega_0 t + \frac{2}{3}\pi\right) \mathbf{i}_C \end{aligned} \quad (2.21)$$

where $\mathbf{i}_A, \mathbf{i}_B$ and \mathbf{i}_C are the unit vectors of the three-dimensional orthogonal frame, respectively. The magnitude of the vector \mathbf{I} could be presented as

$$|\mathbf{I}| = \sqrt{i_a^2 + i_b^2 + i_c^2} = I_m \sqrt{\cos^2 \omega_0 t + \cos^2 \omega_0 t + \cos^2 \omega_0 t} = \sqrt{\frac{3}{2}} I_m. \quad (2.22)$$

It can be seen that the vector \mathbf{I} rotates around the original point of the three-dimensional orthogonal frame. The magnitude and the angular speed of \mathbf{I} are $\sqrt{\frac{3}{2}} I_m$ and ω_0 , respectively. The trajectory of the rotation is a circle, and the projection of the trajectory in the frame is the three-phase current, which is shown in Fig. 2.3.

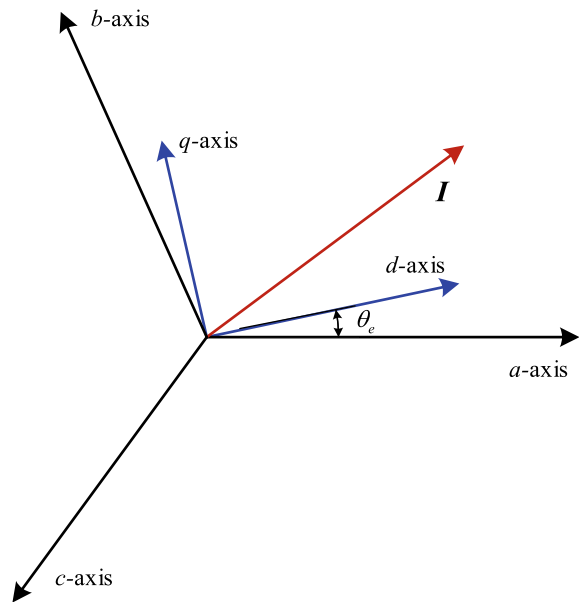
Fig. 2.3 Current vector I in the three-dimensional coordinate frame



The trajectory is located at a plane in the three-dimensional coordinate frame, which is defined as the d - q plane. All the transformations of the coordinate frame are carried out in this plane.

As analyzed in the previous section, the stationary a - b - c frame in the d - q plane is the projection of the three three-dimensional orthogonal coordinate frame, which is shown in Fig. 2.4.

Fig. 2.4 Current vector I in the d - q frame



It can be seen that the α - β orthogonal coordinate frame is defined in Fig. 2.4. The coordinate transformation is to transform the vector in the a - b - c frame to the d - q orthogonal coordinate frame. According to the previous analysis, the vector \mathbf{I} rotates around the original point with the angular speed ω_0 .

The coordinate transformation could be derived from the geometric view. The relationship between the α - β orthogonal coordinate frame and the a - b - c coordinate frame could be presented as

$$\begin{aligned} N_2 i_\alpha &= N_1 i_a + N_1 i_b \cos\left(\frac{2}{3}\pi\right) + N_1 i_c \cos\left(\frac{4}{3}\pi\right), \\ N_2 i_\beta &= N_1 i_b \cos\left(\frac{2}{3}\pi\right) + N_1 i_c \cos\left(\frac{4}{3}\pi\right), \end{aligned} \quad (2.23)$$

where i_α , i_β , N_1 and N_2 are the currents in the α - and β -axes, the number of turns in the windings, respectively. Hence, the transformation matrix between the a - b - c coordinate frame and the α - β orthogonal coordinate frame could be presented as

$$\begin{bmatrix} i_\alpha \\ i_\beta \\ i_0 \end{bmatrix} = \frac{N_1}{N_2} \begin{bmatrix} 1 & -\frac{1}{2} & -\frac{1}{2} \\ 0 & \frac{\sqrt{3}}{2} & -\frac{\sqrt{3}}{2} \\ \frac{1}{\sqrt{2}} & \frac{1}{\sqrt{2}} & \frac{1}{\sqrt{2}} \end{bmatrix} \begin{bmatrix} i_a \\ i_b \\ i_c \end{bmatrix} \quad (2.24)$$

where i_0 is the zero-sequence component of the three-phase currents. As for the three-phase star connection PMSM, the sum of the three-phase currents is zero and the corresponding zero-sequence component i_0 is also zero. Hence, i_0 will be ignored in this section to make the derivation process clearer. Hence, the simplified Clarke transformation could be presented as

$$\begin{bmatrix} i_\alpha \\ i_\beta \end{bmatrix} = \frac{N_1}{N_2} \begin{bmatrix} 1 & -\frac{1}{2} & -\frac{1}{2} \\ 0 & \frac{\sqrt{3}}{2} & -\frac{\sqrt{3}}{2} \end{bmatrix} \begin{bmatrix} i_a \\ i_b \\ i_c \end{bmatrix}. \quad (2.25)$$

The Clarke transformation could also be evaluated from the matrix transformation. The inductance matrix in the SPMSM could be presented as

$$L_{\text{SPM}} = \begin{bmatrix} L_{s\sigma} + L_m & -\frac{1}{2}L_m & -\frac{1}{2}L_m \\ -\frac{1}{2}L_m & L_{s\sigma} + L_m & -\frac{1}{2}L_m \\ -\frac{1}{2}L_m & -\frac{1}{2}L_m & L_{s\sigma} + L_m \end{bmatrix} \quad (2.26)$$

where $L_{s\sigma}$ and L_m are the leakage inductance and the excitation inductance of the three-phase windings, respectively. The coordinate transformation aims to realize the decoupling control of the coupled inductance matrix. According to the basis of the diagonalization transformation, the transformation matrix of the eigenvectors could

be applied to realize the Jordan canonical form transformation. The eigenvalues of the inductance matrix are the single root λ_1 and the double root $\lambda_{2,3}$, which could be presented as

$$\begin{aligned}\lambda_1 &= L_{s\sigma} \\ \lambda_{2,3} &= L_{s\sigma} + \frac{3}{2}L_m.\end{aligned}\quad (2.27)$$

Hence, the eigenvectors can be presented as

$$\mathbf{X}_1 = \begin{bmatrix} x_{11} \\ x_{11} \\ x_{11} \end{bmatrix}, \mathbf{X}_2 = \begin{bmatrix} x_{12} \\ x_{22} \\ -x_{12} - x_{22} \end{bmatrix}, \mathbf{X}_3 = \begin{bmatrix} x_{13} \\ x_{23} \\ x_{13} - x_{23} \end{bmatrix}.\quad (2.28)$$

The transformation matrix can be presented as

$$\mathbf{P} = \begin{bmatrix} x_{12} & x_{13} & x_{11} \\ x_{22} & x_{23} & x_{11} \\ -x_{12} - x_{22} & -x_{13} - x_{23} & x_{11} \end{bmatrix}.\quad (2.29)$$

The coordinate transformation between the a - b - c coordinate frame and the α - β orthogonal coordinate frame could be presented as

$$\begin{bmatrix} i_a \\ i_b \\ i_c \end{bmatrix} = \begin{bmatrix} x_{12} & x_{13} & x_{11} \\ x_{22} & x_{23} & x_{11} \\ -x_{12} - x_{22} & -x_{13} - x_{23} & x_{11} \end{bmatrix} \begin{bmatrix} i_\alpha \\ i_\beta \\ i_0 \end{bmatrix}.\quad (2.30)$$

The Jordan matrix for the inductance matrix of the three-phase SPMSM could be presented as

$$J(\lambda) = \begin{bmatrix} L_{s\sigma} + \frac{3}{2}L_m & & \\ & L_{s\sigma} + \frac{3}{2}L_m & \\ & & L_{s\sigma} + \frac{3}{2}L_m \end{bmatrix}.\quad (2.31)$$

Let the transformation matrix \mathbf{P} be a unit orthogonal matrix, the transformation matrix \mathbf{P} could be presented as

$$\mathbf{P} = \begin{bmatrix} \frac{\sqrt{6}}{3} & 0 & \frac{1}{\sqrt{3}} \\ -\frac{\sqrt{6}}{6} & \frac{\sqrt{2}}{2} & \frac{1}{\sqrt{3}} \\ -\frac{\sqrt{6}}{6} & -\frac{\sqrt{2}}{2} & \frac{1}{\sqrt{3}} \end{bmatrix}.\quad (2.32)$$

The equivalent transformation could be presented as

$$\begin{bmatrix} i_\alpha \\ i_\beta \\ i_0 \end{bmatrix} = \frac{2}{3} \begin{bmatrix} 1 & -\frac{1}{2} & -\frac{1}{2} \\ 0 & \frac{\sqrt{3}}{2} & -\frac{\sqrt{3}}{2} \\ \frac{1}{\sqrt{2}} & \frac{1}{\sqrt{2}} & \frac{1}{\sqrt{2}} \end{bmatrix} \begin{bmatrix} i_a \\ i_b \\ i_c \end{bmatrix}. \quad (2.33)$$

Actually, the coordinate transformation with the orthogonal matrix is the power invariance method, which means that the drive system power in the a - b - c coordinate frame and the α - β coordinate frame remains constant. As for another phase magnitude invariance method, the magnitude of the voltage and current in the a - b - c coordinate frame and the α - β coordinate frame remains constant, whereas the torque and the power should be multiplied by $3/2$ in the α - β frame to obtain the same values as those in the a - b - c coordinate frame. The transformation matrix \mathbf{P} in the α - β frame could be presented as

$$\begin{bmatrix} i_\alpha \\ i_\beta \\ i_0 \end{bmatrix} = \frac{2}{3} \begin{bmatrix} 1 & -\frac{1}{2} & -\frac{1}{2} \\ 0 & \frac{\sqrt{3}}{2} & -\frac{\sqrt{3}}{2} \\ \frac{1}{\sqrt{2}} & \frac{1}{\sqrt{2}} & \frac{1}{\sqrt{2}} \end{bmatrix} \begin{bmatrix} i_a \\ i_b \\ i_c \end{bmatrix}. \quad (2.34)$$

The α - β coordinate frame is the stationary frame, and the elements of the inductance matrix are closely related to the rotor angle; hence, it is essential to eliminate the change caused by the different values of the rotor angle. The Park transformation is applied to transform the variables in the stationary α - β coordinate frame to the rotating d - q coordinate frame. The transformation could be presented as

$$\begin{bmatrix} i_d \\ i_q \end{bmatrix} = \begin{bmatrix} \cos \theta_e & -\sin \theta_e \\ \sin \theta_e & \cos \theta_e \end{bmatrix} \begin{bmatrix} i_\alpha \\ i_\beta \end{bmatrix}, \quad (2.35)$$

$$\begin{bmatrix} i_\alpha \\ i_\beta \end{bmatrix} = \begin{bmatrix} \cos \theta_e & \sin \theta_e \\ -\sin \theta_e & \cos \theta_e \end{bmatrix} \begin{bmatrix} i_d \\ i_q \end{bmatrix}.$$

2.2.2 Mathematical Model of SPMSM

The mathematical modeling of PMSM is the key to realizing the vector control. To simplify the analysis, it is necessary to make the following assumptions: (1) The three-phase stator winding is distributed symmetrically in space and the discrete properties of its structure are ignored. Therefore, the armature reactive magneto motive force generated by stator windings in the air gap is sinusoidal, and the induced back-electromotive force (EMF) is also the sinusoidal wave. (2) The internal permeability of a permanent magnet is consistent with that of air, and the excitation EMF produced in the air gap is also sinusoidal. (3) The iron loss, the terminal effect and the magnetic saturation effect are ignored. And the constant rotor permeability is infinite. (4) The influence of temperature and load effect on the motor parameters is neglected, and there is no damper winding on the rotor.

Fig. 2.5 Physical model of SPMSM

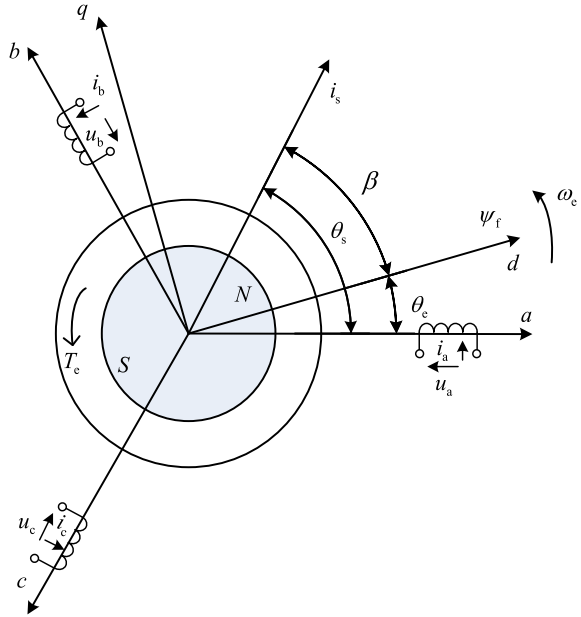


Figure 2.5 shows the surface PMSM physical model. The voltage equation of its three-phase winding can be presented as

$$\begin{bmatrix} u_a \\ u_b \\ u_c \end{bmatrix} = \begin{bmatrix} R_s & 0 & 0 \\ 0 & R_s & 0 \\ 0 & 0 & R_s \end{bmatrix} \begin{bmatrix} i_a \\ i_b \\ i_c \end{bmatrix} + p \begin{bmatrix} \psi_a \\ \psi_b \\ \psi_c \end{bmatrix} \quad (2.36)$$

where ψ_a , ψ_b and ψ_c are flux leakages of three-phase a - b - c , R_s is the stator winding resistance, p is differential operator d/dt , respectively.

The three-phase flux linkage of the SPMSM could be presented as

$$\begin{bmatrix} \psi_a \\ \psi_b \\ \psi_c \end{bmatrix} = L_{abc} \begin{bmatrix} i_a \\ i_b \\ i_c \end{bmatrix} + \psi_f \begin{bmatrix} \cos \theta_e \\ \cos(\theta_e - \frac{2}{3}\pi) \\ \cos(\theta_e + \frac{2}{3}\pi) \end{bmatrix} = \begin{bmatrix} L_a & M_{ab} & M_{ac} \\ M_{ba} & L_b & M_{bc} \\ M_{ca} & M_{cb} & L_c \end{bmatrix} \begin{bmatrix} i_a \\ i_b \\ i_c \end{bmatrix} + \begin{bmatrix} \psi_{fa} \\ \psi_{fb} \\ \psi_{fc} \end{bmatrix} \quad (2.37)$$

where ψ_{fa} , ψ_{fb} and ψ_{fc} are the permanent magnet flux linkage passing through a - b - c winding, ψ_f is the permanent magnet flux linkage, respectively.

The SPMSM is a three-phase non-salient pole synchronous motor, and the air gap is uniform. The self-inductances and the mutual inductances of the a - b - c winding

are constant, which are independent of the rotor position. So, the self-inductances and mutual inductances of the three-phase windings in SPMSM could be presented as

$$L_a = L_b = L_c = L_{s\sigma} + L_m, \quad (2.38)$$

$$M_{ab} = M_{ba} = M_{ac} = M_{bc} = M_{cb} = L_m \cos 120^\circ = -\frac{1}{2}L_m. \quad (2.39)$$

Considering $i_a + i_b + i_c = 0$, (2.37) could be presented as

$$\psi_a = \left(L_{s\sigma} + \frac{3}{2}L_m \right) i_a + \psi_{fa} = (L_{s\sigma} + L_m) i_a + \psi_{fa} = L_s i_a + \psi_{fa} \quad (2.40)$$

where L_m is the equivalent excitation inductance, L_s is the synchronous inductance [5]. ψ_b and ψ_c can be similarly expressed in the form of (2.40). Therefore, (2.37) could be presented as

$$\begin{bmatrix} \psi_a \\ \psi_b \\ \psi_c \end{bmatrix} = (L_{s\sigma} + L_m) \begin{bmatrix} i_a \\ i_b \\ i_c \end{bmatrix} + \begin{bmatrix} \psi_{fa} \\ \psi_{fb} \\ \psi_{fc} \end{bmatrix}. \quad (2.41)$$

The stator current vector \mathbf{i}_s is composed of the current i_a , i_b and i_c in the three-phase winding. The stator flux vector $\boldsymbol{\psi}_s$ can be presented by the full flux of the three-phase winding, and the rotor flux vector $\boldsymbol{\psi}_f$ can be presented by ψ_{fa} , ψ_{fb} and ψ_{fc} . According to (2.40), the stator flux vector $\boldsymbol{\psi}_s$ can be presented as

$$\boldsymbol{\psi}_s = L_{s\sigma} \mathbf{i}_s + L_m \mathbf{i}_s + \boldsymbol{\psi}_f = L_s \mathbf{i}_s + \boldsymbol{\psi}_f \quad (2.42)$$

where $L_{s\sigma} \mathbf{i}_s$ is the flux leakage produced by \mathbf{i}_s corresponding to leakage magnetic field of the stator winding, $L_m \mathbf{i}_s$ is produced by \mathbf{i}_s corresponding to armature field, $\boldsymbol{\psi}_f$ is produced by the permanent magnet.

Hence, (2.36) could be transformed into the vector form, which could be presented as

$$\mathbf{u}_s = R_s \mathbf{i}_s + \frac{d\boldsymbol{\psi}_s}{dt}. \quad (2.43)$$

Substituting (2.42) into (2.43) yields,

$$\mathbf{u}_s = R_s \mathbf{i}_s + L_s \frac{d\mathbf{i}_s}{dt} + \frac{d\boldsymbol{\psi}_f}{dt}. \quad (2.44)$$

Considering $\boldsymbol{\psi}_f = \psi_f \mathbf{e}^{j\theta_e}$, (2.44) could be presented as

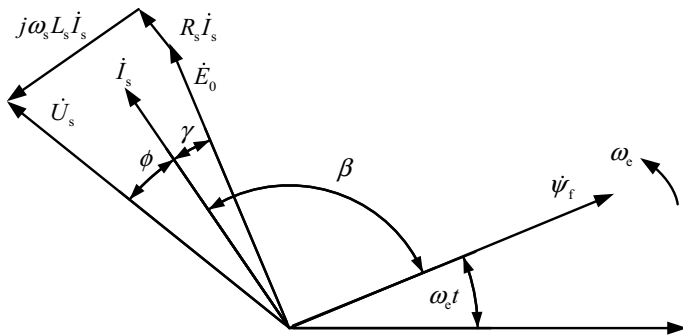


Fig. 2.6 Phasor diagram of SPMSM

$$\mathbf{u}_s = R_s \mathbf{i}_s + L_s \frac{d\mathbf{i}_s}{dt} + \mathbf{j}\omega_e \psi_f \quad (2.45)$$

where $\mathbf{j}\omega_e \psi_f$ is the induced EMF caused by the rotation of the rotor magnetic field. In the steady state, the amplitude of \mathbf{i}_s is constant. Therefore, (2.45) could be presented as

$$\dot{U}_s = R_s \dot{I}_s + \mathbf{j}\omega_e L_s \dot{I}_s + \mathbf{j}\omega_e \psi_f = R_s \dot{I}_s + \mathbf{j}\omega_s L_s I_s + \dot{E}_0. \quad (2.46)$$

The phasor diagram of SPMSM is shown in Fig. 2.6, which can be derived from (2.46).

The electromagnetic torque of the SPMSM could be presented as

$$T_e = P_n \psi_f i_s \sin \beta = P_n \psi_f \times \mathbf{i}_s \quad (2.47)$$

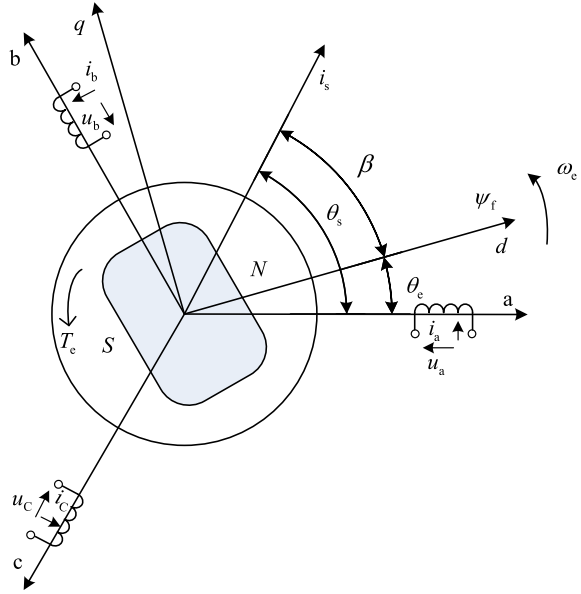
where P_n is the number of pole pairs. Equation (2.47) indicates that in the vector control of torque, the amplitude of the stator current vector \mathbf{i}_s and the space phase angle β relative to ψ_f are used for control. In the sinusoidal steady state, it is equivalent to control the amplitude of the stator current phasor and the phase angle β .

2.2.3 Mathematical Model of IPMSM

Figure 2.7 shows the IPMSM physical model. The air gap of IPMSM is not uniform. Hence, the armature reaction magnetic field will not be the same due to the difference of space phase angle β [6, 7].

As shown in (2.46) and (2.47), the voltage equation and full flux linkage equation of the a - b - c three-phase winding of IPMSM have the same form as SPMSM.

Fig. 2.7 Physical model of three-phase IPMSM



However, since the air gap of IPMSM is not uniform, the self-inductances and mutual inductances of a - b - c three-phase winding are periodic functions of the rotor position.

$$\begin{cases} L_a = L_{s0} + L_{s2} \cos(2\theta_e) \\ L_b = L_{s0} + L_{s2} \cos(2\theta_e - \frac{2}{3}\pi) \\ L_c = L_{s0} + L_{s2} \cos(2\theta_e + \frac{2}{3}\pi) \end{cases} \quad (2.48)$$

$$\begin{cases} M_a = M_{s0} + M_{s2} \cos(2\theta_e) \\ M_b = M_{s0} + M_{s2} \cos(2\theta_e - \frac{2}{3}\pi) \\ M_c = M_{s0} + M_{s2} \cos(2\theta_e + \frac{2}{3}\pi) \end{cases}$$

where L_{s0} , L_{s2} , M_{s0} and M_{s2} are the average magnitude value and the second harmonic of the self-inductance, the average magnitude value and the second harmonic of the mutual inductance, respectively.

As can be seen from the above equation, since the inductances of the a - b - c three-phase winding are the periodic functions of the rotor position, the voltage equations are of the time-varying differential forms. It is essential to apply the decoupling control method to transform the voltage equations.

By applying the Clarke transformation, (2.36) and (2.37) are transformed into the stationary coordinate system of α - β . The voltage equation, the flux linkage and the α - β axis inductance matrix could be presented as

$$\begin{bmatrix} u_\alpha \\ u_\beta \end{bmatrix} = R_s \begin{bmatrix} i_\alpha \\ i_\beta \end{bmatrix} + p \begin{bmatrix} \psi_\alpha \\ \psi_\beta \end{bmatrix}, \quad (2.49)$$

$$\begin{bmatrix} \psi_\alpha \\ \psi_\beta \end{bmatrix} = L_{\alpha\beta} \begin{bmatrix} i_\alpha \\ i_\beta \end{bmatrix} + \psi_f \begin{bmatrix} \cos \theta_e \\ \sin \theta_e \end{bmatrix}, \quad (2.50)$$

$$L_{\alpha\beta} = \begin{bmatrix} L_\alpha & M_{\alpha\beta} \\ M_{\beta\alpha} & L_\beta \end{bmatrix} = \begin{bmatrix} \sum L + \Delta L \cos(2\theta_e) & \Delta L \sin(2\theta_e) \\ \Delta L \sin(2\theta_e) & \sum L - \Delta L \cos(2\theta_e) \end{bmatrix} \quad (2.51)$$

where u_α and u_β are the α - β axis stator voltage components, i_α and i_β are the α - β axis stator current components, ψ_α and ψ_β are the α - β axis stator flux components, $L_{\alpha\beta}$ is the α - β axis stator inductance matrices, $\Sigma L = (L_d + L_q)/2$ and $\Delta L = (L_d - L_q)/2$ are the average inductance and the differential inductance, L_d and L_q are the equivalent d - q axis inductances.

As can be seen from (2.51), the inductances at α - β axes are still periodic functions of the rotor position. By applying the Park transformation, Equations (2.49) and (2.50) are transformed into the d - q coordinate frame. The voltage equation, the flux linkage and the inductance matrix in the d - q coordinate frame could be presented as

$$\begin{bmatrix} u_d \\ u_q \end{bmatrix} = R_s \begin{bmatrix} i_d \\ i_q \end{bmatrix} + p \begin{bmatrix} \psi_d \\ \psi_q \end{bmatrix} + \omega_e \begin{bmatrix} -\psi_q \\ \psi_d \end{bmatrix}, \quad (2.52)$$

$$\begin{bmatrix} \psi_d \\ \psi_q \end{bmatrix} = L_{dq} \begin{bmatrix} i_d \\ i_q \end{bmatrix} + \begin{bmatrix} \psi_f \\ 0 \end{bmatrix}, \quad (2.53)$$

$$L_{dq} = \begin{bmatrix} L_d & 0 \\ 0 & L_q \end{bmatrix} \quad (2.54)$$

where u_d and u_q are the d - q axis stator voltage components, i_d and i_q are the d - q axis stator current components, ψ_d and ψ_q are the d - q axis stator flux components, L_{dq} is the d - q axis stator inductance matrix. As can be seen from (2.54), the inductance matrix in the d - q axes becomes the constant matrix and is no longer the periodic function of the rotor position; thus, the decoupling of the d - q axes could be achieved. The phasor diagram of three-phase IPMSM is shown in Fig. 2.8, and the voltage equation could be presented as

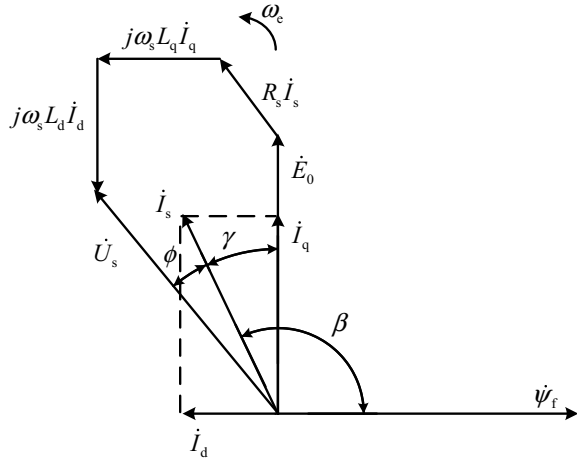
$$\dot{U}_s = R_s \dot{I}_s + \mathbf{j}\omega_s L_d \dot{I}_d + \mathbf{j}\omega_s L_q \dot{I}_q + \dot{E}_0. \quad (2.55)$$

The electromagnetic torque expression of IPMSM in d - q axes can be expressed as

$$T_e = \frac{3}{2} P_n [\psi_f i_q + (L_d - L_q) i_d i_q] \quad (2.56)$$

and the electromechanical dynamic characteristics could be presented as

Fig. 2.8 Phasor diagram of three-phase IPMSM



$$T_e - T_L = J \frac{d\omega_r}{dt} + B\omega_r \quad (2.57)$$

where T_L is the torque load, J is the inertia moment of the rotor, B is the coefficient of viscous friction, and $\omega_r = \omega_e/P_n$ is rotor mechanical angular velocity.

2.3 Vector Control of PMSM

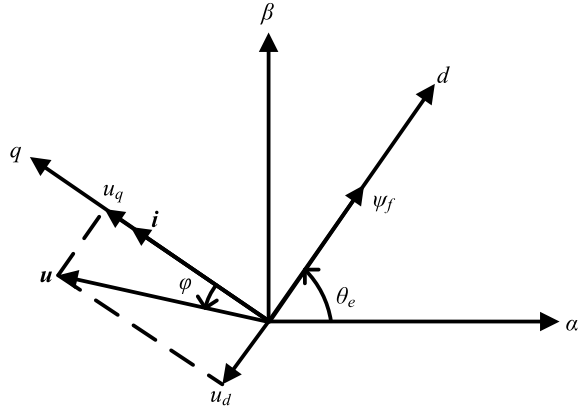
Vector control is based on the rotor flux orientation. Torque control of PMSM can be achieved by controlling the stator current vector. Using vector control method, PMSM can be controlled as the DC motor and the same satisfactory control performance can be obtained. Nowadays, vector control method has been widely used in the high-performance motor drives.

In order to control the electromagnetic torque precisely, the allocation of the excitation current component i_d and the torque current component i_q should be considered according to the electromagnetic torque as shown in (2.56). At present, $i_d = 0$ control and maximum torque per ampere (MTPA) control are the most popular vector control modes.

2.3.1 $i_d = 0$ Vector Control Mode

$i_d = 0$ vector control mode means controlling the excitation current i_d to zero. Consequently, the electromagnetic torque is related to the torque current i_q . As shown in Fig. 2.9, the permanent flux linkage ψ_f is on the d -axis and rotates with the rotor

Fig. 2.9 Space vector diagram of $i_d = 0$ control



electrical position θ_e to achieve the rotor flux orientation. The excitation current is zero, and the torque current equals to the amplitude of the stator current vector. The stator voltage vector is \mathbf{u} , and the stator current vector is \mathbf{i} .

In this control mode, the torque generation is realized by controlling i_q . Therefore, the control system is easy to implement, and high-performance torque control can be achieved. This control mode is especially suitable for the SPMSM drives, since the stator current can be minimized with the same output torque. However, for the interior PMSM, the sacrifice of the reluctance torque component will reduce the efficiency of the motor. With the increase of the load, the stator current increases gradually, and the cross-axis flux increases accordingly, which increases the angle between the stator voltage vector and the stator current vector, resulting in the decrease of the power factor.

2.3.2 Maximum Torque Per Ampere Control

MTPA is a vector control method to minimize the stator current under the same output torque for interior PMSM [8]. The MTPA point is the point closest to the origin among the points on the constant torque curve in the current plane. And, the MTPA point is also the point with the minimum magnitude in the constant torque curve as shown in Fig. 2.10.

In Fig. 2.11, the constant torque locus is shown in the current plane at the synchronous reference frame. As can be seen, no matter whether $\partial T_e / \partial \theta_e > 0$ or $\partial T_e / \partial \theta_e < 0$, the magnitude of the vector is larger than the middle vector. In order to achieve MTPA vector control, the stator current should satisfy the following constraint,

$$\frac{\partial T_e}{\partial \theta_e} = \frac{3P_n}{4} I_s \{ \psi_f \cos \theta_e + (L_d - L_q) I_s \cos 2\theta_e \} = 0 \quad (2.58)$$

Fig. 2.10 MTPA operating points and the constant torque loci in the current plane

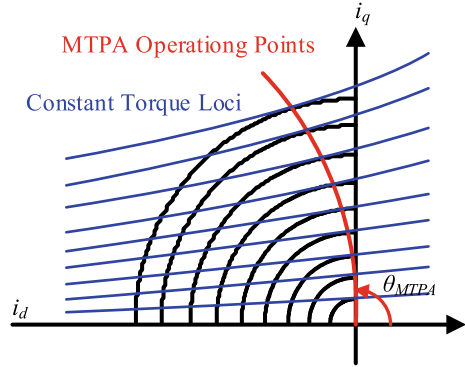
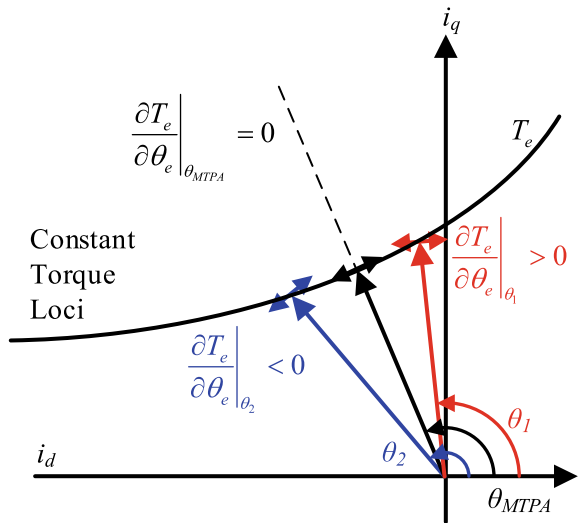


Fig. 2.11 Locus of the constant torque in the current vector plane



where I_S is the magnitude of the stator current vector.

Substituting (2.56) into (2.57), the current angle of the MTPA point θ_{MTPA} can be derived as follows

$$\theta_{MTPA} = \cos^{-1} \left(\frac{-\psi_f + \sqrt{\psi_f^2 + 8(L_d - L_q)^2 I_s^2}}{4(L_d - L_q) I_s} \right). \quad (2.59)$$

By using (2.57), the exciting current and the torque current components in MTPA control mode can be obtained as

$$\begin{cases} i_{d|MTPA}^* = I_s \cos \theta_{MTPA} \\ i_{q|MTPA}^* = I_s \sin \theta_{MTPA} \end{cases} \quad (2.60)$$

where $i_d^*|_{\text{MTPA}}$ is the d -axis current reference in MTPA control mode, $i_q^*|_{\text{MTPA}}$ is the q -axis current reference in MTPA control mode.

Thus, the optimal exciting current and torque current components can be obtained for a desired torque by using the MTPA control strategy.

2.3.3 Flux-Weakening Control

A. Principle of the Flux-Weakening Control

In PMSM drives, the amplitudes of the stator current and the voltage vector are limited by the rated current of the insulated gate bipolar transistor (IGBT) and the DC-link voltage [9]. The maximum voltage and current can be denoted as the voltage limit $U_{s\max}$ and the current limit $I_{s\max}$, respectively. Generally, the amplitude of the stator current and the voltage vector should meet the following constraints:

$$|\mathbf{i}| \leq I_{s\max}, \quad (2.61)$$

$$|\mathbf{u}| \leq U_{s\max} \quad (2.62)$$

where $|\mathbf{i}|$ and $|\mathbf{u}|$ are the amplitude of the stator current vector and stator voltage vector, respectively.

As can be seen from (2.52), (2.53) and (2.54), if PMSM operates in steady state, the differential terms in the voltage equation are equal to zero. Meanwhile, when the motor operates beyond the base speed, the voltage drop on the stator resistance can be neglected. Ultimately, the motor voltage equations can be represented as

$$u_d = -\omega_e L_q i_q, \quad (2.63)$$

$$u_q = \omega_e L_d i_d + \omega_e \psi_f. \quad (2.64)$$

Substituting (2.63) and (2.64) into (2.65), the voltage boundary can be obtained as

$$(L_d i_d + \psi_f)^2 + (L_q i_q)^2 \leq \left(\frac{U_{s\max}}{\omega_e} \right)^2. \quad (2.65)$$

It can be seen from (2.65) that the voltage boundary of the interior PMSM is an elliptical cluster with the point $(-\psi_f/L_d, 0)$ as the center and the length and the radius are reduced proportionally with the increase of the operation speed. The current boundary is shown as (2.66), which is a circle centered on the origin. The radius of the current limit circle is $I_{s\max}$, as shown in Fig. 2.12.

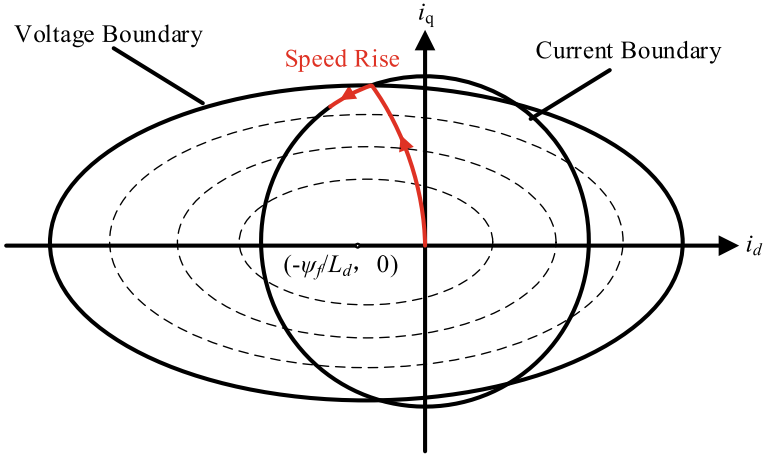


Fig. 2.12 Schematic diagram of voltage and current boundary

$$i_d^2 + i_q^2 \leq I_s^2 \max. \tag{2.66}$$

As the speed increases, the voltage limit ellipse shrinks toward the center point. When the current trajectory runs along the arrow line to the intersection of the voltage boundary and the current boundary, the d -axis current can only move to the left, which is the current trajectory in the flux-weakening operation.

B. Flux-Weakening Control Scheme

The voltage closed-loop flux-weakening method is the most commonly used flux-weakening scheme, as shown in Fig. 2.13. The amplitude of the stator voltage vector $|\mathbf{u}^*|$ is compared with the limit voltage U_{smax} . When $|\mathbf{u}^*| < U_{smax}$, the PI regulator is positively saturated, and therefore, $\Delta i_d = 0$. Otherwise, when $|\mathbf{u}^*| > U_{smax}$, the PI regulator will work to produce a negative Δi_d to reduce the reference of the d -axis current.

The voltage closed-loop flux-weakening method integrated with the vector control strategy is shown in Fig. 2.14. The vector control scheme consists of the current loop and the speed loop. The d - q -axis current references are allocated by MTPA control strategy to maximize the electromagnetic torque when the motor operates below the base speed. The voltage references u_d^* and u_q^* are used to calculate the amplitude of

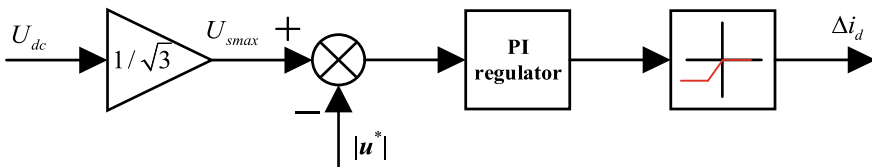


Fig. 2.13 Block diagram of the voltage closed-loop flux-weakening scheme

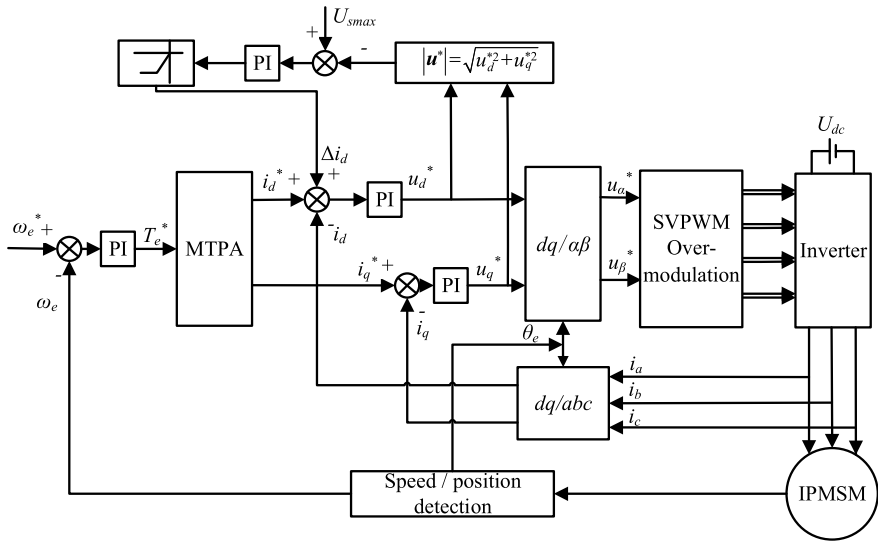


Fig. 2.14 Block diagram of the voltage closed-loop flux-weakening control

the stator voltage vector. When $|u^*| > U_{smax}$, the negative Δi_d is added to the d -axis current reference directly.

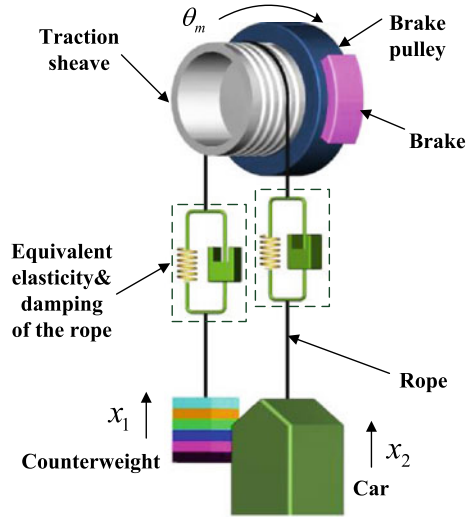
Actually, many flux-weakening control strategies have been designed during past decades, such as the single current regulation flux-weakening method and the voltage angle adjusting method. Although each method has their special features, they should obey the same design principles as described above.

2.4 Dynamic Model of Gearless PMSM Traction Elevators

The drive system, the car and the counterweight are the main parts of the gearless elevator. An electromagnetic brake mounted on the brake pulley is used to hold the rotor at standstill when the elevator converts to standby mode. The dynamic model of direct-drive elevator is established ignoring the effects of the compensation wheel, the weight compensation ropes and the friction damper. As a result, the equivalent model is shown in Fig. 2.15.

Taking the rigidity coefficient and the damping coefficient of the traction rope into consideration, the dynamic model of traction system can be described as follows:

Fig. 2.15 Equivalent model of the direct-drive elevator traction system



$$\begin{cases} M_1 \ddot{x}_1 - k_1(-\theta_m R_m - x_1) + M_1 g - b_1(-\dot{\theta}_m R_m - \dot{x}_1) = 0 \\ M_2 \ddot{x}_2 - k_2(\theta_m R_m - x_2) + M_2 g - b_2(\dot{\theta}_m R_m - \dot{x}_2) = 0 \\ J \ddot{\theta}_m + R_m k_2(\theta_m R_m - x_2) - R_m k_1(-\theta_m R_m - x_1) + R_m b_2(\dot{\theta}_m R_m - \dot{x}_2) \\ - R_m b_1(-\dot{\theta}_m R_m - \dot{x}_1) = T_e \end{cases} \quad (2.67)$$

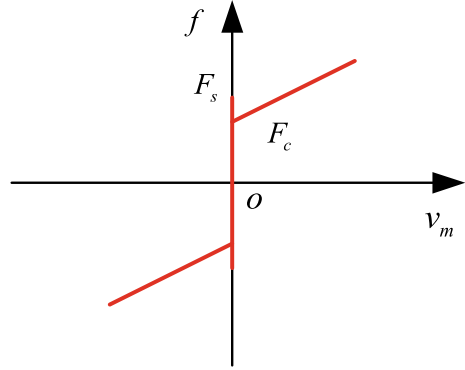
where k_1 and b_1 are the stiffness coefficient and the damping coefficient of the rope on counterweight side, M_1 is the mass of the counterweight, x_1 is the counterweight displacement, g is the coefficient of gravity acceleration, k_2 and b_2 are the stiffness coefficient and the damping coefficient of the rope on car side, M_2 is the mass of the car, x_2 is the car displacement, θ_m is the mechanical position of the traction motor, J is the total inertia of the traction system, R_m is the radius and T_e is the electromagnetic torque generated by traction machine. The relationship between the friction force f and the mechanical velocity v_m can be expressed as follows, which can make it easier to analyze the friction torque characteristics

$$f = \begin{cases} F_l ; & \text{if } v_m = 0 \text{ and } |F_l| < F_s \\ F_s \text{sign}(F_l) ; & \text{if } v_m = 0 \text{ and } |F_l| \geq F_s \\ F_c \text{sign}(v_m) + \sigma v_m ; & \text{if } v_m \neq 0 \end{cases} \quad (2.68)$$

where F_l is the force generated from external parts, F_c is the coulomb friction, σ is the coefficient of viscosity and F_s is the maximum static friction force.

When the brake releases completely, according to the friction model in (2.68), the torque judgment that drives the traction machine from standstill to the rotating state is

Fig. 2.16 Friction model of traction sheave



$$|F_e - (M_2 - M_1)g| > F_s \quad (2.69)$$

where F_e is the force generated by the traction machine. And, the judgment that makes the traction machine convert from the rotating state to standstill is

$$|F_e - (M_2 - M_1)g| < F_c. \quad (2.70)$$

It can be concluded that the force generated by the traction machine to maintain the car at standstill is not a fixed but variable value. To be specific, the model of friction is shown in Fig. 2.16.

According to the friction model, the electromagnetic torque to maintain the traction sheave at standstill is a range. It is difficult to accurately calculate the electromagnetic torque to balance the equivalent load torque from the mathematical model when taking the nonlinear characteristic of mechanical brake releasing into consideration. Therefore, those methods calculating the compensation torque depending on accurate mechanical models cannot achieve good robustness in the startup control of direct-drive elevators.

2.5 Summary

The basic knowledge of PMSM drives has been introduced in this section. The voltage equations of PMSM in the $a-b-c$ coordinate frame are severely coupled, which is mainly caused by the mutual inductances. In order to realize the decoupling control, the $\alpha-\beta$ and the $d-q$ coordinate frames are introduced, which aim to eliminate the effect of the mutual inductances. PMSM models in the $\alpha-\beta$ and $d-q$ coordinate frames are obtained by the coordinate transformation, which are an important tool for the analysis of PMSM drives. The control methods of PMSM based on vector control are then introduced, including the corresponding maximum voltage vector evaluation and field orientation control. At the same time, the dynamic model of the

elevator traction system is also described to illuminate the technical difficulties of the rollback mitigation without using a weight transducer.

References

1. Kim S, Yoon Y, Sul S et al (2010) Parameter independent maximum torque per ampere (MTPA) control of IPM machine based on signal injection[C]. In: 2010 twenty-fifth annual IEEE applied power electronics conference and exposition (APEC), pp 103–108
2. Bolognani S, Petrella R, Prearo A et al (2011) Automatic tracking of MTPA trajectory in IPM motor drives based on AC current injection. *IEEE Trans Ind Appl* 47(1):105–114
3. Mohamed YAI, Lee TK (2006) Adaptive self-tuning MTPA vector controller for IPMSM drive system. *IEEE Trans Energy Convers* 21(3):636–644
4. Butt C, Hoque MA, Rahman MA (2003) Simplified fuzzy logic based MTPA speed control of IPMSM drive. In: 38th IAS annual meeting on conference record of the industry applications conference, vol 1, pp 499–506
5. Ching-Tsai P, Sue SM (2005) A linear maximum torque per ampere control for IPMSM drives over full-speed range. *IEEE Trans Energy Convers* 20(2):359–366
6. Liu K, Zhu ZQ (2014) Online estimation of the rotor flux linkage and voltage-source inverter nonlinearity in permanent magnet synchronous machine drives. *IEEE Trans Power Electron* 29(1):418–427
7. Chen L, Peng FZ (2008) Dead-time elimination for voltage source inverters. *IEEE Trans Power Electron* 23(2):574–580
8. Miao Y, Ge H, Preindl M et al (2017) MTPA fitting and torque estimation technique based on a new flux-linkage model for interior-permanent-magnet synchronous machines. *IEEE Trans Ind Appl* 53(6):5451–5460
9. Lian C, Xiao F, Gao S et al (2019) Load torque and moment of inertia identification for permanent magnet synchronous motor drives based on sliding mode observer. *IEEE Trans Power Electron* 34(6):5675–5683

Chapter 3

Initial Position Detection for PMSM Traction Drives



3.1 Introduction

Permanent magnet synchronous motors (PMSMs) have gained wide attention in traction-drive applications thanks to the high torque-weight ratio. Due to the rapid development of the traction drives with PMSMs, PMSM traction-drive system is widely researched both at home and at abroad. Traction drives with PMSMs have to meet with specific requirements. For the sensorless PMSM traction drive, accurate initial position information is an important guarantee for achieving high torque starting ability. With the increase of traction-drive application requirements, how to simplify the algorithm and improve the signal-to-noise ratio (SNR) should be further investigated for enhancing the initial position detection performance. Additionally, the annoying noise problem caused by the additional signal injection during the detection process has attracted attention. Especially in some special traction-drive applications, such as the traction elevators, the harsh noise could be unbearable.

Traditionally, to simplify the algorithm, the rotor is pulled to a preset position before starting up, or the open-loop control strategy is adopted to operate the motor. Nevertheless, in the traction applications, any rotor fluctuation is prohibited before starting up and enough starting ability with a heavy load is also required. Therefore, it is necessary to detect the initial position at standstill and guarantee the starting performance. The commonly used initial position detection schemes at standstill can be classified into two main categories: pulse signals injection-based methods and high-frequency (HF) signals injection-based methods.

For the pulse signals injection-based methods, the pulse voltages or currents are injected into different directions into the motor winding to excite stator core saturation. In [1], two kinds of suitable sequence DC voltage pulses were applied to detect the magnetic pole position and the magnetic polarity, where one voltage pulse had a short time duration and the other had a long time duration. To overcome the inaccuracy issues of the voltage measurement, a current pulses based initial position detection method was introduced [2]. For these methods, the detection accuracy is

influenced by the amplitude of the injected pulse signals. Larger amplitudes cause vibration and noise, and yet, smaller amplitudes reduce the SNR [3].

The HF signals injection-based methods usually consist of two stages: the magnetic pole position detection and the magnetic polarity identification. At the first stage, HF rotating signals, HF pulsating signals and HF square-wave signals are widely used to serve as the additional injection signals to estimate the rotor position. At the second stage, the magnetic polarity detection schemes can be commonly classified into two kinds: double reverse pulse voltages injection-based method and harmonics extraction-based method.

In double reverse pulse voltages injection-based method, the magnetic polarity can be identified according to the amplitude of the two induced pulse currents. Two transient short voltage pulses with large amplitude were injected into the estimated d -axis to identify the magnetic polarity. A magnetic polarity identification strategy based on the difference of stator current amplitudes was applied. These methods have advantages of high SNR and strong robustness. However, the amplitude and the duration of voltage pulses should be selected carefully; otherwise, it may cause the fault of overcurrent. Moreover, these methods make polarity detection an independent process that interrupts the position estimation. To make the detection process continuous, a magnetic polarity detection strategy based on the amplitude variation of d -axis currents was investigated [4]. This scheme is reliable and stable, but the injected d -axis currents may cause slight vibration of the rotor. For these methods, the annoying noise caused by the induced large-amplitude pulse currents is also unavoidable.

Harmonics extraction-based method can obtain the magnetic polarity information from the induced voltages or currents. Based on the HF rotating injection method, the secondary component of positive sequence currents contains the polarity information. Furthermore, the amplitude of the secondary carrier component can also be utilized to detect the magnetic polarity. Without extra pulse voltage signals injection, these methods could make the detection process continuous. However, higher SNR is necessary to improve the identification accuracy further. A scheme was applied to improve the SNR by increasing the injected magnitude or decreasing the carrier frequency. In [5], secondary harmonics of the zero-sequence carrier voltage were applied to identify the magnetic polarity, which has higher SNR compared with the conventional secondary carrier current harmonics, while the extraction of zero-sequence voltage requires an external resistor network. Alternatively, a hysteresis controller was employed in the polarity detection for noise attenuation. Nevertheless, the extraction and processing of harmonic components increase the complexity of algorithms. In addition, the annoying noise caused by the injected HF signals is also unavoidable.

Some effective methods for HF noise reduction have been proposed in previous studies, such as the low-frequency signals injection method, the low-amplitude signals injection method [6] and the zero-voltage vector injection method. These methods can reduce the HF noise effectively in the low-speed operation region. Nonetheless, considering the SNR and practicality, they are difficult to be used for the initial rotor position detection.

This chapter proposes a pseudorandom HF square-wave voltage injection (PRHFSVI)-based low-noise initial rotor position detection method for sensorless PMSM traction drives [7]. Different from the traditional magnetic polarity detection strategies, the proposed method can identify the magnetic polarity based on the accumulation of the induced random HF current peak pairs. This method focuses on suppressing the harsh noise caused by the additional signal injection during the detection process. Additionally, this scheme does not need to inject the large-amplitude pulse voltage signals and change the amplitude of d -axis currents; hence, it is easy to implement and the detection process is continuous. A saturated peak current delay compensation strategy is proposed to reduce the effects of digital delay on the magnetic polarity detection. Furthermore, power spectral density (PSD) analysis is adopted to provide the theoretical support for noise reduction and the experimental results match well with the theoretical analysis. The proposed low-noise initial rotor position detection method could make elevator ride even more comfortable.

3.2 Basic Principle of Saliency-Tracking-Based Methods

According to the operation speed range of PMSM, the sensorless control methods can be classified into two categories: saliency-tracking-based methods and back electromotive force (EMF) model-based methods. For medium- to high-speed operation, EMF model-based methods have been well-founded and presented satisfying performance. However, the capability to obtain the rotor position deteriorates dramatically in low-speed operation, since the amplitude of the EMF signal becomes too weak to be detected precisely.

Saliency-tracking-based methods, by contrast, perform well at zero and low speeds. The HF signal injection-based method and fundamental PWM excitation-based method both have been proved to be effective.

Since the winding inductance can be expressed related to rotor position when the HF signal is injected, the rotor position information can be extracted effectively. In general, the HF voltage signal is preferred. The impedance increases with the injection frequency, and it results in the increased voltage. If the HF current is injected, the bandwidth of current regulator must be high enough, which is more difficult to be achieved. Besides, the stationary reference frame (SRF) or the estimated rotary reference frame (RRF) can be selected as the signal injection axes generally. The injection mode can be superimposed injection or separate injection; that is, the HF signal is superimposed onto the fundamental frequency signal, or injected directly into the stator windings when the field-oriented control (FOC) is interrupted.

It is worth noting that the injection amplitude and frequency are crucial for sensorless control performance. The determination of injection amplitude is a compromise between position estimation accuracy and control performance. The larger the injection amplitude is, the better position estimation accuracy will be. However, the current and torque ripples will increase, resulting in increased copper loss and the deteriorated control performance. In addition, the determination of the injection frequency

is also worth considering. The higher injection frequency helps to increase the system bandwidth and dynamic performance, but the additional motor loss will increase.

As for HF injection-based sensorless control, there are three methods used widely: HF sinusoidal signal injection-based method, HF square-wave signal injection-based method and HF pulse signal injection-based method.

3.2.1 HF Mathematical Model of PMSM

To facilitate subsequent theoretical analysis of HF signal injection-based method, the HF mathematical model of PMSM should be established.

When PMSM operates at low speed and the injection frequency is set high enough, the voltage drops on stator resistance and the terms associated with the rotor speed can be neglected. Hence, PMSM can be regarded as a purely inductive load, and the HF mathematical model in the RRF can be expressed as follows:

$$\begin{bmatrix} u_{dh} \\ u_{qh} \end{bmatrix} = \begin{bmatrix} L_d & 0 \\ 0 & L_q \end{bmatrix} \frac{d}{dt} \begin{bmatrix} i_{dh} \\ i_{qh} \end{bmatrix} \quad (3.1)$$

where subscript h represents HF components.

By utilizing the coordinate transformation, the above equation can be transformed as follows:

$$\mathbf{R}(\theta_e) \begin{bmatrix} u_{dh} \\ u_{qh} \end{bmatrix} = \mathbf{R}(\theta_e) \begin{bmatrix} L_d & 0 \\ 0 & L_q \end{bmatrix} \frac{d}{dt} \mathbf{R}^{-1}(\theta_e) \begin{bmatrix} i_{\alpha h} \\ i_{\beta h} \end{bmatrix}. \quad (3.2)$$

Then, the HF mathematical model of PMSM in the SRF can be deduced as follows:

$$\begin{bmatrix} u_{\alpha h} \\ u_{\beta h} \end{bmatrix} = \begin{bmatrix} \Sigma L + \Delta L \cos(2\theta_e) & \Delta L \sin(2\theta_e) \\ \Delta L \sin(2\theta_e) & \Sigma L - \Delta L \cos(2\theta_e) \end{bmatrix} \frac{d}{dt} \begin{bmatrix} i_{\alpha h} \\ i_{\beta h} \end{bmatrix}, \quad (3.3)$$

$$\frac{d}{dt} \begin{bmatrix} i_{\alpha h} \\ i_{\beta h} \end{bmatrix} = \frac{1}{\Sigma L^2 - \Delta L^2} \begin{bmatrix} \Sigma L - \Delta L \cos(2\theta_e) & -\Delta L \sin(2\theta_e) \\ -\Delta L \sin(2\theta_e) & \Sigma L + \Delta L \cos(2\theta_e) \end{bmatrix} \begin{bmatrix} u_{\alpha h} \\ u_{\beta h} \end{bmatrix} \quad (3.4)$$

where $u_{\alpha h}$, $u_{\beta h}$, $i_{\alpha h}$, $i_{\beta h}$ are HF voltages and currents in the SRF, respectively. ΣL and ΔL represent the average inductance and the difference inductance, respectively. Specifically, they are defined as $\Sigma L = (L_d + L_q)/2$, $\Delta L = (L_d - L_q)/2$.

3.3 HF Sinusoidal Signal Injection-Based Method

HF sinusoidal signal injection-based method was proposed relatively early, which laid the solid foundation for HF signal injection-based methods. According to the injection frame, two methods of the HF sinusoidal signal injection are widely used: the HF rotating sinusoidal signal injection-based method and the HF pulsating sinusoidal signal injection-based method. HF rotating sinusoidal signal injection-based method is the earliest proposed one, where a rotating HF voltage vector was injected into the SRF, and the position information can be implied in the phase of the induced HF currents, while HF pulsating sinusoidal signal injection-based method usually injects the pulsating voltage signal into the estimated RRF, and the amplitude of the induced HF currents contains the position information. The above two methods are further explained in the following.

3.3.1 HF Rotating Sinusoidal Signal Injection-Based Method

HF rotating sinusoidal signal injection-based method was first proposed by Robert D. Lorenz. The block diagram of HF rotating sinusoidal signal injection-based sensorless PMSM drive is shown in Fig. 3.1. Two orthogonal HF voltage signals are injected into the SRF as follows:

$$\begin{bmatrix} u_{\alpha h} \\ u_{\beta h} \end{bmatrix} = U_h \begin{bmatrix} \cos \omega_h t \\ \sin \omega_h t \end{bmatrix} \tag{3.5}$$

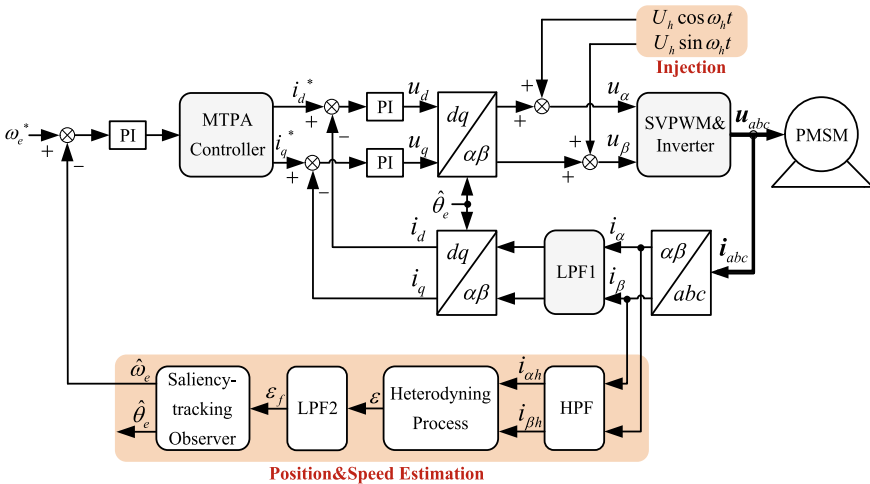


Fig. 3.1 Block diagram of HF rotating sinusoidal signal injection-based sensorless PMSM drive

where U_h and ω_h denote the amplitude and frequency of the injected HF rotating voltage, respectively. When PMSM operates at zero or low speed, the injection frequency is much higher than the fundamental frequency; thus, the HF mathematical model of PMSM in the SRF can be obtained. Then, the induced HF currents can be deduced as follows:

$$\begin{bmatrix} i_{\alpha h} \\ i_{\beta h} \end{bmatrix} = \frac{U_h}{\omega_h(\Sigma L^2 - \Delta L^2)} \begin{bmatrix} \Sigma L \sin \omega_h t + \Delta L \sin(2\theta_e - \omega_h t) \\ -\Sigma L \cos \omega_h t - \Delta L \cos(2\theta_e - \omega_h t) \end{bmatrix}. \quad (3.6)$$

As can be seen, the position information θ_e is contained in the phase of the negative sequence current component. To extract the rotor position from the induced HF currents, the heterodyning process and the saliency-tracking observer can be utilized, as shown in Fig. 3.2. Firstly, the high-pass filter (HPF) is used to separate the induced HF currents. Then, HF currents are multiplied in SRF by $\cos(2\hat{\theta}_e - \omega_h t)$ and $\sin(2\hat{\theta}_e - \omega_h t)$,

$$\begin{aligned} \varepsilon &= i_{\alpha h} \cos(2\hat{\theta}_e - \omega_h t) + i_{\beta h} \sin(2\hat{\theta}_e - \omega_h t) \\ &= \frac{U_h}{\omega_h(\Sigma L^2 - \Delta L^2)} (\Delta L \sin(2\tilde{\theta}_e) + \Sigma L \sin(2\omega_h t - 2\hat{\theta}_e)) \end{aligned} \quad (3.7)$$

where $\hat{\theta}_e$ is the estimated position via the saliency-tracking observer, and $\tilde{\theta}_e$ represents the position estimation error, i.e., $\tilde{\theta}_e = \theta_e - \hat{\theta}_e$. The coordinate distribution of each axis is shown in Fig. 3.3. Furthermore, the low-pass filter (LPF) is used to suppress the HF component and obtain the term related to position estimation error. In the assumption that $\tilde{\theta}_e$ is small enough, ε_f is proportional to $\tilde{\theta}_e$, i.e.,

$$\begin{aligned} \varepsilon_f &= \text{LPF} \left(i_{\alpha} \cos(2\hat{\theta}_e - \omega_h t) + i_{\beta} \sin(2\hat{\theta}_e - \omega_h t) \right) \\ &\approx \frac{2U_h \Delta L}{\omega_h(\Sigma L^2 - \Delta L^2)} \tilde{\theta}_e. \end{aligned} \quad (3.8)$$

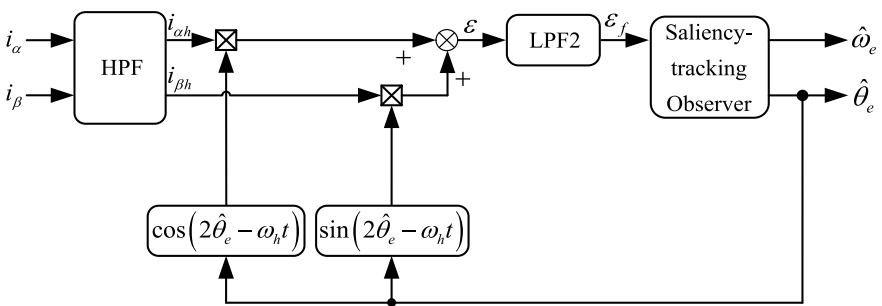
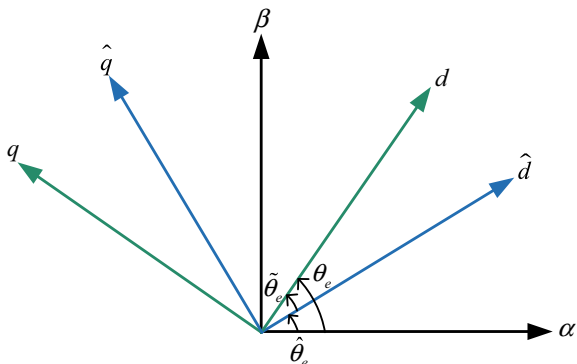


Fig. 3.2 Scheme of position and speed estimation

Fig. 3.3 Coordinate distribution of each axis



Then, ε_f acts as the input of the saliency-tracking observer to estimate the motor speed and position. By driving ε_f to approach to zero, saliency-tracking observer forces the convergence of the estimated position to the actual one, i.e., $\hat{\theta}_e \rightarrow \theta_e$.

HF rotating sinusoidal signal injection-based method has potential stability since it injects symmetrical HF voltages into the SRF. However, this method inevitably brings about current fluctuations and torque ripples, which have an adverse effect on control performance. In addition, the injection frequency is limited to ensure the sinusoid of the injected signal. HPFs and LPFs are needed to extract the signals with different frequencies, while the existence of LPFs would restrict the bandwidth of controllers.

3.3.2 HF Pulsating Sinusoidal Signal Injection-Based Method

To alleviate current fluctuations and torque ripples, the HF pulsating sinusoidal signal injection-based method has been proposed by injecting a pulsating voltage expressed as (3.9) along the estimated RRF. The block diagram of HF pulsating sinusoidal signal injection-based sensorless PMSM drive is shown in Fig. 3.4.

$$\begin{bmatrix} u_{\hat{d}h} \\ u_{\hat{q}h} \end{bmatrix} = \begin{bmatrix} U_h \sin(\omega_h t) \\ 0 \end{bmatrix}. \quad (3.9)$$

According to the HF mathematical model in the RRF, the rotor position can be obtained via coordinate transformation. Accordingly, the HF mathematical model in the estimated RRF is expressed as, where $u_{\hat{d}h}$, $u_{\hat{q}h}$, $i_{\hat{d}h}$ and $i_{\hat{q}h}$ are the HF voltages and currents, respectively.

$$\mathbf{R}(\tilde{\theta}_e) \begin{bmatrix} u_{dh} \\ u_{qh} \end{bmatrix} = \mathbf{R}(\tilde{\theta}_e) \begin{bmatrix} L_d & 0 \\ 0 & L_q \end{bmatrix} \frac{d}{dt} \mathbf{R}^{-1}(\tilde{\theta}_e) \begin{bmatrix} i_{\hat{d}h} \\ i_{\hat{q}h} \end{bmatrix}, \quad (3.10)$$

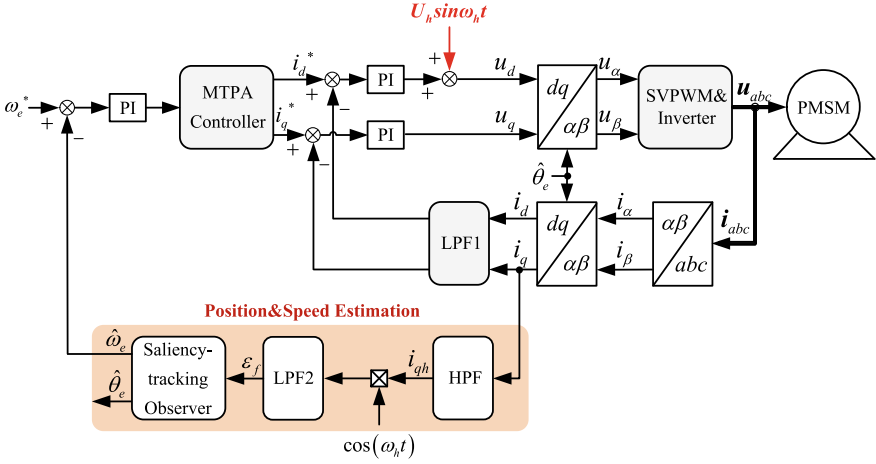


Fig. 3.4 Block diagram of HF pulsating sinusoidal injection-based sensorless PMSM drive

$$\frac{d}{dt} \begin{bmatrix} i_{\hat{d}h} \\ i_{\hat{q}h} \end{bmatrix} = \frac{1}{\Sigma L^2 - \Delta L^2} \begin{bmatrix} \Sigma L - \Delta L \cos(2\tilde{\theta}_e) & -\Delta L \sin(2\tilde{\theta}_e) \\ -\Delta L \sin(2\tilde{\theta}_e) & \Sigma L + \Delta L \cos(2\tilde{\theta}_e) \end{bmatrix} \begin{bmatrix} u_{\hat{d}h} \\ u_{\hat{q}h} \end{bmatrix}. \quad (3.11)$$

Further, substitute (3.9) into (3.11), the induced HF currents in the estimated RRF can be deduced as follows:

$$\begin{bmatrix} i_{\hat{d}h} \\ i_{\hat{q}h} \end{bmatrix} = \frac{U_h}{\omega_h (\Sigma L^2 - \Delta L^2)} \begin{bmatrix} -\Sigma L + \Delta L \cos(2\tilde{\theta}_e) \\ \Delta L \sin(2\tilde{\theta}_e) \end{bmatrix} \cos(\omega_h t). \quad (3.12)$$

As can be seen, $i_{\hat{q}h}$ is approximately zero on the assumption that the position estimation error is small enough. In view of this, only $i_{\hat{d}h}$ is processed by multiplying it by $\cos(\omega_h t)$; thus, ε_f associated with position estimation error can be obtained as (3.13) via LPF. Further, ε_f serves as the input of the saliency-tracking observer, and the position information can be obtained by driving ε_f to zero.

It is worth noting that the retrieve of rotor position depends on the difference inductance ΔL , i.e., on the saliency of PMSM. If ΔL becomes zero, ε_f associated with position estimation error will disappear.

$$\begin{aligned} \varepsilon_f &= \text{LPF}(i_{\hat{d}h} \times \cos(\omega_h t)) \\ &= \frac{U_h \Delta L}{2\omega_h (\Sigma L^2 - \Delta L^2)} \sin(2\tilde{\theta}_e) \\ &\approx \frac{U_h \Delta L}{\omega_h (\Sigma L^2 - \Delta L^2)} \tilde{\theta}_e. \end{aligned} \quad (3.13)$$

Also, there is another way to estimate rotor position. Different from the above method, the following one defines the rotational measurement axes ($d^m q^m$) that lag the estimated RRF $\pi/4$. The adopted coordinate system, the block diagram of HF pulsating sinusoidal signal injection-based sensorless PMSM drive, and the position and speed estimation process are shown in Figs. 3.5 and 3.6, respectively.

By coordinate transformation, the HF mathematical model in the RRF can be transformed into rotational measurement axes, as explained in (3.14). Accordingly, the HF mathematical model in $d^m q^m$ is deduced as (3.15), where u_{dh}^m , u_{qh}^m , i_{dh}^m and i_{qh}^m are the measurement axes HF voltages and currents, respectively.

$$\mathbf{R}\left(\tilde{\theta}_e + \frac{\pi}{4}\right) \begin{bmatrix} u_{dh} \\ u_{qh} \end{bmatrix} = \mathbf{R}\left(\tilde{\theta}_e + \frac{\pi}{4}\right) \begin{bmatrix} L_d & 0 \\ 0 & L_q \end{bmatrix} \frac{d}{dt} \mathbf{R}^{-1}\left(\tilde{\theta}_e + \frac{\pi}{4}\right) \begin{bmatrix} i_{dh}^m \\ i_{qh}^m \end{bmatrix}, \quad (3.14)$$

$$\frac{d}{dt} \begin{bmatrix} i_{dh}^m \\ i_{qh}^m \end{bmatrix} = \frac{1}{\Sigma L^2 - \Delta L^2} \begin{bmatrix} \Sigma L + \Delta L \sin(2\tilde{\theta}_e) & -\Delta L \cos(2\tilde{\theta}_e) \\ -\Delta L \cos(2\tilde{\theta}_e) & \Sigma L - \Delta L \sin(2\tilde{\theta}_e) \end{bmatrix} \begin{bmatrix} u_{dh}^m \\ u_{qh}^m \end{bmatrix} \quad (3.15)$$

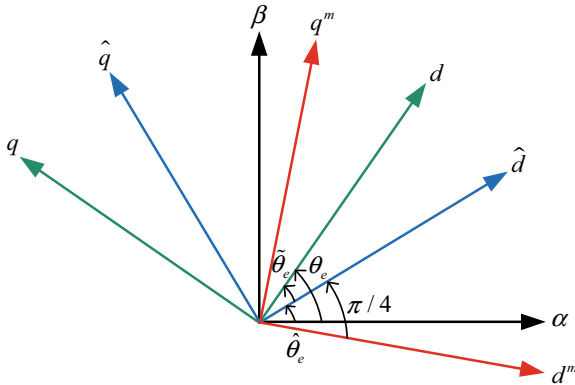


Fig. 3.5 Adopted coordinate system

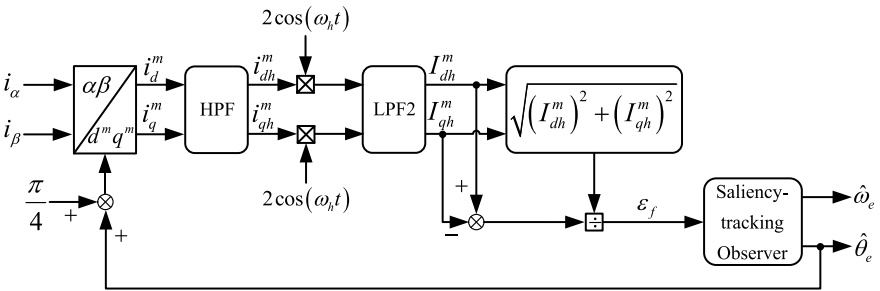


Fig. 3.6 Estimation scheme of position and speed

In (3.14), the injected voltage in estimated RRF can be transformed into rotational measurement axes, as explained in (3.16), thus the induced HF currents in $d^m q^m$ can be deduced as (3.17). Multiply the HF currents by $2\cos(\omega_h t)$, and the amplitude containing the position estimation error can be obtained via LPF, as shown in (3.18).

$$\begin{bmatrix} u_{dh}^m \\ u_{qh}^m \end{bmatrix} = \frac{U_h}{\sqrt{2}} \begin{bmatrix} \sin(\omega_h t) \\ \sin(\omega_h t) \end{bmatrix}, \quad (3.16)$$

$$\begin{bmatrix} i_{dh}^m \\ i_{qh}^m \end{bmatrix} = \frac{-U_h \cos(\omega_h t)}{\sqrt{2}\omega_h(\Sigma L^2 - \Delta L^2)} \begin{bmatrix} \Sigma L - \Delta L \cos(2\tilde{\theta}_e) + \Delta L \sin(2\tilde{\theta}_e) \\ \Sigma L - \Delta L \cos(2\tilde{\theta}_e) - \Delta L \sin(2\tilde{\theta}_e) \end{bmatrix}, \quad (3.17)$$

$$\begin{aligned} \begin{bmatrix} I_{dh}^m \\ I_{qh}^m \end{bmatrix} &= \text{LPF} \left(\begin{bmatrix} i_{dh}^m \\ i_{qh}^m \end{bmatrix} \times 2 \cos(\omega_h t) \right) \\ &= \frac{-U_h}{\sqrt{2}\omega_h(\Sigma L^2 - \Delta L^2)} \begin{bmatrix} \Sigma L - \Delta L \cos(2\tilde{\theta}_e) + \Delta L \sin(2\tilde{\theta}_e) \\ \Sigma L - \Delta L \cos(2\tilde{\theta}_e) - \Delta L \sin(2\tilde{\theta}_e) \end{bmatrix}. \end{aligned} \quad (3.18)$$

After that, the difference is processed, and followed by the normalization, ε_f associated with position estimation error can be expressed as. The saliency-tracking observer is used to further extract the rotor position and speed information.

$$\varepsilon_f = \frac{I_{dh}^m - I_{qh}^m}{\sqrt{I_{dh}^{m2} + I_{qh}^{m2}}} \approx \sqrt{2} \left(1 - \frac{L_d}{L_q} \right) \tilde{\theta}_e \quad (3.19)$$

Compared with the HF rotating sinusoidal signal injection-based method, the HF pulsating sinusoidal signal injection-based method usually injects the voltage into the d axis, resulting in smaller additional current and torque ripples. Besides, signal processing is relatively easy to implement. However, to ensure the sinusoid of the injected voltage, the injection frequency is limited, which is not conducive to the improvement of dynamics.

3.4 HF Square-Wave Signal Injection-Based Method

3.4.1 Basic Principle

HF square-wave signal injection-based method has attracted sustaining attention for higher injection frequency and better dynamic performance. Similar to the HF pulsating sinusoidal signal injection-based method, it also injects the HF voltage into the estimated RRF. The difference is that the injected voltage is a square-wave, not a sinusoidal one. The block diagram of HF square-wave signal injection-based sensorless PMSM drive is shown in Fig. 3.7.

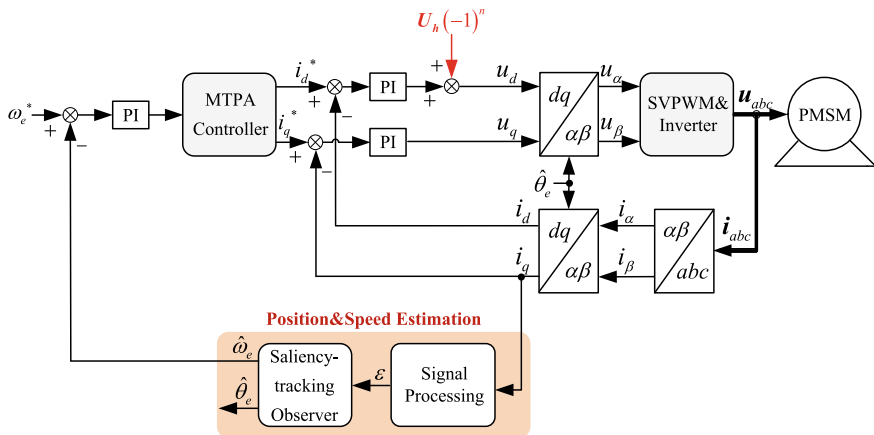


Fig. 3.7 Block diagram of HF square-wave signal injection-based sensorless PMSM drive

The injected voltage is expressed as follows:

$$\begin{bmatrix} u_{dh} \\ u_{qh} \end{bmatrix} = \begin{bmatrix} U_h (-1)^k \\ 0 \end{bmatrix} \quad (3.20)$$

where U_h and k indicate the amplitude and sequence of the injected voltage, respectively. Substitute (3.20) into (3.21) and replace the current differentiation di/dt with $\Delta i/\Delta T$, and thus, the HF current variation in one sampling period ΔT can be deduced as follows:

$$\begin{bmatrix} \Delta i_{dh} \\ \Delta i_{qh} \end{bmatrix} = \frac{\Delta T u_{dh}}{\Sigma L^2 - \Delta L^2} \begin{bmatrix} \Sigma L - \Delta L \cos(2\tilde{\theta}_e) \\ -\Delta L \sin(2\tilde{\theta}_e) \end{bmatrix}. \quad (3.21)$$

As can be seen from, Δi_{qh} contains a position estimation error. Since the injection frequency is relatively high, it can be assumed that the fundamental frequency component is almost constant in one sampling period. Given this, the variation of the sampling current approximates to that of HF current, i.e.,

$$\Delta i_{qh} = i_{qh}[k] - i_{qh}[k-1] \approx i_{\hat{q}}[k] - i_{\hat{q}}[k-1]. \quad (3.22)$$

By utilizing the variation of the sampling current in \hat{q} axis and the injected voltage, τ_f associated with position estimation error can be obtained as. The saliency-tracking observer is further used to obtain the rotor position and speed information. In this way, no digital filter is needed in the process of rotor position and speed estimation. Besides, the LPFs in the current loop can be neglected, due to the higher injection frequency.

$$\begin{aligned} \tau &= \frac{\Delta i_{\hat{q}h}}{u_{\hat{d}h}[k]} \approx \frac{i_{\hat{q}}[k] - i_{\hat{q}}[k-1]}{u_{\hat{d}h}[k]} \\ &\approx \frac{-2\Delta L \Delta T}{\Sigma L^2 - \Delta L^2} \tilde{\theta}_e. \end{aligned} \tag{3.23}$$

It is worth noting that the effects of voltage errors caused by inverter nonlinearities and voltage drops on the position estimation accuracy are not considered in the scheme as shown in Fig. 3.8a. In order to solve the problem, an enhanced scheme for position and speed estimation is introduced as shown in Fig. 3.8b [8]. The current variations $\Delta i_{\hat{q}h-p}$ and $\Delta i_{\hat{q}h-n}$ can be obtained when the positive and negative voltage

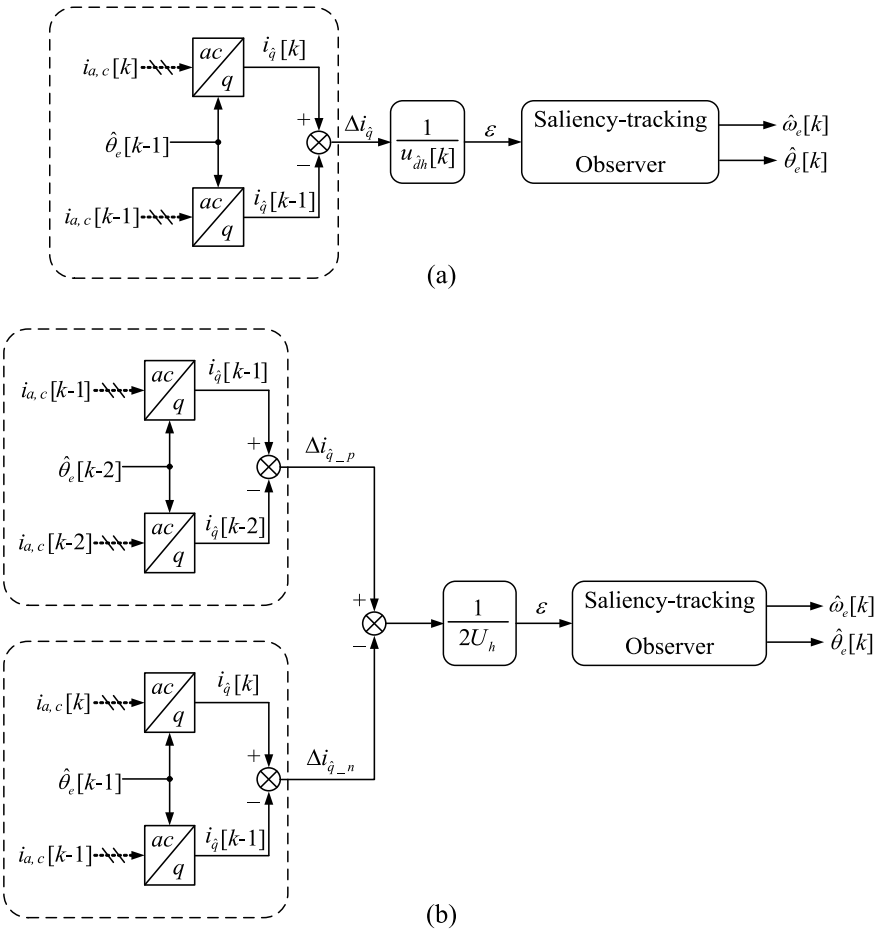


Fig. 3.8 Rotor position and speed estimation process. **a** Conventional scheme without taking voltage errors into account. **b** Enhanced scheme taking voltage errors into account

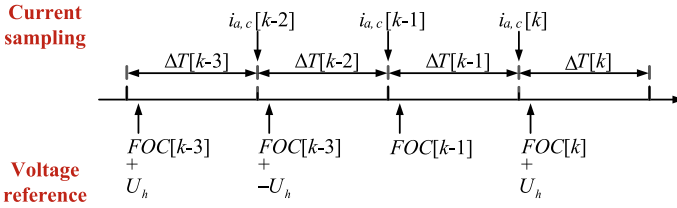


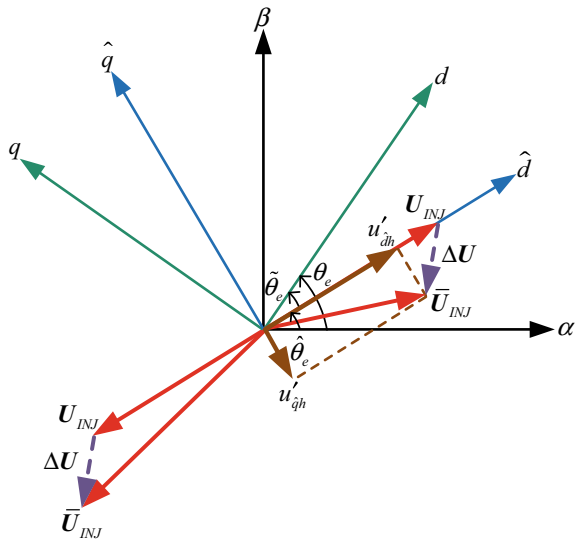
Fig. 3.9 Sequence of the enhanced HF square-wave signal injection-based method

components are injected. Subsequently, two current variations are needed for subtraction to offset the effects of voltage errors on the position estimation. Considering that there is a delay of one sampling period from the given of the voltage reference to the execution of the digital control system, an additional FOC period is required after the injection of the positive and negative HF voltages.

The sequence of the enhanced HF square-wave signal injection-based method is shown in Fig. 3.9. It is worth noting that the enhanced method introduces a delay of 1/3 of the control period so that the bandwidth of the current loop is decreased compared to the conventional HF square-wave signal injection-based method. However, due to the higher injection frequency, the LPF can be omitted in the feedback of the current loop. Therefore, the current-loop bandwidth of the enhanced injection method is still higher than that of the HF sinusoidal signal injection-based one. The specific theoretical analysis is introduced as follows.

When the voltage errors are taken into account, the injected voltage will be distorted from U_{INJ} to \bar{U}_{INJ} as shown in Fig. 3.10. The voltage in the estimated RRF can be modified as follows:

Fig. 3.10 Phasor diagram of the voltage



$$\begin{bmatrix} u'_{\hat{d}h} \\ u'_{\hat{q}h} \end{bmatrix} = \begin{bmatrix} U_h(-1)^k - U_{\hat{d},err} \\ -U_{\hat{q},err} \end{bmatrix} \quad (3.24)$$

where $U_{\hat{d},err}$ and $U_{\hat{q},err}$ are the voltage errors in the estimated RRF, and assume they are approximately invariant in one injection period. Substitute (3.24) into HF mathematical model of PMSM as shown in (3.11), and replace the current differentiation di/dt with $\Delta i/\Delta T$. Thus, the HF current variation in one sampling period ΔT can be deduced as follows:

$$\begin{bmatrix} \Delta i_{\hat{d}h} \\ \Delta i_{\hat{q}h} \end{bmatrix} = \frac{\Delta T}{\Sigma L^2 - \Delta L^2} \begin{bmatrix} \left[\Sigma L - \Delta L \cos(2\tilde{\theta}_e) \right] [U_h(-1)^k] \\ -\Delta L \sin(2\tilde{\theta}_e) [U_h(-1)^k] \\ -\left[\Sigma L - \Delta L \cos(2\tilde{\theta}_e) \right] U_{\hat{d},err} + \Delta L \sin(2\tilde{\theta}_e) U_{\hat{q},err} \\ \Delta L \sin(2\tilde{\theta}_e) U_{\hat{d},err} - \left[\Sigma L + \Delta L \cos(2\tilde{\theta}_e) \right] U_{\hat{q},err} \end{bmatrix}. \quad (3.25)$$

As can be seen from, the current variation in \hat{q} axis $\Delta i_{\hat{q}h}$ is affected by the voltage errors; thus, the retrieved rotor position and speed information would be also adversely affected. To improve the robustness to voltage errors, two current variations $\Delta i_{\hat{q}h_p}$ and $\Delta i_{\hat{q}h_n}$ are all calculated when the positive and negative voltage components are injected, respectively. After that, $\Delta i_{\hat{q}h_p}$ and $\Delta i_{\hat{q}h_n}$ are needed for the subtraction to offset the effects of voltage errors and obtaining τ' associated with the position estimation error, and τ' can be expressed as follows:

$$\begin{aligned} \tau' &= \frac{\Delta i_{\hat{q}h_p} - \Delta i_{\hat{q}h_n}}{2U_h} \\ &\approx \frac{(i_{\hat{q}}[k-1] - i_{\hat{q}}[k-2]) - (i_{\hat{q}}[k] - i_{\hat{q}}[k-1])}{2U_h} \\ &\approx \frac{-2\Delta L \Delta T}{\Sigma L^2 - \Delta L^2} \tilde{\theta}_e. \end{aligned} \quad (3.26)$$

Similarly, τ'_f associated with position estimation error is used as the input of the saliency-tracking observer to further obtain rotor position and speed information.

3.4.2 Experimental Comparison

The conventional scheme and the enhanced one are compared via an experimental platform with a 400 W PMSM, the parameters of which are listed in Table 3.1. The dead time of the inverter is set to 2, 2.5, 3 and 4 μ s. The actual rotor position of PMSM is obtained by an encoder with a resolution of 2048 bits. The DC motor mechanically couples with PMSM as a load. In the experiment, the PWM frequency

Table 3.1 Prototype parameters for position sensorless control

Rated power (W)	400
Rated frequency (Hz)	97.9
Stall current (A)	2.9
Number of poles	4
d -axis inductance (mH)	10
q -axis inductance (mH)	13
Stator resistance (Ω)	2.3
Flux linkage (Wb)	0.12

is 5 kHz, and the sampling and control frequency is 10 kHz; that is, the digital signal processor (DSP) is configured as a double-sampling double update mode.

The experimental comparison between the conventional and the enhanced HF square-wave signal injection-based method with different injection voltages and dead time values is performed, as shown in Fig. 3.11. From top to bottom, the actual operation frequency f_r of PMSM, the q -axis current i_q , the position estimation error and the phase current i_a are shown, respectively. In the experiment, the rotor position used in the Park and inverse Park transformation is the estimated one, and the actual speed obtained by the encoder serves as the feedback of the speed loop, which reduces the effects of the position estimation result. PMSM operates at 0.5 Hz with no load, then the rated step load is added, and the motor runs in the motoring state. After about 12 s, the load direction is reversed to make the motor work in the regenerating state. Then after 12 s, PMSM is operating again with no load.

It can be seen from Fig. 3.11a, c, e that the fluctuation of the position estimation error decreases with the increase of the injection amplitude. A similar conclusion can be drawn from Fig. 3.11b, d, f. As the amplitude of the injection voltage increases, its ratio with respect to the voltage errors is increased, so that the effects of injection voltage on the induced HF currents are increased accordingly.

Besides, as can be seen from Fig. 3.11e, g, when the conventional HF square-wave signal injection-based method is applied and the dead time is increased from 2 to 4 μ s at the injection voltage of 30 V, the fluctuation of the position estimation error ascends significantly. Further, the fluctuation of torque and speed fluctuation will be increased severely. While in Fig. 3.11f, h, when the enhanced HF square-wave signal injection-based method is applied, the fluctuation of the position estimation error is almost insensitive to the dead time. The enhanced HF square-wave signal injection-based method achieves the stronger robustness to the voltage errors, compared with the conventional one. More importantly, the fluctuation of the position estimation error is much smaller than that of the conventional HF square-wave signal injection-based method, as can be seen in Fig. 3.11.

Under the same conditions that the injection voltage is 30 V and the dead time is 2 μ s, the harmonic components comparison of the HF pulsating sinusoidal signal injection-based method, the conventional HF square-wave signal injection-based method and the enhanced HF square-wave signal injection-based method are

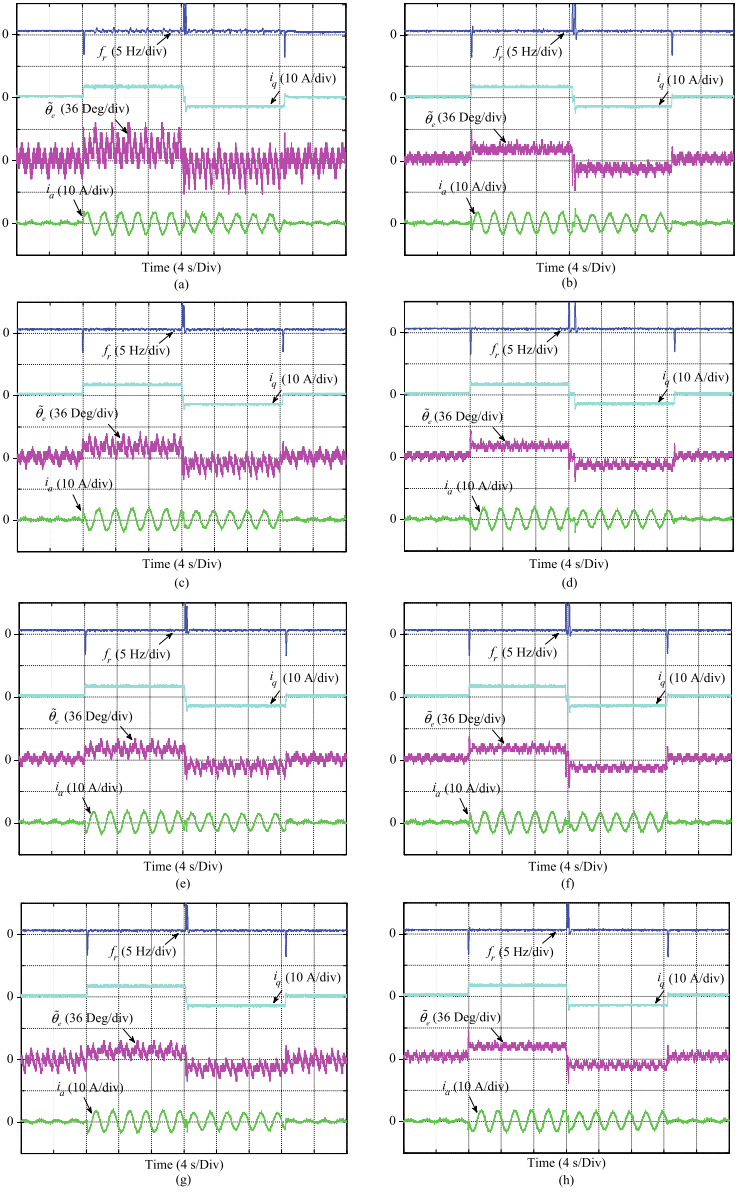


Fig. 3.11 Experimental waveform comparison between conventional and enhanced HF square-wave signal injection-based methods. **a** Conventional scheme with injected voltage of 10 V and dead time of 2 μ s. **b** Enhanced scheme with injected voltage of 10 V and dead time of 2 μ s. **c** Conventional scheme with injected voltage of 20 V and dead time of 2 μ s. **d** Enhanced scheme with injected voltage of 20 V and dead time of 2 μ s. **e** Conventional scheme with injected voltage of 30 V and dead time of 2 μ s. **f** Enhanced scheme with injected voltage of 30 V and dead time of 2 μ s. **g** Conventional scheme with injected voltage of 30 V and dead time of 4 μ s. **h** Enhanced scheme with injected voltage of 30 V and dead time of 4 μ s

performed, as shown in Fig. 3.12a–c, respectively. Since the digital control system is configured as the double-sampling double update mode, the sampling frequency is 10 kHz. In order to ensure a sufficient carrier ratio, the injection frequency of the HF pulsating sinusoidal signal injection-based method is determined as 1/10 of the sampling frequency, i.e., 1 kHz. Besides, the injection frequency of the conventional and the enhanced HF square-wave signal injection-based method can reach 1/2 and 1/3 of the sampling frequency, respectively, that is, 5 and 3.33 kHz.

As can be seen from Fig. 3.12, the induced HF current of the conventional and the enhanced HF square-wave signal injection-based method is significantly smaller, compared with that of the HF pulsating sinusoidal signal injection-based method. Considering that the enhanced HF square-wave signal injection-based method can use a smaller injection voltage, the induced HF current can be further reduced, resulting in the decreased additional loss and noise.

Compared with the HF sinusoidal signal injection-based method, the HF square-wave signal injection-based method can achieve a higher injection frequency and usually can reach half of the switching frequency. By using the double-sampling double update mode, the injection frequency can even reach switching frequency. Accordingly, the speed feedback is rather timely, which helps for the increased bandwidth and the improved dynamic performance. However, the losses of HF square-wave signal injection-based method are relatively high.

3.5 Initial Magnet Polarity Detection

3.5.1 Conventional Initial Magnet Polarity Detection Method

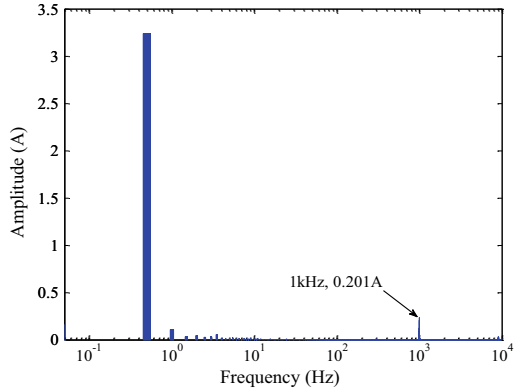
Figure 3.13 shows the scheme of the initial magnetic pole position estimation for the traction machine before motor startups by injecting HF pulsating sinusoidal voltage signal. A closed-loop current control scheme based on the vector control is adopted. As can be seen, the HF current signals, $i_{\hat{d}i}$ and $i_{\hat{q}i}$, are obtained by a high-pass filter (HPF) and rotating coordinate transformation according to the measured stator currents, i_a , and i_c . After that, current signal i_{mpy} containing the rotor position information can be obtained by multiplying $i_{\hat{d}i}$ and $i_{\hat{q}i}$,

$$i_{mpy} = \Delta L \left(\frac{U_i}{\omega_i L_d L_q} \right)^2 \frac{1 - \cos 2\omega_i t}{2} \left(\Sigma L \sin 2\tilde{\theta}_e + \frac{1}{2} \Delta L \sin 4\tilde{\theta}_e \right). \quad (3.27)$$

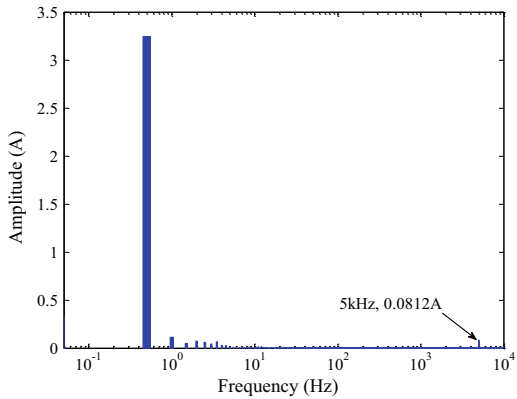
From (3.27), it can be seen that i_{mpy} contains both signals related to the rotor position and the HF components. Then, a low-pass filter (LPF) is adopted to filter the HF component. The position error signal can be expressed as follows:

$$\varepsilon(\tilde{\theta}_e) = \text{LPF}(i_{mpy})$$

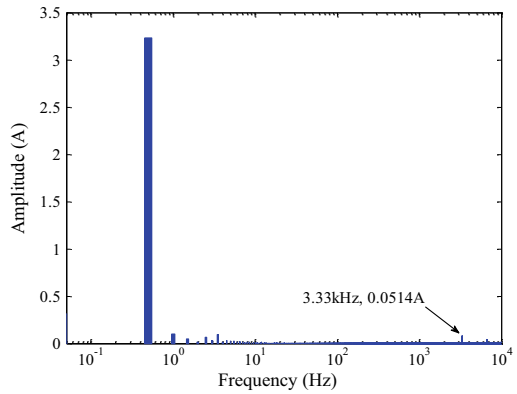
Fig. 3.12 Phase current harmonic comparison among three HF signal injection-based methods in the RRF at the same load with injected voltage of 30 V and dead time of 2 μ s. **a** HF pulsating sinusoidal signal injection-based method. **b** HF square-wave signal injection-based method with conventional signal processing. **c** HF square-wave signal injection-based method with enhanced signal processing



(a)



(b)



(c)

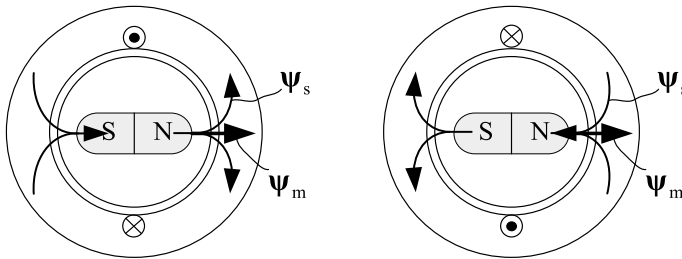


Fig. 3.14 Principle of the polarity identification based on saturation

the winding inductance. On the contrary, the stator iron will be unsaturated, and thus, the winding inductance will decrease.

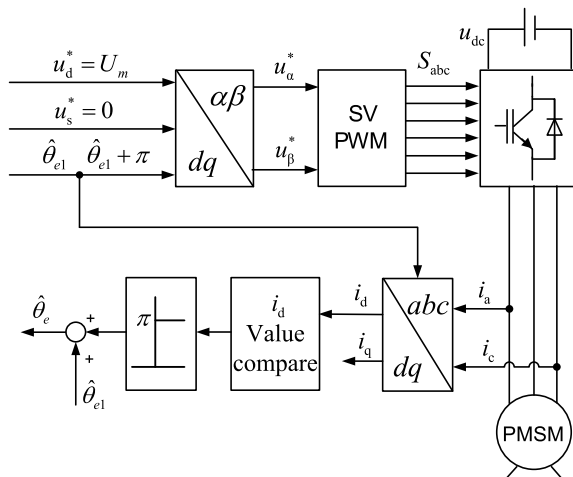
Based on the characteristic of stator iron, two pulse voltage vectors in the estimated pole position $\hat{\theta}_{e1}$ and the opposite direction $\hat{\theta}_{e1} + \pi$ are injected to identify the polarity, as shown in Fig. 3.15.

By comparing the magnitude of the d -axis current excited by the two pulse voltage vectors, the polarity can be identified easily. And the initial rotor position can be obtained from the estimated magnetic pole position by a compensation position value,

$$\hat{\theta}_e = \begin{cases} \hat{\theta}_{e1} & \text{if } (i_{sd1} > i_{sd2}) \\ \hat{\theta}_{e1} + \pi & \text{if } (i_{sd1} < i_{sd2}) \end{cases} \quad (3.31)$$

where i_{sd1} and i_{sd2} denote the responding d -axis currents of the two injected pulse voltage vectors, respectively.

Fig. 3.15 Diagram of the rotor polarity identification and compensation



3.5.2 Proposed Continuous Initial Magnet Polarity Detection Method

Figure 3.16 shows the scheme of initial rotor position detection with the proposed initial position detection method, which mainly contains three parts: the pseudo-random HF signals generation (Part 1), the HF signals demodulation (Part 2) and the current loop (Part 3). The relationship and operation principles of the three parts are described as follows [9].

As can be seen from Fig. 3.16, two different frequency square-wave voltage signals and their corresponding normalized signals are generated in Part 1. The HF signals are randomly injected into the estimated reference frame as shown in Part 3. The normalized signals are used for the demodulation to eliminate the influence of motor parameters in Part 2. In Part 3, three-phase currents of PMSM are sampled in each

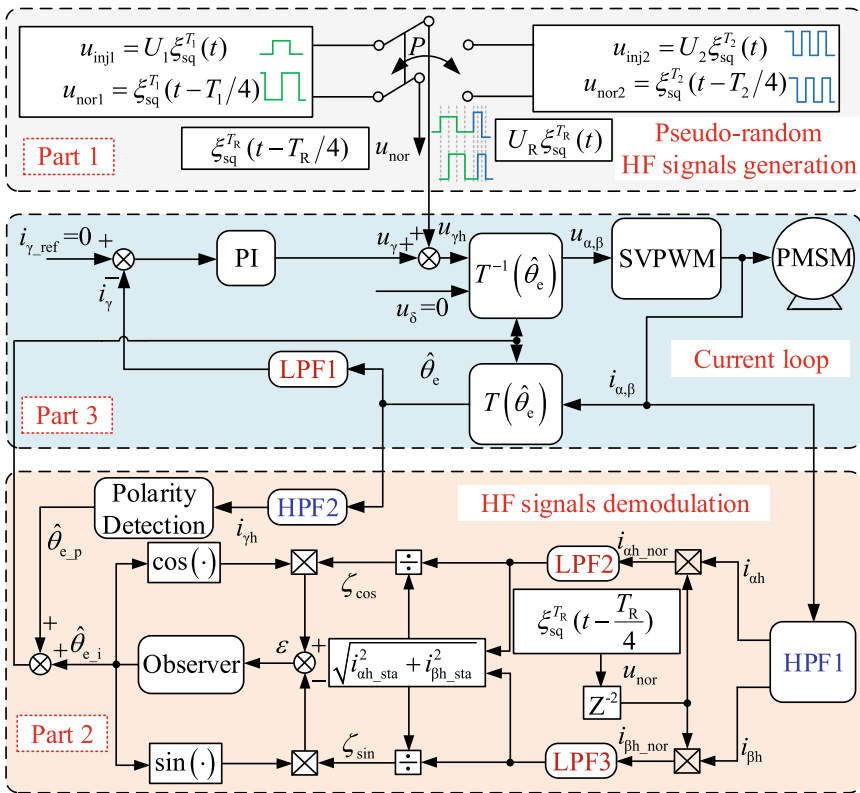


Fig. 3.16 Block diagram of the proposed initial position detection scheme

control interrupt, which contains the fundamental and the HF currents. The fundamental currents obtained through the low-pass filters (LPFs) are used for the current-loop control, as shown in Part 3. Meanwhile, the HF currents obtained through the high-pass filters (HPFs) are used for the demodulation to detect the magnetic pole position and the magnetic polarity in Part 2. Finally, the initial position can be obtained by correcting the magnetic pole position according to the magnetic polarity.

In the proposed scheme, large-amplitude pulse voltages injection can be avoided. Hence, the harsh noise caused by them can be suppressed. Moreover, the audible HF noise also can be reduced with pseudorandom signals injection compared with fixed-frequency signals injection. Therefore, the goal of low-noise initial position detection for PMSMs is achieved.

3.6 Experimental Evaluation

The proposed method was verified on a 2.2-kW IPMSM platform. The parameters of IPMSM are listed in Table 3.2. The PWM carrier frequency is set as 6 kHz. Both the LPFs and the HPFs used in this scheme are designed as second-order Butterworth filters. The cut-off frequency of LPF1 is set as 100 Hz. The cut-off frequencies of LPF2 and LPF3 are both set as 600 Hz. The cut-off frequencies of HPF1 and HPF2 are both set as 200 Hz. A commercial sound-level meter BSWA 308 was used to evaluate the harsh noise reduction effect of the proposed method.

Figure 3.17 shows the initial position detection results using the proposed method with and without the digital delay compensation during the magnetic polarity detection process. The rotor position is preset to 288° . As can be seen from Fig. 3.17a, the estimated magnetic pole position first converges to 291° and is positive with the digital delay considered. Hence, there is no need for a correction with 180° , and the initial rotor position can be obtained as 291° with an error of 3° . Further, it can be seen that the overall detection process takes only 61 ms, and the detection speed has been optimized. Nevertheless, if the digital delay is not considered, the magnetic polarity

Table 3.2 IPMSM parameters

Parameter names	Values
Rated power (kW)	2.2
Rated torque (Nm)	21
Rated frequency (Hz)	50
Pairs of poles	3
Rated voltage (V)	380
Rated current (A)	5.6
Phase resistance (Ω)	2.53
<i>d</i> -axis inductance (mH)	45
<i>q</i> -axis inductance (mH)	60

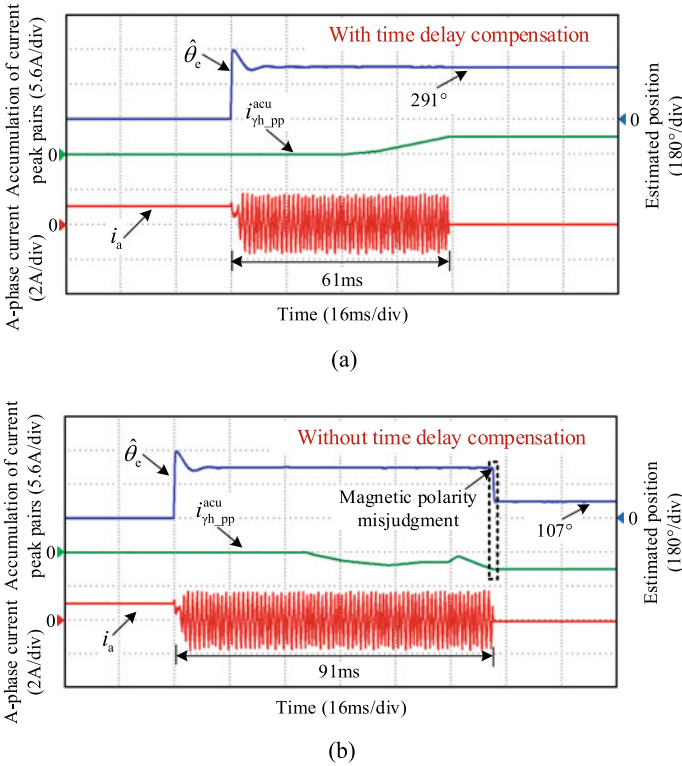
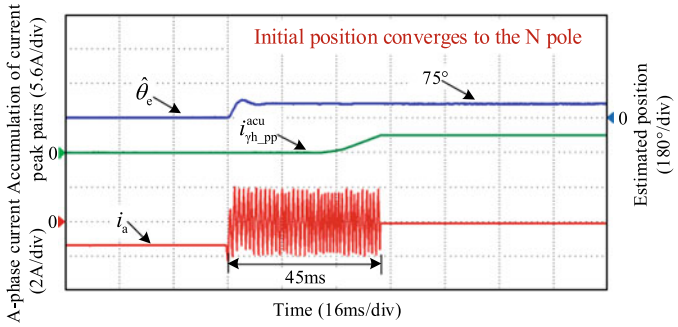


Fig. 3.17 Experimental results of initial position detection at a given position of 288° with the proposed method. **a** Magnetic polarity detection with time delay compensation. **b** Without time delay compensation

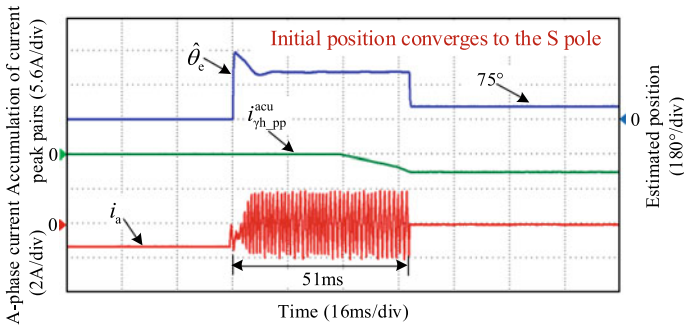
is misjudged, as shown in Fig. 3.17b. As the magnetic pole position converges to 287° , $i_{yh_pp}^{acu}$ is confusing and eventually converges to a negative value. Hence, there is a mistaken correction with 180° , and the initial rotor position can be obtained as 107° with an error of 181° .

To verify the stability of this method, the preset initial position is continuously adjusted. The initial position detection results at a given position of 72° with the proposed method are shown in Fig. 3.18. When the estimated magnetic pole position converges to 75° , as shown in Fig. 3.18a, $i_{yh_pp}^{acu}$ is positive. While in Fig. 3.18b, the estimated magnetic pole position converges to 255° and $i_{yh_pp}^{acu}$ is negative. Finally, the initial rotor position also can be identified accurately.

In addition, the identification accuracy of 20 different preset positions in an electrical cycle has been tested to verify the effectiveness of the proposed method. As shown in Fig. 3.19, the statistical results show the proposed method has higher identification accuracy and the maximum position error is 3° . For this method, the main factors which impact the detection accuracy are the motor saliency, the inverter nonlinearity and the digital delay effects. If higher detection accuracy is



(a)



(b)

Fig. 3.18 Experimental results of initial position detection at a given position of 72° with the proposed method. **a** γ -axis corresponds to the N pole. **b** γ -axis corresponds to the S pole

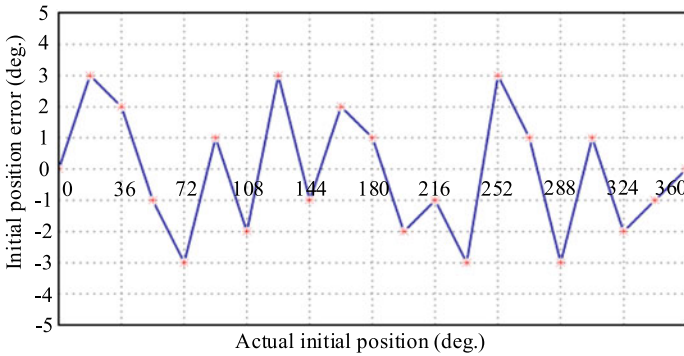


Fig. 3.19 Statistical results of Initial position observation error in an electrical cycle with the proposed method

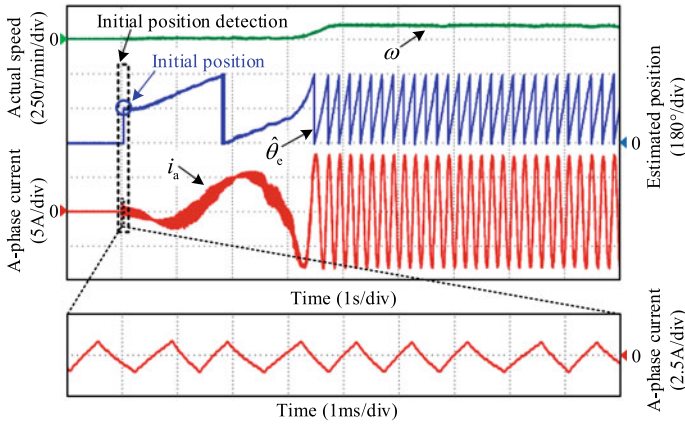


Fig. 3.20 Experimental results for starting up with rated load using the proposed method

required, look-up table-based offline compensation strategies can be applied. Moreover, effective online compensation strategies can be employed to reduce the inverter nonlinearity and the digital delay effects.

Figure 3.20 shows the experimental results for starting up with rated load using the proposed method. The load IM provides a constant torque before the test IPMSM starting up. To ensure continuity, the PRHFSVI method is still used to control the motor after starting up. The results show that the initial rotor position can be detected accurately and quickly. The motor also can start up smoothly with the proposed method.

Figure 3.21 shows the comparison of initial rotor position detection results with the double reverse pulse voltage injection method, the fixed-frequency voltage injection method and the proposed method. The rotor is preset at the same position of 108° . As can be seen from Fig. 3.21, all three methods can accurately detect the initial position. However, in Fig. 3.21a, the amplitude of the instantaneous peak current reaches about 7.5 A (the rated current is 5.6 A). Therefore, during the experiments, it was found that besides the shrill HF noise, the harsh noise caused by induced large-amplitude pulse currents cannot be ignored. Moreover, with the fixed-frequency voltage injection method, the HF noise caused by fixed-frequency signals is still shrill. However, with the proposed method, the annoying noise can be suppressed effectively.

Figure 3.22 shows the experimental results of the inverter output voltage and the induced phase current, their experimental PSD analysis and the phase current simulation PSD analysis with the fixed-frequency and the pseudorandom frequency injection methods. For the fixed-frequency injection using 750 Hz, the discrete peaks present on 750 Hz, 2.25 kHz and 3.75 kHz, etc. For the fixed-frequency injection using 1 kHz, the discrete peaks present on 1 kHz, 3 kHz and 5 kHz, etc. Nevertheless, for the pseudorandom frequency signals injection, the peaks on 750 Hz, 1 kHz and their odd harmonics are suppressed effectively and the power density spectrum is

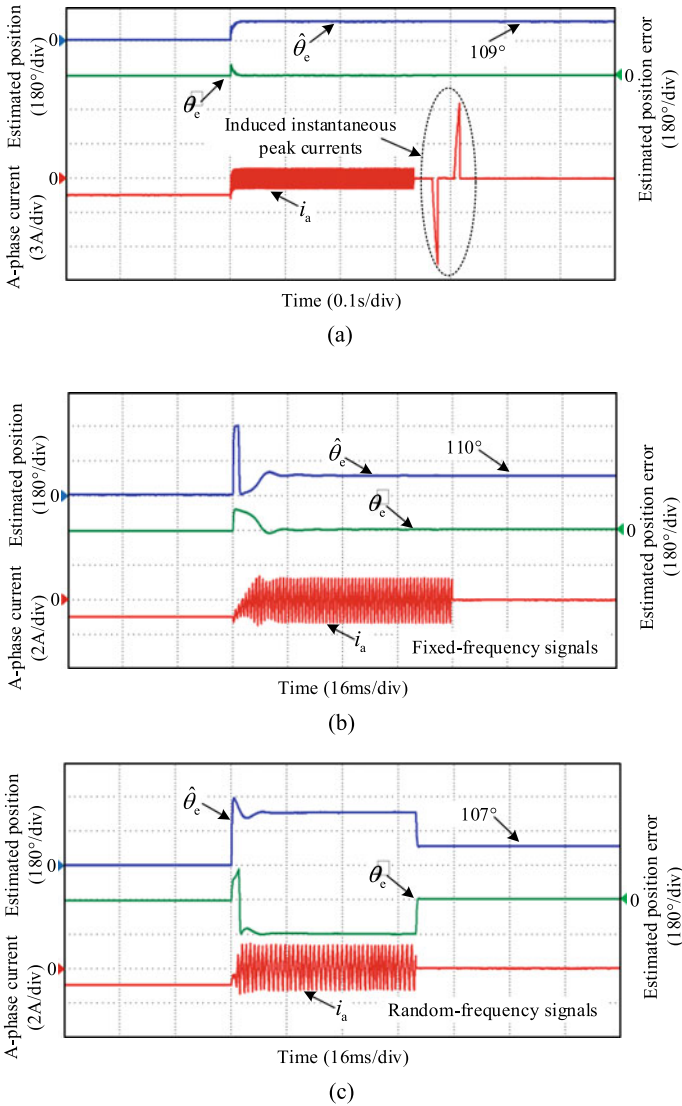


Fig. 3.21 Comparison of initial rotor position detection results at the same position of 108° . **a** Double reverse pulse voltage injection. **b** Fixed-frequency voltage injection. **c** Proposed method

also broadened both in simulation and in experimental results. Hence, this method can make the noise softer.

Figure 3.23 shows the sound-level comparison among the double reverse pulse voltage injection, the fixed-frequency voltage injection and the proposed method with the sound level meter BSWA 308. The sound level is measured on ten different

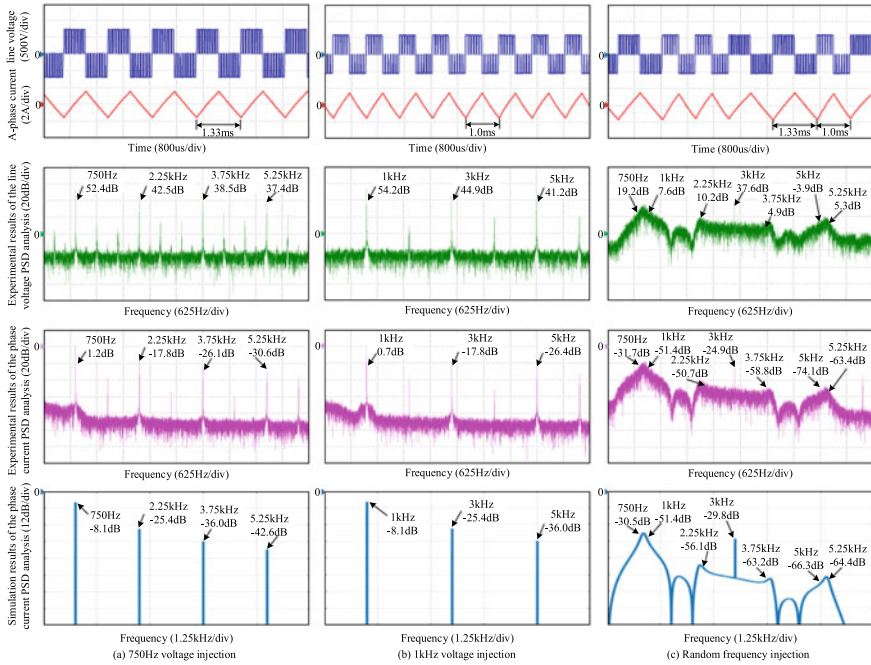


Fig. 3.22 Experimental and simulation analysis of the audible HF noise for initial position detection. **a** 750 Hz voltage injection. **b** 1 kHz voltage injection. **c** Random frequency injection

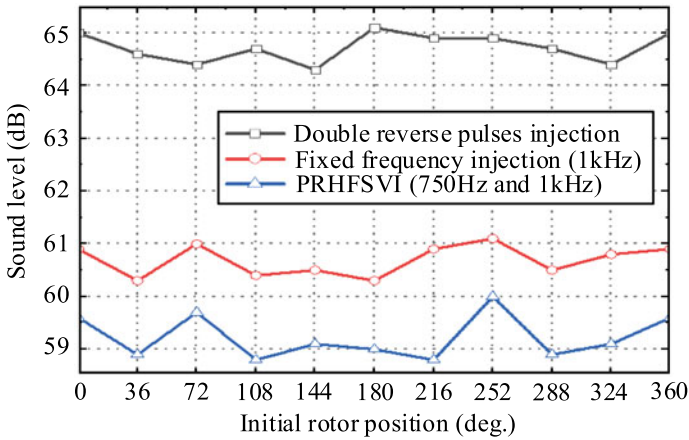


Fig. 3.23 Sound-level comparison among the double reverse pulse voltage injection, the fixed-frequency voltage injection and the proposed method

preset initial positions among the above three methods, respectively. The sound-level meter shows that the normal indoor noise is about 41.7 dB. When the inverter operates, the noise becomes about 57.1 dB. As can be seen from Fig. 3.23, the noise of initial position detection using the proposed method is the lowest. The sound-level difference among the three methods is about 4 dB and 2 dB, which means that the noise source power is reduced by 60.2% and 36.7%, respectively. From the actual auditory effect, the noise becomes softer with the proposed method. It is noteworthy that the sound level comparison is consistent with the PSD analysis results and experimental results.

3.7 Summary

The saliency-based sensorless control for PMSM traction drives is introduced in detail in the chapter. The HF model and the basic principle of the sensorless method based on saliency tracking and two kinds of injection methods which are sinusoidal and square-wave signal injection are firstly demonstrated. Then, the initial magnet polarity detection methods including conventional one and the continuous one are presented in detail. At last, experimental evaluation is addressed.

References

1. Boussak M (2005) Implementation and experimental investigation of sensorless speed control with initial rotor position estimation for interior permanent magnet synchronous motor drive. *IEEE Trans Power Electron* 20(6):1413–1422
2. Antonello R, Tinazzi F, Zigliotto M (2015) Benefits of direct phase voltage measurement in the rotor initial position detection for permanent-magnet motor drives. *IEEE Trans Ind Electron* 62(11):6719–6726
3. Ji-Hoon J, Jung-Ik H, Ohto M et al (2004) Analysis of permanent-magnet machine for sensorless control based on high-frequency signal injection. *IEEE Trans Ind Appl* 40(6):1595–1604
4. Zhang X, Li H, Yang S et al (2018) Improved initial rotor position estimation for PMSM drives based on HF pulsating voltage signal injection. *IEEE Trans Ind Electron* 65(6):4702–4713
5. Xu P, Zhu ZQ (2017) Initial rotor position estimation using zero-sequence carrier voltage for permanent-magnet synchronous machines. *IEEE Trans Ind Electron* 64(1):149–158
6. Tauchi Y, Kubota H (2014) Audible noise reduction method in IPMSM position sensorless control based on high-frequency current injection. In: *Proc. IEEE int. power electron. conf.*, pp 3119–3123
7. Bi G, Wang G, Zhang G et al (2020) Low-noise initial position detection method for sensorless permanent magnet synchronous motor drives. *IEEE Trans Power Electron* 35(12):13333–13344
8. Ni R, Xu D, Blaabjerg F, Lu K, Wang G, Zhang G (2017) Square-wave voltage injection algorithm for PMSM position sensorless control with high robustness to voltage errors. *IEEE Trans Power Electron* 32(7):5425–5437
9. Bi G, Wang G, Zhang G, Zhao N, Xu D (2020) Low-noise initial position detection method for sensorless permanent magnet synchronous motor drives. *IEEE Trans Power Electron* 35(12):13333–13344

Chapter 4

Speed Detection Method at Low-Speed Operation



4.1 Introduction

Permanent magnet synchronous motors (PMSMs) have been applied widely due to their advantages in terms of high power density, high torque-to-inertia ratio and high efficiency. Recently, they have been adopted more popularly in the gearless elevators of modern buildings [1]. Compared with traditional systems, PMSM-based gearless elevators show high performance at start-up, stopping and moving and can be designed more compactly [2]. Safety, stability and comfort are the essential demands of elevator systems [3]. To achieve a good riding comfort, accurate speed feedback should be obtained in real time for the closed-loop control system of a PMSM. However, during low-speed operation, strong jerks can be caused by inaccuracies and large time delays of the speed feedback, which result in the discomfort of the passengers [4]. Poor speed performance can be improved by installing a high precision encoder, while the cost of system is inevitably increased.

Quadrature encoder pulse (QEP) sensors and linear hall sensors are widely used in PMSMs to obtain speed information. Several methods have been proposed to increase measurement accuracy when low-resolution QEP sensors are adopted. One promising scheme, presented in [5], is the so-called the rotor position extrapolation algorithm using a polynomial estimator. In [6], the instantaneous speed was estimated by a Luenberger observer based on a motion model of a PMSM. Then, the estimation error was corrected by the angular position obtained by the synchronous or asynchronous sampling method. Compared to conventional observers, this method improves the resolution of the instantaneous velocity especially in the low-speed region. The rotor position signal obtained by hall sensors often contains large harmonic components, which can influence the accuracy of the speed [7]. In order to remove high-order harmonics, a novel rotor position detection method based on the synchronous frequency extractor (SFE) was utilized in [8], which was confirmed to effectively reduce the estimation error. In [9], an improved method using the periodic timer interrupt function and a simplified estimation to obtain position information based on hall sensors was presented.

In this chapter, a novel filtering method adopting a nonlinear tracking differentiator (NTD) is proposed for direct-drive permanent magnet traction machines, which tracks the speed signal more accurately [10]. After analyzing the limitations of conventional speed measurement methods for low-speed operations, the NTD-based digital filter is adopted to achieve effective speed measurement at low speeds. Then the parameter selection of the proposed digital filter is discussed by analyzing the basic theory and frequency characteristic of the NTD. This shows a higher performance that relieves the time delay and suppresses external disturbances. Simulation and experimental results verify the feasibility of the proposed speed measurement method on an 11.7 kW elevator machine [11].

4.2 Limitation of the Conventional Speed Calculation

The permanent magnet traction machine of an elevator should operate at ultra-low speeds to satisfy the demands of riding comfort, and the speed should decrease to 0.5 rpm. To assure the good performance of the system, accurate speed information is expected in such situations.

Generally, the average speed is detected with the M, T or M/T method. The M method is often suitable for high-speed calculations, while the T method is commonly used in low-speed calculation. On the other hand, both high and low speeds can be calculated by the M/T method. However, a large detection delay is caused by the T method and M/T method when calculating ultra-low speeds, because the encoder pulse interval is much longer than the speed sampling period.

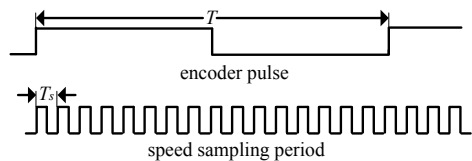
If the encoder generates 2048 signals per revolution, there are 8192 incremental count values per revolution after the quadrature processing. This means that the speed between two count pulses can be expressed as

$$n = \frac{60}{8192 * T} \quad (4.1)$$

where n represents the average speed, and T represents the interval of the pulses. When $n = 7.32$ rpm, T is calculated to be 1 ms, and when $n = 0.5$ rpm, T will be 14.65 ms, while the sampling time of the speed loop is 1 ms.

Figure 4.1 shows the relationship between the encoder pulse and the speed sampling period during ultra-low-speed operation when the speed is 0.5 rpm, where

Fig. 4.1 Relation between the encoder pulse and the speed sampling period at low-speed operation



T_s is the sampling time of the speed loop. It can be seen that the speed is calculated after more than 14 execution cycles of the speed loop, which causes a large time delay. This delay deteriorates the dynamic response of the system, resulting in instability. Furthermore, large vibrations may occur during the steady state, which is not allowed in elevator applications. If a higher resolution encoder is used to avoid the time delay, it increases the cost. However, when the speed is calculated by the M method, the sampling time is fixed. The time delay is smaller when T_s is set shorter. Although the encoder pulses may not change in several sampling cycles during low speed, the average speed can be obtained by the low-pass filtering method.

When getting the raw speed by the M method, a digital filter should be used before it feeds back to the speed controller. Low-pass filters (LPFs) are widely used in conventional speed estimation, whose filtering performance can be regulated by changing the cut-off frequency. The lower the cut-off frequency is, the smoother the filtered signal becomes. However, this can also result in a larger time delay. Therefore, an advanced filtering method based on the nonlinear tracking differentiator (NTD) is proposed in this chapter to overcome the disadvantages of the LPF and to track the actual speed more effectively.

4.3 Speed Detection Based on the NTD Theory

The NTD was originally proposed by Prof. Han. It is mainly used to extract continuous signals and differential signals from non-continuous signals that have interference by noise. By using a nonlinear function, the method adopts integral calculation instead of differentiation, which suppresses the noise amplification. Furthermore, the input of the NTD is the discrete position signal, which is suitable for both incremental and absolute encoders. The principle of the NTD is described as follows.

For a double integral plant

$$\begin{cases} \dot{x}_1 = \dot{x}_2 \\ \dot{x}_2 = u(x_1, x_2), u \leq M \end{cases} \quad (4.2)$$

A suitable $u(x_1, x_2)$ can be selected to guarantee a fast convergence from x_1 and x_2 to 0. Let $x_1 = x_1 - v$, this solution satisfies $\lim_{t \rightarrow \infty} x_1(t) = v$, $\lim_{t \rightarrow \infty} x_2(t) = \dot{v}$, where x_1 is the desired trajectory of v , and x_2 is its derivative. This means that when v is regarded as the input of the system, it is tracked quickly and effectively by x_1 . Instead of containing all of the information of v , x_1 can extract its effective and continuous signal. Several adjustable parameters are included in $u(x_1, x_2)$. By changing these parameters, the filtering performance can be improved. $u(x_1, x_2)$ is the so-called optimal control synthesis (OCS) function which introduces considerable numerical errors into discrete-time implementations. Equation (4.2) can be discretized as

$$\begin{cases} x_1(k+1) = x_1(k) + T_s x_2(k) \\ x_2(k+1) = x_2(k) + T_s u(k) \end{cases} \quad (4.3)$$

Based on the analysis above, the NTD for speed measurements is defined as

$$\begin{cases} \omega_n(k+1) = \omega_n(k) + T_s \omega_d(k) \\ \omega_d(k+1) = \omega_d(k) + T_s \text{fst}(\omega_n(k) - \omega(k), \omega_d(k), M, h) \end{cases} \quad (4.4)$$

where M is the convergence factor, h is the filtering factor, ω is the raw speed, ω_n is the speed processed by the NTD, and ω_d is its derivative. $\text{fst}(\omega_n(k) - \omega(k), \omega_d(k), M, h)$ is a nonlinear OCS function of the NTD filtering part. The parameters M and h influence the dynamic performance and ability of the noise suppression, respectively.

$\text{fst}(\omega_n(k) - \omega(k), \omega_d(k), M, h)$ is an OCS function which is selected to obtain fast convergence of the NTD. Considering that the practical system is discretely calculated by the processing chip, it is more suitable to deduce the expression of $\text{fst}(\omega_n(k) - \omega(k), \omega_d(k), M, h)$ under the condition of discretization. Based on the theory of optimum time control, the expression of $\text{fst}(\omega_n(k) - \omega(k), \omega_d(k), M, h)$ can be deduced as follows.

Let $\Delta\omega(k) = \omega_n(k) - \omega(k)$ and assume that the initial value is $\omega = [\Delta\omega(0), \omega_d(0)]^T$. Then after k steps of iterations, the solution of (4.4) is

$$\begin{aligned} \begin{bmatrix} \Delta\omega(k) \\ \omega_d(k) \end{bmatrix} &= \begin{bmatrix} 1 & kT_s \\ 0 & 1 \end{bmatrix} \begin{bmatrix} \Delta\omega(0) \\ \omega_d(0) \end{bmatrix} + \begin{bmatrix} 1 & (k-1)T_s \\ 0 & 1 \end{bmatrix} \begin{bmatrix} 0 \\ T_s \end{bmatrix} \text{fst}(0) \\ &+ \cdots + \begin{bmatrix} 1 & T_s \\ 0 & 1 \end{bmatrix} \begin{bmatrix} 0 \\ T_s \end{bmatrix} \text{fst}(k-2) + \begin{bmatrix} 0 \\ T_s \end{bmatrix} \text{fst}(k-1). \end{aligned} \quad (4.5)$$

Assuming

$$\begin{bmatrix} \Delta\omega(k) \\ \omega_d(k) \end{bmatrix} = \begin{bmatrix} 0 \\ 0 \end{bmatrix}. \quad (4.6)$$

The expression of the initial values can be expressed as

$$\begin{aligned} \begin{bmatrix} \Delta\omega(0) \\ \omega_d(0) \end{bmatrix} &= \begin{bmatrix} kT_s^2 \\ -T_s \end{bmatrix} \text{fst}(k-1) + \begin{bmatrix} (k-1)T_s^2 \\ -T_s \end{bmatrix} \text{fst}(k-2) \\ &+ \cdots + \begin{bmatrix} 2T_s^2 \\ -T_s \end{bmatrix} \text{fst}(1) + \begin{bmatrix} T_s^2 \\ -T_s \end{bmatrix} \text{fst}(0). \end{aligned} \quad (4.7)$$

According to (4.7), when $fst(i)(i = 0, 1, \dots, k - 1) = +M$, the collection of initial points $\{a_{+k}\}$ can be expressed as

$$\begin{bmatrix} \Delta\omega \\ \omega_d \end{bmatrix} = \begin{bmatrix} \frac{1}{2}k(k+1)T_s^2M \\ -kT_sM \end{bmatrix}. \quad (4.8)$$

When $fst(i)(i = 0, 1, \dots, k - 1) = -M$, the collection of initial points $\{a_{-k}\}$ can be expressed as

$$\begin{bmatrix} \Delta\omega \\ \omega_d \end{bmatrix} = \begin{bmatrix} -\frac{1}{2}k(k+1)T_s^2M \\ kT_sM \end{bmatrix}. \quad (4.9)$$

When $fst(k-1) = +M, fst(i) = -M(i = 0, 1, \dots, k-2)$, the collection of initial points $\{b_{+k}\}$ can be expressed as

$$\begin{bmatrix} \Delta\omega \\ \omega_d \end{bmatrix} = \begin{bmatrix} -\frac{1}{2}k(k+1)T_s^2M - 2T_s^2M \\ (k-2)T_sM \end{bmatrix}. \quad (4.10)$$

When $fst(k-1) = -M, fst(i) = +M(i = 0, 1, \dots, k-2)$, the collection of initial points $\{b_{-k}\}$ can be expressed as

$$\begin{bmatrix} \Delta\omega \\ \omega_d \end{bmatrix} = \begin{bmatrix} \frac{1}{2}k(k+1)T_s^2M - 2T_s^2M \\ -(k-2)T_sM \end{bmatrix}. \quad (4.11)$$

Figure 4.2 shows the location of a_{+k}, a_{-k}, b_{+k} and b_{-k} .

Definition 1 $SA(k)$ is the synchronous area of the amount of initial points ω . These points converge to the origin in k steps of iterations. $SA(k)$ is a convex polygon with

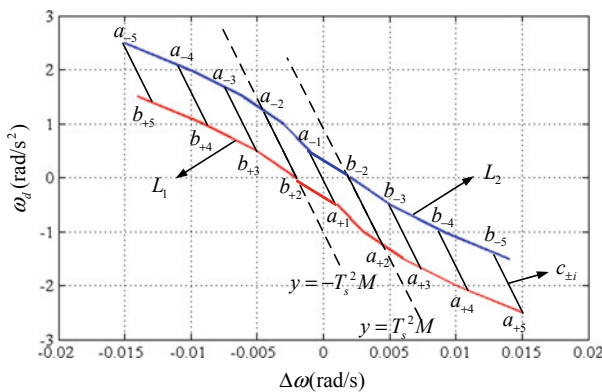


Fig. 4.2 Coordinate curves of initial value

$2k$ lines. For example, $SA(1)$ is the line of $a_{+1}a_{-1}$, while $SA(2)$ is the parallelogram of $a_{-2}b_{-2}a_{+2}b_{+2}$ and so on.

Definition 2 L_1, L_2 Denote the fold lines $a_{+k}, a_{+(k-1)}, \dots, a_1, b_2, \dots, b_{+(k-1)}, b_{+k}$ as L_1 and $a_{-k}, a_{-(k-1)}, \dots, a_{-1}, b_{-2}, \dots, b_{-(k-1)}, b_{-k}$ as L_2 . As analyzed above, when ω is on or beneath L_1 , the control value fst is selected as $+M$; when ω is on or above L_2 , fst is selected as $-M$; and when ω is between L_1 and L_2 , fst is selected in $[-M, +M]$.

As can be seen from Fig. 4.2, the state variable of the system converges to 0 in limited sampling periods through its relevant trajectory when $fst(i)$ changes under different rules. For example, if the initial point of ω is above L_2 , fst will be selected as $-M$. Under the control force of fst , the point will move to L_2 . Then it will converge to 0 in limited sampling periods along its specific area. In particular, when the points are in the middle of lines $a_i b_{-i}$ and $a_{-i} b_i$, fst is selected as 0, which means that they will move to $a_{\pm i}$ without a control force.

The name of the midpoint of $a_i b_{-i}$ and $a_{-i} b_i$ is $c_{\pm i}$, which is shown in Fig. 4.2. Thus, the coordinate of c_{+k} and c_{-k} can be expressed as:

$$\begin{bmatrix} \Delta\omega \\ \omega_d \end{bmatrix} = \begin{bmatrix} \frac{1}{2}k(k+1)T_s^2M - T_s^2M \\ -(k-1)T_sM \end{bmatrix} \quad (4.12)$$

and

$$\begin{bmatrix} \Delta\omega \\ \omega_d \end{bmatrix} = \begin{bmatrix} -\frac{1}{2}k(k+1)T_s^2M + T_s^2M \\ (k-1)T_sM \end{bmatrix}. \quad (4.13)$$

Condition 1 Beyond $SA(2)$ When the initial points are beyond $SA(2)$, the OCS function $fst1$ can be deduced as follows.

As can be concluded from (4.8) to (4.13), these points can be contained by the six parabolas that follow

$$\left\{ \begin{array}{l} \Delta\omega = \frac{\omega_d^2 - T_s M \omega_d}{2M}, \omega_d < 0 \\ \Delta\omega = -\frac{\omega_d^2 - T_s M \omega_d}{2M}, \omega_d > 0 \\ \Delta\omega = \frac{\omega_d^2 - 5T_s M \omega_d + 2T_s^2 M^2}{2M}, \omega_d < 0 \\ \Delta\omega = -\frac{\omega_d^2 - 5T_s M \omega_d + 2T_s^2 M^2}{2M}, \omega_d > 0 \\ \Delta\omega = \frac{\omega_d^2 - 3T_s M \omega_d}{2M}, \omega_d < 0 \\ \Delta\omega = -\frac{\omega_d^2 - 3T_s M \omega_d}{2M}, \omega_d > 0 \end{array} \right. \quad (4.14)$$

Define $y = \Delta\omega + T_s \omega_d$, and (4.14) can be rewritten by three equations which can be expressed as

$$\begin{cases} \omega_d - \text{sign}(y) \frac{M}{2} \left(T_s - \sqrt{\frac{8|y|}{M} + T_s^2} \right) = -\text{sign}(y) T_s M (a_{\pm i}) \\ \omega_d - \text{sign}(y) \frac{M}{2} \left(T_s - \sqrt{\frac{8|y|}{M} + T_s^2} \right) = \text{sign}(y) T_s M (b_{\pm i}) \\ \omega_d - \text{sign}(y) \frac{M}{2} \left(T_s - \sqrt{\frac{8|y|}{M} + T_s^2} \right) = 0 (c_{\pm i}) \end{cases} \quad (4.15)$$

Define the auxiliary equation as

$$g(\omega_g, y) = \omega_d - \text{sign}(y) \frac{M}{2} \left(T_s - \sqrt{\frac{8|y|}{M} + T_s^2} \right). \quad (4.16)$$

It can be known that $g(c_{+i}) = g(c_{-i}) = 0$, $g(a_{+i}) = g(b_{+i}) = T_s M$, and $g(a_{-i}) = g(b_{-i}) = -T_s M$.

According to the analysis above and by applying the power function in nonlinear control, the OCS function beyond SA(2) can be obtained as

$$fst1 = \begin{cases} -M \text{sign}(g(\omega_d, y)), |g(\omega_d, y)| \geq T_s M \\ -\frac{g(\omega_d, y)}{T_s}, |g(\omega_d, y)| < T_s M \end{cases} \quad (4.17)$$

This guarantees fast convergence from ω_n to ω , which means that the effective and continuous signal of the speed will be extracted accurately and fast.

Condition 2 Inside SA(2) It can be seen from Fig. 4.2 that SA(2) is surrounded by fourfold lines, whose expression is written as

$$\begin{cases} y + T_s \omega_d = T_s^2 M, (a_{-2} b_{-2}) \\ y + T_s \omega_d = -T_s^2 M, (a_{+2} b_{+2}) \\ y = T_s^2 M, (a_{+2} b_{-2}) \\ y = -T_s^2 M, (a_{-2} b_{+2}) \end{cases} \quad (4.18)$$

When $k = 2$, the solution of $fst(0)$ can be obtained from (4.7) as

$$fst(0) = \frac{\Delta\omega(0) + 2T_s\omega_n(0)}{T_s^2} = \frac{\omega_d(0) + y(0)/T_s}{T_s}. \quad (4.19)$$

Combining (4.18) and (4.19), the OCS function inside SA(2) can be obtained as:

$$fst2 = \frac{\omega_d + y/T_s}{T_s} \quad (4.20)$$

where $|\omega_d + y/T_s| \leq T_s M$, $|y| \leq T_s^2 M$.

Above all, the OCS function in this chapter is set as a sectional type. When the initial point is beyond SA(2), fst is selected as the maximum value ($\pm M$) to move it

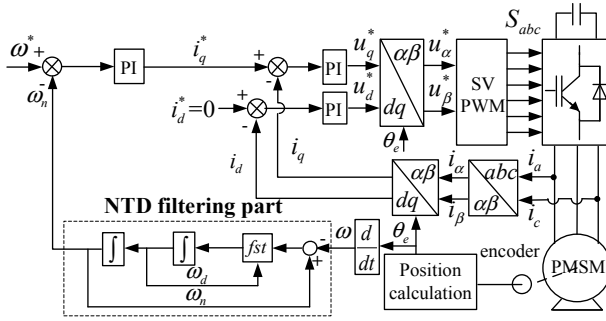


Fig. 4.3 Structure of the elevator traction machine drive

toward the inner SA(2). Then, fst is selected as $fst2$ to make it converge to the origin as quickly as possible.

In order to suppress noise in the input signal and to avoid chattering in the switch function, let $h = nT_s$, where n is the amplification of T_s . This means that the sampling step in the OSC function is increased, which helps to filter high-frequency signals but inevitably causes a time delay.

As a result, the expression of the OSC function is obtained as

$$fst(\omega_n(k) - \omega(k), \omega_d(k), M, h) = - \begin{cases} Ma/d, & |a| \leq d \\ M \text{sign}(a), & |a| > d \end{cases} \quad (4.21)$$

where

$$a = \begin{cases} \omega_d + y/h, & |y| \leq d_0 \\ \omega_d + \frac{a_0 - d}{2} \text{sign}(y), & |y| > d_0 \end{cases}, \quad (4.22)$$

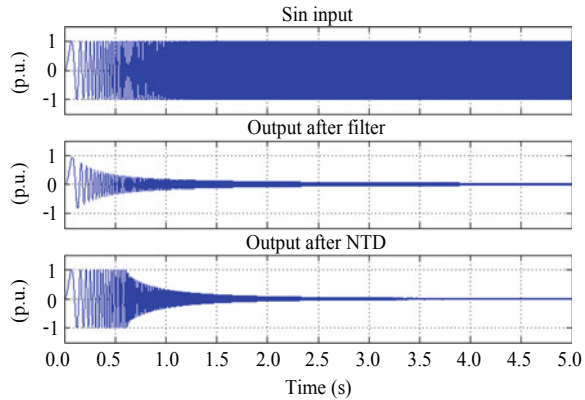
$$\begin{cases} d = Mh \\ d_0 = dh \\ y = \omega_n - \omega + h\omega_d \\ a_0 = \sqrt{d^2 + 8M|y|} \end{cases}. \quad (4.23)$$

Based on the conclusion above, the closed-loop control system of an elevator is established where the NTD acts as a digital filter of raw speed, as shown in Fig. 4.3.

4.4 Frequency-Response Analysis and Parameter Selection

The NTD is a nonlinear system as a result of using a nonlinear function. Therefore, the conventional analysis methods of a linear system cannot be used to analyze its frequency characteristics. Here, a chirp signal is used to realize the frequency sweep

Fig. 4.4 Frequency sweep results of low-pass filter and NTD



measurement in order to obtain the frequency response of the NTD. Input the chirp signal to the NTD and observe its output. The frequency–response is obtained and compared with that of a first-order Butterworth LPF, which shows the advantage of the NTD.

Note the response of the NTD is related to the input amplitude, which should be considered in the sweep measurement. In the practical experimental platform, every variable whose range is from 0 to 1 is calculated by per unit values in the controller chip. When the input is between 0 and 1, the NTD shows the same characteristics because the amplitude of the input is in the same response interval. Therefore, the chirp signal is set to be 0–500 Hz with its amplitude set 1. The NTD parameters are selected as follows: $M = 500$ and $h = 0.01$. The cut-off frequency of the first-order Butterworth LPF is 17 Hz. The analysis results are shown in Fig. 4.4.

Note that the frequency of the chirp signal changes uniformly over time, meaning that the time in the horizontal axis can be regarded as the frequency, and the amplitude in vertical axis can be regarded as the gain of the system. Define the width in the horizontal axis when the amplitude drop is from 1 to 0.707 as the bandwidth. It can be found that with an increase of the frequency, the amplitude of the LPF decreases gradually which indicates a narrow bandwidth. Meanwhile, the NTD shows a constant output amplitude during the low-frequency region and a wider bandwidth can be achieved. In addition, when reaching the cut-off frequency, the LPF shows slower attenuation ratio of amplitude when compared with that of the NTD. In conclusion, the NTD appears to have a better filtering property.

By using frequency sweep measurement, the influence of parameter M can be detected. Keeping $h = 0.01$ and giving various values of M , different analysis results are shown in Fig. 4.5.

It can be illustrated that with an increase of M , the bandwidth becomes wider, which means that the NTD obtains a faster response and stronger stability. Generally, the bandwidth of the NTD will be proportional to \sqrt{M} .

As analyzed previously, M is the maximum value of the OCS function. When a larger value of M is selected, the force of the control variable to the system is

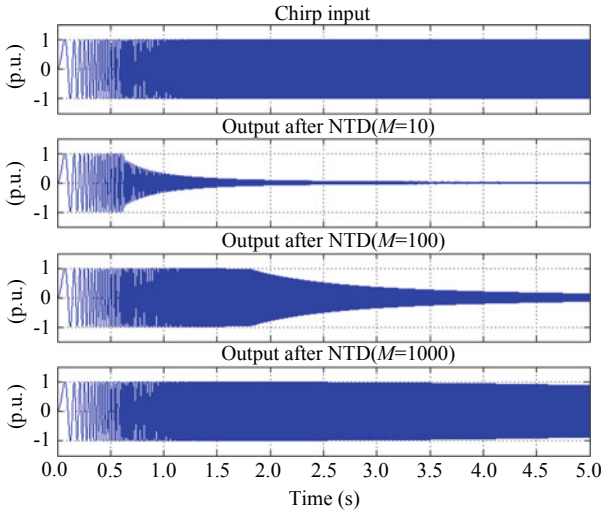


Fig. 4.5 Frequency sweep results of NTD using various M

stronger, which means a higher tracking speed. However, since M is proportional to the bandwidth of the system, a larger M does not assure the filtering effect of the high-frequency noise. The scale of M can be selected from 500 to 1000 with no high-frequency existing.

Then by observing the output of the NTD when inputting a sinusoidal signal mixed with random noise, the filtering effects for different values of h can be detected. Set the frequency of standard sinusoidal signal as 1 Hz and the amplitude as 1. The analysis results are shown in Fig. 4.6 when $M = 500$, and $h = 5T_s$, $10T_s$, $20T_s$ and $30T_s$, respectively.

In Fig. 4.6, each of the four figures shows the expected output and the output of the NTD when the sinusoidal input contains random noise. It can be seen that the filtering performance of the NTD is improved significantly with the increasing of h , which means that it can perform better in extracting an effective signal. However, h mainly influences the effects of noise suppression. As analyzed before, $h = nT_s$, which enlarges the sampling step in the OSC function. Thus, the changing rate of the control variable is reduced. This means that when the input speed is in a higher frequency, the output remains unchanged instead of tracking it. Hence, the high-frequency noise is filtered and the effective signal is extracted. However, the value of h should be limited because a time delay is present when it is selected to be larger. This affects the stability of the system when it is out of range. Therefore, h is usually selected from 3 to $20T_s$ in practical applications.

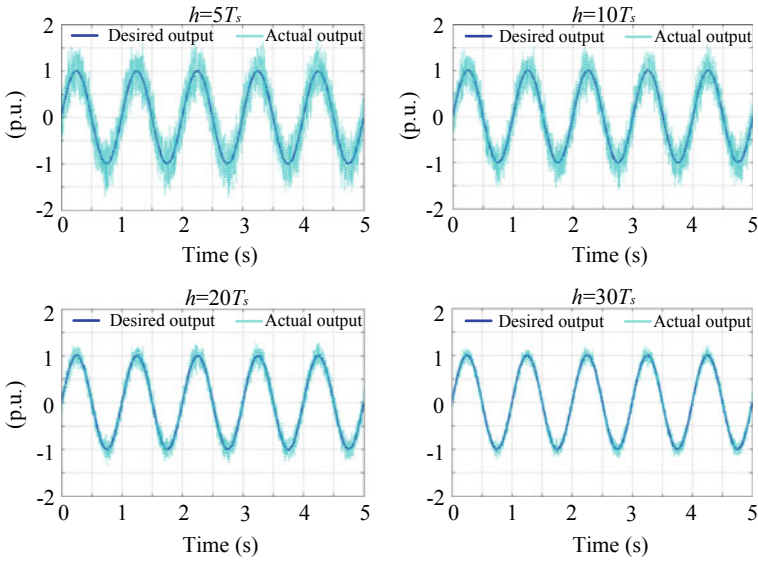


Fig. 4.6 Filtering effect of various h

4.5 Signal Processing of the SIN/COS Encoder

The interface board connecting the encoder (ERN1387) and the TMS320F2808 DSP is a SIN/COS Encoder Feedback PG-Card as shown in Fig. 4.7. The signal connection and signal processing circuit are also illustrated in Fig. 4.7. The differential signals

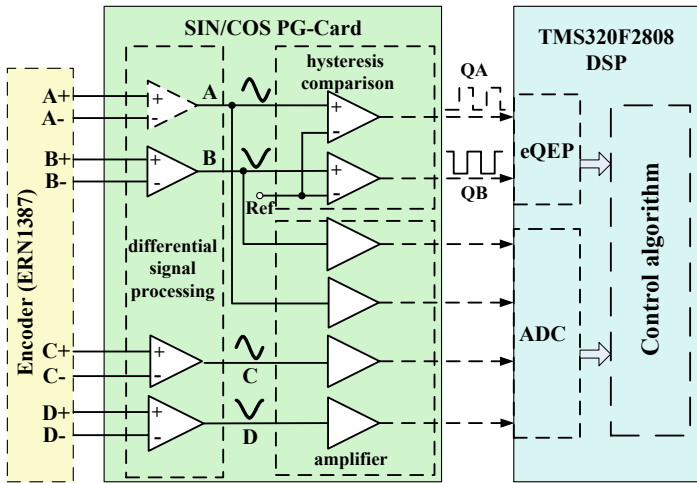


Fig. 4.7 Schematic diagram of the interface board connecting the encoder and the microprocessor

$\pm A$, $\pm B$, $\pm C$ and $\pm D$ from the encoder are processed by a differential operational circuit in the PG-Card, then four sinusoidal outputs A, B, C and D can be got. The commutation signals C and D appear as one sinusoidal or cosine period, respectively, per revolution. And they can be used to calculate the absolute position of the rotor. The sinusoidal incremental signals A and B are phase-shifted by 90° and appear as 2048 sinusoidal or cosine periods per revolution. Signals A and B are then processed by a hysteresis comparison circuit, and this circuit produces two 90° phase-shifted square-wave pulse trains QA and QB. Particularly, the edges of QA and QB will make the register (its value denotes the incremental count) in eQEP count up or down.

The position calculation algorithm is executed by the TMS320F2808 DSP. The position is updated at each PWM period (i.e., $100 \mu s$). The detailed calculation method is shown in Fig. 4.8. The rotor position θ_m can be calculated

$$\theta_m = \frac{2\pi}{M} \left(N + \theta_{div} \cdot \frac{2}{\pi} \right) \tag{4.24}$$

where N is the incremental count, M is the maximum incremental count value, and it equals 8192 for the 2048 P/R Sin-Cos encoder, θ_{div} is the subdivision calculated from the quadrature signals by the arc-tangent function. In Fig. 4.8, the rotor changes its direction at time t_1 . The experimental waveforms of the sinusoidal incremental signals (A and B), the square-wave pulse trains (QA and QB) and the incremental count are shown in Fig. 4.9. The position subdivision results are shown in Fig. 4.10. The resolution of the subdivision depends on the precision of the A/D conversion and the signal quality of A and B.

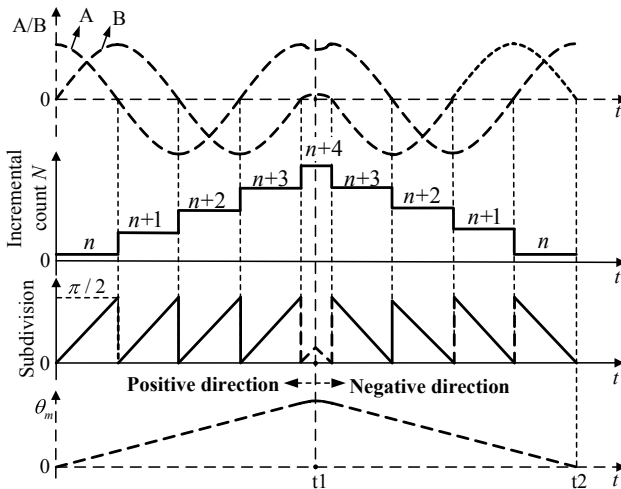


Fig. 4.8 Rotor position calculation process by using the Sin-Cos encoder

Fig. 4.9 Experimental waveforms of the rotor position calculation by using the Sin-Cos encoder (Sin-Cos signals, A-B quadrature signals and incremental count value)

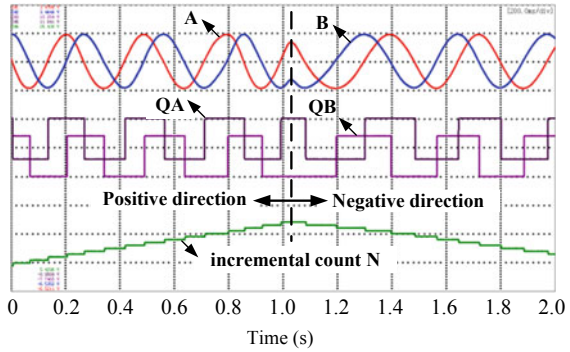
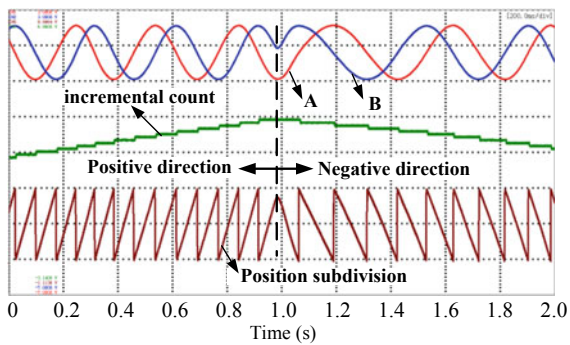


Fig. 4.10 Experimental waveforms of the rotor position calculation by using the Sin-Cos encoder (Sin-Cos signals, incremental count value and position subdivision result)



4.6 Simulation and Experimental Results

4.6.1 Simulation Results

A simulation has been carried out to compare the proposed filtering strategy in MATLAB/Simulink. The parameters of the traction machine system used in simulation and experiment are the same and are given in Table 4.1.

The NTD parameters are selected as follows: $M = 1000$, $h = 0.01$, and the cutoff frequency of the Butterworth LPF is 17 Hz because it is practically applied in the experimental platform. This set of the cutoff frequency assures both the rapidity and smoothness of the transient response. The PI control parameters are selected as follows: $K_{p\omega} = 3.61$, $K_{i\omega} = 83.33$, $K_{pc} = 37.49$ and $K_{ic} = 575.04$, which have been regulated to be optimal parameters. When the speed of the traction machine is changed from 0 to 2.5 rpm, simulation results of the LPF and the NTD are shown in Figs. 4.11 and 4.12, respectively.

Figures 4.11a and 4.12a show simulation results from 0 to 0.6 s. It can be seen that the speed through the low-pass filter has a larger time delay (0.045 s) than that of the NTD (0.022 s), which influences stability when using it as the speed feedback.

Table 4.1 Parameters of experimental traction machine

Parameters names	Values
Rated power (P_n)	11.7 kW
Rated torque (T_n)	670 Nm
Rated line current (I_n)	23 A
Rated line voltage (U_n)	380 V
Rated speed (ω_n)	167 r/min
Stator resistance (R_s)	0.23 Ω
d -axis inductance (L_{df})	15 mH
q -axis inductance (L_{qf})	15 mH
Number of pole pairs (P)	12
Moment of inertia (J)	3.19 kg m ²

Fig. 4.11 Filtering results of the low-pass filter

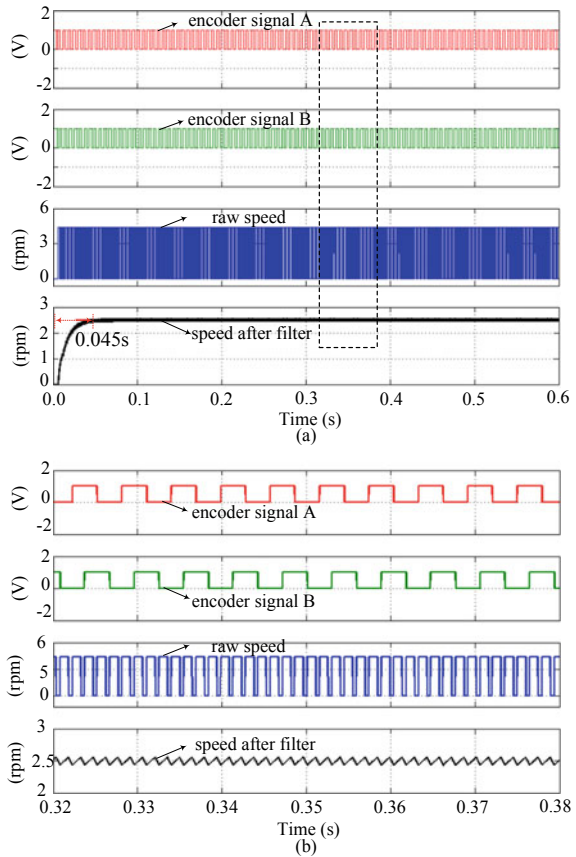
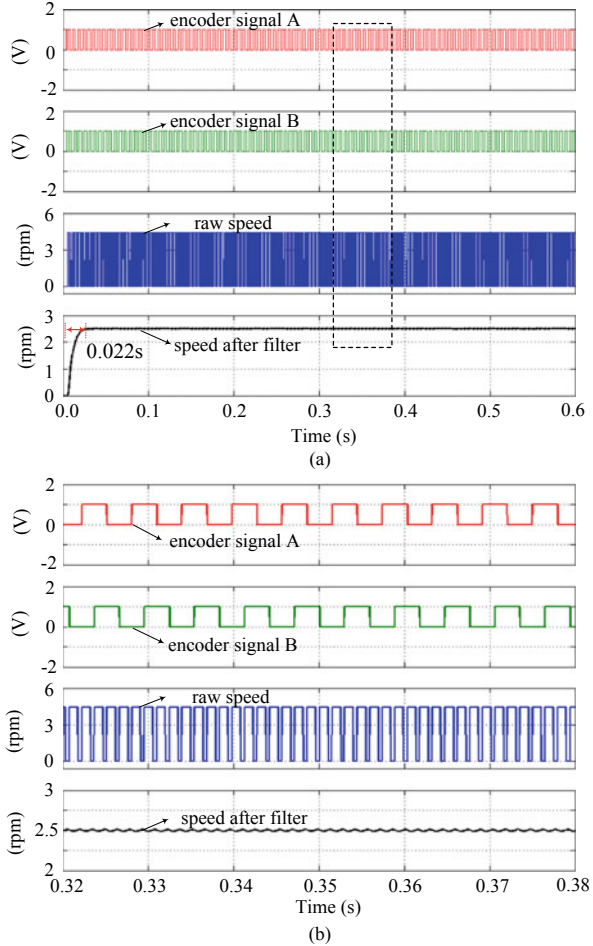


Fig. 4.12 Filtering results of the NTD



Figures 4.11b and 4.12b show zoomed results of the speed. This detailed information can be compared to evaluate the performance in the steady state. From the results, the speed signal obtained by using the NTD is smoother, with less vibration at low speeds.

4.6.2 Experimental Results

The proposed NTD filtering strategy was verified on an 11.7 kW elevator traction machine using a commercial inverter. The experimental platform is shown in Fig. 4.13a, and Sin-Cos encoder (ERN1387) with 2048 P/R is installed on the machine. The parameters of PMSM are listed in Table 4.1. The PWM frequency of

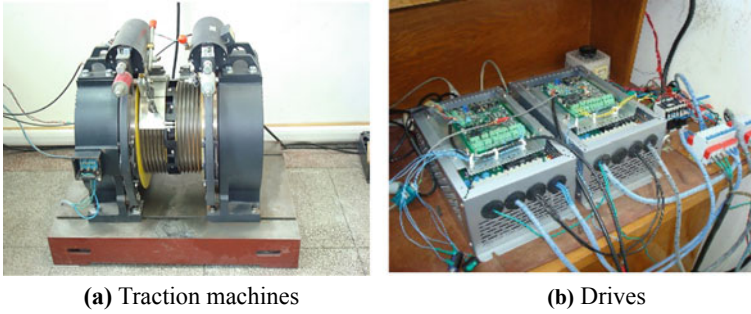


Fig. 4.13 Experimental platform of 11.7 kW elevator traction machine

the inverter is 6 kHz. The whole control algorithm is executed by a STM32F103VB ARM chip. The control period of the speed loop is 1 ms.

The performance of the tracking and filtering can be changed with different parameters of the NTD. In order to assure both the stability of the system and a rapid response, the NTD parameters are selected as follows: $M = 200$, $h = 0.01$, and the cutoff frequency of the LPF is still 17 Hz. The regulated controlling parameters of the speed loop and current loop are $K_{p\omega} = 3.61$, $K_{i\omega} = 83.33$ and $K_{pc} = 37.49$, $K_{ic} = 575.04$, respectively. The machine shows acceptable vibration at the steady state and achieves the response of speed loop and current loop as quickly as possible.

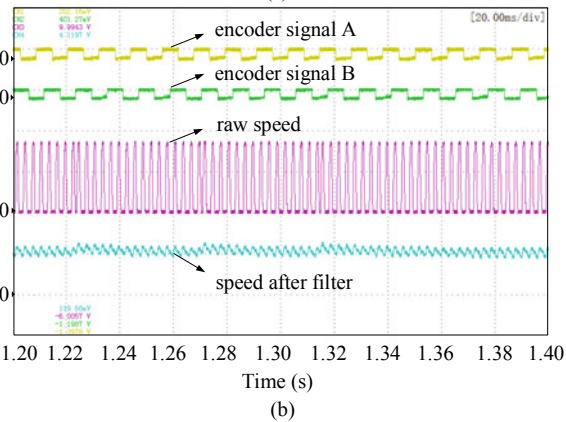
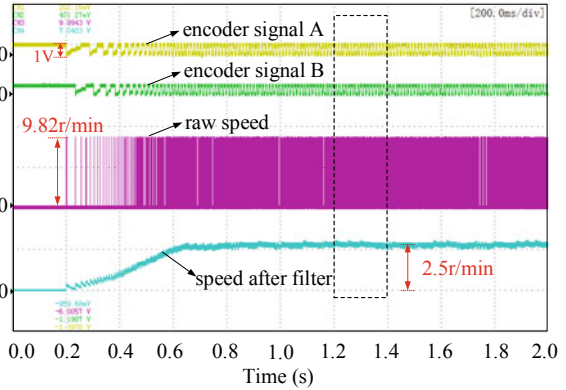
In order to evaluate the filtering effects of the proposed method, the accurate speed ω_{div} calculated from the position subdivision of the machine by a Sin-Cos encoder is introduced. According to this reference signal, the effects of the LPF and NTD will be compared intuitively.

1. Filtering effects of a first-order Butterworth LPF and the NTD: Accurate speed ω_{div} is used as the speed feedback. When the speed of the traction machine is 2.5 rpm, the experimental waveforms are shown in Figs. 4.14 and 4.15.

Similar to the simulation results, the speed signal obtained by the NTD is smoother and shows a smaller time delay than that of the first-order Butterworth LPF, with less vibration at low speeds.

2. Control effect using the filtering speed as feedback: The speed subdivision ω_{div} can be regarded as the accurate speed of machine. Hence, it reflects the actual running situation. Using the filtered speed signal as the speed feedback of the machine, the practical control effects of the filtering methods can be obtained from the experimental waveforms of ω_{div} . In order to verify the advantage of the proposed filtering strategy, different types of first-order LPFs (Butterworth, Chebyshev and elliptic filters) were applied to calculate the speed in practical operation. The cutoff frequencies for all of the filters were set 17 Hz. When the speed of the traction machine is 5 rpm, the experimental waveforms are shown in Fig. 4.16. The second waveforms are the speed subdivision ω_{div} , and the bottom waveforms are the speed feedback.

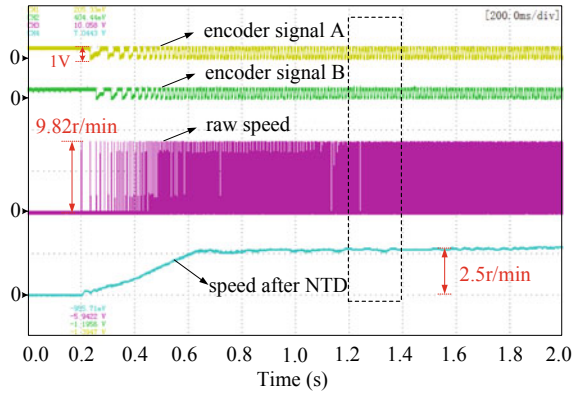
Fig. 4.14 Experimental results of LPF



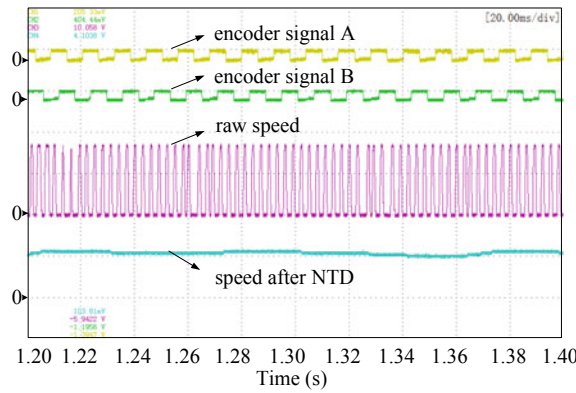
It can be seen from Fig. 4.16a–c that the speed subdivisions ω_{div} when using LPFs of all types show overshoot during the rising process. This means a slight vibration of the traction machine. Furthermore, during the steady state, the speed is not stable enough due to the presence of obvious ripples. These will have impacts on the riding comfort of passengers. By contrast, the speed subdivision using the NTD is shown in Fig. 4.16d. The results show a stable performance during the transient state without any overshoot, and the speed is smoother in the steady state, ensuring the comfort of the passengers.

At ultra-low-speed operation, when the speed reference is set as 0.5 rpm, the experimental results are shown in Fig. 4.17. It can be seen from Fig. 4.17a, c that the speed subdivisions when using a Butterworth LPF and a elliptic LPF contain serious vibrations in the transient state, which is highlighted in the figures. By contrast, the speed subdivisions using a Chebyshev LPF and the NTD display a relatively stable performance in the transient state. In terms of the transient state, there is no big difference between the Chebyshev LPF and the NTD. During the period of the steady state, there still exists a rotor vibration when using the Chebyshev LPF

Fig. 4.15 Experimental results of NTD



(a)



(b)

as shown in Fig. 4.17b. However, it is reduced when using the NTD as shown in Fig. 4.17d.

The stability of ultra-low speed is very important because it influences the comfort of passengers during start-up. In general, the NTD is a high-efficiency filtering method with a smaller time delay and better filtering effects than other types of LPFs when its parameters are selected appropriately.

4.7 Summary

A novel speed filtering method for permanent magnet traction machines to improve low-speed performance is presented in this chapter. Based on the theory of the nonlinear tracking differentiator (NTD), the method can relieve vibrations of the speed and reduce the time delay. Based on the analysis of the nonlinear OCS function and the impacts of its parameters, optimal parameters can be obtained which

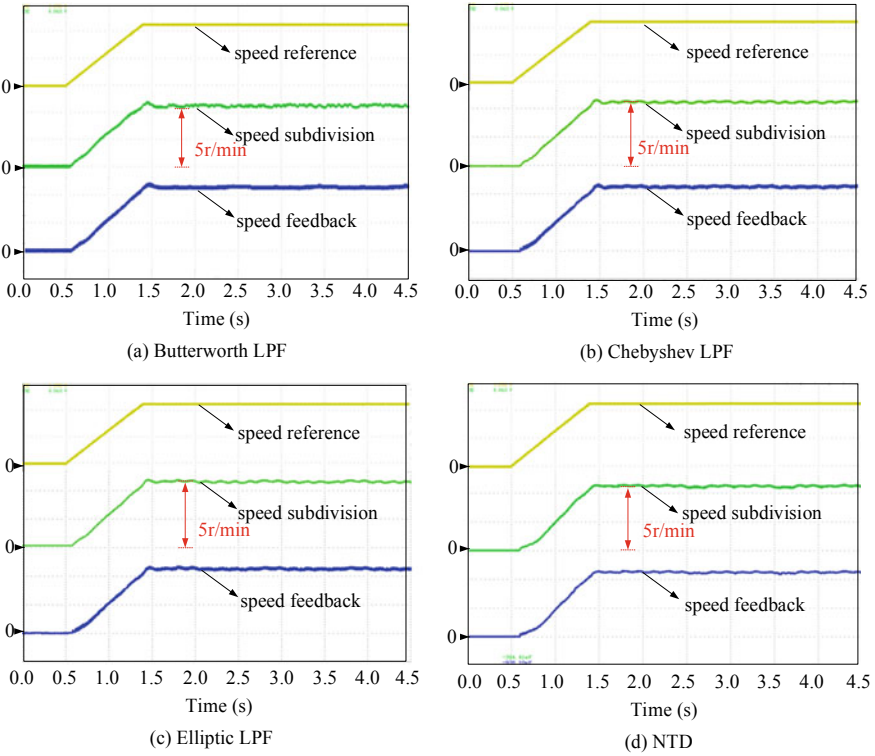


Fig. 4.16 Experimental results at 5 rpm

show more efficient performance and satisfy demands for stability. Furthermore, when using the speed signal through the nonlinear tracking differentiator as the feedback of a speed closed-loop control system, the motor shows a better performance compared with other types of low-pass filters. Therefore, smooth operation can be achieved at low speeds. Experimental results confirm the feasibility of the proposed strategy.

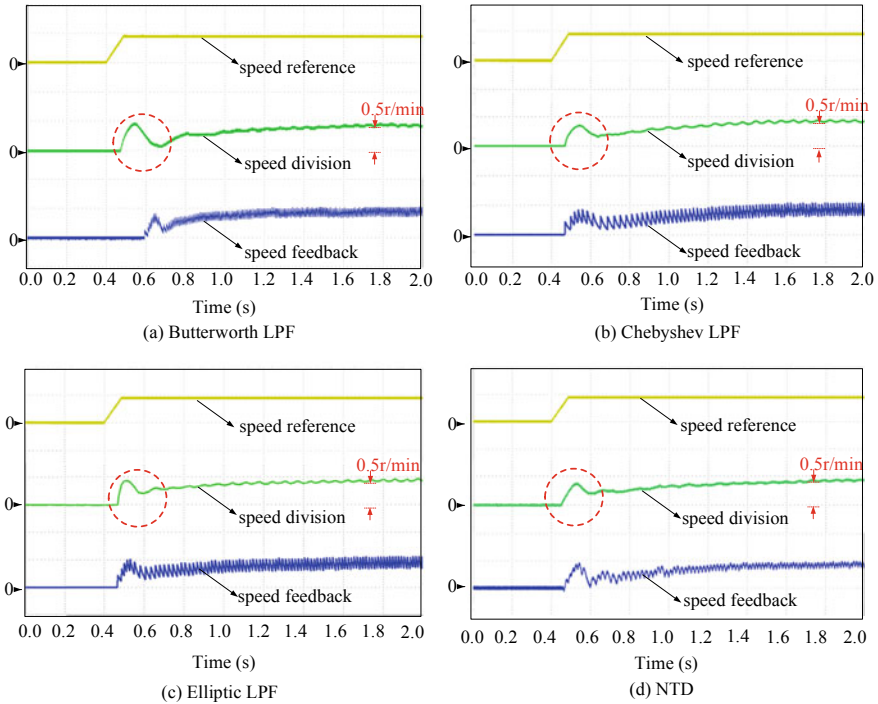


Fig. 4.17 Experimental results at 0.5 rpm

References

1. Feng L, Anwen S, Yinnan Z et al (2014) A rapid and high-accuracy control scheme of starting torque for elevators without a weight transducer. In: 2014 IEEE 23rd international symposium on industrial electronics (ISIE), pp 733–738
2. Yetiş H, Boztepe H, Yaşa Y et al (2013) Comparative design of direct drive PM synchronous motors in gearless elevator systems. In: 2013 3rd international conference on electric power and energy conversion systems, pp 1–5
3. Wang G, Zhang G, Yang R et al (2012) Robust low-cost control scheme of direct-drive gearless traction machine for elevators without a weight transducer. *IEEE Trans Ind Appl* 48(3):996–1005
4. Blanuša B, Knežević B (2013) Optimal flux control of elevator drive. In: 2013 XXIV international conference on information, communication and automation technologies (ICAT), pp 1–6
5. Feng Z, Acarnley PP (2008) Extrapolation technique for improving the effective resolution of position encoders in permanent-magnet motor drives. *IEEE/ASME Trans Mechatron* 13(4):410–415
6. Li H, Xie H, Yi X et al (2011) Research on low speed control of permanent magnet synchronous motor based on state observer. In: 2011 4th international conference on biomedical engineering and informatics (BMEI), pp 2018–2022
7. Zhang X, Zhang W (2014) An improved rotor position estimation in PMSM with low-resolution hall-effect sensors. In: 2014 17th international conference on electrical machines and systems (ICEMS), pp 2722–2727

8. Song X, Fang J, Han B (2016) High-precision rotor position detection for high-speed surface PMSM drive based on linear hall-effect sensors. *IEEE Trans Power Electron* 31(7):4720–4731
9. Yang Y, Ting Y (2014) Improved angular displacement estimation based on hall-effect sensors for driving a brushless permanent-magnet motor. *IEEE Trans Ind Electron* 61(1):504–511
10. Wang G, Wang B, Zhao N et al (2017) A novel filtering method based on a nonlinear tracking differentiator for the speed measurement of direct-drive permanent magnet traction machines. *J Power Electron* 17(2):358–367
11. Bai Y, Wang G, Zhang G et al (2021) Position and speed detection method based on cross-decoupling network filtering for gearless traction motor drives at low-speed operation. *IEEE Trans Power Electron* 36(10):11862–11874

Chapter 5

Starting Torque Control Based on Dichotomy and Staircase Methods



5.1 Introduction

This chapter proposes a novel low-cost control strategy of gearless traction permanent magnet synchronous machine for direct-drive elevator applications. It can improve robustness of the weight-sensorless traction machine system with an ordinary incremental encoder installed. In order to improve the riding comfort for the passengers during the brake releases, a novel starting torque compensation strategy without a weight transducer is present. After analyzing the dynamic characteristics and the friction torque of the elevator traction system, two starting torque compensation methods based on the dichotomy and the staircase method are proposed for the weight-sensorless elevator applications. In this way, an electromagnetic torque can be generated to balance the load torque, and the sliding can be prevented when the elevator brake releases during the starting operation. To achieve the current vector decoupling control for the traction machine installed with an incremental encoder, the initial rotor position estimation at standstill based on a hybrid signals injection method is adopted. Firstly, a high-frequency oscillating sinusoidal voltage signal is injected to obtain the magnetic pole position. Then, two pulse voltage vectors are injected in the positive and the negative direction to identify the magnet polarity.

For the weight-sensorless elevator application, the starting torque compensation is a challenging technique to achieve high comfort by installing an ordinary incremental encoder. Several researches on load torque estimation during rotating have been proposed to improve dynamic performance of the drives. But they are not suitable for the application of the elevator during the starting operation [1–3]. In [4], a load torque estimation method based on the mechanical model is proposed when the brake releases. The load torque is estimated by measuring the motor acceleration, and the information can be obtained simply by the incremental encoder. The feature of the method is that, since the accurate inertia of the traction mechanical system should be known, it is quite difficult to compensate the starting torque with an ordinary incremental encoder installed on the direct-drive traction machine.

For the traction machine installed with an incremental encoder, initial rotor position estimation is important for the starting operation. If the initial position is inaccurate, the torque output ability may decrease, and more serious is that the rotor may temporarily rotate inverse [5]. The pulse voltage signal injection method is based on estimating the minimum inductance, which can be applied to both interior and surface PMSMs [6–8]. The maximum current appears when the pulse voltage vector aligns with the rotor magnet position. But it is difficult to obtain accurate estimation position when the pulse voltage injected within small range near the magnet position. The rotating or oscillating high-frequency sinusoidal voltage signal injection methods have been proposed to estimate rotor position [6–15]. The structure saliency of interior PMSM makes it effective to use rotating carrier-frequency image tracking techniques to identify and track the orientation of magnet position even at standstill [9–12]. It is found that the oscillating carrier signal injection is more suitable for surface PMSM [13–17]. The excitation by the carrier current changes the saturation level when its direction coincides with the magnet field, and the current harmonics of the second-order component are then processed to serve for the polarity estimation. The major drawback of the polarity estimation method adopting the rotating or oscillating carrier signal is the poor signal-to-noise ratio in applications [18]. Most of the initial position estimation schemes are proposed for interior PMSM with obvious saliency. But for the traction surface-mounted PMSM, the special issue should be considered to achieve the accurate position estimation at standstill.

In this chapter, a starting torque compensation method is studied for weighting the transducer sensorless elevator. Based on analyzing the dynamic characteristics and the friction torque of the traction system, two starting torque compensation methods without weighing transducer installed are proposed to meet the starting control requirements of the gearless elevator traction system [19]. To obtain the initial rotor position of the traction machine at standstill, a hybrid signal injection method is proposed. A high-frequency sinusoidal voltage signal is injected to detect the magnet pole position. Then, two voltage pulse vectors in both the positive and the negative directions are injected to identify the magnet polarity. The experimental results demonstrate the feasibility of the low-cost control strategy with an 11.7 kW traction machine.

5.2 Torque Compensation Based on Dichotomy Method

In order to make the motor operate from standstill to the rotating state, the electromagnetic torque has to meet the condition:

$$|T_e - T_l| > T_{FS}. \quad (5.1)$$

Rearranging (5.1), the following equation is derived,

$$T_e - (T_l + T_f) = 0. \quad (5.2)$$

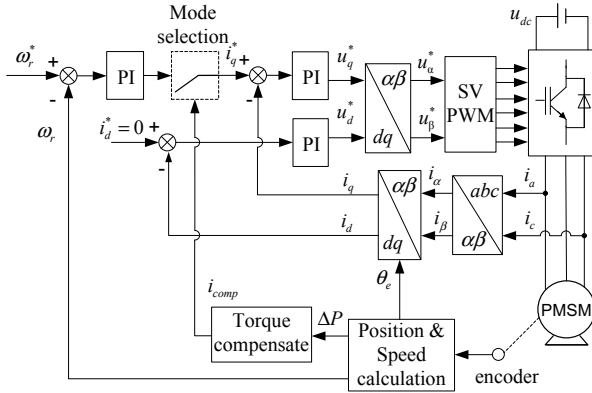


Fig. 5.1 Scheme of the starting torque compensation

Before the brake release, the load torque and the friction torque are unknown but fixed values. The torque compensation value to keep the elevator in balance can be calculated by solving (5.2).

Equation (5.2) can be solved through the dichotomy method. The strategy of the starting torque compensation method is shown in Fig. 5.1. And the torque compensation scheme using the dichotomy method is shown in Fig. 5.2. T_n is the rated electromagnetic torque, T_e is the generated electromagnetic torque, and $T_l + T_f$ is the sum of the load torque and the friction torque.

If $T_e < T_l + T_f$, the generated torque is less than the sum of the load torque and the friction torque, and the motor will rotate reverse. If $T_e > T_l + T_f$, the generated torque is greater than the resultant load torque, and the motor will rotate forward. If $T_e = T_l + T_f$, the generated torque is equal to the resultant load torque, and the car will keep standstill.

The output torque T_e is adjusted according to the rotation direction. The strategy is that before starting the elevator, the traction wheel is locked by the brake, and the motor output torque is zero. After releasing the brake, if the load torque is greater than zero, the car will slide reverse. If the load torque is less than zero, the car will slide forward. If the torque is equal to zero, the total weight of the car is equal to

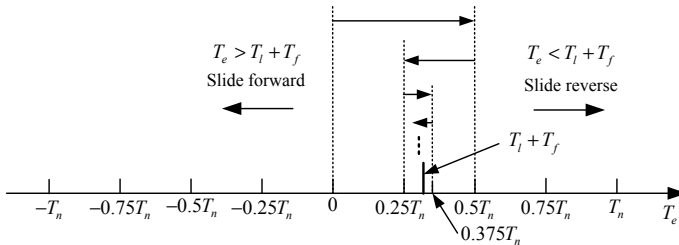


Fig. 5.2 Scheme of starting torque compensation based on the dichotomy method

the counterweight, the motor will keep standstill, and there is no need to adjust T_e . Assuming that the load torque is greater than zero, after the brake releases, the car will slide reverse. After having detected the reverse signal, adjust T_e to $0.5T_n$. Then, there are three possibilities as follows according to the relation between T_e and $T_l + T_f$:

1. The car still slides reverse, which means that the load torque is greater than $0.5T_n$, then half of the last increment is added to the previous torque set-point value, that is $T_e = 0.5T_n + 0.5T_n \times 0.5 = 0.75 T_n$.
2. The car slides forward, which means that the load is less than $0.5T_n$, then subtract half of the last decrement from the previous torque set-point value, that is $T_e = 0.5T_n - 0.5T_n \times 0.5 = 0.25 T_n$.
3. The car keeps standstill, which means that the electromagnetic torque is equal to the load torque, and there is no need to adjust further.

If the load torque is less than zero, the compensation process is similar to the situation analyzed above. So, the subsequent adjustment to the output torque is based on the motor rotation direction according to the above strategy. Each motor torque reference is given by adding or subtracting half of the last increment or decrement to the previous torque set-point value, which is same to the dichotomy. In this series of the adjustment process, the motor generated torque value may be $0 \rightarrow 0.5 T_n \rightarrow 0.25 T_n (0.75T_n) \rightarrow 0.125 T_n (0.375 T_n, 0.625 T_n, 0.875 T_n) \dots$ Namely,

$$T_e(n) = T_n \sum_{n=1}^n K(n) \frac{1}{2^n}. \quad (5.3)$$

where $T_e(n)$ is the set-point value of the motor output torque at the n th time, and $K(n)$ is a value determined by the rotation direction for this time. That is,

$$K(n) = \begin{cases} 1, & \text{if (slide forward)} \\ -1, & \text{if (slide reverse)} \end{cases}. \quad (5.4)$$

From (5.2), as long as the calculation accuracy is high enough, the motor generated torque can approximate an arbitrary load torque through this method. In this way, it can make the elevator keep in balance. If the friction torque is zero, in principle, the motor output torque can approximate the load torque through the infinite step adjustment. However, the actual friction torque is not zero, and it is not a fixed value when the car is in balance, so there is no need for the torque output to be an accurate value. Consequently, the torque can reach equilibrium with the finite step adjustments.

With the method of the starting torque compensation using the dichotomy method, the sliding distance of the car is far less than the one generated in the conventional starting method, and the adjustment is more rapid. In theory, the sliding distance of the car only depends on the resolution of the encoder. The disadvantage of the

method is that the adjustment of the current will make the noise and the motor may oscillate several times during the adjustment process. However, this method can be applied in the situation where a large starting torque is needed and the device is not sensitive to the oscillation.

5.3 Torque Compensation Based on Staircase Method

In order to solve the oscillation existed in the dichotomy compensation method, a stairway-type torque compensation method is also proposed, as shown in Fig. 5.3.

From Fig. 5.3, after the brake releases, the direction of the compensation torque is determined based on the rotation direction of the traction wheel, and then the compensation value is decided. If the car slides reverses, ΔT_e is added to the electromagnetic torque reference. If the car still slides reverses, go on adding ΔT_e until sliding direction changes. Once only the car slides reverses, subtract $\Delta T_e/2$ from the last torque set-point value. Then, the system will go to the speed closed-loop adjustment with zero-servo control mode, and no more torque compensation is needed. When the subtraction of the electromagnetic torque and the load torque reaches the range of twice of the friction torque, the traction system will be in balance. The maximum compensation will occur in the situation where the load approaches the maximum value. At this time, the compensation value reaches the maximum value.

If ΔT_e is too small, the more steps adjustment needs, and the sliding distance is larger. Otherwise, if ΔT_e is too large, the needed adjustment value for the speed loop is increased, and the sliding distance may be obvious. Concerning the action of the friction torque, as Fig. 5.3 shows, if $\Delta T_e < 2T_{FS}$, the system can be in balance without the speed loop adjustment, and the compensation effect is the best.

Figure 5.4 shows the flow chart of the starting torque compensation based on the staircase method. According to the principle of the vector controlled permanent

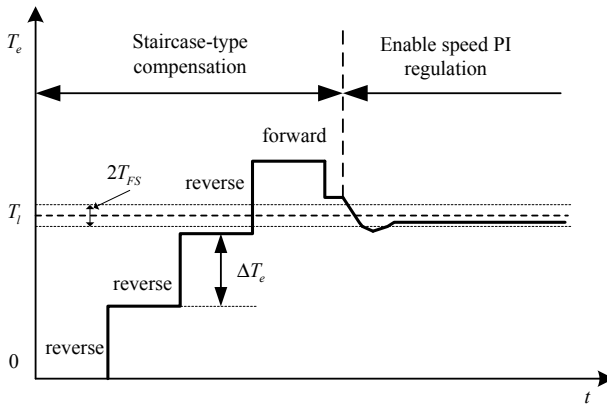


Fig. 5.3 Scheme of starting torque compensation based on staircase method

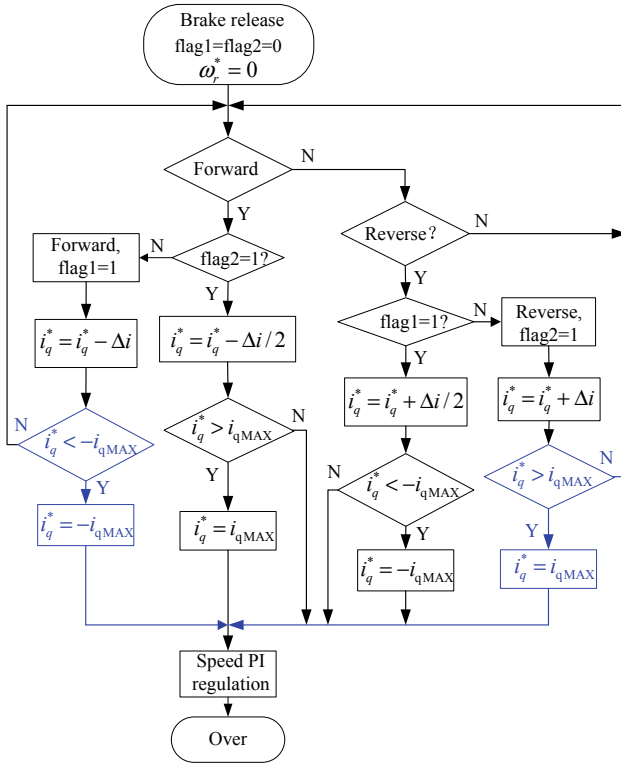


Fig. 5.4 Flow chart of the staircase-type starting torque compensation

magnet synchronous machine, the relation of the electromagnetic torque and q -axis current component can be expressed as follows:

$$T_e = \frac{3}{2} P [\psi_f i_q + (L_d - L_q) i_d i_q]. \tag{5.5}$$

where i_d and i_q are d - and q -axes stator current components, P is number of pole pairs, L_d and L_q are d - and q -axes inductances, and ψ_f is permanent magnet flux linkage.

From, if the reference of i_d is zero, then T_e is proportional to i_q . So by adjusting the reference of i_q , it is equivalent to change the output of electromagnetic torque. As described in Fig. 5.4 if the rotor rotates forward at first, the torque compensation in the opposite direction is adopted. And the flag of the rotating forward (flag1) is set with 1. Subtract a fixed value, Δi , from the current reference value. If the rotor still rotates forward in the next adjustment period, which means that the load torque is still greater than the set-point value of i_q , go on subtracting Δi from i_q until the rotor

rotates in the opposite direction. If the rotor rotates in the opposite direction, which means that the generated torque is greater than the load torque, $\Delta i/2$ is added to the set-point value of i_q . After that, the conventional PI-type zero-speed closed-loop adjustment is adopted. If the rotor rotates reverse at first, the analysis is similar to the case introduced above. Another case, if the motor does not slide, there is no need to adjust the q -axis current set-point value.

5.4 Experimental Evaluation

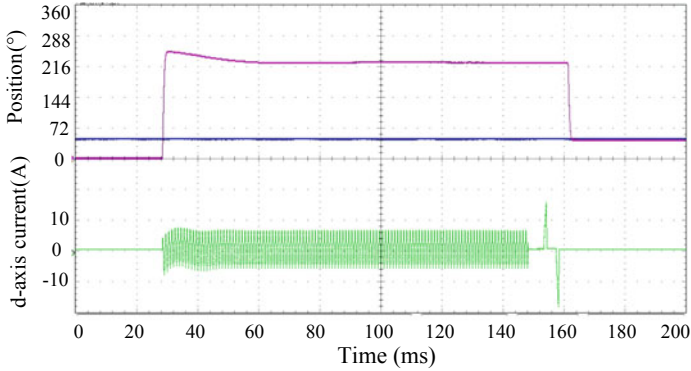
The experimental setup includes two 11.7 kW permanent magnet traction machines and their drives shown in Fig. 4.13. A same power traction machine is connected to emulate the load through a separate drive. The parameters of PMSM are listed in Table 4.1. An ordinary incremental encoder with resolution of 2048 P/R is installed on the machine. TMS320F2808 DSP is used to execute the all algorithm. PWM switching frequency of inverter is 10 kHz. The periods of current loop and speed loop are set as 100 μ s and 1 ms, respectively. The magnitude and the frequency of the high-frequency oscillating sinusoidal voltage signal are 152 V and 1 kHz, respectively. The magnitude and the pulse width of the pulse voltage are 190 V and 900 μ s, respectively. And the proportional and integral gains of (14) are set as 10 and 350, respectively.

Figure 5.5 shows the experimental result of the initial rotor position estimation using the hybrid signal injection method. Figure 5.5a is the estimation result when the actual rotor position is 45.1° in electrical degree. The estimated magnetic pole position output from the PI regulator is $\hat{\theta}_{e1} = 222.3^\circ$. Then, two pulse voltage vectors in the direction of 222.3° and 42.3° are injected into the stator windings, respectively. By comparing the magnitude of the two d -axis current responses, it can be decided that the final estimated rotor position is 42.3°. And the position estimation error is 2.8° in electrical degree.

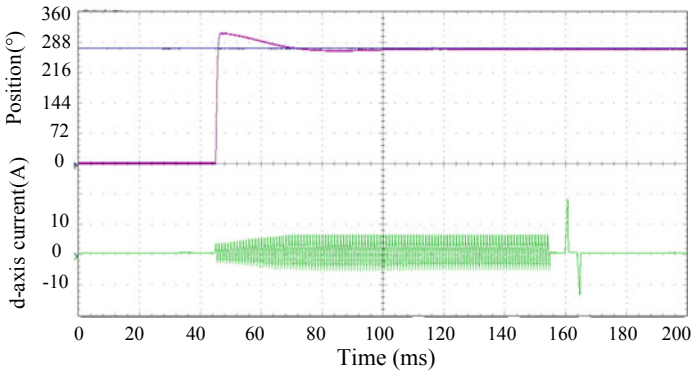
Figure 5.5b shows the experimental result when the actual rotor position is 265.6°. The estimated magnetic pole position is $\hat{\theta}_{e1} = 268.7^\circ$. Then, two pulse voltage vectors in the direction of 268.7° and 88.7° are injected into stator windings, respectively. By comparing the two d -axis currents, the final estimated rotor position is 268.7°. The position estimation error is -3.1° in electrical degree.

Figure 5.6 shows the estimation results during one electrical revolution. As a result, the average absolute value of the estimation error is 2.6°. In the worst case, the maximum estimation error is 5.7°. During the initial rotor position estimation, the rotor is at standstill. And the performance of the proposed position estimation can be acceptable for the starting requirement of the traction machine installed with an incremental encoder.

Figure 5.7 shows the starting torque compensation results by using the dichotomy method with 10%, 40%, 60% and 100% rated load, respectively. From the waveform of q -current, it can be seen that after finite step adjustment, the set-point value of q -current by the dichotomy method can balance the load torque at the end. And



(a) Estimation result when $\theta_e=45.1^\circ$



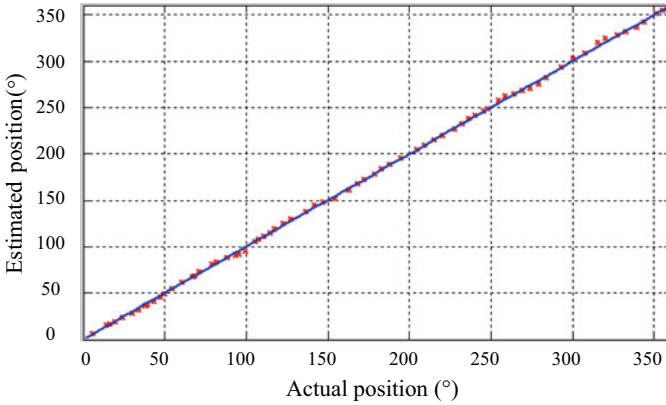
(b) Estimation result when $\theta_e=265.6^\circ$

Fig. 5.5 Experimental Waveforms of the initial position estimation

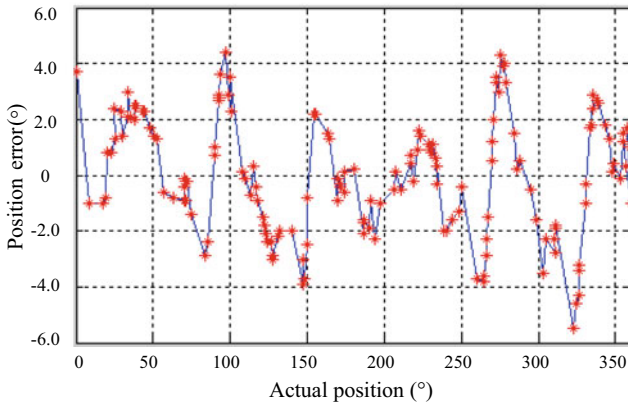
the sliding distance only three pulses, namely 0.46 mm. Since for the machine with traction wheel diameter is 40 cm, one pulse corresponds 0.153 mm. The sliding is so slight, and it can be tolerated.

Figure 5.8 shows the starting torque compensation results by using the staircase method with 10%, 40%, 60% and 100% rated load, respectively. The incremental compensated torque value ΔT_e is set as 15% of the rated torque. From the waveform of q -current, it can be seen that the maximum change times of sliding direction is only twice during the compensation period. As results, the mitigation of vibration is improved obviously. So, it is a better compensation strategy for the weight-sensorless elevator. In this way, an electromagnetic torque can be produced to balance the load torque for preventing sliding when the brake releases at elevator starting operation.

Figure 5.9 shows the transient response when the torque control mode change to the zero-speed closed-loop control mode using the staircase compensation method. As shown in Fig. 5.9, the change of the two modes is smooth. At the end of the torque



(a) Relation of the estimated position and the actual position



(b) Relation of the estimation error and the actual position

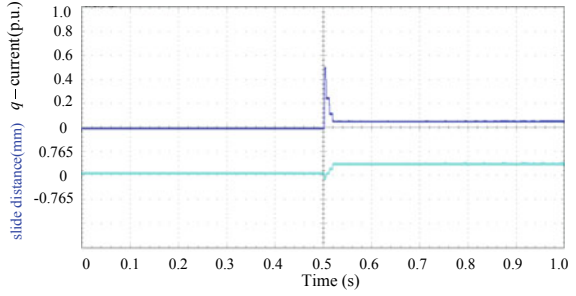
Fig. 5.6 Experimental results of initial rotor position estimation during one electrical revolution

control mode, since the difference between the generated torque and the load torque is with $\pm \Delta T_e$, and the force balance of the system is near achieved. So, the transient shock can be avoided.

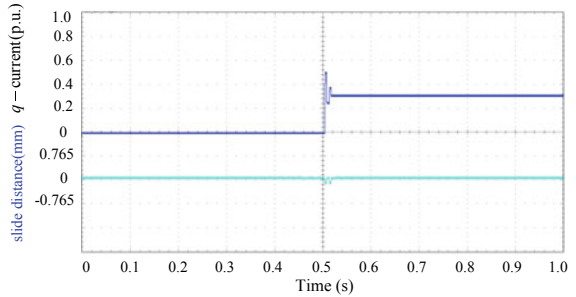
Two conventional starting control methods, the zero-speed and the zero-position closed-loop control schemes without torque control mode are usually adopted for elevator machine drives. In this way, the weight transducer could not be needed.

But a high-resolution encoder should be installed. If the position information is accurate enough, both the two control methods for elevator starting can be satisfactory. However, when a low-resolution encoder is adopted, like 2048P/R, the anti-sliding performance of the two methods is poor without any compensation. Figure 5.10 shows the experimental results by using the two methods without the weight transducer when load is 70% rated value. In Fig. 5.10a, the sliding distance is

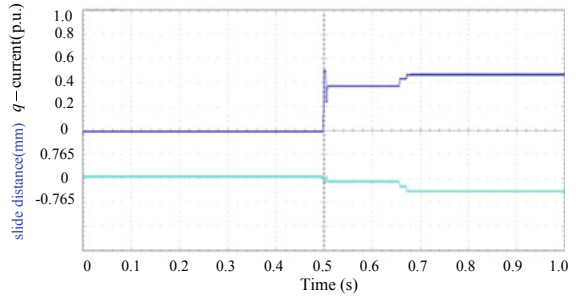
Fig. 5.7 Starting torque compensation results using dichotomy method



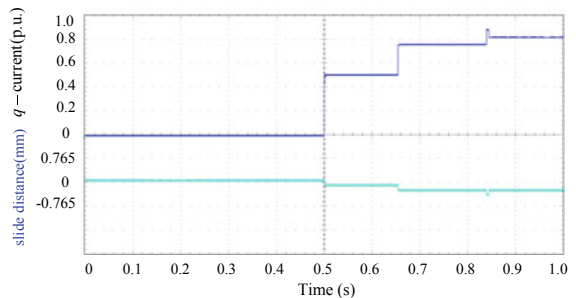
(a) With 10% rated load



(b) With 40% rated load

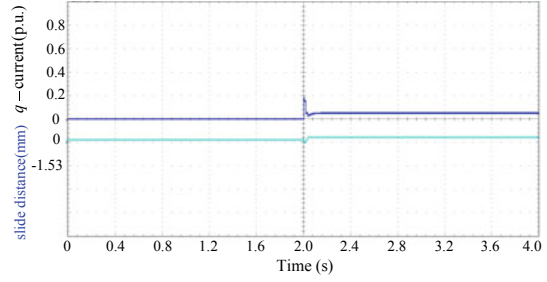


(c) With 60% rated load

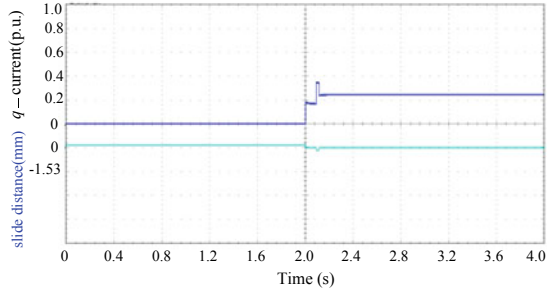


(d) With 100% rated load

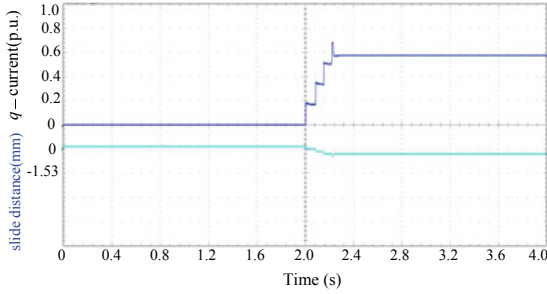
Fig. 5.8 Starting torque compensation results using the staircase method



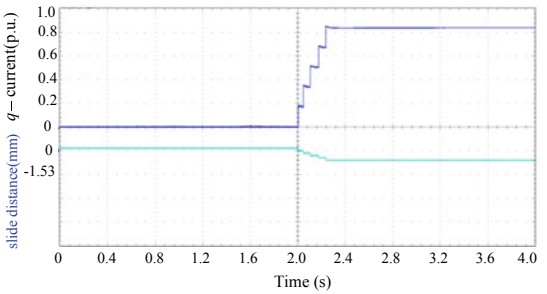
(a) With 10% rated load



(b) With 40% rated load



(c) With 60% rated load



(d) With 100% rated load

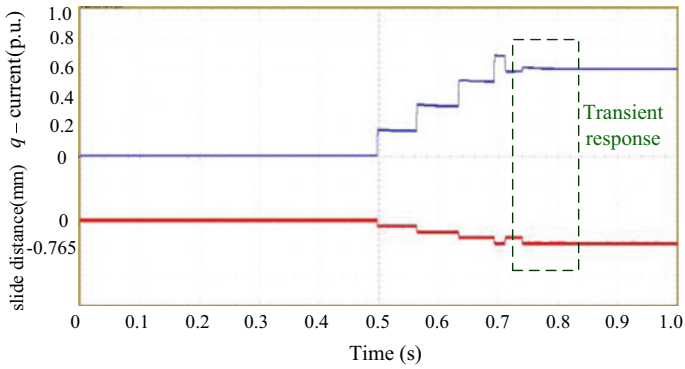
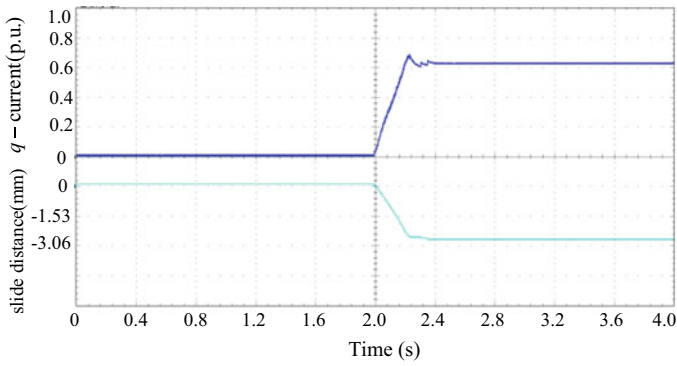
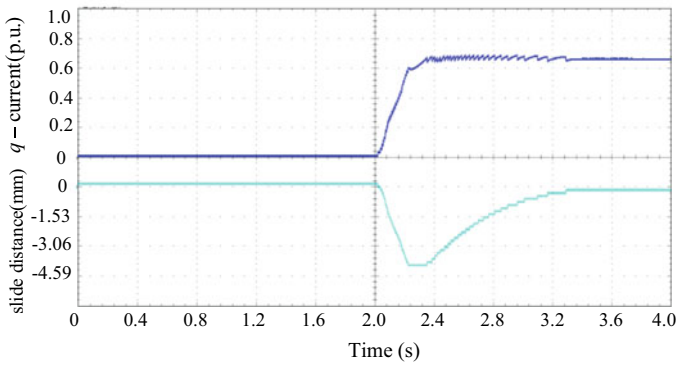


Fig. 5.9 Transient response of the two modes change with staircase method



(a) speed closed-loop control with zero reference



(b) position closed-loop control with zero reference

Fig. 5.10 Experimental results using the two conventional compensation methods without weight transducer

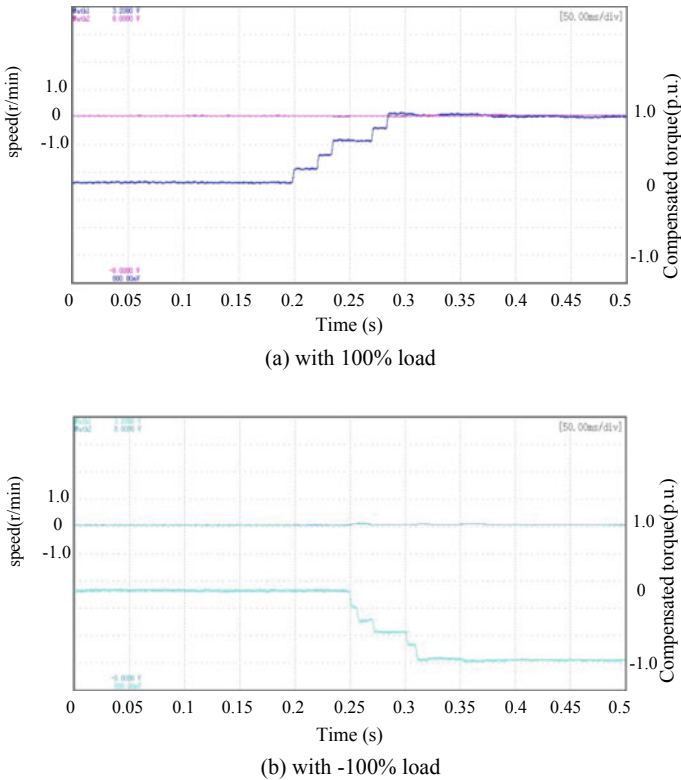


Fig. 5.11 Experimental results in real elevator system with the staircase method

near 3 mm using zero-speed control scheme. And in Fig. 5.10b, the sliding distance is over 4 mm adopting zero-position control scheme. Comparing the results between the proposed method and the conventional methods, the advantage of the proposed method can be verified.

Figure 5.11 shows the experimental results in a real elevator system adopting the staircase compensation method. Figure 5.11a, b is the results with 100% and -100% rated load, respectively. Comparing with the results in Fig. 5.8, the compensation effect is similar. But the respond time is different due to influence of brake structure and system inertia. The torque compensation method is effective for the weight-sensorless elevator direct-dive traction system.

5.5 Summary

A low-cost control strategy for the elevator adopting a direct-drive permanent magnet traction machine installed with an ordinary incremental encoder was studied in this

chapter. Two novel starting torque compensation methods using the dichotomy and the staircase manners were proposed for the weight-sensorless elevator. In this way, the sliding distance of the car can be controlled to be an acceptant value during the brake releases. This chapter also presented an initial rotor position estimation method for the surface-mounted permanent magnet traction machine using the hybrid signals injection before the elevator start-ups. The magnetic pole position is estimated by the injecting high-frequency oscillating sinusoidal voltage signal. A PI tracing observer is used to regulate the position error signal. In order to identify the magnet polarity more simply, two pulse voltage signals are injected into the estimated position in the positive and the negative directions. The validity of the proposed control strategy is verified through the experiment with an 11.7 kW traction machine.

References

1. Kim NJ, Moon HS, Hyun DS (1996) Inertia identification for the speed observer of the low speed control of induction machines. *IEEE Trans Ind Appl* 32(6):1371–1379
2. Staffler W, Schrodler M (2010) Extended mechanical observer structure with load torque estimation for sensorless dynamic control of permanent magnet synchronous machines. In: 2010 14th international power electronics and motion control conference (EPE 2010), pp 18–22
3. Yasser AR, Ibrahim M (2007) A hybrid-type variable-structure instantaneous torque control with a robust adaptive torque observer for a high-performance direct-drive PMSM. *IEEE Trans Ind Electron* 54(5):2491–2499
4. Bolognani S, Faggion A, Sgarbossa L, Peretti L (2007) Modeling and design of a direct-drive lift control with rope elasticity and estimation of starting torque. In: Proc. 2007 IEEE industrial electronics society 33rd annual conference (IECON 2007), pp 828–832
5. Yu JS, Kim SH, Lee BK, Won CY, Hur J (2007) Fuzzy-logic-based vector control scheme for permanent-magnet synchronous motors in elevator drive applications. *IEEE Trans Ind Electron* 54(4):2190–2200
6. Nakashima S, Imagaki Y, Miki I (2000) Sensorless initial rotor position estimation of surface permanent magnet synchronous motor. *IEEE Trans Ind Appl* 36(6):1598–1603
7. Tursini M, Petrella R, Parasiliti F (2003) Initial rotor position estimation method for PM motors. *IEEE Trans Ind Appl* 39(6):1630–1640
8. Yan Y, Zhu JG, Guo YG (2008) Initial rotor position estimation and sensorless direct torque control of surface-mounted permanent magnet synchronous motors considering saturation saliency. *IET Electr Power Appl* 2(1):42–48
9. Corley MJ, Lorenz RD (1998) Rotor position and velocity estimation for a salient-pole permanent magnet synchronous machine at standstill and high speeds. *IEEE Trans Ind Appl* 34(4):784–789
10. Raca D, Garcia P, Reigosa DD, Briz F, Lorenz RD (2010) Carrier-signal selection for sensorless control of PM synchronous machines at zero and very low speeds. *IEEE Trans Ind Appl* 46(1):167–178
11. Kim H, Huh KK, Lorenz RD, Jahns TM (2004) A novel method for initial rotor position estimation for IPM synchronous machine drives. *IEEE Trans Ind Appl* 40(5):1369–1378
12. Jeong YS, Lorenz RD, Jahns TM, Sul SK (2005) Initial rotor position estimation of an interior permanent-magnet synchronous machine using carrier-frequency injection methods. *IEEE Trans Ind Appl* 41(1):38–45
13. Jang JH, Sul SK, Ha JI, Ide K, Sawamura M (2003) Sensorless drive of surface-mounted permanent-magnet motor by high-frequency signal injection based on magnetic saliency. *IEEE Trans Ind Appl* 39(4):1031–1039

14. Jang JH, Ha JI, Ohto M, Ide K, Sul SK (2004) Analysis of permanent-magnet machine for sensorless control based on high-frequency signal injection. *IEEE Trans Ind Appl* 40(6):1595–1604
15. Ha JI, Ide K, Sawa T, Sul SK (2003) Sensorless rotor position estimation of an interior permanent-magnet motor from initial states. *IEEE Trans Ind Appl* 39(3):761–767
16. Holtz J (2008) Acquisition of position error and magnet polarity for sensorless control of PM synchronous machines. *IEEE Trans Ind Appl* 44(4):1172–1180
17. Consoli A, Scarcella G, Scelba G, Testa A, Royak S (2009) Phase modulation-based technique for saliency position estimation of IPMSMs. In: *IEEE energy conversion congress and exposition 2009 (ECCE 2009)*, pp 2489–2495
18. Raca D, Harke MC, Lorenz RD (2008) Robust magnet polarity estimation for initialization of PM synchronous machines with near-zero saliency. *IEEE Trans Ind Appl* 44(4):1199–1209
19. Wang G, Zhang G, Yang R, Xu D (2012) Robust low-cost control scheme of direct-drive gearless traction machine for elevators without a weight transducer. *IEEE Trans Ind Appl* 48(3):996–1005

Chapter 6

Fuzzy Self-tuning Torque Control Strategy



6.1 Introduction

To improve the starting performance of permanent magnet traction machine without a weight transducer in gearless elevator, an adaptive starting torque compensation strategy is proposed in this chapter [1]. The dynamic model of the direct-drive elevator traction system considering the rope elasticity, the brake releasing and the friction torque is established. Based on the dynamic model, the characteristics of the synthetic load torque exerted on the traction machine during elevator start-up are obtained. In order to balance the unknown load torque for the gearless elevator, a fuzzy self-tuning strategy is adopted to generate a suitable starting torque for compensation by tuning the change rate of electromagnetic torque according to the encoder signal. The torque compensator is designed with the aim of getting a minimized sliding distance and avoiding traction sheave reversal. Both simulation and experimental results are provided to verify that the proposed weight-transducerless adaptive starting torque compensation strategy can achieve superior riding comfort of shorter sliding distance, faster dynamic response and smaller sliding speed.

Various enhanced control strategies have been proposed to improve the robustness against load disturbance when the motor is running [2–8]. However, they are unsuitable for the application of the starting torque compensation considering the special requirements of gearless elevator traction system. During the brake releasing when the elevator operates from the stand-by mode to the running mode, both the sliding distance and mechanical vibration should be considered in order to ensure the riding comfort of the elevator. The generated torque of the traction machine must track the unknown load torque accurately and quickly. In [9], the starting torque compensation was equivalent to a searching issue based on friction model. However, the difference of neighboring torque references was quite large, and the initial difference can reach the rated value, which can cause mechanical vibration. In [10], two starting torque compensation methods using the dichotomy and the staircase method were proposed for weight-transducerless elevator installed with an incremental encoder. Although the compensation method can track the final load torque effectively, the variation

of neighboring electromagnetic torques is still a step type during the compensation process. In order to achieve more comfortable riding of the gearless elevator, the torque generated by the traction machine should be a continuous type during elevator start-up. In [11], the rope elasticity was considered in the elevator modeling, and the load torque was estimated through the acceleration evaluation by the quadratic error comparison. This method can achieve the torque compensation with feedforward action in the speed control loop. However, the inertia of the elevator traction system should be known.

In [9–11], the assumption that the brake released instantaneously was made in the model and this led to a big change in the torque generated by traction machine when estimating the load torque. However, in practical elevator traction applications, the brake releases gradually, and the synthetic load torque exerted on the traction machine changes during the process. It is worth developing new methods to avoid mechanical noise caused by the large electromagnetic torque variation. Since the gearless elevator drive system is one of the most high-performance drives, the Sin-Cos encoder is widely adopted to get a more accurate rotor position. Compared with the incremental encoder, the quadrature signals of the Sin-Cos encoder can be used to calculate the subdivision and improve the resolution [12, 13]. The starting torque compensation without a weight transducer is very meaningful to improve the robustness of gearless elevator using the Sin-Cos encoder.

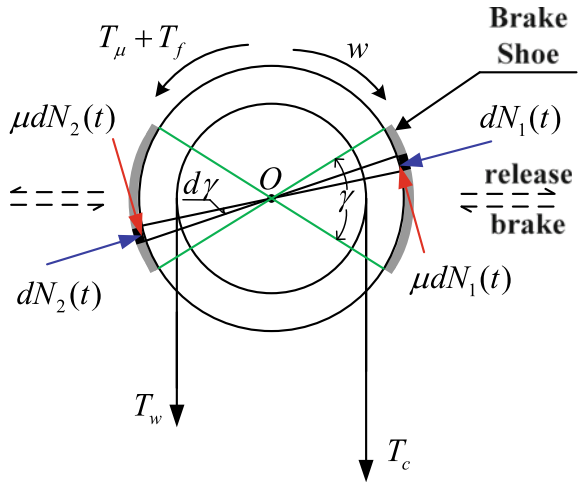
In this chapter, based on the analysis of the dynamic characteristics of the gearless traction system during elevator start-up, a novel adaptive starting torque compensation strategy is proposed to improve the system robustness and the riding comfort. This chapter is organized as follows. Firstly, in order to explore the characteristics of the synthetic load torque exerted on the traction sheave, a dynamic model of the gearless elevator traction system is built in 6.2. According to the model characteristics, an adaptive weight-transducerless starting torque compensation strategy based on fuzzy self-tuning is proposed in 6.3. The compensation strategy is accomplished by self-tuning the current loop reference only based on the feedback information of the Sin-Cos encoder in 6.4. In 6.5, the control strategy is verified by simulation and experimental results.

6.2 Analysis of the Brake Releasing Process

Figure 6.1 shows the dynamic analysis of the traction system. An area element on the interface of the brake pulley and the brake shoe which corresponds to an angular element $d\gamma$ is selected to be studied, and γ is the wrap angle of the brake. Assume the pressure exerted by the brake shoe on the area element is $dN_i(t)$. During the brake releasing, the deformation of the brake shoes gets smaller, resulting in the decrease of $dN_i(t)$. The friction torque of each element is given as

$$dT_f = \mu dN_i(t) R_z \quad (6.1)$$

Fig. 6.1 Force analysis of the traction sheave and the brake sheave



where μ is the friction coefficient between the pulley and the brake.

Assuming that the deformation of each element is the same during the brake releasing, which means the change rate of $dN_i(t)$ for each element is the same. It can be expressed as

$$dN(t) = dN_i(t) \quad i = 1, 2, 3 \dots \tag{6.2}$$

The total friction torque exerted on the brake pulley by the brake shoes can be calculated by integration

$$\begin{aligned} T_f &= \int dT_f = \mu dN(t) \int_0^\gamma R_z d\gamma + \mu dN(t) \int_\pi^{\pi+\gamma} R_z d\gamma \\ &= \mu(2\gamma dN(t))R_z \end{aligned} \tag{6.3}$$

Equation (6.3) can be rewritten as (6.3) if $2\gamma dN(t)$ is replaced by equivalent pressure $N(t)$,

$$T_f = \mu N(t)R_z. \tag{6.4}$$

When the brake is releasing, the pressure $N(t)$ between the brake pulley and the brake shoe is decreasing and so is the maximum static friction between them.

Ideally, if the electromagnetic torque is equal to the total load torque during the brake releasing, the traction machine will keep still. Then the torque that the rope exerts on the traction wheel is constant. More specifically, in Fig. 6.1, T_c and T_w equal $M_c gR$ and $M_w gR$, respectively.

However, it is difficult for the traction machine to produce electromagnetic torque to balance the unknown and changing equivalent load torque precisely at zero speed.

If the starting torque is not well compensated, the traction machine will slide a distance due to torque unbalance during the brake releasing. The variations of the velocity and the acceleration of the system would cause the change of stretching force on the rope of both sides. The torque that the rope exerts on the traction sheave is given by (6.5) [1].

$$\begin{aligned}
 T_{sum0} = & R(M_c g - M_w g) \\
 & + Rk_2(-\theta_m R - x_2) + Rb_2(-\theta_m \dot{R} - \dot{x}_2) \\
 & - Rk_1(\theta_m R - x_1) + Rb_1(\dot{\theta}_m R - \dot{x}_1).
 \end{aligned}
 \tag{6.5}$$

In order to obtain the characteristics of T_{sum} during the brake releasing, the electromechanical simulation model of the direct-drive elevator system is established as Fig. 6.2. The electromagnetic brake is modeled as a first-order system based on its characteristics. The parameters of the traction machine model and the elevator mechanical model are listed in Appendix. Additionally, $N_0 = 6000$ N, $\mu = 0.6$, and $R(M_c g - M_w g) = -530$ Nm. The ideal or realistic situation is selected through the terminal 1 or 2 correspondingly. In the realistic situation, the conventional vector

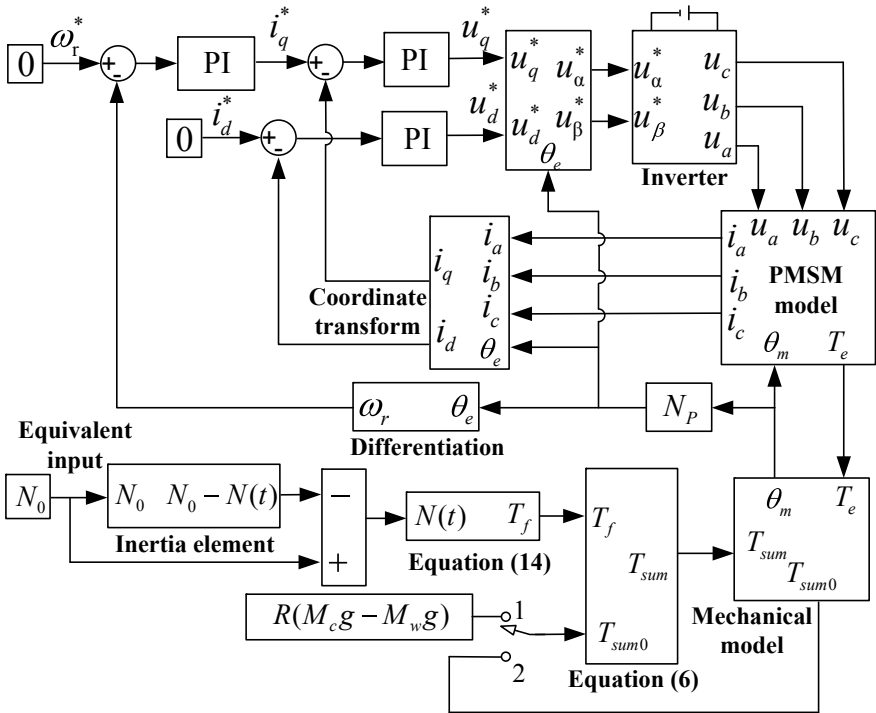


Fig. 6.2 Simulation block diagram of the direct-drive elevator system

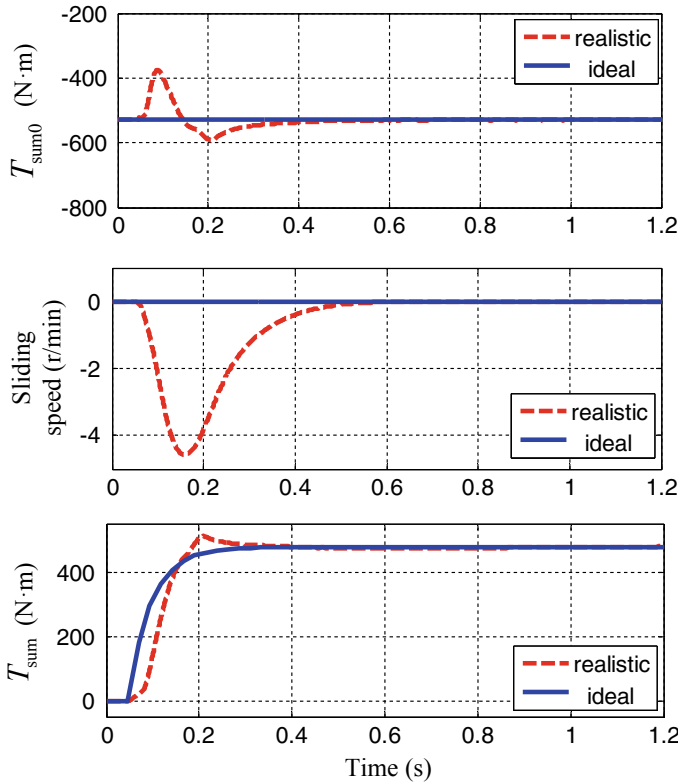


Fig. 6.3 Simulation results of the elevator system

control strategy is used. Both the speed controller and the current controllers are PI regulators. Simulation results are illustrated in Fig. 6.3.

From Fig. 6.3, it can be seen that T_{sum} in real condition is smaller than that in ideal condition when the sliding speed is increasing, and the contrary is the case when the sliding speed is decreasing. That means the sliding speed and the range of the speed variation would keep relatively small if T_e tracks T_{sum} well in the ideal situation. Since the brake releasing time would change due to the brake shoe abrasion and the adjustment of the braking force, the time constant of the brake is changing, and it is difficult to establish a precise mathematical model to describe the change of T_{sum} in ideal situation.

6.3 Starting Torque Control Strategy

According to the dynamic analysis of the traction machine system above, the control scheme of the starting torque compensation for direct-drive elevator machine is

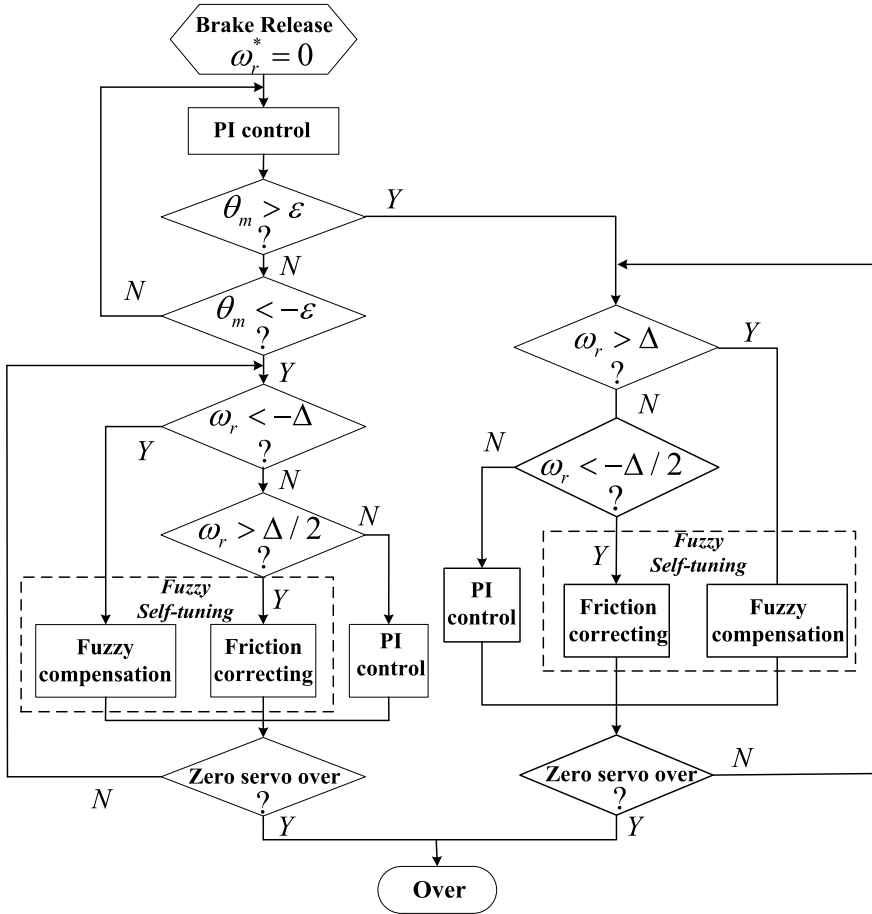


Fig. 6.6 Flowchart of the adaptive starting torque compensation

can be described as follows:

$$i_{q1}^*(k) = U_{p\omega}(k) + U_{i\omega}(k) = k_{p\omega}e(k) + \frac{T_s e(k)}{\tau_{i\omega}} + U_{i\omega}(k - 1) \quad (6.6)$$

where $U_{p\omega}$, $U_{i\omega}$, $k_{p\omega}$ and $\tau_{i\omega}$ are the proportional output, integral output, proportional gain and integral time constant of speed PI controller, respectively; T_s is the sampling period; $e(k)$ is the error between the speed reference and feedback; k denotes the value at time kT_s .

In addition, i_{q2}^* is the integration of the fuzzy self-tuning output k_i^* , and its mathematical representation is

$$i_{q2}^*(k) = i_{q2}^*(k-1) + k_t^*(k) \quad (6.7)$$

In Fig. 6.4, i_q^* is equal to the sum of i_{q1}^* and i_{q2}^* . Since the bandwidth of current loop is wider than the one of speed loop, the system can reach balance rapidly if i_q^* matches the load torque.

In Fig. 6.5, the solid line denotes the torque T_{sum} exerted on the traction sheave. T_e shown by the dotted line should trace the torque T_{sum} in order to make the sliding distance as short as possible. At time t_p , the brake releases completely, and T_e should satisfy the range $[T_c - F_c R, T_c + F_c R]$ to make the traction machine keep standstill, where $T_c = (M_c g - M_w g)R$. The detailed flow chart of the proposed starting torque compensation is described as Fig. 6.6, in which ε and Δ denote the threshold of sliding distance and sliding speed, respectively. The starting torque compensation strategy can be divided into four stages as follows.

Stage I $[0, t_1]$: The load torque $T_{\text{sum}0}$ is less than the sum of friction torque T_f and T_{μ} , and the traction sheave keeps standstill. The motor-generated torque is zero in this stage.

Stage II $[t_1, t_2]$: $T_{\text{sum}0}$ is larger than the maximum static friction torque, and the car begins to slide. Since the sliding distance is less than the threshold of the switch judger, the PI controller is active, and the output of the fuzzy self-tuning is zero. As the bandwidth of speed loop is limited and the output of the PI controller could not track the load torque timely, the sliding speed would increase in this stage.

Stage III $[t_2, t_3]$: At time t_2 , the sliding distance is larger than the threshold ε , and the sliding speed is larger than the threshold Δ . The compensation mode changes from PI control to the fuzzy compensation. The electromagnetic torque can trace the load torque with the suitable output of the fuzzy compensator. The control mode would switch between the PI control mode and the fuzzy compensation mode several times in this stage due to the speed variation. Because the load torque increases much faster than the output of the PI controller, the sliding speed direction is invariable, and the fuzzy compensation mode takes a dominant role. Since the brake releases completely at time t_p , the variation of torque T_{sum} is very small after time t_p .

Stage IV $[t_3, t_4]$: At time t_3 , the sliding speed is less than the threshold Δ , and the PI control mode is active. The sliding speed will decrease to zero at time t_4 with the speed PI regulator. If T_e satisfies $[T_c - F_c R, T_c + F_c R]$ at time t_4 , the sliding friction force would change into static friction force, and T_{sum} would be equal to T_e rapidly. If T_e is larger than $T_c + F_c R$ at time t_4 , the friction correcting mode would be active, and T_e would minus $F_c R$ in case of a reversed sliding distance.

6.4 Design of the Fuzzy Self-tuning Torque Compensator

The fuzzy self-tuning torque compensator is adopted to track the change of the synthetic load torque. Once it is active, a corresponding electromagnetic torque is generated by the traction machine to keep the elevator car slide at a small speed. The

structure of the fuzzy self-tuning torque compensator is illustrated in Fig. 6.7. The fuzzy compensator has two inputs, namely the sliding speed error ω_r and the change of the sliding speed error α . The output of the fuzzy compensator is k_t . And the output of the friction correcting mode is Δi_f . The sum of k_t and Δi_f is k_t^* which represents the change rate of q -axis current reference i_q^* . For convenience, the input variables ω_r and α are changed into \tilde{e} and $\tilde{c\tilde{e}}$ using the scaling factors K_e and K_{ce} , respectively, and the output of the fuzzy controller \tilde{u} is also processed by the quantification factor K_u to get the crisp value k_t .

The universes of discourse of the input fuzzy variables, \tilde{e} and $\tilde{c\tilde{e}}$, are $[-6, -1]U[1, 6]$ and $[-3, 3]$, respectively. The universe of discourse of the output variable \tilde{u} is $[-6, -1]U[1, 6]$. The universes of discourse of \tilde{E} and \tilde{U} are divided into six fuzzy sets, respectively, and the universe of discourse of $\tilde{C\tilde{E}}$ is divided into three fuzzy sets. Considering the sensitivity and stability of the fuzzy compensator, the membership functions of the input and output variables are shown in Fig. 6.8.

The change characteristics of T_{sum} modeled in Sect. 6.2 are considered to design the fuzzy control rules. The control target is to obtain a minimized sliding distance and to avoid the change of sliding direction. So, the increasing rate of T_e should become larger to reduce the sliding distance when the sliding speed becomes larger. On the other hand, the increasing rate of T_e should decrease moderately to avoid motor reversal when the sliding speed becomes smaller. In addition, using the sliding acceleration as an auxiliary judgment to regulate T_e can ensure it to track the load disturbance timely. The fuzzy control rules are shown in Table 6.1. There are 18 rules for the starting torque compensator. The control rule R_i is designed as follows: if \tilde{e} is \tilde{E}_j and $\tilde{c\tilde{e}}$ is $\tilde{C\tilde{E}}_k$, then \tilde{u} is \tilde{U}_m , where $i = 1, 2, \dots, 18$, and $j, m = 1, 2, \dots, 6$ $k = 1, 2, 3$.

The minimum operation is used to get the fuzzy set of the output:

$$\mu(\tilde{U}_i) = \min\{ \mu(\tilde{E}_i), \mu(\tilde{C\tilde{E}}_i) \} . \tag{6.8}$$

For example, if $\tilde{e} = 2.5$ and $\tilde{c\tilde{e}} = 0.5$, the control rules R_{11} and R_{14} are active to calculate the output fuzzy set. According to the control rule R_{11} , the weighting coefficient of output fuzzy set $NS(\tilde{u})$ can be obtained

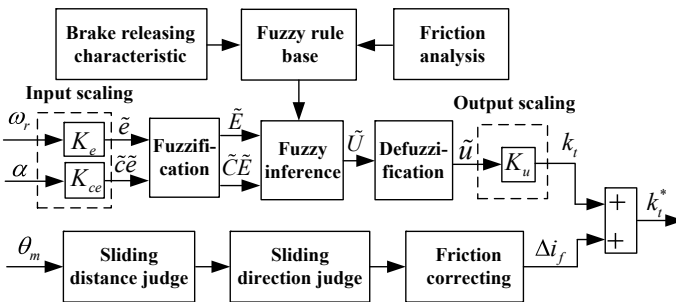


Fig. 6.7 Simplified block diagram of the fuzzy self-tuning torque compensator

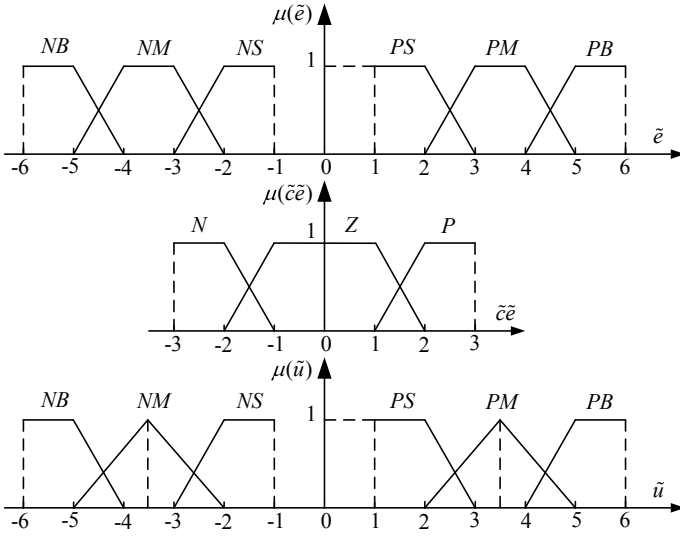


Fig. 6.8 Membership function of \tilde{e} , $\tilde{c}\tilde{e}$ and \tilde{u}

Table 6.1 Fuzzy control rules

\tilde{U}		\tilde{E}					
		NB	NM	NS	PS	PM	PB
$\tilde{C}\tilde{E}$	P	PM(1)	PM(4)	PS(7)	NB(10)	NB(13)	NB(16)
	Z	PB(2)	PM(5)	PS(8)	NS(11)	NM(14)	NB(17)
	N	PB(3)	PB(6)	PB(9)	NS(12)	NM(15)	NM(18)

$$\mu(NS(\tilde{u})) = \min\{ \mu(PS(\tilde{e})), \mu(Z(\tilde{c}\tilde{e}))\} = \min\{ 0.5, 1\} = 0.5. \quad (6.9)$$

Based on the control rule R_{14} , the weighting coefficient of output fuzzy set $NM(\tilde{u})$ can be got

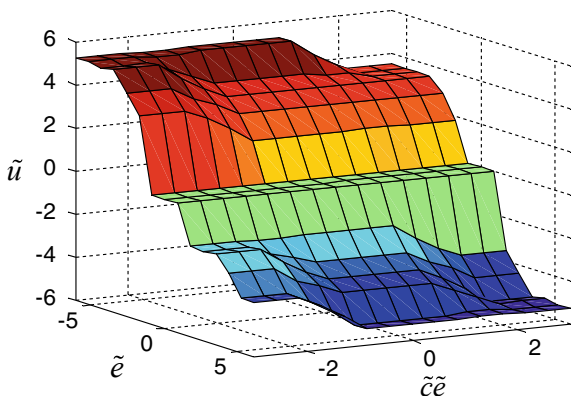
$$\mu(NM(\tilde{u})) = \min\{ \mu(PM(\tilde{e})), \mu(Z(\tilde{c}\tilde{e}))\} = \min\{ 0.5, 1\} = 0.5. \quad (6.10)$$

Actually, the output fuzzy set is the union of $NS(\tilde{u})$ and $NM(\tilde{u})$, which can be expressed as

$$0.5^\mu(NS(\tilde{u})) \vee 0.5^\mu(NM(\tilde{u})). \quad (6.11)$$

The center average defuzzifier is adopted to transform the output of the fuzzy inference to a crisp value \tilde{u} in the fuzzy controller:

Fig. 6.9 Relationship of the fuzzy self-tuning torque compensation rules



$$\tilde{u} = \frac{\sum \mu(\tilde{U}_i) \cdot u_i}{\sum \mu(\tilde{U}_i)}. \quad (6.12)$$

where u_i is the center of the corresponding fuzzy set, which equals the mean value of the points whose membership is one in the fuzzy set. In this scheme, the centers of $NS(\tilde{u})$ and $NM(\tilde{u})$ are -1.5 and -3.5 , respectively. The crisp value \tilde{u} can be calculated as follows:

$$\tilde{u} = \frac{0.5 \times (-1.5) + 0.5 \times (-3.5)}{0.5 + 0.5} = -2.5. \quad (6.13)$$

Based on the defuzzification above, the relationship between the inputs and the output is shown in Fig. 6.9.

In the scheme, the ranges of ω_r and α in the fuzzy controller are $[-0.032, -0.004]U[0.004, 0.032]$ rad/s and $[-80, 80]$ rad/s², respectively; the range of the output k_t is $[-0.1\%I_N, -0.02\%I_N]U[0.02\%I_N, 0.1\%I_N]$, where I_N denotes the rated current. The values of \tilde{e} and \tilde{c}_e can be obtained

$$\tilde{e} = \begin{cases} 6; & \omega_r \in [0.024, 0.032] \text{ rad/s} \\ 250\omega_r; & \omega_r \in [-0.024, -0.004]U[0.004, 0.024] \text{ rad/s} \\ -6; & \omega_r \in [-0.032, -0.024] \text{ rad/s} \end{cases}, \quad (6.14)$$

$$\tilde{c}_e = \begin{cases} 3; & \alpha \in [60, 80] \text{ rad/s}^2 \\ 0.05\alpha; & \alpha \in [-60, 60] \text{ rad/s}^2 \\ 3; & \alpha \in [-80, -60] \text{ rad/s}^2 \end{cases}. \quad (6.15)$$

As a result, the value of $k_t(k)$ can be calculated by output scaling function

$$k_t(k) = 0.00016I_N \tilde{u}(k). \quad (6.16)$$

6.5 Experimental Evaluation

The proposed adaptive starting torque compensation method is experimented at an 11.7 kW gearless elevator traction machine without using the weight transducer as shown in Fig. 4.13. The parameters of the permanent magnet traction machine are listed in Table 4.1. A Sin-Cos encoder (ERN1387) with 2048 P/R is installed on the machine. TMS320F2808 DSP is used to execute all the control algorithms. The PWM frequency of the inverter is 10 kHz. The period of the current loop is 100 μ s, and the speed control is activated every 1 ms. The proposed compensation algorithm is executed every 100 μ s. In the switch judger, the threshold of the sliding distance ε is 0.06 mm, and the threshold of the sliding speed Δ is 0.004 rad/s. To verify the proposed starting torque compensation strategy, the experimental results of the conventional PI control are shown for comparison. The PI controller parameters are carefully designed as shown in Appendix B to satisfy the zero-speed traction mode. The parameters of current PI controllers are $k_{pi} = 37.49$ and $\tau_{ii} = 1.739 \times 10^{-3}$ s, and the parameters of speed controller are $k_{p\omega} = 3.61$ and $\tau_{i\omega} = 0.012$. The same PI parameters are used in Fig. 6.4 to cooperate with the fuzzy self-tuning torque compensation strategy.

Experimental results using the proposed compensation strategy and the conventional PI control method under different loads are illustrated in Figs. 6.10, 6.11 and 6.12. In each figure, from top to bottom, the quadrature signals from the Sin-Cos encoder, the sliding distance of the traction machine and the q -axis current (expressed by per-unit value) are shown, respectively. The sliding distances using the conventional PI control and the proposed method are 1.2 mm and 0.18 mm in Fig. 6.10, 4.0 mm and 0.35 mm in Fig. 6.11 and 7.2 mm and 0.65 mm in Fig. 6.12, respectively.

From the results, it can be concluded that the sliding distance becomes much shorter and the sliding speed reaches zero faster when the proposed compensation strategy is adopted. Besides, the q -axis current response is much faster especially at the beginning stage of the sliding process, which means that the motor-generated torque tracks the load torque timely. And this causes a relatively small sliding speed. Figure 6.13 shows a more visualized sliding distance comparison of the two methods under various loads, which verifies the effectiveness of the proposed method further.

6.6 Summary

In this chapter, an adaptive starting torque compensation method of gearless traction machine for direct-drive elevator without using a weight transducer has been proposed. The dynamic analysis of the brake releasing process shows that the synthetic load torque in actual condition is smaller than that in ideal condition when the sliding speed is increasing, and the contrary is the case when the sliding speed is decreasing. The adaptive compensation strategy consists of three modes including the PI control, the fuzzy compensation and the friction correcting. The rules of the

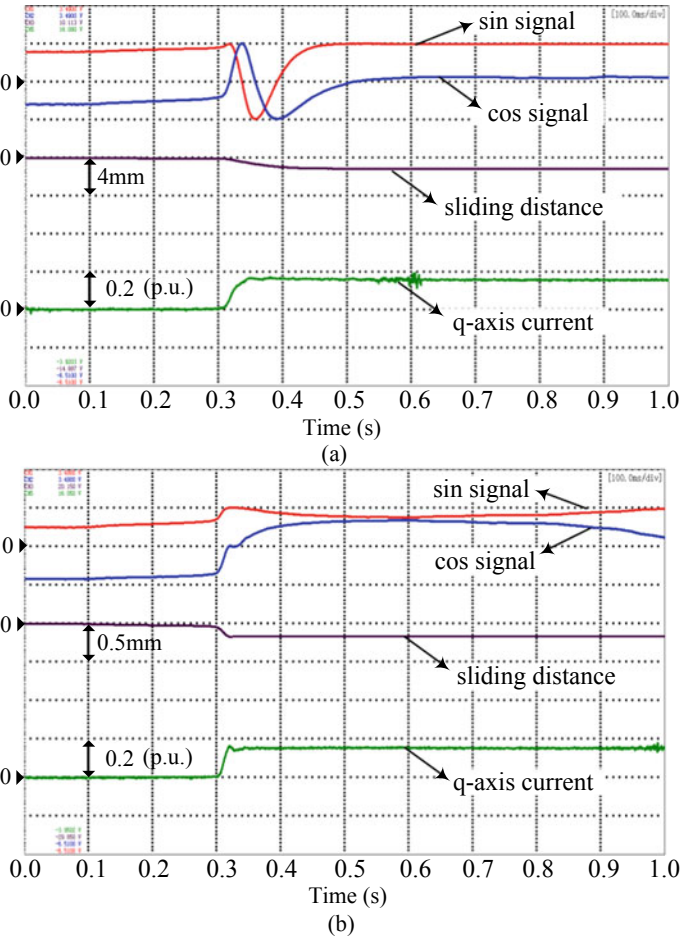


Fig. 6.10 Experimental comparison between **a** conventional PI control and **b** proposed compensation strategy under 20% rated load

torque compensator are designed in order to get a shorter sliding distance and avoid sliding direction reversal. The effectiveness of the method is verified both in simulation and experiment. By adopting the compensation strategy, the electromagnetic torque generated by the gearless machine tracks the load torque better during elevator start-up. It performs better at improving riding comfort of the gearless elevator with a shorter sliding distance.

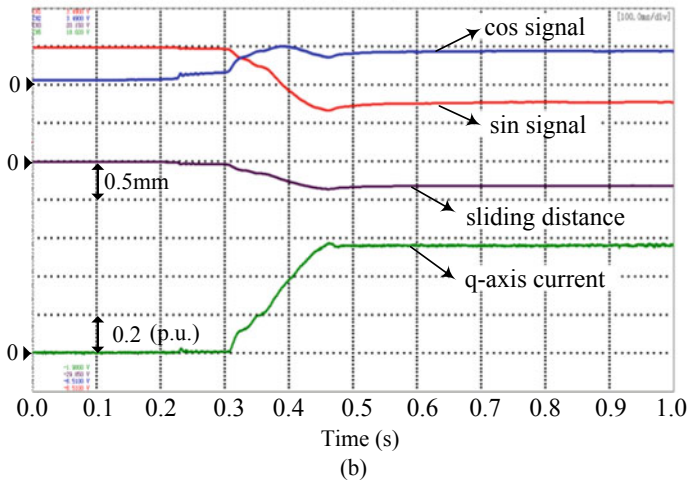
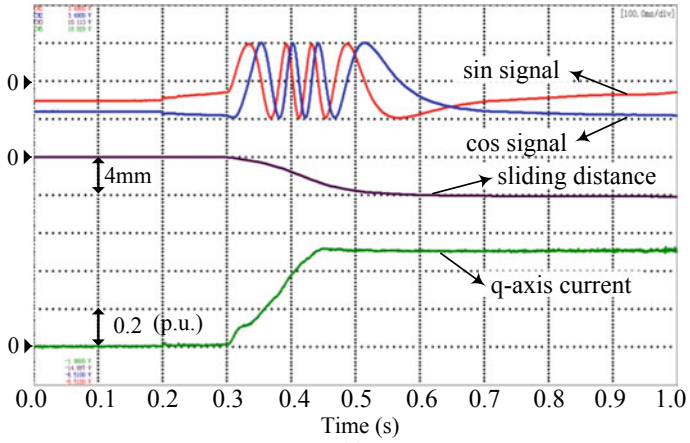


Fig. 6.11 Experimental comparison between **a** conventional PI control and **b** proposed compensation strategy under 60% rated load

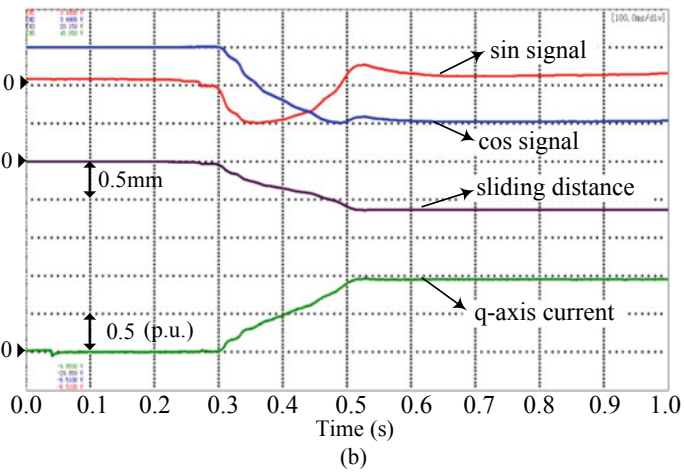
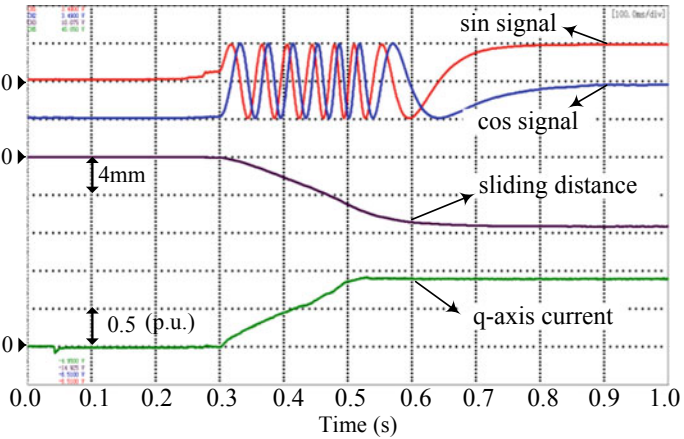


Fig. 6.12 Experimental comparison between conventional PI control and proposed compensation strategy under rated load

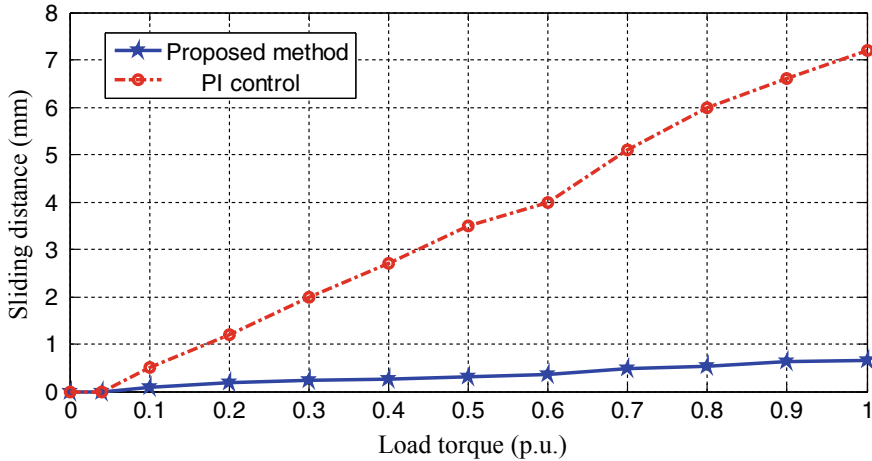


Fig. 6.13 Sliding distance comparison of the two methods under different loads

References

1. Wang G et al (2014) Weight-transducerless starting torque compensation of gearless permanent-magnet traction machine for direct-drive elevators. *IEEE Trans Ind Electron* 61(9):4594–4604
2. Kim W, Shin D, Chung CC (2013) Microstepping using a disturbance observer and a variable structure controller for permanent-magnet stepper motors. *IEEE Trans Ind Electron* 60(7):2689–2699
3. Wang H, Kong H, Man Z, Tuan DM, Cao Z, Shen W (2013) Sliding mode control for steer-by-wire systems with AC motors in road vehicles. *IEEE Trans Ind Electron* 61(3):1596–1611
4. Choi HH, Jung JW (2013) Discrete-time fuzzy speed regulator design for PM synchronous motor. *IEEE Trans Ind Electron* 60(2):600–607
5. Yasser AR, Ibrahim M (2007) A hybrid-type variable-structure instantaneous torque control with a robust adaptive torque observer for a high-performance direct-drive PMSM. *IEEE Trans Ind Electron* 54(5):2491–2499
6. Smadi IA, Omori H, Fujimoto Y (2012) Development, analysis, and experimental realization of a direct-drive helical motor. *IEEE Trans Ind Electron* 59(5):2208–2216
7. Errouissi R, Ouhrouche M, Chen WH, Trzynadlowski AM (2012) Robust cascaded nonlinear predictive control of a permanent magnet synchronous motor with antiwindup compensator. *IEEE Trans Ind Electron* 59(8):3078–3088
8. Vu NTT, Yu DY, Choi HH, Jung JW (2013) T–S fuzzy-model-based sliding-mode control for surface-mounted permanent-magnet synchronous motors considering uncertainties. *IEEE Trans Ind Electron* 60(10):4281–4291
9. Hong XY, Deng Z, Wang SR, Huang LJ, Li WH, Lu ZY (2010) A novel elevator load torque identification method based on friction model. In: Proc. 25th annu. IEEE APEC, pp 2021–2024
10. Wang G, Zhang G, Yang R, Xu D (2012) Robust low-cost control scheme of direct-drive gearless traction machine for elevators without a weight transducer. *IEEE Trans Ind Appl* 48(3):996–1005
11. Bolognani S, Faggion A, Sgarbossa L, Peretti L (2007) Modelling and design of a direct-drive lift control with rope elasticity and estimation of starting torque. In: Proc. 33rd annu. IEEE IECON, pp 828–832

12. Kim JC, Kim JM, Kim CU, Choi C (2006) Ultra precise position estimation of servomotor using analog quadrature encoders. In: Proc. applied power electronics conference and exposition (APEC), pp 930–934
13. Hung VH, Jae WJ (2011) An efficient approach to correct the signals and generate high-resolution quadrature pulses formagnetic encoders. IEEE Trans Ind Electron 58(8):3634–3646

Chapter 7

Starting Torque Control Strategy Based on Offset-Free Model Predictive Control Theory



7.1 Introduction

After years of application and investigation, although the compensation strategies using weight transducers can meet the requirement of elevator operation, there are still limitations: (1) Load information transmitted via the communication board may be interfered because of the long cable and complicated electromagnetic environment. (2) As for weight transducers installed at the bottom of the elevator car, the compressed deformation of anti-vibration rubber and the carload are not completely colinear. The obtained load information may have deviation. (3) The performance of compensation strategies during the elevator startup depends on on-site commissioning, so the uncertainty is not easily avoided. Therefore, weight-transducerless torque control strategies during the elevator startup have been a key research topic. The so-called transducerless torque control strategies refer that the elevator control system can generate a suitable electromagnetic torque to avoid rollback of the elevator car based on the feedback signal from the encoder instead of relying on the weight transducers to get the carload information. It should achieve a smooth startup with acceptable sliding distance and no mechanical vibration.

Various advanced control strategies have been proposed to improve the robustness against load disturbance [1–3]; however, these methods are not suitable for the starting torque control of elevators. In [4], the load torque was tracked by the compensation torque calculated by two kinds of adjusting methods using dichotomy and staircase algorithms, respectively. However, during the elevator startup, the mechanical vibration still exists. In [5], the novel torque control strategy can be described as a searching logic based on a friction model. However, mechanical vibration cannot be avoided because of the large step of the neighboring torque references. In [6], the disturbance torque was obtained through estimating the acceleration by the quadratic error comparison. But the accurate mechanical model should be needed to calculate the load torque. In [7], a torque compensation strategy based on adaptive fuzzy control was proposed. It provided an appropriate torque according to the speed and acceleration of the traction sheave. Although this strategy can reduce sliding distance and

avoid mechanical vibration, it should use accurate subdivided position information based on Sin-Cos encoder. For the elevator installed with an incremental encoder, this control strategy is difficult to achieve satisfactory performance of anti-rollback.

Model predictive control (MPC) was successfully used in chemical process control and extended to electrical control field recently [8–10], because of adjustable dynamic response and high control accuracy. The special characteristics can meet the requirements of anti-rollback control for weight-transducerless elevator startup. Usually, the predictive variables of conventional MPC are calculated without considering the disturbance. The difference between the predictive variables and the actual ones are corrected in the cost function, in order to reduce the effect of disturbance on the predictive variables during receding optimization process. But the uncertainty and nonlinearity of the mechanical model, as well as intense disturbance, can cause the mismatch of predictive model, which leads to steady-state speed error in the zero-servo operation during the brake releasing.

In this chapter, a novel anti-rollback strategy adopting offset-free model predictive control strategy for direct-drive elevators installed with a general incremental encoder is proposed to improve the riding comfort [11]. It can achieve smaller sliding distance and no mechanical vibration. This chapter is organized as follows. Firstly, dynamic mechanical model of the elevator traction system is analyzed in 7.2, in order to illuminate the advantages of the proposed method. Secondly, the offset-free model predictive control for anti-rollback of weight-transducerless elevators is established in 7.3, including the receding optimization process and the predictive controller. Additionally, the stability of the offset-free MPC is analyzed and the root locus is shown in 7.3.1. Finally, the control strategy is verified by simulation and experimental results in 7.4.

7.2 Dynamic Model of Elevator Traction System

Gearless elevator is composed of the traction machine, the car and the counterweight. The traction sheave and the brake pulley are installed on the rotor of permanent magnet traction machine. An electromagnetic brake is mounted around the brake pulley to hold the traction system still when the elevator operates in standby mode.

The dynamic mechanical equations of the counterweight side can be expressed as follows:

$$m_w \dot{x}_1 - c_1(\theta R - x_1) - d_1(\dot{\theta} R - \dot{x}_1) = 0, \quad (7.1)$$

$$m_w g - c_1 \Delta x_{10} = 0 \quad (7.2)$$

where c_1 and d_1 are the rigidity coefficient and the damping coefficient of the rope on counterweight side, m_w is the mass of the counterweight, Δx_{10} is the elongation of the rope on counterweight side in steady-state, θ is the mechanical position of the traction sheave, x_1 is the counterweight displacement.

Similarly, the dynamic mechanical equation of the car side can be expressed as follows:

$$m_c \dot{x}_2 - c_2(-\theta R - x_2) - d_2(-\dot{\theta} R - \dot{x}_2) = 0, \quad (7.3)$$

$$m_c g - c_2 \Delta x_{20} = 0 \quad (7.4)$$

where c_2 and d_2 are the rigidity coefficient and the damping coefficient of the rope on car side, m_c is the mass of the car, Δx_{20} is the elongation of the rope on car side in steady state, x_2 is the car displacement.

Considering the friction torque exerted on the pulley by the brake, the kinematic analysis of the traction sheave can be described by (7.5), (7.6) and (7.7). Particularly, J is the normal value of inertia, Δ is the difference between the actual value and the normal value of the inertia, $T_{d\Delta}$ is the equivalent torque caused by Δ . T_f is the friction torque between the brake pulley and the brake. T_μ is the friction torque caused by other factors of the system. T_e is the electromagnetic torque generated by traction machine. T_l is the resultant friction torque exerted on traction sheave. R is the radius of brake pulley. T_d is the composite disturbance torque, which is unknown when the brake is released.

$$T_e - T_d = (J + \Delta)\ddot{\theta} \quad (7.5)$$

where

$$T_d = \begin{cases} T_{d\Delta} ; & T_f + T_\mu > T_l \\ T_l - (T_f + T_\mu) + T_{d\Delta}; & \text{otherwise} \end{cases}, \quad (7.6)$$

$$\begin{aligned} T_l = & R(m_c g - m_w g) + R c_2(-\theta R - x_2) + R d_2(-\dot{\theta} R - \dot{x}_2) \\ & - R c_1(\theta R - x_1) + R d_1(\dot{\theta} R - \dot{x}_1). \end{aligned} \quad (7.7)$$

According to the friction model, the electromagnetic torque to keep the traction wheel at standstill is not a fixed value. The accurate electromagnetic torque to balance the equivalent load torque is difficult to be calculated through the mathematical model considering the nonlinear characteristic of mechanical brake releasing. Therefore, those methods calculating the accurate compensation torque based on mechanical model are not easily implemented in this case.

Using the low-resolution incremental encoder as the feedback device, the conventional PI control cannot meet the requirement of rapid adjustment and small mechanical vibration simultaneously during the brake releasing. Compared with the conventional PI control, MPC can achieve faster response speed, bigger equivalent gain when the input is small and vice versa. Thus, MPC can be used to reduce the sliding distance during the elevator startup. However, conventional model predictive control is difficult to be used as the speed regulator at zero-servo operation. If the reference speed and the feedback speed are zero, the output of the speed loop is zero. The traction machine will certainly slide when the load is exerted on the shaft. So the steady-state speed error is inevitable. Therefore, investigating advanced MPC method during elevator startup which is suitable for the low-resolution incremental encoder is definitely significant.

7.3 Offset-Free MPC for Anti-rollback During the Elevator Startup

7.3.1 Establishment of the Offset-Free MPC for Elevator Startup

Figure 7.1 shows the scheme of the proposed offset-free model predictive control strategy of direct-drive permanent magnet traction machine during the elevator startup. In Fig. 7.1, PI regulators are used in the current loops. For the speed loop, offset-free model predictive control strategy is used instead of the conventional PI

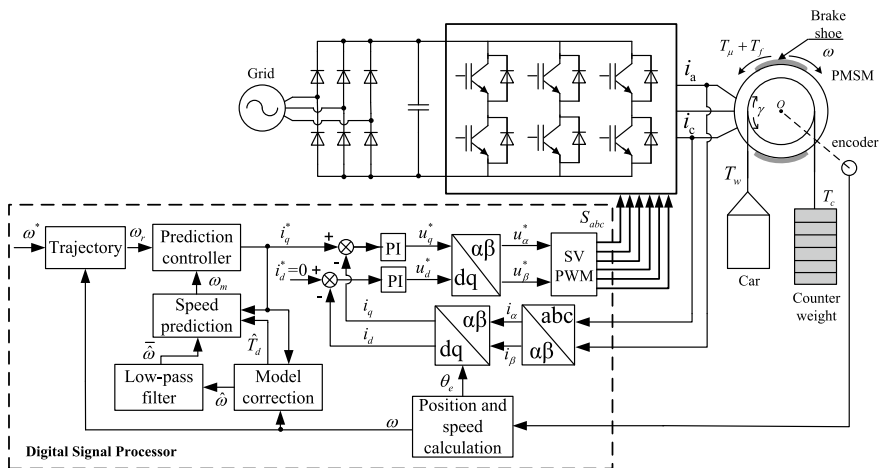


Fig. 7.1 Scheme of offset-free model predictive control strategy of traction machine for anti-rollback during the elevator startup

regulator. Additionally, in order to suppress the negative effects caused by model mismatch and eliminate the speed error in steady state, the model correction scheme is designed. And receding optimization cannot only reduce the sliding distance, but also enhance the robustness against load disturbance during the brake releasing.

In order to analyze conveniently, the mechanical model (7.5) can be converted to

$$\dot{\omega} = K_t(i_q^* - i_{qd} - B\omega/K_t)/J \quad (7.8)$$

where $K_t = 1.5n_p\psi_f$, $i_{qd} = T_d/K_t$, i_{qd} represent the equivalent current of composite load torque. However, i_{qd} is not considered in predictive model when using the conventional MPC without offset-free strategy. During the elevator startup, the composite disturbance torque exerting on the traction wheel changes complexly and intensely, so the precision of this value directly affects the accuracy of the prediction model. After zero-order-hold discretization of (7.8), it can be expressed as

$$\omega_m(k+1) = \alpha_m\omega_m(k) + K_m(1 - \alpha_m)[i_q^*(k) - i_{qd}(k)] \quad (7.9)$$

where $\omega_m(k+1)$ represents the predictive speed at time $k+1$, $K_m = K_t/J$ and $\alpha_m = \exp(BT_s/J)$, T_s is the sampling time. After iteration, the following expression can be obtained

$$\begin{aligned} \omega_m(k+n) = & K_m(1 - \alpha_m)(1 + \alpha_m + \dots + \alpha_m^{n-1})[i_q^*(k) \\ & - i_{qd}(k)] + \alpha_m^n\omega_m(k), n = 1, 2, \dots, P. \end{aligned} \quad (7.10)$$

where P is the predictive step. Since the sampling period is short enough, the composite disturbance torque can be considered as a constant. Therefore, the estimated disturbance and speed can be applied to modify the predictive model during each sampling period, so as to eliminate steady-state speed error and enhance robustness against the composite disturbance torque during the brake releasing.

Choose θ , ω and T_d as state variables, and the state equation can be obtained based on (7.5)

$$\begin{cases} \dot{\mathbf{x}} = \mathbf{A}\mathbf{x} + \mathbf{B}\mathbf{u} \\ \mathbf{y} = \mathbf{C}\mathbf{x} \end{cases} \quad (7.11)$$

In (7.11), $\mathbf{x} = [\theta \ \omega \ T_d]^T$, $\mathbf{u} = T_e$, $\mathbf{y} = \theta$ and

$$\mathbf{A} = \begin{bmatrix} 0 & 1 & 0 \\ 0 & -\frac{B}{J} & -\frac{1}{J} \\ 0 & 0 & 0 \end{bmatrix}, \quad \mathbf{B} = \begin{bmatrix} 0 \\ \frac{1}{J} \\ 0 \end{bmatrix}, \quad \mathbf{C} = \begin{bmatrix} 1 \\ 0 \\ 0 \end{bmatrix}.$$

According to (7.11), the state equation with estimated feedback can be expressed as follows:

$$\dot{\hat{\mathbf{x}}} = \mathbf{A}\hat{\mathbf{x}} + \mathbf{B}\mathbf{u} + \mathbf{L}(\mathbf{y} - \mathbf{C}\hat{\mathbf{x}}) \quad (7.12)$$

Equation (7.12) can be expressed in detail as:

$$\begin{bmatrix} \dot{\hat{\theta}} \\ \dot{\hat{\omega}} \\ \dot{\hat{T}}_d \end{bmatrix} = \begin{bmatrix} 0 & 1 & 0 \\ 0 & -\frac{B}{J} & -\frac{1}{J} \\ 0 & 0 & 0 \end{bmatrix} \begin{bmatrix} \hat{\theta} \\ \hat{\omega} \\ \hat{T}_d \end{bmatrix} + \begin{bmatrix} 0 \\ \frac{1}{J} \\ 0 \end{bmatrix} T_e + \begin{bmatrix} l_1 \\ l_2 \\ l_3 \end{bmatrix} (\theta - \hat{\theta}) \quad (7.13)$$

Equation (7.13) is the estimated value of \mathbf{x} , \mathbf{L} is the feedback gain matrix, $\mathbf{L} = [l_1 \ l_2 \ l_3]^T$, which is determined by the pole placement. \mathbf{L} can make an approach, respectively.

According to (7.13), the composite disturbance torque and speed estimation can be expressed as (7.14) and (7.15)

$$\hat{T}_d = \left(\frac{l_3}{s} - J l_2 \right) \frac{1}{s + l_1} (\omega - \hat{\omega}) \quad (7.14)$$

$$(Js + B)\hat{\omega} = T_e - \left(\frac{l_3}{s} - J l_2 \right) \frac{1}{s + l_1} (\omega - \hat{\omega}) \quad (7.15)$$

The viscous friction coefficient can be ignored because it is relatively small. And the estimated speed is filtered by a low-pass filter, whose cutoff frequency is f_c . The discrete expressions of (7.14) and (7.15) can be obtained as

$$\begin{cases} e(k) = \frac{1}{1+T_s l_1} e(k-1) + \frac{T_s l_1}{1+T_s l_1} [\omega(k) - \bar{\omega}(k)] \\ u(k) = u(k-1) + T_s l_3 e(k) \\ \hat{T}_d(k) = J l_2 e(k) - u(k) \\ \hat{\omega}(k) = \frac{K_r T_s [i_q(k-1) + \hat{i}_{qd}(k)]}{J} + \hat{\omega}(k-1) \\ \bar{\omega}(k) = \frac{1}{1+2\pi T_s f_c} \bar{\omega}(k-1) + \frac{2\pi T_s f_c}{1+2\pi T_s f_c} \hat{\omega}(k) \end{cases} \quad (7.16)$$

In (7.16), $e(k)$ and $u(k)$ are intermediate variables, which is the filtered estimated speed. $\hat{T}_d(k)$ is the estimated equivalent current of composite disturbance torque at the time k . Then in (7.11), $\omega_m(k)$ and $i_{qd}(k)$ are replaced by $\bar{\omega}(k)$ and $\hat{i}_{qd}(k)$, respectively. The initial value of predictive speeds within the predictive step P can be corrected during each sampling period. Then (7.17) can be obtained

$$\begin{aligned} \omega_m(k+n) &= K_m (1 - \alpha_m) (1 + \alpha_m + \dots + \alpha_m^{n-1}) [i_q^*(k) \\ &\quad - \hat{i}_{qd}(k)] + \alpha_m^n \bar{\omega}(k), \quad n = 1, 2, \dots, P. \end{aligned} \quad (7.17)$$

Therefore, the outputs of the predictive model at time $k, k + 1, k + 2 \dots k + P$ can be expressed in a matrix form as follows:

$$\mathbf{W}_m(k) = \mathbf{W}_f(k) + \mathbf{W}_s(k)[i_q^*(k) - \hat{i}_{qd}(k)]. \quad (7.18)$$

In (7.18),

$$\begin{cases} \mathbf{W}_m(k) = [\omega_m(k+1) \cdots \omega_m(k+P)]^T \\ \mathbf{W}_f(k) = [\alpha_m \cdots \alpha_m^P]^T \bar{\omega}(k) \\ \mathbf{W}_s(k) = K_m(1 - \alpha_m)[1 \cdots 1 + \alpha_m \cdots + \alpha_m^{P-1}]^T \end{cases}. \quad (7.19)$$

7.3.2 Cost Function Design

Select first-order exponential function as the reference trajectory which can be expressed as follows:

$$\omega_r(k+i) = \omega^*(k+i) - \alpha_r^i[\omega^*(k) - \omega(k)], i = 1, 2, \dots, P \quad (7.20)$$

where ω_r is the reference trajectory, ω^* is the mechanical angular velocity reference, T_r is the time constant, and $\alpha_r = \exp(-T_s/T_r)$.

Overcomplicated cost function will increase the amount of computation. In model correction block, the initial predictive speed error has been corrected. So there is no need to correct it in the cost function again, which can effectively reduce the computational burden. The second-order cost function is chosen as follows:

$$J_P = [\mathbf{W}_r(k) - \mathbf{W}_m(k)]^T \mathbf{Q}[\mathbf{W}_r(k) - \mathbf{W}_m(k)] + Ri_q^{*2} \quad (7.21)$$

where $\mathbf{Q} = \text{diag}[q_1^2 \cdots q_p^2]$, $R = r^2$, $\mathbf{W}_r(k) = [\omega_r(k+1) \cdots \omega_r(k+P)]^T$. $q_1 \cdots q_p$ are the weight variables for predictive steps, r is the weight variable of the output current. Let $\partial J_P / \partial i_q^* = 0$, the output of the MPC controller can be obtained

$$i_q^*(k) = (\mathbf{W}_s^T \mathbf{Q} \mathbf{W}_s + R)^{-1} \mathbf{W}_s^T \mathbf{Q} [\mathbf{W}_r(k) - \mathbf{W}_f(k) - \mathbf{W}_s \hat{i}_{qd}(k)] \quad (7.22)$$

7.3.3 Stability Analysis of the Proposed Speed Controller

Parameters of the MPC strategy can affect both the dynamic response and the stability of the system. In addition, the model mismatch will also affect the stability of the system. In order to facilitate the stability analysis of the traction system, the first-order inertia and filters are ignored. Let $k_1 = -Jl_2, k_2 = l_3$, then the following discrete transfer functions can be obtained, as shown in Fig. 7.2.

$$G_c^{-1}(z) = (W_s^T Q W_s + R)^{-1} W_s^T Q \tag{7.23}$$

$$G_i^{-1}(z) = W_s \tag{7.24}$$

$$G_w^{-1}(z) = [\alpha_m \cdots \alpha_m^p]^T \tag{7.25}$$

$$G_p^{-1}(z) = \frac{k_t T_s z^{-1}}{(J + \Delta)(1 - z^{-1})} \tag{7.26}$$

where Δ reflects the matching level between the two variables. Under the steady-state condition, the larger Δ can be obtained, the stronger the capability of correcting the mismatch can be. Because the speed in steady state is relatively small, the coefficient of friction viscosity can be ignored. Let

$$G_1^{-1}(z) = (k_1 + \frac{T_s k_2 z^{-1}}{1 - z^{-1}}) \cdot \frac{1}{k_t} \tag{7.27}$$

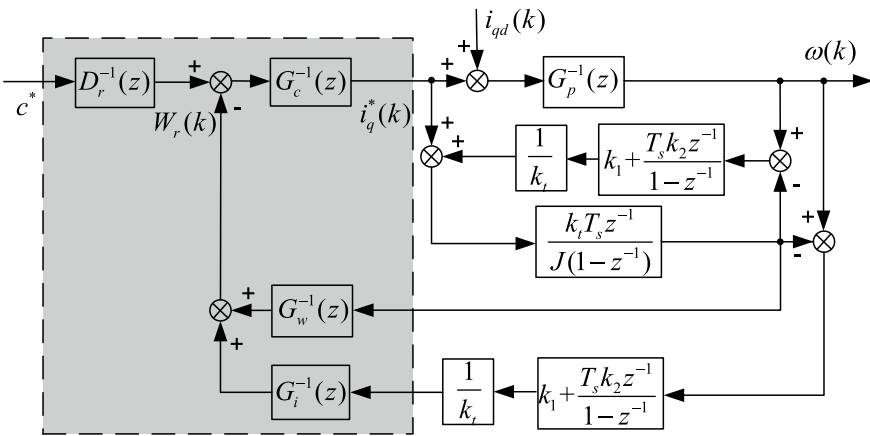


Fig. 7.2 Discrete block diagram of the offset-free MPC for traction machine

$$\mathbf{G}_2^{-1}(z) = \frac{k_r T_s z^{-1}}{J(1 - z^{-1})} \quad (7.28)$$

Simplify the flowchart and the closed-loop transfer function can be got:

$$\begin{aligned} \omega(k) = & \frac{\mathbf{G}_c^{-1}(z)\mathbf{G}_p^{-1}(z)(1 + \mathbf{G}_1^{-1}(z)\mathbf{G}_2^{-1}(z))}{\mathbf{G}_m^{-1}(z)} \cdot \omega_r(k + H) \\ & + \frac{\mathbf{G}_p^{-1}(z)(1 + \mathbf{G}_1^{-1}(z)\mathbf{G}_2^{-1}(z))}{\mathbf{G}_m^{-1}(z)} \cdot i_{qd}(k) \end{aligned} \quad (7.29)$$

$$\begin{aligned} \mathbf{G}_m^{-1}(z) = & 1 + \mathbf{G}_1^{-1}(z)\mathbf{G}_2^{-1}(z) + \mathbf{G}_c^{-1}(z)\mathbf{G}_w^{-1}(z)\mathbf{G}_2^{-1}(z) \\ & + \mathbf{G}_c^{-1}(z)\mathbf{G}_p^{-1}(z)\mathbf{G}_w^{-1}(z)\mathbf{G}_1^{-1}(z)\mathbf{G}_2^{-1}(z) \\ & + \mathbf{G}_c^{-1}(z)\mathbf{G}_p^{-1}(z)\mathbf{G}_i^{-1}(z)\mathbf{G}_1^{-1}(z) \\ & - \mathbf{G}_c^{-1}(z)\mathbf{G}_i^{-1}(z)\mathbf{G}_1^{-1}(z)\mathbf{G}_2^{-1}(z) \end{aligned} \quad (7.30)$$

Then the characteristic equation of the system can be obtained

$$\mathbf{G}_m^{-1}(z) = 0 \quad (7.31)$$

Organize the characteristic equation into the root locus form on Δ :

$$1 + \Delta \frac{1 + N_1 z^{-1} + N_2 z^{-2} + N_3 z^{-3}}{J + M_1 z^{-1} + M_2 z^{-2} + M_3 z^{-3}} = 0 \quad (7.32)$$

Assume $A_1 = \mathbf{G}_c^{-1}(z)\mathbf{G}_w^{-1}(z)$, $A_2 = \mathbf{G}_c^{-1}(z)\mathbf{G}_i^{-1}(z)$ then

$$\begin{cases} N_1 = -3 + \frac{(1-A_2)T_s k_1 + A_1 k_r T_s}{J} \\ N_2 = 3 + \frac{(1-A_2)T_s(k_2 T_s - 2k_1) - 2A_1 k_r T_s}{J} \\ N_3 = -1 - \frac{(1-A_2)T_s(k_2 T_s - k_1) - A_1 k_r T_s}{J} \\ M_1 = -3J + T_s k_1 + A_1 k_r T_s \\ M_2 = 3J + T_s(k_2 T_s - 2k_1) - 2A_1 k_r T_s + \frac{A_1 k_r T_s k_1}{J} \\ M_3 = -J - T_s(k_2 T_s - k_1) + A_1 k_r T_s + \frac{A_1 k_r T_s(k_2 T_s - k_1)}{J} \end{cases} \quad (7.33)$$

According to the results of (7.33), k_1 and k_2 have impacts on the stability of the system, so when $k_2 = 23,000$, $k_1 = 50, 100$ and 200 , the root locus on Δ can be described as shown in Fig. 7.3. If the root locus is inside the unit circle, the control strategy will be considered as a stable algorithm. From Fig. 7.3, if $k_1 = 50$, only $|\Delta| < 0.268$ should be needed. Similarly if $k_1 = 100$ and 200 , $|\Delta| < 0.677$ and $|\Delta| < 0.13$ should be satisfied, respectively. In practical applications, k_1 should be chosen according to the mismatch, in order to meet the stability requirement.

When $k_1 = 100$, $k_2 = 23,000, 33,000$ and $43,000$, the root locus on Δ can be obtained as shown in Fig. 7.4. From Fig. 7.4, if $k_2 = 23,000$, only $|\Delta| < 0.677$ will be

Fig. 7.3 Root locus on different values of k_1 when $k_2 = 23,000$

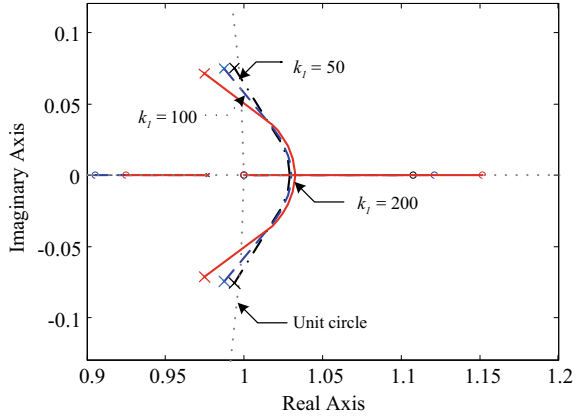
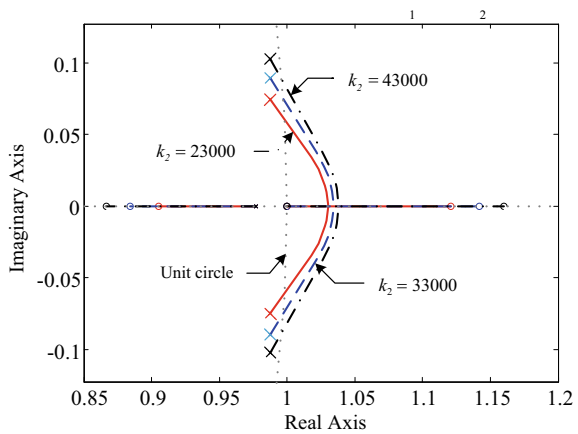


Fig. 7.4 Root locus on different values of k_2 when $k_1 = 100$



needed. Similarly if $k_2 = 33,000$, just $|\Delta| < 0.548$, If $k_2 = 43,000$, just $|\Delta| < 0.452$. In summary, selecting suitable values of k_1 and k_2 can make models which are at different mismatch levels stable.

7.4 Simulation and Experimental Evaluation

7.4.1 Simulation Results

The direct-drive permanent magnet traction system without the weight transducer by using PI, MPC with and without using the proposed offset-free strategy as the speed loop regulator during the elevator startup is simulated by MATLAB/Simulink, respectively. Parameters of permanent magnet traction machine are shown in Table

4.1. The control parameters are as follows: $P = 4$, $\alpha_m = 0.97$, $\alpha_r = e^{-5}$ s, $q_1 = 12$, $q_2 = 9$, $q_3 = 6$, $q_4 = 3$, $r = 0.1$. The speed loop PI regulator parameters are $k_{pw} = 35$, $k_{iw} = 100$, which are designed optimally.

Figures 7.5 and 7.6 show the simulation results under 50% and 100% rated load, respectively. Among them, the incremental count value (INC) is got through a 2048-bit incremental encoder established in Simulink. The relationship between sliding distance and INC is $d = 0.15 \times INC$ (mm).

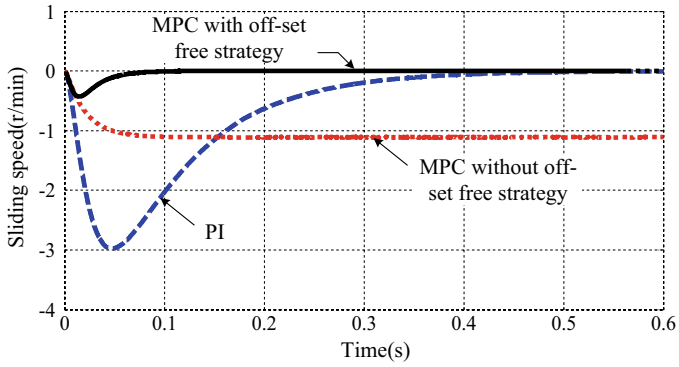
As can be seen from Fig. 7.5, under 50% rated load, the maximum sliding speed of the offset-free MPC is 0.4r/min, and the sliding distance is 0.15 mm. In contrast, the maximum sliding speed of PI control reaches 3r/min, and the sliding distance is 4.65 mm. The sliding speed of MPC without using offset-free strategy has a steady-state error, which is 1.1r/min, and the sliding distance increases with time. From Fig. 7.6, under rated load, the maximum sliding speed of the offset-free MPC is 0.9r/min, and the sliding distance is 0.30 mm. In contrast, the maximum sliding speed of PI control reaches 6r/min, and the sliding distance is 9.45 mm. The sliding speed of MPC without using offset-free strategy has a steady-state error, which is 2.1r/min, and the sliding distance increases when time goes on. By contrast, the sliding speed of proposed offset-free MPC is the smallest, and the regulating time is the shortest. Additionally the steady-state speed has no error. Because the response speed of the q -axis current using offset-free MPC is faster than other two methods, the maximum sliding speed is reasonably small. Therefore, the sliding distance can be reduced.

As can be seen from Figs. 7.5c and 7.6c, the response speed of offset-free MPC is faster than PI and the conventional MPC without offset-free strategy. In order to reduce the sliding distance during the elevator startup, the proportional of PI should be selected as large as possible. But the large proportional will cause overshoot and mechanical vibration. So the proportional cannot be that large. However, the equivalent gain of MPC can be large when the input is small.

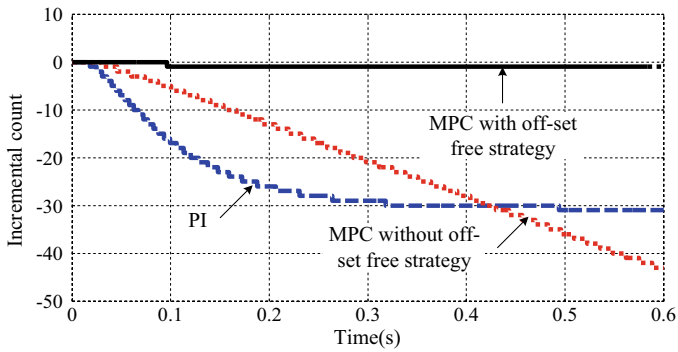
Therefore, the response is faster than PI. During the dynamic period when the q -axis current rises fast, the model corrector comes into use. So the q -axis current of offset-free MPC generated from the corrected model contains the equivalent composite disturbance compensation, but the conventional MPC does not. Therefore, the response speed of offset-free MPC is faster. During the steady-state period, the q -axis current is generated by the offset-free MPC with model corrector. However, the q -axis current of the conventional MPC equals the equivalent current of composite disturbance. But it is generated by the continuous steady-state speed error which should be prevented.

7.4.2 Experimental Results

The proposed anti-rollback control strategy was verified on an 11.7 kW elevator traction machine using a commercial inverter. The traction machine parameters used in the experiment are the same as simulation parameters as shown in Table 4.1.



(a)



(b)

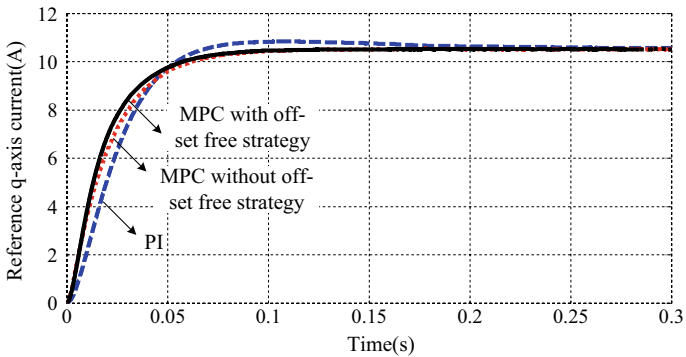
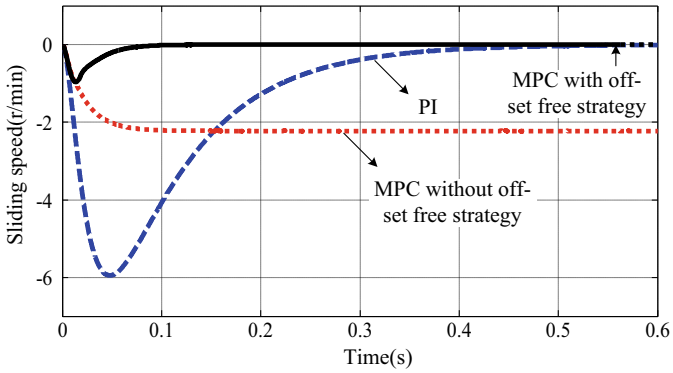
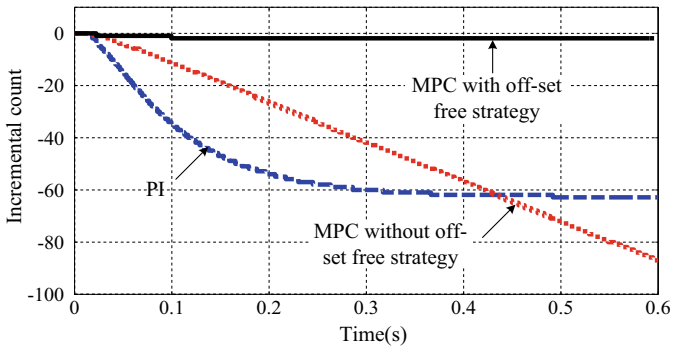


Fig. 7.5 Simulation results under 50% rated load. **a** Comparison of the sliding speed. **b** Comparison of the incremental count. **c** Comparison of the generated q -axis current reference



(a)



(b)

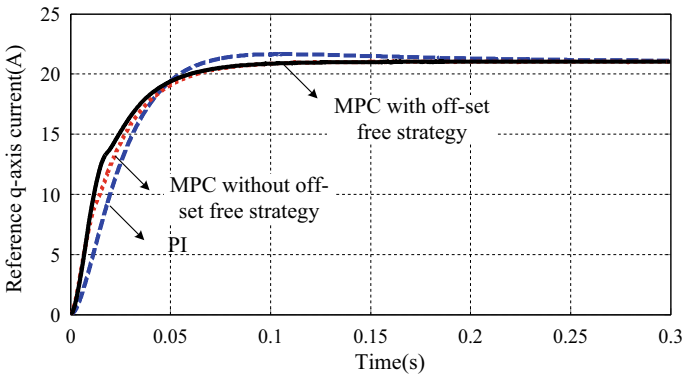


Fig. 7.6 Simulation results under 100% rated load. **a** Comparison of the sliding speed. **b** Comparison of the incremental count. **c** Comparison of the generated *q*-axis current reference

The whole control algorithm is executed by a TMS320F2808 DSP chip. The clock frequency is 150 MHz. And the event manager is used to generate 6 drive signals to control 6 IPMs. The type of IPMs is PM75RSE120. The PWM frequency of three-phase inverter is 10 kHz, and the control period of current loop is 100. The control period of speed loop is 1 ms. In experiments, $P = 4$, $\alpha_m = 0.97$, $\alpha_r = e^{-5}$, $q_1 = 12$, $q_2 = 9$, $q_3 = 6$, $q_4 = 3$, $r = 0.1$. Parameters of the speed PI regulator ($k_{pw} = 35$ and $k_{iw} = 100$) have been regulated to the best, which means they do not cause vibration in the steady state and can make the response of speed loop and current loop as fast as possible, in order to reduce the sliding distance. The HEIDENHAIN ERN 1387 Sin-Cos encoder with a resolution of 2048 was installed on the machine. Only the incremental signals were used for the anti-rollback control, and the Sin-Cos signals were just used for comparing the sliding distance.

Firstly, an experiment using MPC without using offset-free strategy as the speed regulator under 60% rated load was carried out. The experimental result is shown in Fig. 7.7. In steady state, the traction machine is still sliding at the speed of 2.9r/min. This kind of continuous sliding speed has been verified in simulation. As can be seen, the sliding speed is that large. And it is not allowed during the zero-servo operation because the elevator car keeps sliding.

Fig. 7.7 Experimental result using MPC without offset-free strategy under 60% rated loads. **a** The experimental result. **b** The detailed waveforms in the steady state

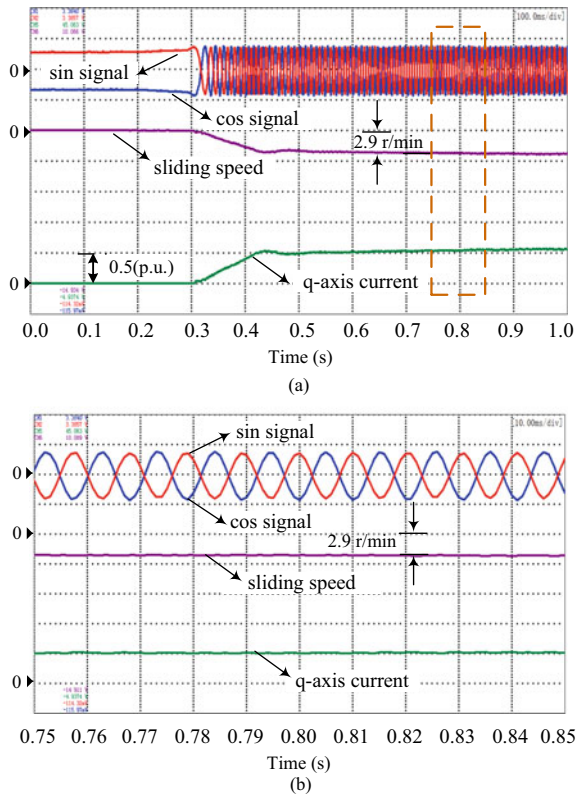
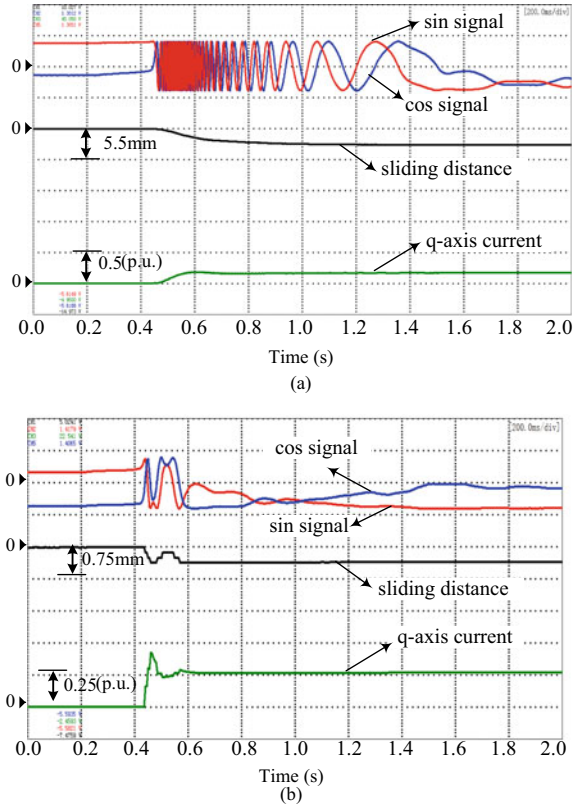


Fig. 7.8 Experimental comparison of the two methods under 20% rated load. **a** PI speed regulator. **b** Offset-free MPC



Under the same experimental conditions, the experimental results of the PI speed regulator and the offset-free MPC are compared. Figures 7.8, 7.9 and 7.10 show the experimental results under 20%, 60% and 100% of rated load, respectively. As can be seen, under 20% of rated load, the sliding distance with PI speed regulator is 2.85 mm, the sliding distance with offset-free MPC is only 0.45 mm.

Under 60% of rated load, the sliding distance with PI speed regulator is 5.20 mm, the sliding distance with offset-free MPC is only 1.35 mm. Under 100% of rated load, the sliding distance with PI speed regulator is 8.25 mm, the sliding distance with offset-free MPC is only 1.5 mm. In summary, using the proposed offset-free MPC can get much shorter sliding distance, shorter regulating time, smaller sliding speed and better riding comfort.

From experimental results, the proposed offset-free MPC has a good performance with a fast response, no mechanical vibration and no steady-state speed error. During the dynamic regulating period, the q -axis current rises fast because of characteristics of the MPC strategy and the model corrector. Because of the model corrector, the steady-state speed error is prevented. So the maximum sliding speed and sliding distance are both small.

Fig. 7.9 Experimental comparison of the two methods under 60% rated load. **a** PI speed regulator. **b** Offset-free MPC

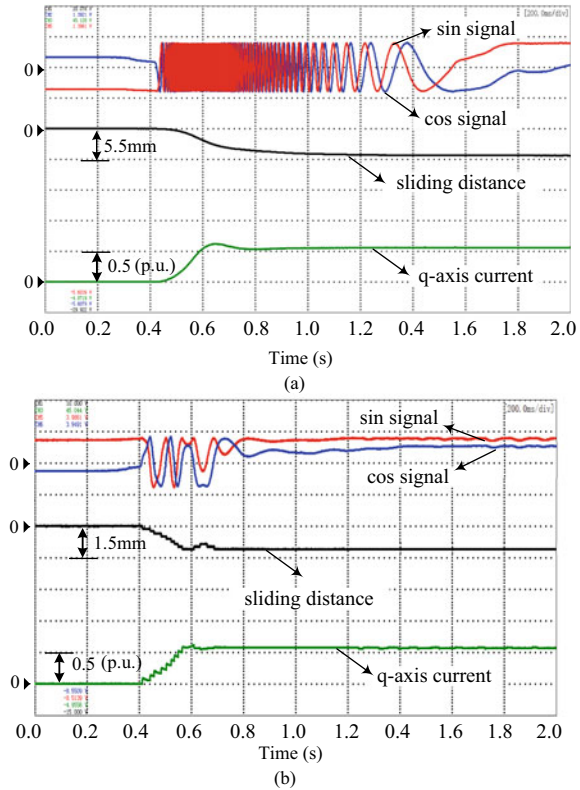


Figure 7.11 shows the comparison between the PI speed regulator and the proposed offset-free MPC under different loads. From Fig. 7.11, the sliding distances of the proposed method are much shorter than those of PI speed regulator under different loads. Therefore, the proposed method can effectively solve the key technical issue on weight-transducerless direct-drive permanent magnet traction machine system during the elevator startup.

7.5 Summary

This chapter proposed a weight-transducerless anti-rollback torque control strategy based on offset-free MPC of direct-drive elevator traction machine which can properly work with an incremental encoder. The control strategy can overcome the mismatch between the predictive model and the real system caused by the nonlinear changing load characteristics when the brake is released and enhanced the capability of balancing uncertain load torque. The estimated speed value obtained from model correction block used as the initial value of the predictive speed can reduce

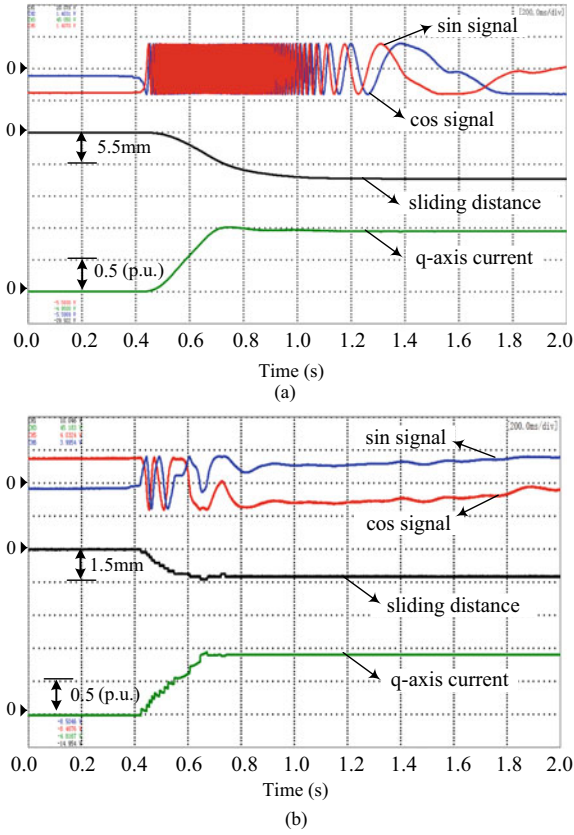


Fig. 7.10 Experimental comparison of the two methods under 100% rated load. **a** PI speed regulator. **b** Offset-free MPC

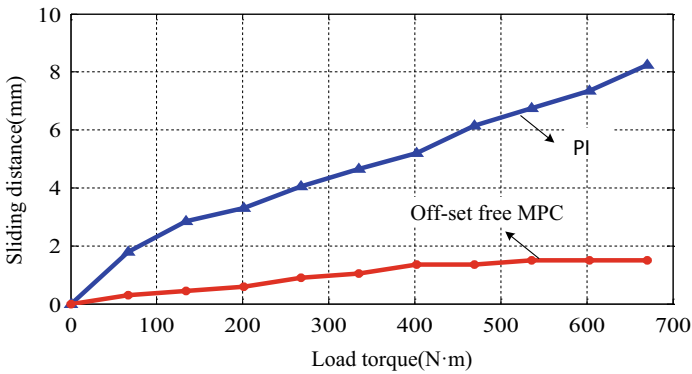


Fig. 7.11 Sliding distance comparison of the two methods under different loads

the computational amount of cost function. Instead of using the conventional PI as the speed regulator, the offset-free MPC can effectively improve the dynamic performance and provide the torque control signal without weight transducer so as to improve the robustness of the system. Significantly, it can achieve a shorter sliding distance, as well as a smaller sliding speed without steady-state error during the zero-servo operation. Therefore, the riding comfort can be improved when the elevator converts from standby mode to running mode. Both simulation and experimental results verify the effectiveness of the proposed anti-rollback control method.

References

1. Leu VQ, Choi HH, Jung J (2012) Fuzzy sliding mode speed controller for PM synchronous motors with a load torque observer. *IEEE Trans Power Electron* 27(3):1530–1539
2. Euntai K, Sungryul L (2005) Output feedback tracking control of MIMO systems using a fuzzy disturbance observer and its application to the speed control of a PM synchronous motor. *IEEE Trans Fuzzy Syst* 13(6):725–741
3. Grignon D, Chen X, Kar N, Qian H (2014) Estimation of load disturbance torque for DC motor drive systems under robustness and sensitivity consideration. *IEEE Trans Ind Electron* 61(2):930–942
4. Wang G, Zhang G, Yang R, Xu D (2012) Robust low-cost control scheme of direct-drive gearless traction machine for elevators without a weight transducer. *IEEE Trans Ind Appl* 48(3):996–1005
5. Hong X, Deng Z, Wang S, Hang L, Li W, Lu Z (2010) A novel elevator load torque identification method based on friction mode. In: Proc. 25th annu. IEEE APEC, pp 2021–2024
6. Bolognani S, Faggion A, Sgarbossa L, Peretti L (2007) Modelling and design of a direct-drive lift control with rope elasticity and estimation of starting torque. In: Proc. 33rd annu. IEEE IECON, pp 828–832
7. Wang G, Xu J, Li T, Zhang G, Zhan H, Ding L, Xu D (2014) Weight-transducerless starting torque compensation of gearless permanent-magnet traction machine for direct-drive elevators. *IEEE Trans Ind Electron* 61(9):4594–4604
8. Guzman H, Barrero F, Duran MJ (2015) IGBT-gating failure effect on a fault-tolerant predictive current-controlled five-phase induction motor drive. *IEEE Trans Ind Electron* 62(1):15–20
9. Choi D, Lee K (2015) Dynamic performance improvement of AC/DC converter using model predictive direct power control with finite control set. *IEEE Trans Ind Electron* 62(2):757–767
10. Zhao D, Liu C, Stobart R, Deng J, Winward E, Dong G (2014) An explicit model predictive control framework for turbocharged diesel engines. *IEEE Trans Ind Electron* 61(7):3540–3552
11. Wang G, Qi J, Xu J et al (2015) Antirollback control for gearless elevator traction machines adopting offset-free model predictive control strategy. *IEEE Trans Industr Electron* 62(10):6194–6203

Chapter 8

Enhanced MPC for Rollback Mitigation During Elevator Startup



8.1 Introduction

Various advanced control strategies have been proposed to optimize the speed-control performance and enhance the robustness against unknown disturbance [1–4]. However, the weight-transducerless control for anti-rollback of elevator car should consider special requirements of riding comfort. Recently, some novel solutions have been proposed [5–8]. In [9], through evaluating the rate of change of speed by the quadratic error comparison, the load torque can be calculated accurately according to the established mechanical model. In [10], a novel torque control strategy based on the friction model of traction system was described as a searching logic. In [11], the load torque was traced by the compensation torque calculated by dichotomy and staircase algorithms, respectively. However, mechanical vibration is difficult to be avoided due to the sudden change of torque reference. In [12], an accurate speed measurement method for Sin-Cos encoder was introduced, and a feedforward compensation strategy adopting load torque observer was proposed to improve the performance of elevators. In [13], an adaptive torque compensation strategy based on fuzzy self-tuning of the rate of change of electromagnetic torque was proposed. And the accurate subdivided position information based on Sin-Cos encoder is needed. However, for the elevator installed with an ordinary-resolution encoder, the performance of this control strategy will deteriorate.

Therefore, the weight-transducerless starting torque control strategy using ordinary-resolution encoders becomes a key technique of modern elevator applications. This kind of control strategy should have the function of rollback mitigation, which means that it can provide a smooth startup with little sliding distance and acceptable mechanical vibration. Since the rollback mitigation control should be accomplished in a very short time to balance the uncertain and nonlinear load torque, the preferred control method should have good dynamic performance. Model predictive control (MPC) can get a faster response by adjusting parameters of the trajectory function. In addition, MPC also has advantages, such as small overshoot and high control accuracy. It has been successfully applied in motor drives, power converters

and other industry applications. Considering the characteristics of MPC, it can be a potential approach for anti-rollback control of weight-transducerless elevators.

But the conventional MPC speed controller is difficult to achieve high-performance control of the elevator starting torque. During the brake releasing, the near-zero speed is difficult to be calculated from ordinary-resolution encoder. And the uncertain disturbance caused by the nonlinear change of braking torque will lead to the mismatch of predictive model. This kind of model mismatch will cause inaccurate prediction and speed error at steady state. The active disturbance rejection control (ADRC) can attribute the uncertainty factors of the plant to unknown disturbance which can be calculated. Nowadays, ADRC has been successfully applied in power electronics and electrical drives [14]. ADRC mainly consists of the nonlinear tracking differentiator (NTD), the extended state observer (ESO) and the regulating law. ESO has excellent dynamic performance, which can quickly trace the change of unknown disturbance without accurate mathematical disturbance model. And NTD can effectively extract continuous signal and differential signal from non-continuous input signal [15]. Therefore, the combination of advantages of ADRC and MPC can achieve high-performance control of direct-drive elevators.

In this chapter, a novel rollback mitigation control strategy adopting enhanced MPC with an ESO and a NTD is proposed to enhance the riding comfort of the weight-transducerless elevator installed with an ordinary-resolution encoder [16]. And the proposed method can improve the dynamic and steady performance without requiring the weight information of passengers during the brake releasing process. The torque current reference can trace the uncertain load more quickly because of the speed MPC involved. Additionally, the ESO can eliminate the steady-state speed error caused by the conventional speed MPC strategy, which is critical for anti-rollback control of weight-transducerless elevator drive. Especially, the accurate speed feedback can be acquired from the NTD to enhance the rollback mitigation. The external disturbance information obtained by the ESO is added into the predictive model to match the model in each sampling period.

8.2 Analysis of the Conventional MPC

According to [17], the conventional MPC is illustrated, in order to explain the drawbacks of conventional MPC during the zero-speed operation. The mechanical model of the traction machine is expressed in Laplace domain,

$$\omega_f(s) = \frac{T_e(s) - T_d(s)}{Js + B} \quad (8.1)$$

where ω_f is the angular speed feedback generated from the raw speed, T_d represents all uncertain disturbances including the influence of the rigidity and damper of rope, B is the friction factor, and s is the Laplace operator. The disturbance T_d is usually

ignored in the conventional predictive model. After zero-order-hold discretization of (8.1) and iteration, the discrete predictive model can be expressed as

$$\begin{aligned} \omega_m(k+n) = & K_m(1-\alpha_m)(1+\alpha_m+\dots+\alpha_m^{n-1})i_q^*(k) \\ & + \alpha_m^n \omega_m(k), \quad n = 1, 2, \dots, P \end{aligned} \quad (8.2)$$

where $\omega_m(k+n)$ represents the predictive angular speed at time $k+n$, $K_m = K_{to}/J_o$, $K_{to} = 1.5n_p\psi_f$, n_p is the number of pole pairs, ψ_f is the rotor flux, J_o is the nominal values of the total inertia and $\alpha_m = \exp(B_o T_s/J_o)$, B_o is the nominal values of the friction factor, T_s is the sampling period, P is the predictive step, i_q^* is the reference q -axis current. However, i_q is replaced by i_q^* in (8.2). Therefore, the outputs of the predictive model at time $k, k+1, k+2 \dots k+P$ can be converted into a matrix form as follows:

$$\mathbf{W}_m(k) = \mathbf{W}_f(k) + \mathbf{W}_s(k)i_q^*(k), \quad (8.3)$$

$$\begin{cases} \mathbf{W}_m(k) = [\omega_m(k+1) \dots \omega_m(k+P)]^T \\ \mathbf{W}_f(k) = [\alpha_m \dots \alpha_m^P]^T \omega_f(k) \\ \mathbf{W}_s(k) = K_m(1-\alpha_m)[1 \dots 1 + \alpha_m \dots + \alpha_m^{P-1}]^T \end{cases}. \quad (8.4)$$

In this predictive control method, to some degree, the actual speed will be closer to the trajectory speed with a larger predictive step. But it will cause huge computation amount which cannot be executed completely in a limited control period. The reference trajectory and the cost function also affect the computation amount.

The first-order exponential function is chosen as the reference trajectory which is expressed as follows:

$$\omega_r(k+n) = \omega^*(k+n) - \alpha_r^n [\omega^*(k) - \omega(k)] \quad (8.5)$$

where ω_r is the reference trajectory and ω^* is the setpoint value, which is zero during the elevator startup. $\alpha_r = e^{-T_s/T_r}$, in which T_r is the time constant related to the desired response time. Considering the effect of the external disturbance and the noise, there will be an error between outputs of the predictive model and the real plant. Therefore, a corrector should be added into the predictive cost function. The predictive error e can be expressed as

$$e(k+P-1) = \dots = e(k+1) = e(k) = \omega_f(k) - \omega_m(k). \quad (8.6)$$

The second-order cost function J_p is chosen as follows:

$$J_p = [\mathbf{W}_r(k) - \mathbf{W}_m(k) - \mathbf{E}(k)]^T \times \mathbf{Q}[\mathbf{W}_r(k) - \mathbf{W}_m(k) - \mathbf{E}(k)] + R i_q^{*2} \quad (8.7)$$

where $\mathbf{Q} = \text{diag}[q_1^2 \dots q_p^2]$, $R = r^2$, $\mathbf{W}_r(k) = [\omega_r(k+1) \dots \omega_r(k+P)]^T$, $\mathbf{E}(k) = [e(k+1) \dots e(k+P)]^T$. $q_1, q_2 \dots q_p$ are the weight variables for predictive steps, R is the weight variable of the output current. Let $\partial J_p / \partial i_q^* = 0$, the output of the MPC controller can be obtained

$$i_q^*(k) = (\mathbf{W}_s^T \mathbf{Q} \mathbf{W}_s + R)^{-1} \mathbf{W}_s \mathbf{Q} [\mathbf{W}_a(\omega^*(k) - \omega_f(k)) - \mathbf{W}_b \omega_m(k)] \quad (8.8)$$

where $\mathbf{W}_a(k) = [(1 - \alpha_r) \dots (1 - \alpha_r^P)]^T$, $\mathbf{W}_b(k) = [(1 - \alpha_m) \dots (1 - \alpha_m^P)]^T$, and $i_q^*(k)$ is used as the q -axis reference current of the PI current regulator.

From (8.8), during the elevator startup, ω^* should be set as zero. If the conventional MPC works well, ω_f and ω_m should converge to zero. Then, the elevator car can maintain standstill during the zero-servo operation. If all the conditions analyzed above are met, $i_q^*(k)$ will be zero since MPC is equivalent to a proportional controller. But if $i_q^*(k)$ equals zero, the electromagnetic torque generated by $i_q^*(k)$ cannot balance the disturbance torque. The sliding speed ω_f would not be zero. So, it is a self-contradiction.

Therefore, the real situation is that the sliding speed ω_f , which is a fixed value during the zero-servo operation, maintains the output of electromagnetic torque to balance the disturbance torque. The conventional MPC is not suitable to regulate the speed loop during the elevator startup.

8.3 Establishment of the Enhanced MPC Speed Controller

To overcome the drawbacks of the conventional MPC, an enhanced MPC is proposed, and the scheme is shown in Fig. 8.1. The enhanced MPC strategy is used instead of the conventional PI regulator in the speed loop. Additionally, the NTD is used to improve the precision of the speed feedback. The precise speed feedback information is used in trajectory and ESO blocks to generate the speed trajectory and the

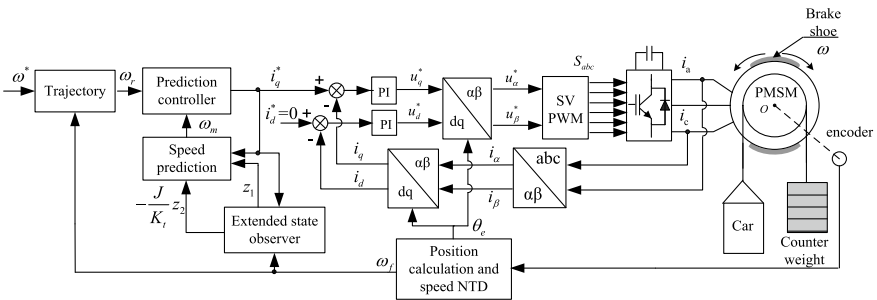


Fig. 8.1 Scheme of enhanced model predictive control strategy for traction machine to mitigate rollback during elevator startup

disturbance information, respectively. And the disturbance information is used in the speed prediction. The angular speed trajectory and predictive speeds are used as the inputs of the prediction controller. After calculation, the q -axis current reference is generated to control the electromagnetic torque.

MPC will cause relatively large steady-state error, if the disturbance is intense and unknown. So, the ESO scheme is designed to mitigate the negative effects caused by the unknown external disturbance and reduce the sliding distance. The receding optimization can enhance the robustness against load disturbance during the elevator startup process.

In order to consider and analyze the influence of coefficient mismatch and disturbance, (8.1) can be changed into (8.9)

$$\dot{\omega}_f(t) = \frac{K_{to} + K_{t\Delta}}{J_o + J_\Delta} i_q^*(t) - \frac{B_o + B_\Delta}{J_o + J_\Delta} \omega_f(t) - \frac{T_d(t)}{J_o + J_\Delta} \quad (8.9)$$

where $K_{t\Delta}$ is the mismatch error of K_{to} , J_Δ and B_Δ are the mismatch errors of the total inertia and the friction factor, J_o and B_o are the nominal values of the inertia and the friction factor, respectively. In order to obtain the predictive state equation, (8.9) can be expressed as follows:

$$\begin{cases} \dot{\omega}_f(t) = \frac{K_{to}}{J_o} i_q^*(t) - \frac{B_o}{J_o} \omega_f(t) - \frac{K_{t\Delta}}{J_o} i_{qd}(t) \\ i_{qd}(t) = -\frac{T_d(t)}{K_{to}} + \frac{K_{t\Delta}}{K_{to}} i_q^*(t) - \frac{B_\Delta}{K_{to}} \omega_f(t) - \frac{J_\Delta}{K_{to}} \dot{\omega}_f(t) \end{cases} \quad (8.10)$$

where i_{qd} includes the equivalent current of uncertain disturbance torque T_d and the mismatch error of both the inertia and the friction factor. The estimated value of i_{qd} can be generated by ESO, so the mismatch of the predictive model can be compensated. During the elevator startup, the uncertain disturbance torque exerting on the traction sheave can be traced accurately and quickly. After zero-order-hold discretization of (8.10) and iteration, it can be expressed as

$$\begin{aligned} \omega_m(k+n) &= K_m(1-\alpha_m)(1+\alpha_m+\dots+\alpha_m^{n-1}) [i_q^*(k) - i_{qd}(k)] \\ &+ \alpha_m^n \omega_m(k), \quad n = 1, 2, \dots, P \end{aligned} \quad (8.11)$$

In (8.11), the disturbance has been considered in the predictive model, which is different from (8.2). The uncertain disturbance torque can be treated as a constant because of short sampling period. Therefore, the estimated disturbance and speed generated from ESO can be utilized to adjust the predictive model during each sampling period, thus enhancing robustness against the uncertain disturbance torque.

The disturbance affecting the output can be extended into a new state by using ESO. In other words, the ESO is established to obtain this new state by a special feedback structure. It does not depend on the specific mathematical model to obtain the disturbance information and does not need to measure its effect directly. According

to these characteristics, it is suitable and practical to use ESO to estimate the equivalent load torque of traction machine during the elevator converts from standby mode to running mode.

According to (8.10), the ESO can be established as follows:

$$\begin{cases} \dot{z}_1(t) = z_2(t) + \alpha_{01}(\omega_f(t) - z_1(t)) + \frac{K_{to}}{J_o}i_q^*(t) - \frac{B_o}{J_o}\omega_f(t) \\ \dot{z}_2(t) = \alpha_{02}(\omega_f(t) - z_1(t)) \end{cases} \quad (8.12)$$

where z_1 and z_2 are two variables of the ESO, α_{01} and α_{02} are parameters of the ESO, $z_1(t) \rightarrow \omega_f(t)$ and $z_2(t) \rightarrow -K_{to}i_{qd}(t)/J_o$. Therefore, the equivalent current component of disturbance torque i_{qd} and the initial predictive speed can be obtained. After discretization of (8.12), it can be expressed as

$$\begin{cases} z_1(k+1) = (1 - T_s\alpha_{01})z_1(k) + T_s(z_2(k) + (\alpha_{01} - \frac{B_o}{J_o})\omega_f(k) + \frac{K_{to}}{J_o}i_q^*(k)) \\ z_2(k+1) = z_2(k) + T_s\alpha_{02}(\omega_f(k) - z_1(k)) \end{cases} \quad (8.13)$$

Then in (8.11), $\omega_m(k)$ and $i_{qd}(k)$ are replaced by $z_1(k)$ and $-J_o z_2(k)/K_{to}$, respectively. The initial value of predictive speeds within the predictive step P can be rolling corrected during each sampling period, so (8.14) can be obtained

$$\begin{aligned} \omega_m(k+n) &= K_m(1 - \alpha_m)(1 + \alpha_m + \dots + \alpha_m^{n-1}) \\ [i_q^*(k) + \frac{J_o}{K_{to}}z_2(k)] + \alpha_m^n z_1(k), \quad n = 1, 2, \dots, P. \end{aligned} \quad (8.14)$$

Therefore, the outputs of the predictive model at time $k, k+1, k+2 \dots k+P$ can be converted into a matrix form as follows:

$$\mathbf{W}_m(k) = \mathbf{W}_f(k) + \mathbf{W}_s(k) \begin{bmatrix} i_q^*(k) + \frac{J_o}{K_{to}}z_2(k) \end{bmatrix} \quad (8.15)$$

In the ESO, the initial predictive speed has been corrected at each sampling time. So, the function of correcting the initial predictive speed can be eliminated, which can effectively reduce the computational burden. Moreover, the predictive error caused by the disturbance has been corrected in the predictive model. There is no need correcting it in the cost function anymore like (8.7). If the third order or above is used in the cost function, the computational process would be too complicated. And the processor may not complete the computation in the fixed time. But the first order cannot meet the requirement of fast response. The second-order cost function of the enhanced MPC is chosen as follows:

$$J_P = [\mathbf{W}_r(k) - \mathbf{W}_m(k)]^T \mathbf{Q}[\mathbf{W}_r(k) - \mathbf{W}_m(k)] + R i_q^{*2} \quad (8.16)$$

Let $\partial J_p / \partial i_q^* = 0$, the output of the enhanced model predictive controller can be obtained

$$i_q^*(k) = (\mathbf{W}_s^T \mathbf{Q} \mathbf{W}_s + R)^{-1} \mathbf{W}_s^T \mathbf{Q} \left[\mathbf{W}_r(k) - \mathbf{W}_f(k) + \mathbf{W}_s \frac{J_o}{K_{to}} z_2(k) \right] \quad (8.17)$$

Additionally, there should be some variable constraints in the enhanced controller. Let I_{qo} represent the rated value of i_q . Therefore, $-I_{qo} \leq i_q^* \leq I_{qo}$ should be met. To avoid the intense vibration, $-15\%I_{qo} \leq i_q^*(k) - i_q^*(k-1) \leq 15\%I_{qo}$ should be met. And to improve the robustness, ω_m should be restricted to a scale from $-10\%\omega_{mo}$ to $10\%\omega_{mo}$ where ω_{mo} is the nominal value of the mechanical angular velocity.

8.4 Stability Analysis and Parameter Selection of the ESO

In this section, the stability of the proposed method is analyzed first, because many variables are involved and the design is relatively complicated. To begin with, let $I_{qd}(t) = -K_{to}i_{qd}(t)/J_o$ to simplify the arithmetic and show the process clearly. Because the sliding speed ω_f and B are relatively small, $B_o\omega_f(t)/J_o$ can be ignored when analyzing the stability. Then, (8.10) can be rearranged into the state form

$$\begin{bmatrix} \dot{\omega}_f(t) \\ \dot{i}_{qd}(t) \end{bmatrix} = \begin{bmatrix} 0 & 1 \\ 0 & 0 \end{bmatrix} \begin{bmatrix} \omega_f(t) \\ i_{qd}(t) \end{bmatrix} + \begin{bmatrix} \frac{K_{to}}{J_o} i_q^*(t) \\ c(t) \end{bmatrix} \quad (8.18)$$

where $c(t)$ is the rate of change of $i_{qd}(t)$, and (8.5) can be written as the state form

$$\begin{bmatrix} \dot{z}_1(t) \\ \dot{z}_2(t) \end{bmatrix} = \begin{bmatrix} -\alpha_{01} & 1 \\ -\alpha_{02} & 0 \end{bmatrix} \begin{bmatrix} z_1(t) \\ z_2(t) \end{bmatrix} + \begin{bmatrix} \alpha_{01} & 1 \\ \alpha_{02} & 0 \end{bmatrix} \begin{bmatrix} \omega_f(t) \\ 0 \end{bmatrix} + \begin{bmatrix} \frac{K_{to}}{J_o} i_q^*(t) \\ c(t) \end{bmatrix} \quad (8.19)$$

By subtracting (8.18) from (8.19), the error equation can be obtained

$$\begin{bmatrix} \dot{z}_1(t) - \dot{\omega}_f(t) \\ \dot{z}_2(t) - \dot{i}_{qd}(t) \end{bmatrix} = \begin{bmatrix} -\alpha_{01} & 1 \\ -\alpha_{02} & 0 \end{bmatrix} \begin{bmatrix} z_1(t) - \omega_f(t) \\ z_2(t) - i_{qd}(t) \end{bmatrix} \quad (8.20)$$

Let $\begin{cases} e_1(k) = z_1(k) - \omega_f(k) \\ e_2(k) = z_2(k) - i_{qd}(k) \end{cases}$, $e = \begin{bmatrix} e_1(t) \\ e_2(t) \end{bmatrix}$, then

$$\dot{e} = \begin{bmatrix} -\alpha_{01} & 1 \\ -\alpha_{02} & 0 \end{bmatrix} e. \quad (8.21)$$

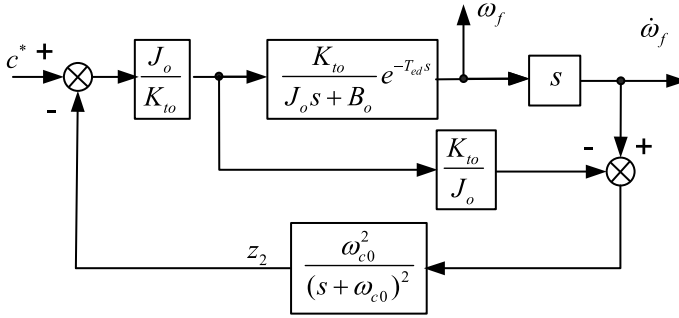


Fig. 8.2 Equivalent structure of the extended state observer

According to Routh–Hurwitz criterion, if $\alpha_{01} > 0$ and $\alpha_{02} > 0$, the ESO is stable. So if these parameters are chosen suitably, the system can be stable and makes $z_1 \rightarrow \omega_f$ and $z_2 \rightarrow i_{qd}$ fast.

In order to facilitate the analysis, the ESO parameters are selected as $\alpha_{01} = 2\omega_{c0}$, $\alpha_{02} = \omega_{c0}^2$, in which ω_{c0} is the bandwidth of the ESO. According to (8.12), the structure of the ESO can be described as an internal model control structure, which is shown in Fig. 8.2. The model of ESO is equivalent to the differential of the real plant. Therefore, the transfer function of the plant model is obtained

$$G_p(s) = \frac{K_{to}s}{J_o s + B_o} e^{-T_{ed}s} \quad (8.22)$$

where T_{ed} is the equivalent delay time mainly caused by speed sampling, low-pass filter and digital control delay. The relevant part of the model can be expressed as

$$G_m(s) = \frac{K_{to}}{J_o}. \quad (8.23)$$

The transfer functions of the controller and the extended state conversion can be, respectively, described as

$$G_{imc}(s) = \frac{J_o}{K_{to}}, \quad (8.24)$$

$$F_{imc}(s) = \frac{\omega_{c0}^2}{(s + \omega_{c0})^2}. \quad (8.25)$$

From (8.22) to (8.25), the multiplicative uncertainty expression and the complementary sensitivity function are shown as follows:

$$M(s) = \frac{G_p}{G_m} - 1 = \frac{J_o s}{J_o s + B_o} e^{-T_{ed}s} - 1, \quad (8.26)$$

$$\delta(s) \approx G_m \cdot G_{imc} \cdot F_{imc} = \frac{\omega_{c0}^2}{(s + \omega_{c0})^2}. \quad (8.27)$$

To guarantee the robustness of internal model control, the condition should be met

$$\|\delta(\omega)M(\omega)\|_\infty = \sup_\omega |\delta(\omega)M(\omega)| < 1. \quad (8.28)$$

Substitute (8.26) and (8.27) into (8.28), then the result can be obtained

$$\sup_\omega |\delta(s)M(s)| = \sup_\omega \left| \frac{\omega_{c0}^2}{(j\omega + \omega_{c0})^2} \left[\frac{J_o j\omega}{J_o j\omega + B_o} e^{-T_{ed}j\omega} - 1 \right] \right| < 1. \quad (8.29)$$

According to (8.27), as ω_{c0} increases, the bandwidth of $\delta(\omega)$ extends to high frequency. The possibility that $\sup_\omega |\delta(\omega)M(\omega)|$ becomes greater than 1 will increase, which means the stability of the system will deteriorate. The equivalent delay time T_{ed} of the observer can be expressed in Bode diagram graphically. When T_{ed} is equal to 0.001, 0.005 and 0.03, respectively, the Bode diagram of $M(\omega)$ is shown in Fig. 8.3. As T_{ed} increases, the frequency of peak amplitude of $M(\omega)$ reduces. Therefore, the possibility of $\sup_\omega |\delta(\omega)M(\omega)|$ becoming greater than 1 will increase, which means the stability of the system will also deteriorate.

It is necessary to take the performance requirements, the stability of ESO and the quick adjustment, together into consideration when choosing ω_{c0} and T_{ed} . Therefore, when selecting ω_{c0} , both the convergence speed and the stability of the ESO should be considered. If ω_{c0} is relatively large, the convergence speed of ESO increases, but the stability of the system will be impaired. Therefore, based on the requirements of the real plant, the parameter ω_{c0} needs to be carefully adjusted. Additionally, T_{ed} is mainly decided by speed sampling method and raw speed processing method. Usually, the sampling period is fixed, so it is important to adopt a suitable raw speed processing method.

8.5 Application of the NTD in Speed Sampling

Based on the analysis above, the equivalent delay time T_{ed} significantly affects the stability of the ESO. Therefore, T method and M/T method are difficult to be used in speed detection because of variable speed sampling time. Additionally, the sliding speed during the elevator startup is relatively small when the starting torque control algorithm performs effectively. Conventionally, the raw speed signal is obtained by using M method. Then, the speed feedback can be got after processing the raw speed through a low-pass filter. However, the speed feedback not only contains noise and vibration, but also has a large time delay caused by the filter. Under the circumstances

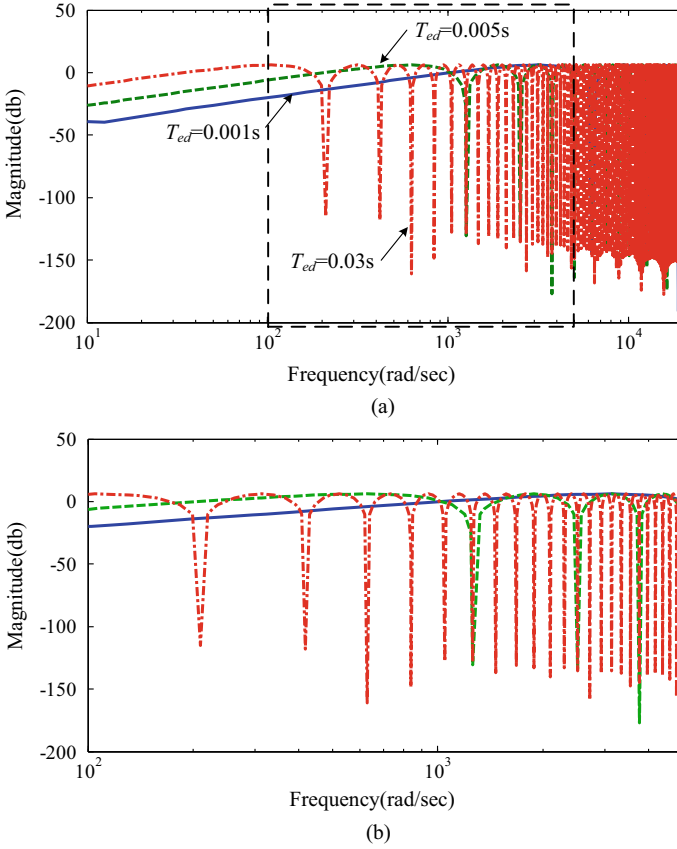


Fig. 8.3 Influence of the equivalent filter parameters on $M(\omega)$. **a** The Bode diagram. **b** The magnified Bode diagram

of rollback mitigation requiring accurate adjustment, these disadvantages will obviously deteriorate the control performance and cause mechanical vibration at steady state.

Nonlinear tracking differentiator was originally proposed by Prof. Han [18]. It can be used to extract continuous signals and differential signals from non-continuous signals. When the parameters are selected carefully, it has a shorter time delay and stronger noise suppression ability than the conventional low-pass filter. Therefore, this method can be used to process the raw speed signal as a high-performance filter.

The state equation of NTD can be expressed as follows:

$$\begin{cases} \omega_f(k+1) = \omega_f(k) + T_s \omega_d(k) \\ \omega_d(k+1) = \omega_d(k) + T_s nlf(\omega_f(k) - \omega(k), \omega_d(k), R, H_0) \end{cases} \quad (8.30)$$

where R is the convergence factor, H_o is the filtering factor, mainly affecting the filtering effect, ω_d is the rate of change of ω_f , ω is the raw speed, and the nonlinear function $nlf(\omega_f(k) - \omega(k), \omega_d(k), R, H_0)$ can be defined as follows:

$$nlf(\omega_f(k) - \omega(k), \omega_d(k), R, H_0) = - \begin{cases} R \text{sign}(A), & |A| > D \\ R \frac{A}{D}, & |A| \leq D \end{cases} \quad (8.31)$$

where

$$A = - \begin{cases} \omega_d(k) + \frac{A_0 - D}{2} \text{sign}(y), & |y| > D_0 \\ \omega_d(k) + \frac{y}{H_0}, & |y| \leq D_0 \end{cases}, \quad (8.32)$$

$$A_0 = \sqrt{D^2 + 8R|y|}, \quad (8.33)$$

$$y = \omega_f(k) - \omega(k) + H_0 \omega_d(k), \quad (8.34)$$

$$D_0 = H_0 D, \quad (8.35)$$

$$D = R H_0. \quad (8.36)$$

8.6 Analysis of Parameter Selection

(1) *Parameters of MPC*: The larger the predictive step P is, the longer the executive time of the control algorithm would become. Considering a fixed-point DSP-based commercial drive is used in the experiment, the predictive step is selected as 5, which can both ensure the predictive accuracy and reduce the computational burden. In terms of weight factor of each predictive step, it can be selected as large as possible on the premise that overshoot and strong vibrations should be avoided, and the weight factor reflects the importance of each step. Normally, the weight factor of the former step is larger than that of the latter one, because the former one is more precise than the latter one with the same i_q^* at the time k . The weight factor of i_q^* should be a little smaller considering the dynamics of the control strategy. If the weight factor of i_q^* is relatively large, the change of at each sampling time would be restricted to a small scale. The trajectory coefficients are selected according to how fast the actual speed approaching to the trajectory is expected.

(2) *Parameters of ESO*: According to the second-order system expression, the settling time t_s and the overshoot are the main dynamic performance factors. And the overshoot needs to be zero because of the requirement of the anti-rollback control. Therefore, only t_s is taken into account when choosing ω_{c0} . So using a unit step

disturbance as the input, and the response of (8.25) can be expressed as

$$F_{imc}(t) = 1 - \omega_{c0}t e^{-\omega_{c0}t} = 1 - (1 + \omega_{c0}t)e^{-\omega_{c0}t}. \quad (8.37)$$

According to the definition of the settling time, $|F_{imc}(t_s) - F_{imc}(\infty)| = \lambda$, where $F_{imc}(\infty) = 1$ and $\lambda \triangleq 2\%$, then the result can be got

$$(1 + \omega_{c0}t_s)e^{-\omega_{c0}t_s} = 0.02. \quad (8.38)$$

After calculation, the relation between t_s and ω_{c0} can be obtained

$$t_s = 5.85/\omega_{c0}. \quad (8.39)$$

However, considering there are some differences between the real system and the ideal one, design margins should be reserved to make the system be robust. So the equation below can be used to decide ω_{c0} ,

$$t_s = 15/\omega_{c0}. \quad (8.40)$$

(3) *Parameters of NTD*: Since R is the convergence factor, it determines the tracking performance of rotor speed. The larger R is, the better tracking ability is. But the high-frequency noise will be caused, if R is relatively large. According to [13], the scale of R can be selected from 500 to 1000 with no high-frequency noise existing. If the noise is contained in the output, the filtering factor H_o should be adjusted to reduce the influence of noise. On the premise that the tracking performance can be ensured, R should be selected as small as possible. Usually, the range of H_o can be from $0.00002R$ to $0.00004R$, which guarantees both the filter performance and time lag limitation.

8.7 Experimental Evaluation

8.7.1 Experimental Setup

The proposed rollback mitigation control strategy was verified on an 11.7 kW elevator traction machine using a commercial inverter. And the experimental platform is shown in Fig. 4.13, and a same type traction machine is mechanically connected to emulate the load of elevator car. Parameters of the permanent magnet traction machine used in the experiment are shown in Table 4.1. The PWM frequency of inverter is 10 kHz. The whole control algorithm is executed by a TMS320F2808 DSP chip. The control period of speed loop is 1 ms.

According to the analysis above, the parameters of enhanced MPC are selected in experiments as follows: $P = 5$, $\alpha_m = 0.98$, $q_1 = 15$, $q_2 = 11$, $q_3 = 8$, $q_4 = 5$, $r =$

0.1, and $T_s = 1$ ms. The parameter ω_{c0} of ESO is set as 250. The NTD parameters are selected as follows: $R = 500$, and $H_0 = 0.015$.

In order to compare the proposed method with the conventional PI cascade control system, parameters of the speed PI controller ($k_p = 35$, $k_i = 100$) have been regulated to the optimum, which means they cause acceptable vibration at steady state and can make the response of speed loop and current loop as fast as possible to reduce the sliding distance. An encoder with an ordinary resolution of 2048 was installed on the machine, and only the orthogonal pulse, signals A and B were used for the rollback mitigation control.

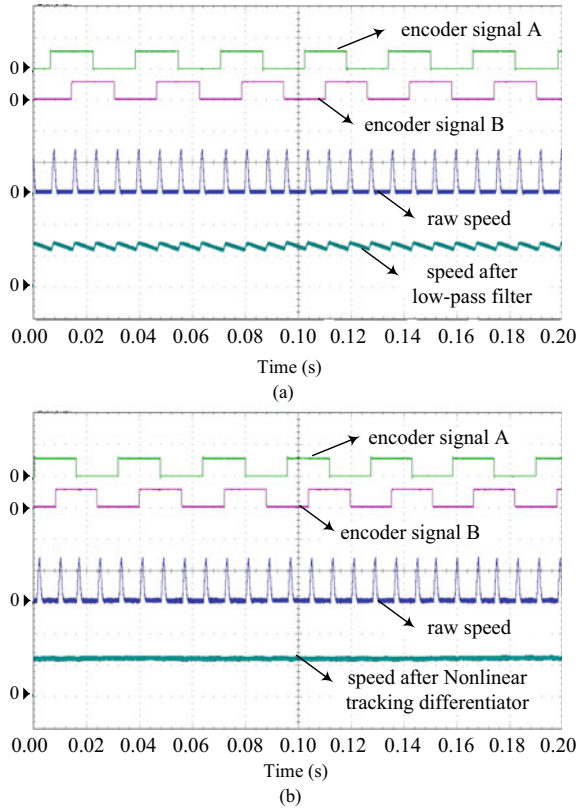
8.7.2 Performance of NTD

The performance of tracking and filtering can be changed with different parameters of NTD. The NTD parameters are selected as follows: $R = 500$, $H_0 = 0.015$. And the cutoff frequency of the low-pass filter is 17 Hz. When the speed of the traction machine is 2r/min, the experimental waveforms of sampling speeds using the low-pass filter and the nonlinear tracking differentiator are shown, respectively, in Fig. 8.4a, b. The middle waveform is the raw speed signal, and the bottom waveforms in Fig. 8.4a, b are the speed signal through the low-pass filter and the nonlinear tracking differentiator, respectively. From the results, the speed signal obtained by using NTD is smoother, with less vibration at low-speed region.

8.7.3 Performance of the Internal Current Loop Adopting PI Regulator

The whole control strategy is ultimately executed by a fixed-point DSP chip, in which the current loop regulating period is one-tenth of the speed loop. The response of the current loop using optimal PI controller is sufficiently fast for this direct-drive application from experimental results as shown in Fig. 8.5. So if the parameters of PI controller are well-designed, it can make the current feedback trace the current reference well for achieving effective rollback mitigation. The most important thing in resolving the rollback problem is that the output of the speed controller must match the uncertain and changing load torque. Compared with the MPC regulating both internal and external loops, the enhanced MPC strategy can not only increase the robustness of the system, but also effectively reduce the amount of calculation.

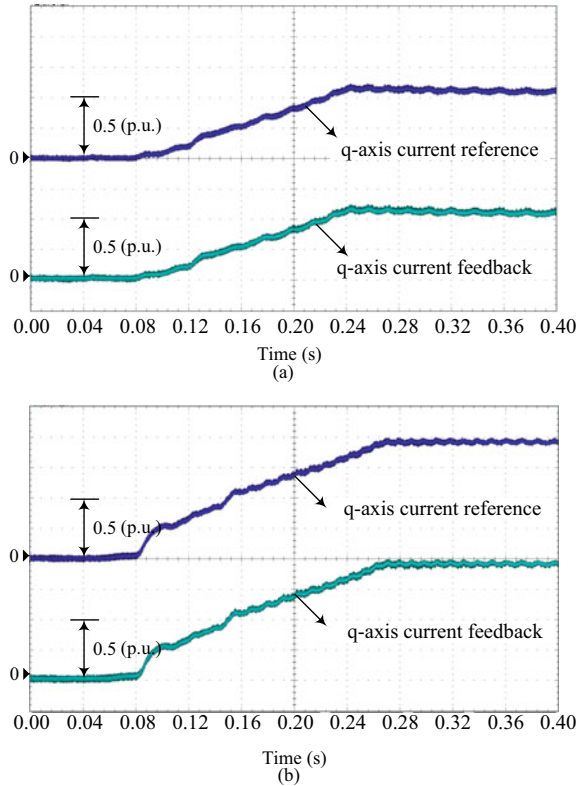
Fig. 8.4 Comparison of the experimental waveforms of sampling speeds using low-pass filter and NTD. **a** Using the low-pass filter. **b** Using the NTD



8.7.4 Experimental Comparison Between Conventional and Proposed Enhanced MPC

An experimental comparison between conventional MPC without ESO and enhanced MPC with ESO under 60% rated load was carried out. The experimental results are shown in Fig. 8.6. The middle waveform is the sliding speed, and the bottom waveform is the q -axis current. From Fig. 8.6, the traction sheave is still sliding at the speed of 1.8r/min when using the conventional MPC, the reason is that the q -axis current used to balance the disturbance is generated by the steady-state speed error which should be prevented. The steady-state speed error will cause the elevator car sliding.

Fig. 8.5 Experimental comparison of q -axis reference and feedback currents under different loads. **a** Under 60% rated load. **b** Under rated load

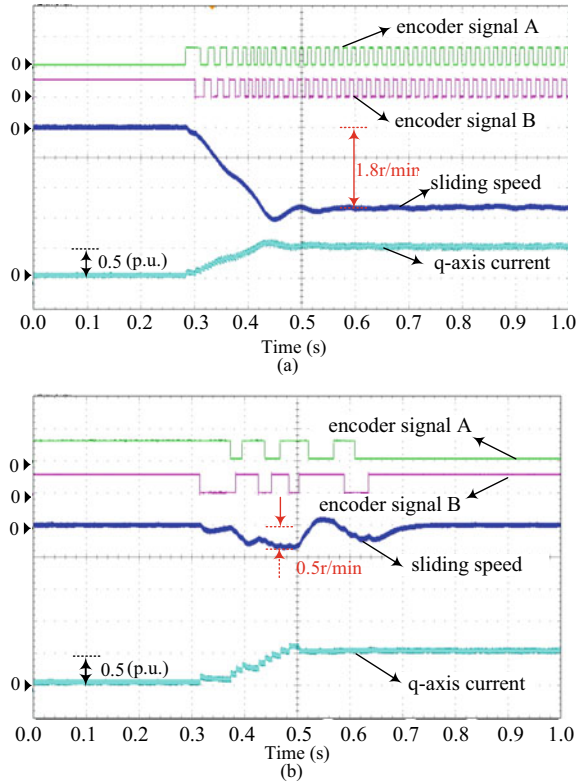


8.7.5 Control Performance Comparison of PI, Conventional MPC and Proposed Enhanced MPC

Under the same experimental conditions, the experimental results of the PI speed regulator and the enhanced MPC with NTD and with low-pass filter are compared. There is no difference in basic parameters between enhanced MPC with NTD and with low-pass filter. Figures 8.7, 8.8 and 8.9 show the experimental results under 20%, 60% and 100% of rated load, respectively. In terms of the sliding distance, there is no obvious difference between the enhanced MPC with NTD and with low-pass filter. Under 20% of rated load, the sliding distance with PI speed regulator is 2.30 mm, while the sliding distance with enhanced MPC is only 0.75 mm. During the steady state, there still exists vibration when using the enhanced MPC with low-pass filter as shown in Figs. 8.7b, 8.8b and 8.9b. However, the vibration is eliminated when using the enhanced MPC with NTD as shown in Figs. 8.7c, 8.8c and 8.9c.

Under 60% of rated load, the sliding distance with PI speed regulator is 4.13 mm, while the sliding distance of enhanced MPC with NTD is only 1.50 mm. Under rated load, the sliding distance with PI speed regulator is 7.00 mm, while the sliding

Fig. 8.6 Experimental comparison of the two methods under 60% rated load. **a** Conventional MPC without the ESO. **b** Enhanced MPC with the ESO



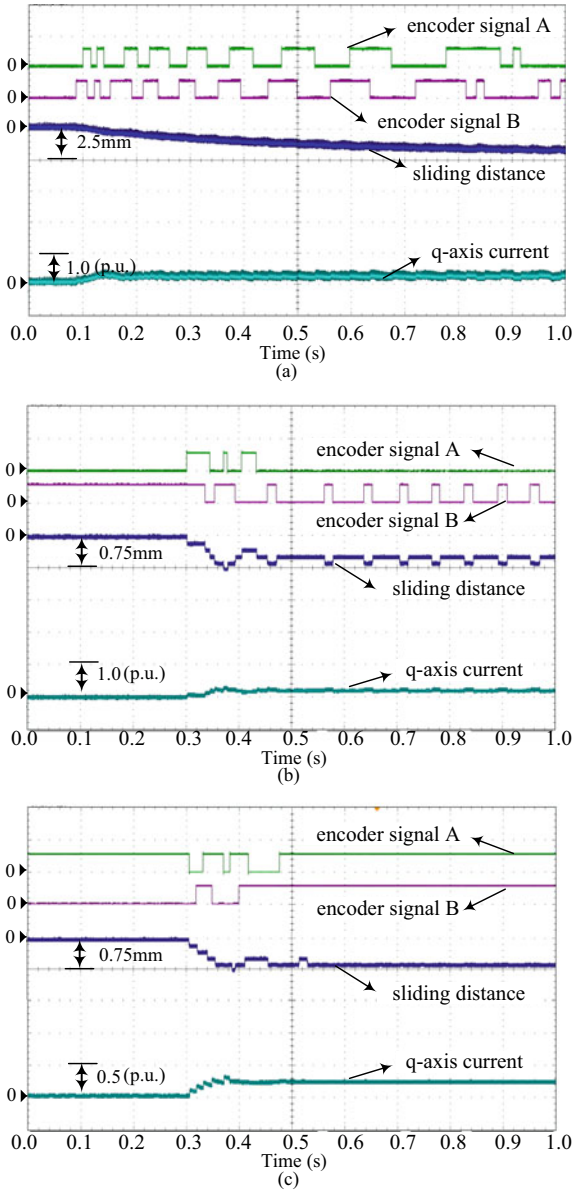
distance of enhanced MPC with NTD is only 1.80 mm. In summary, the proposed enhanced MPC with NTD can get much shorter sliding distance, smaller sliding speed, better riding comfort, and no vibration at steady state.

Figure 8.10 shows the comparison between the PI speed regulator and the proposed enhanced MPC with NTD under different loads. From Fig. 8.10, the sliding distances of the proposed method are much shorter than those of PI speed regulator under different loads. Therefore, the proposed method can effectively solve the technical difficulties of weight-transducerless elevator drives.

8.8 Summary

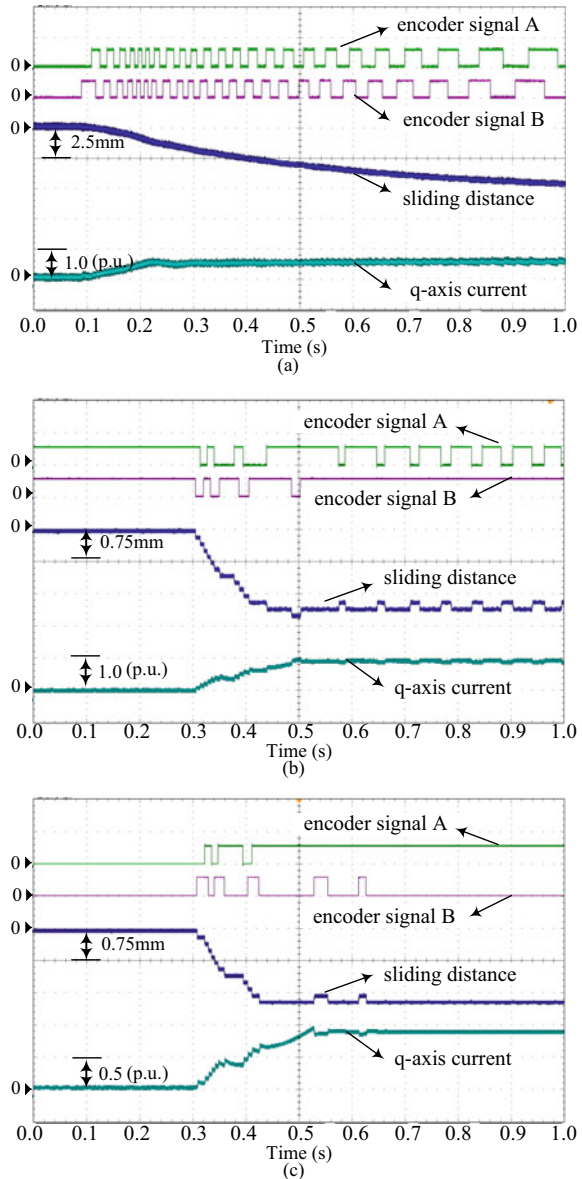
This chapter proposes a novel weight-transducerless starting torque control strategy based on enhanced MPC with ESO for direct-drive elevator traction system which can achieve high performance with an ordinary-resolution encoder. In order to overcome the mismatch of predictive model caused by the braking torque and the unknown carload, the ESO is used to rectify the predictive model. Both the stability and the

Fig. 8.7 Experimental comparison of the three methods under 20% rated load. **a** PI speed regulator. **b** Enhanced MPC with low-pass filter. **c** Enhanced MPC with NTD



parameter selection of the observer are analyzed. The NTD can make the speed feedback contain less vibration than the conventional low-pass filter. The estimated speed obtained from the ESO used as the initial value of the predictive speed can reduce the computational burden of the cost function. Instead of taking the conventional PI as the speed regulator, the enhanced MPC with ESO can effectively improve

Fig. 8.8 Experimental comparison of the three methods under 60% rated load. **a** PI speed regulator. **b** Enhanced MPC with low-pass filter. **c** Enhanced MPC with NTD



the dynamic performance without weight transducers, which benefits the robustness of the system. Therefore, the riding comfort can be improved when the elevator operates from the standby mode to the running mode. Experimental results verify that the proposed control strategy can achieve shorter sliding distance and smaller sliding speed without steady-state error for the direct-drive elevators installed with an ordinary-resolution encoder.

Fig. 8.9 Experimental comparison of the three methods under 100% rated load. **a** PI speed regulator. **b** Enhanced MPC with low-pass filter. **c** Enhanced MPC with NTD

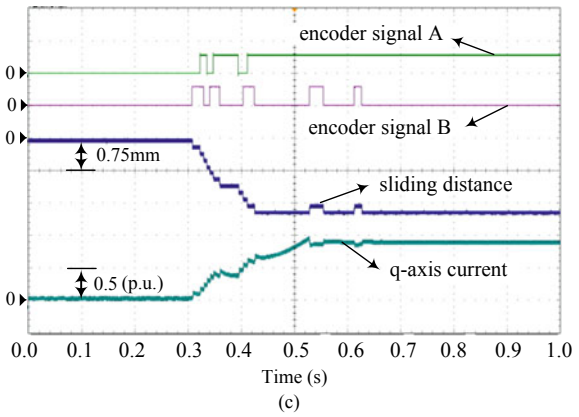
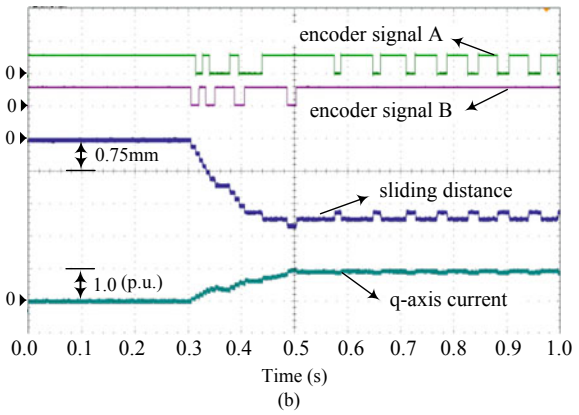
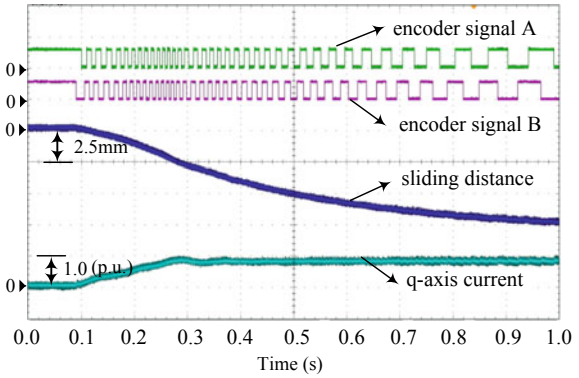
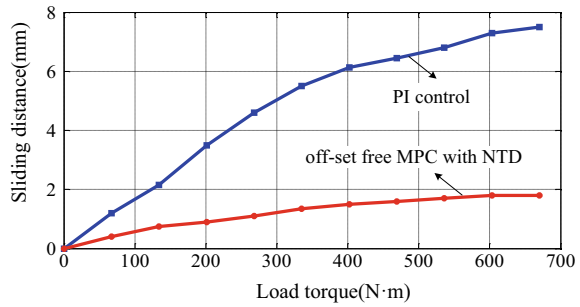


Fig. 8.10 Sliding distance comparison of the two methods under different loads



References

1. Jung JW, Leu VQ, Do TD, Kim EK, Choi HH (2015) Adaptive PID speed control design for permanent magnet synchronous motor drives. *IEEE Trans Power Electron* 30(2):900–908
2. Niu L, Xu D, Yang M, Gui X, Liu Z (2015) On-line inertia identification algorithm for PI parameters optimization in speed loop. *IEEE Trans Power Electron* 30(2):849–858
3. Zhang X, Sun L, Zhao K, Sun L (2013) Nonlinear speed control for PMSM system using sliding-mode control and disturbance compensation techniques. *IEEE Trans Power Electron* 28(3):1358–1365
4. Grignon D, Chen X, Kar N, Qian H (2014) Estimation of load disturbance torque for DC motor drive systems under robustness and sensitivity consideration. *IEEE Trans Ind Electron* 61(2):930–942
5. Hong X, Deng Z, Wang S, Huang L, Li W, Lu Z (2010) A novel elevator load torque identification method based on friction model. In: Proc. 25th annu. IEEE APEC, pp 2021–2024
6. Wang G, Zhang G, Yang R, Xu D (2012) Robust low-cost control scheme of direct-drive gearless traction machine for elevators without a weight transducer. *IEEE Trans Ind Appl* 48(3):996–1005
7. Liu F, Shen A, Zhang Y, Fu W (2014) A rapid and high-accuracy control scheme of starting torque for elevators without a weight transducer. In: 2014 IEEE 23rd international symposium on industrial electronics (ISIE), IEEE, pp 733–738
8. Wang G, Xu J, Li T, Zhang G, Zhan H, Ding L, Xu D (2014) Weight-transducerless starting torque compensation of gearless permanent magnet traction machine for direct-drive elevators. *IEEE Trans Ind Electron* 61(9):4594–4604
9. Bolognani S, Faggion A, Sgarbossa L et al (2007) Modelling and design of a direct-drive lift control with rope elasticity and estimation of starting torque. In: Proc. 33rd annu. IEEE IECON, pp 828–832
10. Hong X, Deng Z, Wang S et al (2010) A novel elevator load torque identification method based on friction mode. In: Proc. 25th annu. IEEE APEC, pp 2021–2024
11. Wang G, Zhang G, Yang R et al (2012) Robust low-cost control scheme of direct-drive gearless traction machine for elevators without a weight transducer. *IEEE Trans Ind Appl* 48(3):996–1005
12. Feng L, Anwen S, Yinnan Z et al (2014) A rapid and high-accuracy control scheme of starting torque for elevators without a weight transducer. In: 2014 IEEE 23rd international symposium on industrial electronics (ISIE), pp 733–738
13. Wang G, Xu J, Li T et al (2014) Weight-Transducerless starting torque compensation of gearless permanent-magnet traction machine for direct-drive elevators. *IEEE Trans Ind Electron* 61(9):4594–4604
14. Chang X, Li Y, Zhang W et al (2015) Active disturbance rejection control for a flywheel energy storage system. *IEEE Trans Ind Electron* 62(2):991–1001

15. Tian D, Shen H, Dai M (2014) Improving the rapidity of nonlinear tracking differentiator via feedforward. *IEEE Trans Ind Electron* 61(7):3736–3743
16. Wang G, Wang Y, Xu J et al (2016) Weight-transducerless rollback mitigation adopting enhanced MPC with extended state observer for direct-drive elevators. *IEEE Trans Power Electron* 31(6):4440–4451
17. Preindl M, Bolognani S (2013) Model predictive direct speed control with finite control set of PMSM drive systems. *IEEE Trans Power Electron* 28(2):1007–1015
18. Han J (2009) From PID to active disturbance rejection control. *IEEE Trans Ind Electron* 56(3):900–906

Chapter 9

ADRC Strategy for Gearless PMSM Traction Elevators



9.1 Introduction

Gearless traction systems have become the trend of modern elevators because it is easy to implement the non-machine room application. Several key issues of gearless traction systems should be concerned in the control strategy: (1) riding comfort during startup; (2) stability and security during the operation period; (3) high efficiency and strong robustness. Due to the advantages of high power density, high torque-to-inertia ratio and high efficiency, the permanent magnet synchronous motor (PMSM) has been applied widely as the traction machine of the elevator. In zero-servo process during which the elevator operates from start-by mode to running mode, the traction motor should generate a suitable electromagnetic torque immediately to balance the unknown and nonlinear load torque exerted on the traction wheel. Thus, the riding comfort could be assured. Originally, weight transducers should be installed. However, the longline transmission of the weight transducer and non-ideal environment would deteriorate the stability and the riding comfort, as well as increase the cost of the traction system. As a result, the starting torque compensation strategy without installing weight transducers has become the research hotspot.

Several researches have been carried out to improve the performance and enhance the robustness against unknown disturbance [1–3]. Furthermore, a variety of advanced control strategies have been presented to reduce the sliding distance and speed in weight-transducerless elevators. In [4], a compensation strategy based on the friction model was proposed. The load torque was calculated and compensated by the control system. However, as the friction model is not accurate enough to calculate the load, the calculated torque reference may have step change, which will cause mechanical vibration. In [5], the dichotomy and the staircase method were adopted in the starting torque compensation for weight-transducerless traction machine. The compensation method could track the equivalent load torque effectively. However, the variation of neighboring electromagnetic torques was also a step type which would cause vibration during the zero-servo process. In [6], an observer-based feedforward compensation of load torque was introduced to prevent car sliding

during the starting process by focusing on the change of inertia. In [7], an adaptive torque compensation strategy based on fuzzy control was proposed. It provided estimated information for load torque according to the speed and acceleration of the motor. In spite of the smaller sliding distance and suppressed mechanical vibration by adopting this strategy, the acceleration information of the motor was difficult to be obtained because of the interference caused by the derivative calculation. Furthermore, a torque compensation strategy based on offset-free model predictive control (MPC) which can enhance the capability of balancing uncertain load torque was proposed in [8]. This strategy can reduce the sliding distance efficiently and get faster response. However, an accurate plant model is needed in model correction and receding optimization.

Active disturbance rejection control (ADRC) has been successfully applied in motor drive system. It is summarized as the combination of nonlinear tracking differentiator (NTD), extended state observer (ESO) and nonlinear proportional–integral–derivative (NLPID). Owing to the independence of the accurate plant model, ADRC strategies can be adopted as a robust control strategy against parameter variations, disturbances and noise. Recently, ADRC has been widely used in PMSM control such as transducerless position estimation combining with high-frequency signal injection, high-speed vehicle control, vibration suppression control and speed calculation of PMSM servo systems. By adopting nonlinear state feedback, the robustness of controller can be enhanced and the dynamic performance can be improved [9]. As the load torque can be regarded as a part of the total disturbance of the system, ADRC is suitable to be applied in the weight-transducerless elevator drives to generate a matched compensation torque during the startup process.

In this chapter, a novel ADRC scheme based on ESO and nonlinear error feedback (NLEF) for gearless elevator traction machine drives is proposed [10]. This strategy can reduce the sliding distance during startup process and enhance the robustness against the uncertain load disturbance and particular parameter errors. The ESO can estimate the total disturbance of the system and generate a matched q -axis current reference to reject the interference of the system. Furthermore, as reversal sliding is caused by the integrator of conventional proportional–integral (PI) controller in the speed loop, the PI speed regulator is replaced by a NLEF controller to accelerate the response. Both the stability and the parameter selection of ESO and NLEF controller are analyzed to prove the robustness of the controller.

9.2 Establishment of ESO for Direct-Drive Elevator Traction System

Figure 9.1 shows the proposed scheme of the ADRC for the direct-drive permanent magnet traction machine during the elevator startup. In Fig. 9.1, PI regulators are used in the current loop, and ESO is adopted to estimate the nonlinear and uncertain disturbance. Then a current feedforward component will be added to the q -axis

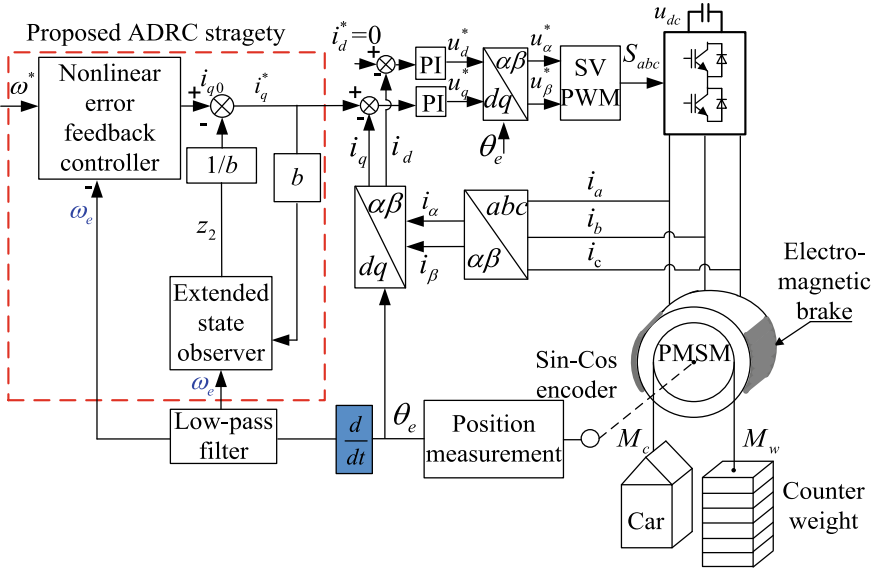


Fig. 9.1 Scheme of ADRC during the elevator startup

current reference. Additionally, in order to avoid the negative effects of sliding back caused by the integrator of speed loop, NLEF control strategy applying a power function is adopted. The proposed strategy not only accelerates the response speed, but also enhances the robustness against load disturbance during the brake releasing process.

ESO is the core part of ADRC. It is independent of the accurate mathematical model of the controlled object which changes with the environment and operating conditions. By adjusting the input through the feedback control, total disturbance can be estimated and suppressed timely, which is beneficial to improve the robustness and dynamic performance of traction system. The ESO can be illustrated as follows.

For a first-order system, the state equation can be expressed as

$$\begin{cases} \dot{x}_1 = f + bu \\ y = x_1 \end{cases} \tag{9.1}$$

where y is the output of the system, f is a multivariable function of both the state and the external interference representing the total disturbance, u is the input and b is the gain of it.

The objective here is to make y as desired by using u as the manipulative variable. In conventional control strategy, f should be expressed as a specific mathematical version which is complex and inaccurate. However, in ESO theory, f does not need to be expressively known. Adopting the idea of state observer, f can be obtained from

the output information because all factors which influence the system operation could be reflected in the output.

Assuming $x_2 = f$, (9.1) can be written as

$$\begin{cases} \dot{x}_1 = x_2 + bu \\ \dot{x}_2 = c(t) \end{cases} \quad (9.2)$$

where $c(t)$ is the derivative of x_2 . The state observer established by (9.2) is

$$\begin{cases} \dot{z}_1 = z_2 + l_1(x_1 - z_1) + bu \\ \dot{z}_2 = l_2(x_1 - z_1) \end{cases} \quad (9.3)$$

where $z_1 \rightarrow x_1$, $z_2 \rightarrow f$. The effect of uncertain $c(t)$ is modified by the error between the actual value x_1 and observed value z_1 . If l_1 and l_2 are selected reasonably, f can be observed effectively. When the input u is selected as

$$u = u_0 - \frac{f}{b}, \quad (9.4)$$

system (9.2) will be changed into a cascade integral form which can be controlled easily by making u_0 a function of error [11]. In this way, the control issue is transformed to the estimation and rejection of the total disturbance [12].

The mechanical equation of the traction machine can be expressed as

$$\dot{\omega} = \frac{1}{J}(T_e - T_L) - \frac{B}{J}\omega \quad (9.5)$$

where ω is the angular speed generated from the raw speed calculation, T_L represents the equivalent load torque including the influence of the rigidity and damper of rope, J is the rotational inertia, and B is the viscous friction coefficient.

In double-loop motor controlling structure, (9.5) can be transferred into the form of system (9.2) equivalently as

$$\begin{cases} \dot{x}_1 = x_2 + bi_q^* \\ \dot{x}_2 = d(t) \end{cases} \quad (9.6)$$

where $d(t) = (T_e - T_L)/J - B\omega/J - bi_q^*$, x_1 represents the angular speed feedback ω .

Actually, the speed information is often obtained by using sensors in practical applications. In the traction control system, differentiated position results are used as the calculated speed feedback. According to (9.3) and (9.6), the second-order observer can be established as

$$\begin{cases} \dot{z}_1 = z_2 - l_1(z_1 - \omega_e) + bi_q^* \\ \dot{z}_2 = -l_2(z_1 - \omega_e) \end{cases} \quad (9.7)$$

where ω_e is the estimated speed obtained by the differentiation of the position.

9.3 Stability Analysis and Parameter Selection

To ensure the feasibility of the proposed method, the stability of the control system should be investigated. In this part, the stability of ESO is analyzed first. And on that basis, the parameter selection of ESO is given considering the response speed of the system.

According to the analysis above, (9.7) can be rewritten as the matrix form (9.8)

$$\dot{\mathbf{Z}} = \mathbf{AZ} + \mathbf{BU} \quad (9.8)$$

where $\dot{\mathbf{Z}} = [\dot{z}_1, \dot{z}_2]^T$, $\mathbf{Z} = [z_1, z_2]^T$, $U = [\omega_e, i_q^*]$, $\mathbf{A} = \begin{bmatrix} -l_1, 1 \\ -l_2, 0 \end{bmatrix}$, $\mathbf{B} = \begin{bmatrix} l_1, b \\ l_2, 0 \end{bmatrix}$.

The characteristic determinant of (9.8) is $|s\mathbf{I} - \mathbf{A}| = \begin{vmatrix} s + l_1, 1 \\ l_2, s \end{vmatrix} = s^2 + l_1s + l_2$.

According to Hurwitz criterion, $l_1 > 0$, $l_2 > 0$ are needed.

For tuning simplicity, the observer gains l_1 and l_2 can be selected as $l_1 = 2p$ and $l_2 = p^2$, respectively. p determines the bandwidth of the observer, which makes both of the observer poles placed at p . The larger p , the faster the disturbance is observed by ESO and compensated by the controller, while more high-frequency noises will be contained in the result obtained from the observer. It is a common trade-off of the disturbance observer. As for a second-order ESO, the trade-off has less effect on the system. However, when the order of ESO is higher than 3, the serious influence by this trade-off becomes obvious. According to the analysis in [13], p cannot be selected too large or it will lie out of the stable region. When a higher-order observer is established, more advanced methods should be adopted to enhance the performance of the ESO. For example, adaptive law can be applied in the parameter tuning of the observer [14]. When selecting the suitable gains, the system parameters will be adjusted automatically to ensure the stability. Besides, speed predictive controller can also be used to enhance the performance of the observer. Based on the model of PMSM and the theory of MPC, the predictive speed is used as the input of the ESO. As a result, the available bandwidth of the observer will be improved.

The transfer function between z_2 and $d(t)$ can be derived as

$$\frac{z_2(s)}{d(s)} = \frac{l_2}{l_2 + l_1s + s^2} \quad (9.9)$$

where $z_2(s)$ is the observed disturbance and $d(s)$ is the actual disturbance. When selecting $l_1 = 2p$, $l_2 = p^2$, (9.9) can be expressed as

$$\frac{z_2(s)}{d(s)} = \frac{p^2}{(s+p)^2} \quad (9.10)$$

To evaluate the performance of a system, the settling time and the overshoot are the main dynamic performance indexes. As the overshoot of (9.9) is zero, the settling time becomes the only factor while choosing p . Define T_{eso} as the settling time of (9.9). According to [13], T_{eso} can be calculated as

$$T_{eso} = 5.85/p \quad (9.11)$$

which represents the response speed for $z_2(t)$ tracking $d(t)$.

As analyzed above, the response speed and the performance of the disturbance rejection both depend on the value of p . However, larger p will cause instability and vibration when ESO is applied in the closed-loop system. In addition, other parameters of the ESO will also influence the performance of the whole system such as the control gain b .

When using ESO as the compensation of the current loop input, the response speed will depend on the parameters of the observer. In (9.8), z_2 is regarded as the observed value of the total disturbance and can be used as the feedforward of the system to reject this disturbance in advance. The expression of z_2 can be obtained from (9.8) as

$$(s^2 + l_1s + l_2)z_2 = l_2s\omega_e - l_2bi_q^* \quad (9.12)$$

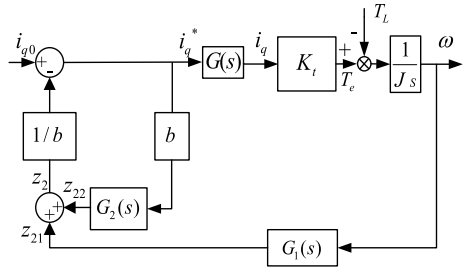
which is a double-input–single-output system. According to the superposition theorem, z_2 can be divided as the output generated by i_q^* and ω_e , respectively. It can be expressed as

$$\begin{cases} (s^2 + l_1s + l_2)z_{21} = l_2s\omega_e \\ (s^2 + l_1s + l_2)z_{22} = -l_2bi_q^* \\ z_2 = z_{21} = z_{22} \end{cases} \quad (9.13)$$

Putting z_2 as the feedforward, the simplified structure of the control system is shown in Fig. 9.2.

In Fig. 9.2, i_{q0} represents the output of speed loop, which is theoretically equal to zero in steady state. The current reference is the summation of i_{q0} and z_2/b . K_t is the actual torque per ampere of the motor. $G(s)$ is the transfer function of current loop after calibration. $G_1(s)$ and $G_2(s)$ are transfer functions under the action of ω_e and i_q^* , respectively. $G(s)$, $G_1(s)$ and $G_2(s)$ can be expressed as

Fig. 9.2 Simplified structure of the control system



$$\begin{cases} G(s) = \frac{1}{\tau s + 1} \\ G_1(s) = \frac{l_2 s}{s^2 + l_1 s + l_2} \\ G_2(s) = \frac{-l_2 b}{s^2 + l_1 s + l_2} \end{cases} \quad (9.14)$$

where $\tau = 0.6$ ms, representing the equivalent time constant of the current loop.

Moving T_L to the action point of i_{q0} and regarding i_q^* as the output, the transfer function can be expressed as

$$G_H(s) = \frac{b}{G_2(s) + b + \frac{G_1(s)G(s)b_0}{s}} \quad (9.15)$$

where $b_0 = K_t/J$. As τ is far less than l_1 , it can be ignored. Combined with (9.14), (9.15) can be changed into

$$G_H(s) = \frac{s^2 + l_1 s + l_2}{s^2 + l_1 s + Kl_2} \quad (9.16)$$

where $K = b_0/b$. According to (9.16), the characteristic equation of system is

$$s^2 + l_1 s + Kl_2 = 0 \quad (9.17)$$

As analyzed above, $l_1, l_2 > 0$. As a result, $K > 0$ is needed to ensure the stability of the whole control system. So when $l_1 = 2p, l_2 = p^2$, the root locus of K starts at $(-2p, 0)$ and $(0, 0)$ and then separates at $(-p, 0)$, extending to both sides toward the directions parallel with imaginary axis, which means that the system is constantly stable when $K > 0$.

It can be concluded that the system will achieve optimized performance and fast response when selecting the poles as $s_1 = s_2 = -p$, in which case $K = 1$ and the transfer function $G_H(s) = 1$. It can be known that when $K = 1$, the output of the system is equal to the input without time delay and state error. The observed value of the total disturbance z_2 will offset the actual interference of the system including external torque and control error. In addition, the output of speed loop i_{q0} will damp to zero in steady state, which means that the speed of motor can be kept zero and

the sliding distance can be small enough. When $K \neq 1$, the poles of the system will deviate and the accuracy of controller will decrease, which results in a larger sliding distance and a slower response.

However, when $K = 1$, the gain of input b will be chosen as $b = b_0 = K_t/J$, which is not feasible because K_t and J are difficult to be accurately obtained. These two parameters will change within a certain range during elevator operation, which can be expressed as

$$b_0 = \frac{K_t}{J} = \frac{K_{t0} + \Delta K_t}{J_0 + \Delta J} \quad (9.18)$$

where K_{t0} and J_0 are the normal values, and ΔK_t and ΔJ are the mismatch errors of K_{t0} and J_0 , respectively. According to the practical situation of the traction system, ΔK_t and ΔJ are selected as follows for analysis,

$$\begin{aligned} \Delta K_t &= \pm 0.5K_{t0} \\ \Delta J &= \pm 0.5J_0. \end{aligned} \quad (9.19)$$

Then selecting b as K_{t0}/J_0 , K will be written as

$$K = \frac{\frac{K_{t0} + \Delta K_t}{J_0 + \Delta J}}{\frac{K_{t0}}{J_0}}. \quad (9.20)$$

Combining (9.19) and (9.20), the range of K can be calculated as

$$\begin{cases} 0.5K_{t0} \leq K_{t0} + \Delta K_t \leq 1.5K_{t0} \\ 0.5J_0 \leq J_0 + \Delta J \leq 1.5J_0 \\ 1/3 < J < 3 \end{cases}. \quad (9.21)$$

Plugging $l_1 = 2p$, $l_2 = p^2$ into (9.17), the equation of system pole is

$$s^2 + 2ps + p^2K = 0. \quad (9.22)$$

Then the root contours of p and K can be described as shown in Fig. 9.3.

Figure 9.3 shows the root contours of p and K when $1/3 < K < 3$ and $p = 10, 40, 60$ and 100 , respectively. It illustrates that the contours start at $(-1.82p, 0)$ and $(-0.18p, 0)$. Then they move toward the midpoint through real axis and separate at $(-p, 0)$, extending to both sides toward the directions parallel with imaginary axis to $(-p, j\sqrt{2}p)$ and $(-p, -j\sqrt{2}p)$. From Fig. 9.3, the change tendency of the bandwidth of the system can be acquired with different values of p . When higher p is selected, the faster response speed will be achieved. However, it is also shown in Fig. 9.3 that the range of poles on real axis is $[-1.82p, -0.18p]$, which means that when p is selected as a larger value, the uncertainty of poles increases. The system

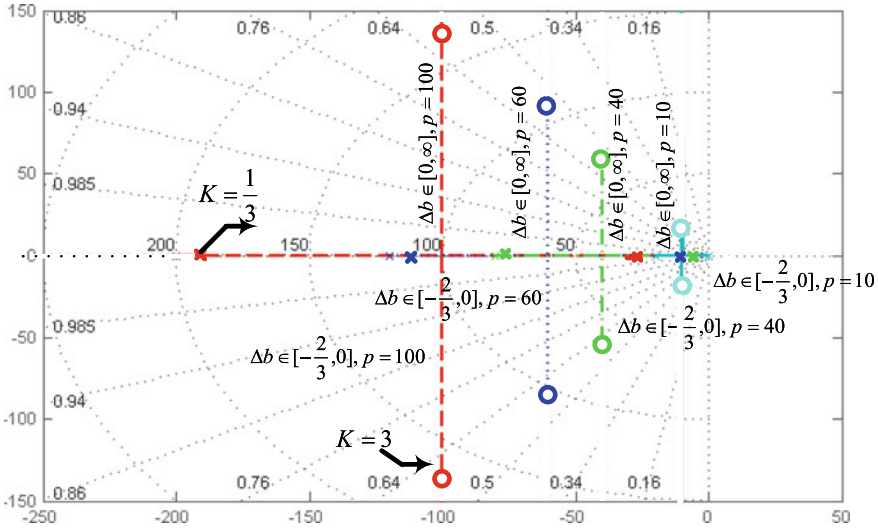


Fig. 9.3 Root contours of p and K

response will be susceptible to the perturbation of motor parameters. Therefore, the range of p should be limited to ensure the high performance of the system. Several experiments have been done on the practical platform to obtain the available range of p . With larger p , the system shows a better performance. However, when p is selected as large as 112, the system starts to vibrate in steady state. This means that p should be selected below 112 when adopting the ESO. Considering there are some differences among various operating conditions, design margins should be reserved to make the system robust. As a result, the pole of the system is selected as $p \leq 100$.

9.4 NLEF Controller

As analyzed above, ESO estimates and rejects the uncertain and nonlinear total disturbance of the elevator traction system. Then the nonlinear system is modified as a cascade integral form, which will simplify the design of error feedback controller. In the PI control scheme, using the linear error feedback, the controller adds an integrator to eliminate the static error, which has been verified by internal model principle. However, after applying ESO to eliminate the total disturbance of the traction system, the integrator is not necessary because ESO will compensate the uncertain external interference timely by feeding forward the q -axis current. As a result, the output of speed loop i_{q0} will be zero in steady state. When using a PI controller in the speed loop, the output of integrator is the summation of speed error. As a result, the opposite speed error is needed to make the output of the integrator zero, which means that the motor should roll back after sliding. The distance of

this reversal is uncertain because it depends on the external disturbance and actual operating conditions. Therefore, a NLEF controller using power function is applied to compensate the absence of integrator and reduce the sliding distance. Selecting the power of error as decimals to get rough feedback, the system can achieve faster response speed and stronger robustness.

Let the input of system (9.6) as $i_q^* = i_{q0} - \frac{z_2}{b_0}$, it is converted to a cascade integral form

$$\dot{\omega} = i_{q0}. \quad (9.23)$$

Defining the nonlinear error feedback as:

$$\begin{cases} i_{q0} = K_{NL}|e|^\alpha \text{sign}(e) \\ e = \omega^* - \omega \end{cases}, \quad (9.24)$$

where K_{NL} is the gain of controller, ω^* is the speed reference which is kept zero during startup. Therefore, (9.23) can be changed into

$$\dot{e} = -K_{NL}|e|^\alpha \text{sign}(e). \quad (9.25)$$

The general solution of (9.25) is

$$\begin{cases} \frac{\text{sign}(e_0)}{(|e_0|^{\alpha-1} + (\alpha-1)K_{NL}t)^{\frac{1}{\alpha-1}}}, \alpha > 1 \\ x_0 e^{-K_{NL}t}, \alpha = 1 \\ \text{sign}(e_0)(|e_0|^{1-\alpha} - (1-\alpha)K_{NL}t)^{\frac{1}{1-\alpha}}, \alpha < 1 \end{cases} \quad (9.26)$$

where e_0 is the initial error. It is shown from (9.26) that there are three circumstances:

1. $\alpha > 1$ (smooth feedback), the error is attenuating at a speed of $(K_{NL})^{\frac{1}{1-\alpha}}$;
2. $\alpha = 1$ (linear feedback), the error is attenuating at a speed of $e^{-K_{NL}t}$;
3. $\alpha < 1$ (rough feedback), when $t = |e_0|^{1-\alpha}/K_{NL}(1-\alpha)$, the error has already attenuated to zero.

The analysis of (9.26) illustrates that when $\alpha < 1$, the rough feedback will force the error to attenuate to zero in limited time, which means that the control efficiency of rough feedback is better than smooth feedback and linear feedback.

However, as the switching function is used in the rough feedback, the input will have impulse force to the system especially when K_{NL} is large. In addition, the error will attenuate at extremely high acceleration, which may cause overshoot at jump point. These will influence the control performance and even be harmful to the traction machine. In order to smooth the transient profile around the zeros, the power function *fal* is applied to be the decay law of the error controller[15]. It can be expressed as

$$fal(e, \alpha, \delta) = \begin{cases} \frac{e}{\delta^{1-\alpha}}, & |e| < \delta \\ |e|^\alpha \text{sign}(e), & |e| \geq \delta \end{cases} \quad (9.27)$$

where $0 < \alpha < 1$ and $0 < \delta < 1$. According to (9.27), the error state equation can be written as

$$\dot{e} = K_{NL} fal(e, \alpha, \delta). \quad (9.28)$$

On the basis of Lyapunov theory, select the Lyapunov function as

$$V(x) = \frac{e^2}{2}. \quad (9.29)$$

When $|e| < \delta$, $\dot{e} = -K_{NL} \frac{e}{\delta^{1-\alpha}}$, so

$$\dot{V}(x) = e \cdot \dot{e} = -K_{NL} \cdot \frac{e^2}{\delta^{1-\alpha}} \leq 0. \quad (9.30)$$

When $|e| \geq \delta$, $\dot{e} = -K_{NL} |e|^\alpha \text{sign}(e)$, so

$$\dot{V}(x) = e \cdot \dot{e} = -K_{NL} \cdot |e|^{\alpha+1} \leq 0. \quad (9.31)$$

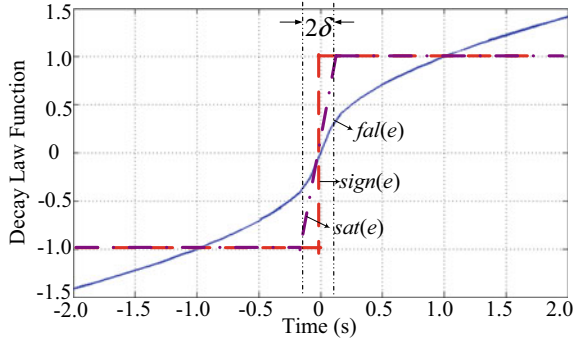
It can be seen that both (9.30) and (9.31) are negative definite, which means that the controller is asymptotically stable in the range of error.

The initial error of system is $e_0 = 0$. During startup, the motor speed ω attenuates to zero from negative, so e will attenuate to zero from positive, which means that the moving state point is located in the space where $e > 0$.

When $|e| \geq \delta$, $\dot{e} = -K_{NL} |e|^\alpha \leq 0$. The decay law of the error controller is a decreasing function, and the state point will move to the switching surface at the acceleration of $-K_{NL} |e|^\alpha$. Therefore, with the increasement of K_{NL} , the approaching speed will be higher, which can enhance the ability of disturbance rejection and get faster response speed.

When the point arrives at switching surface, it turns to the stage of $0 < e < \delta$, in which $\dot{e} = -K_{NL} \frac{e}{\delta^{1-\alpha}} < 0$. In this stage, the decay law is weakened compared with the exponential approach law, which avoids the severe vibration when state point crosses over the switching surface. Compared with the switch function and saturation function in common use of nonlinear control, fal has more reasonable approaching mode. The characteristic curves of three functions are shown in Fig. 9.4.

Fig. 9.4 Characteristic curves of three nonlinear functions



9.5 Experimental Evaluation

9.5.1 Experimental Setup

The proposed novel ADRC strategy was verified on an 11.7 kW elevator traction machine using a commercial inverter. The experimental platform is shown in Fig. 4.13. A same traction machine is mechanically connected to emulate the load of elevator car. A Sin-Cos encoder (ERN1387) with 2048 P/R is installed on the machine. The PWM frequency of inverter is set as 6 kHz. The whole control algorithm is executed by a STM32F103VB ARM chip. The control period of the speed loop is set as 1 ms. The parameters of the permanent magnet traction machines are shown in Table 4.1.

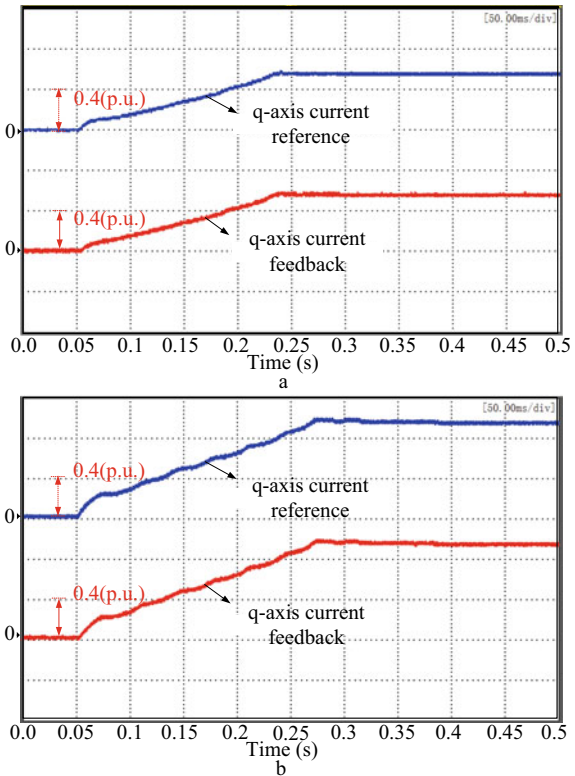
In order to assure both the stability of the system and the rapid response, the pole of ESO is selected as: $p = 60$. The speed feedback is calculated by the subdivided signals from the Sin-Cos encoder, which is more accurate. The Sin-Cos signals are used for comparing the sliding distance and speed. In addition, the Sin-Cos encoder will also generate an incremental count value whose range is 0–8191 per revolution, used to calculate the sliding distance. As the diameter of the traction sheave is 600 mm, the sliding distance per count value is 0.23 mm.

In order to compare the proposed strategy with the conventional PI control effectively, parameters of the PI speed controller have been regulated to the optimal as $K_{p\omega} = 35$, $K_{i\omega} = 100$, by which acceptable vibration at steady state and the fast response will be achieved. Such is the same case in current loop when selecting the parameters as $K_{pc} = 37.49$, $K_{ic} = 575.04$. For the NLEF controller, the control parameters are selected as: $K_{NL} = 22.3$, $\alpha = 0.5$ and $\delta = 0.05$.

9.5.2 Performance of the Inner Current Loop

The whole control algorithm is executed by an ARM chip, and the PWM frequency of inverter is set as 6 kHz. The control period of the speed loop is set as 1 ms, which means that the current loop regulating period is one-sixth of that of the speed loop. The response of the current loop using optimal PI controller is sufficiently fast. Figure 9.5a, b shows the current response of the traction system, with the optimal parameters as $K_{pc} = 37.49$ and $K_{ic} = 575.04$. It can be seen that with the well-designed parameters, the current feedback can trace the current reference well. The proposed ADRC strategy focuses more on the rapid balance between the output of the speed controller and the changing disturbance.

Fig. 9.5 Experimental results of q -axis current reference and feedback with PI regulator. **a** Under 60% rated load. **b** Under 100% rated load



9.5.3 Experimental Results of ESO with Different Gain B

Under the same experimental conditions, the experimental results of the PI speed regulator and that of adding the ESO for compensation with $b = 1$ and $b = K_{t0} / J_0$ are shown in Fig. 9.6. These experimental results are executed under 60 and 100% of rated load.

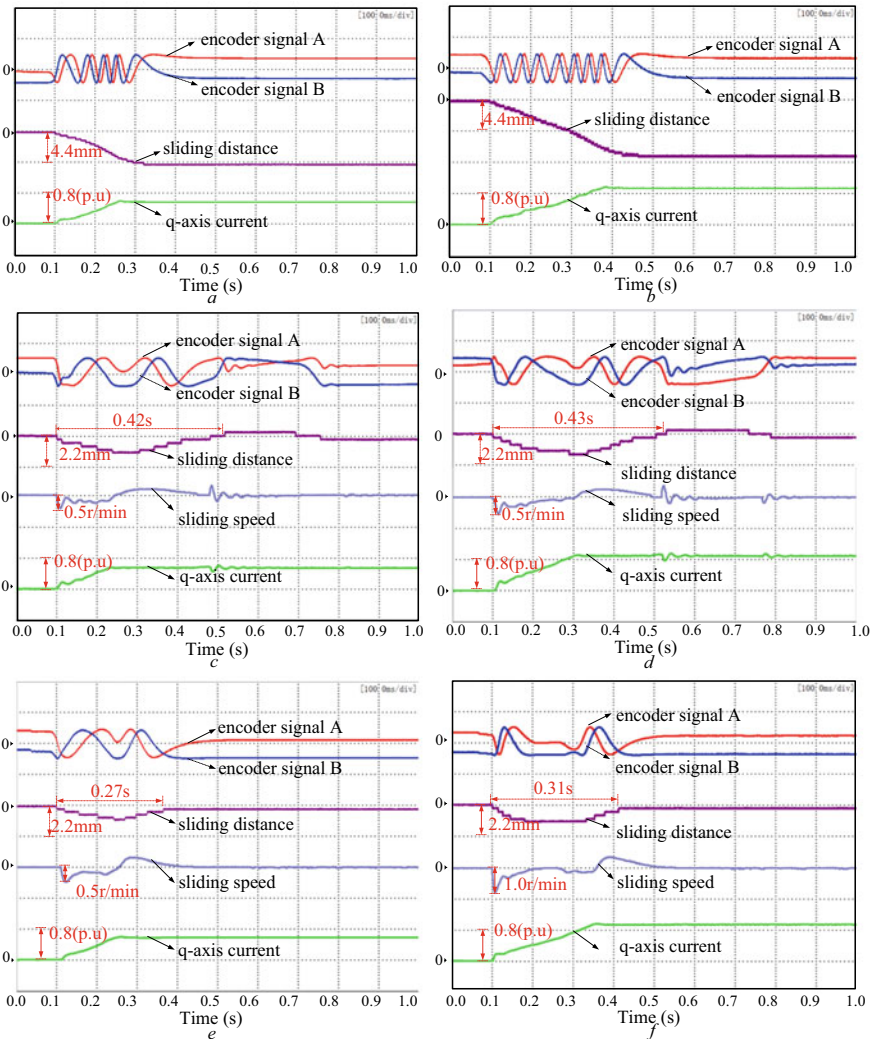


Fig. 9.6 Experimental result only using PI speed regulator and that of adding the ESO. **a** Under 60% rated load only using PI speed regulator. **b** Under 100% rated load only using PI speed regulator. **c** Under 60% rated load adding ESO when $b = 1$. **d** Under 100% rated load adding ESO when $b = 1$. **e** Under 60% rated load adding ESO when $b = K_{t0}/J_0$. **f** Under 100% rated load adding ESO when $b = K_{t0}/J_0$

In Fig. 9.6a, b, the middle waveforms are the sliding distance and the bottom waveforms are the q -axis current. From Fig. 9.6a, b, the sliding distance is as large as 4.37 mm under 60% of rated load and 7.59 mm under 100% load. This means severe negative influence on the riding comfort of the passengers.

In Fig. 9.6c–f, the second waveforms are the sliding distance and the third ones are the sliding speed. From Fig. 9.6c, d, the sliding distance is reduced to 1.15 mm under 60% rated load and 1.38 mm under 100% rated load when b is selected as: $b = 1$. It is also can be seen that after sliding, the motor will roll back to the opposite direction for about 1.38 mm under 60% rated load and 1.61 mm under 100%. In addition, as can be seen from the third waveforms of Fig. 9.6c, d, the sliding speed is about 0.5r/min and the motor vibrates during the zero-servo process with an overshoot of about 0.3r/min which forces the motor to slide back. This is due to the integrator in the PI controller of speed loop. Furthermore, the q -axis current has slight fluctuation in steady state, which means that the system is not stable enough.

To optimize the performance of system, let $b = K_{t0}/J_0$, which is the normal parameter of the traction machine. The experimental results are shown in Fig. 9.6e, f. As can be seen, the sliding distance is reduced to 1.15 mm under 100% rated load. Compared with Fig. 9.6c, d, the response time is reduced from 0.42 to 0.27 s when exerting 60% rated load and 0.43–0.31 s under 100% rated load. Particularly, q -axis current is smoother and steadier during the zero-servo process without any vibration. In addition, the distance of the sliding reversal is reduced to 0.92 mm under both 60 and 100% rated load. In summary, when $b = K_{t0}/J_0$, the system obtains a faster response speed and stronger robustness.

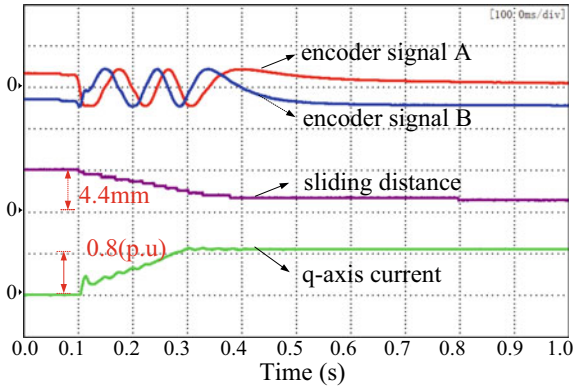
9.5.4 Experimental Results of ESO Combining with NLEF

As analyzed above, the integrator in speed loop causes the overshoot of speed which leads to the opposite sliding. It should be refrained by canceling the integrator, which will inevitably degrade the performance of the regulator with only proportional control. Under the same parameters of the control system, the experimental result of ESO with only proportional control in speed loop is shown in Fig. 9.7. As can be seen, the sliding distance rises to 4.37 mm under 100% rated load. As a result, the adoption of a high-efficiency speed loop regulator such as NLEF controller is needed.

Using the proposed control scheme with ESO and NLEF, the experiments are executed under the same experimental conditions. Under 20%, 60% and 100% rated load when selecting gain $b = 1$ and $b = K_{t0}/J_0$, respectively, the experimental results are shown in Fig. 9.8.

As can be seen from Fig. 9.8a–c, the sliding distance of the motor is as short as 0.23, 0.69 and 1.15 mm under different rated load, and the sliding direction reversal is avoided. In addition, these figures also illustrate that the sliding speed is lower and smoother without overshoot and serious vibration. The maximum speed is around 0.5r/min with a fast response in as short as 0.22 s under 100% rated load. These

Fig. 9.7 Experimental result using ESO canceling integrator



results indicate that the system will achieve shorter zero-servo time and provide better riding comfort.

However, it can be seen that when selecting $b = 1$, the q -axis current shows an urgent peak at the beginning of the motor operation under any loads, which has been circled in the figure. The urgent peak means that there is a heavy shock torque generated by the motor. This shock will cause harmful impact on the traction machine such as mechanical looseness and parts depreciation especially when the load torque is large. Even sometimes it will influence the stability of the system. Compared with $b = 1$, Fig. 9.8d–f shows the experimental results with $b = K_{t0}/J_0$. It can be seen that when b is selected as K_{t0}/J_0 , the q -axis current becomes smoother and steadier, and the peak is eliminated. During the dynamic regulating period, the q -axis current rises fast and smoothly owing to the characteristics of rough feedback and the optimized poles. Taking the advantages of the NLEF controller, the problem of sliding back is prevented. So the maximum sliding speed and sliding distance are both small.

The research topic of weight-transducerless control strategy for gearless elevator has been studied for several years. The reference [8] was proposed by our previous researchers adopting MPC. It was a model-based control strategy which had been realized on the same experimental platform. When adopting the offset-free MPC strategy in [8], the sliding distances in 20%, 60% and 100% rated load are 0.45 mm, 1.35 mm and 1.5 mm, respectively, while the ones adopting ADRC are 0.23 mm, 0.69 m and 1.15 mm. The comparison among the PI speed regulator, the offset-free MPC and the proposed ADRC strategy with ESO and NLEF controller under different loads are shown in Fig. 9.9. From Fig. 9.9, the sliding distance and speed of the proposed method are the shortest compared with the others under various loads, verifying its good performance with a fast response, no mechanical vibration and no steady-state speed error.

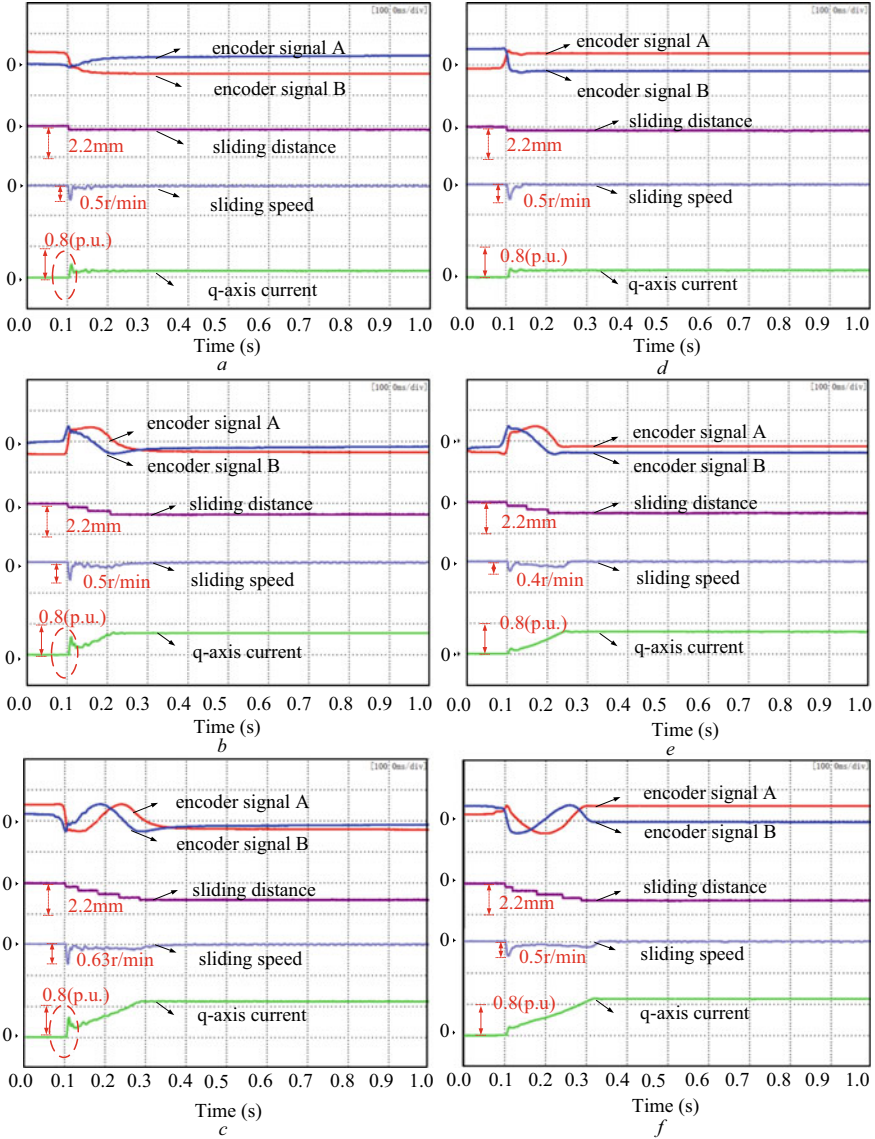


Fig. 9.8 Experimental result using ESO and NLEF. **A** Under 20% rated load when $b = 1$. **B** Under 60% rated load when $b = 1$. **c** Under 100% rated load when $b = 1$. **d** Under 20% rated load when $b = K_{t0}/J_0$. **e** Under 60% rated load when $b = K_{t0}/J_0$. **f** Under 100% rated load when $b = K_{t0}/J_0$

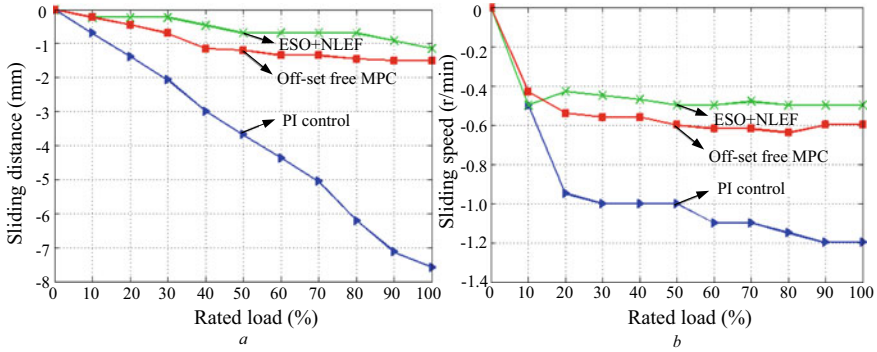


Fig. 9.9 Comparison among the PI speed regulator, the offset-free MPC and the proposed ADRC under various loads. **a** Sliding distance. **b** Sliding speed

9.6 Summary

This chapter presents a novel ADRC scheme based on ESO and NLEF controller for direct-drive elevator traction machine drives to estimate and reject the total disturbance in order to reduce the sliding distance during startup and enhance the robustness. On behalf of the core part of ADRC, the ESO acts as a current compensation model to enhance the ability of rejecting interference of the system. In order to overcome the sliding back of the elevator car caused by the integral term of conventional PI controller, the nonlinear rough feedback is used in the regulator of speed loop to accelerate the response speed. Both the stability and the parameter selection of ESO and NLEF controller are analyzed, especially when considering normal parameters of the traction machine. Instead of applying the conventional PI as the speed regulator, the proposed control strategy adopting ADRC with ESO and NLEF can effectively improve the dynamic performance and provide the suitable and smooth equivalent current reference, which benefits the robustness of the system and decreases the striking. Therefore, the riding comfort can be improved due to the smaller sliding distance and lower sliding speed during the zero-servo process. Experimental results verify the effectiveness and feasibility of the proposed control strategy without vibration and overshoot for the direct-drive elevators.

References

1. Türker T, Buyukkeles U, Bakan AF (2016) A robust predictive current controller for PMSM drives. *IEEE Trans Industr Electron* 63(6):3906–3914
2. Kumar GLSNVAV, Jain AK (2014) Robust design and analysis with wide speed operation of surface mounted PMSM drive. In: 2014 IEEE international conference on power electronics, drives and energy systems (PEDES), Mumbai, pp 1–6
3. Linares-Flores J, García-Rodríguez C, Sira-Ramírez H et al (2015) Robust backstepping

- tracking controller for low-speed PMSM positioning system: design, analysis, and implementation. *IEEE Trans Industr Inf* 11(5):1130–1141
4. Hong X, Deng Z, Wang S, Huang L et al (2010) A novel elevator load torque identification method based on friction model. In: *IEEE APEC in proc. 25th annu*, pp 2021–2024
 5. Wang G, Zhang G, Yang R et al (2012) Robust low-cost control scheme of direct-drive gearless traction machine for elevators without a weight transducer. *IEEE Trans Ind Appl* 48(3):996–1005
 6. Shen A (2015) Initial rotor position estimation and sliding preventing for elevators with surface-mounted PMSMs. *Int J Electron* 103(3):1–17
 7. Wang G, Xu J, Li T et al (2014) Weight-transducerless starting torque compensation of gearless permanent magnet traction machine for direct-drive elevators. *IEEE Trans Ind Electron* 60(9):4594–4604
 8. Wang G, Qi J, Xu J et al (2015) Antirollback control for gearless elevator traction machines adopting offset-free model predictive control strategy. *IEEE Trans Ind Electron* 62(10):6194–6203
 9. Li J, Xia Y, Qi X et al (2015) Absolute stability analysis of non-linear active disturbance rejection control for single-input–single-output systems via the circle criterion method. *IET Control Theory Appl* 9(15):2320–2329
 10. Wang G, Wang B, Chen L et al (2017) Weight-transducerless control strategy based on active disturbance rejection theory for gearless elevator drives. *Electric Power Appl IET* 11(2):289–299
 11. Rahman MM, Chowdhury AH (2015) Comparative study of ADRC and PID based load frequency control. In: *2015 international conference on electrical engineering and information communication technology (ICEEICT)*, Dhaka, pp 1–5
 12. Han J (2009) From PID to active disturbance rejection control. *IEEE Trans Ind Electron* 56(3):900–906
 13. Gao ZQ (2003) Scaling and bandwidth-parameterization based controller tuning. In: *Proceedings of the 2003 American control conference*, pp 4989–4996
 14. Xue W, Bai W, Yang S et al (2015) ADRC with adaptive extended state observer and its application to air–fuel ratio control in gasoline engines. *IEEE Trans Ind Electron* 62(9):5847–5857
 15. Fadali MS (2014) On the stability of Han’s ADRC. In: *2014 American control conference*, Portland, OR, pp 3597–3601